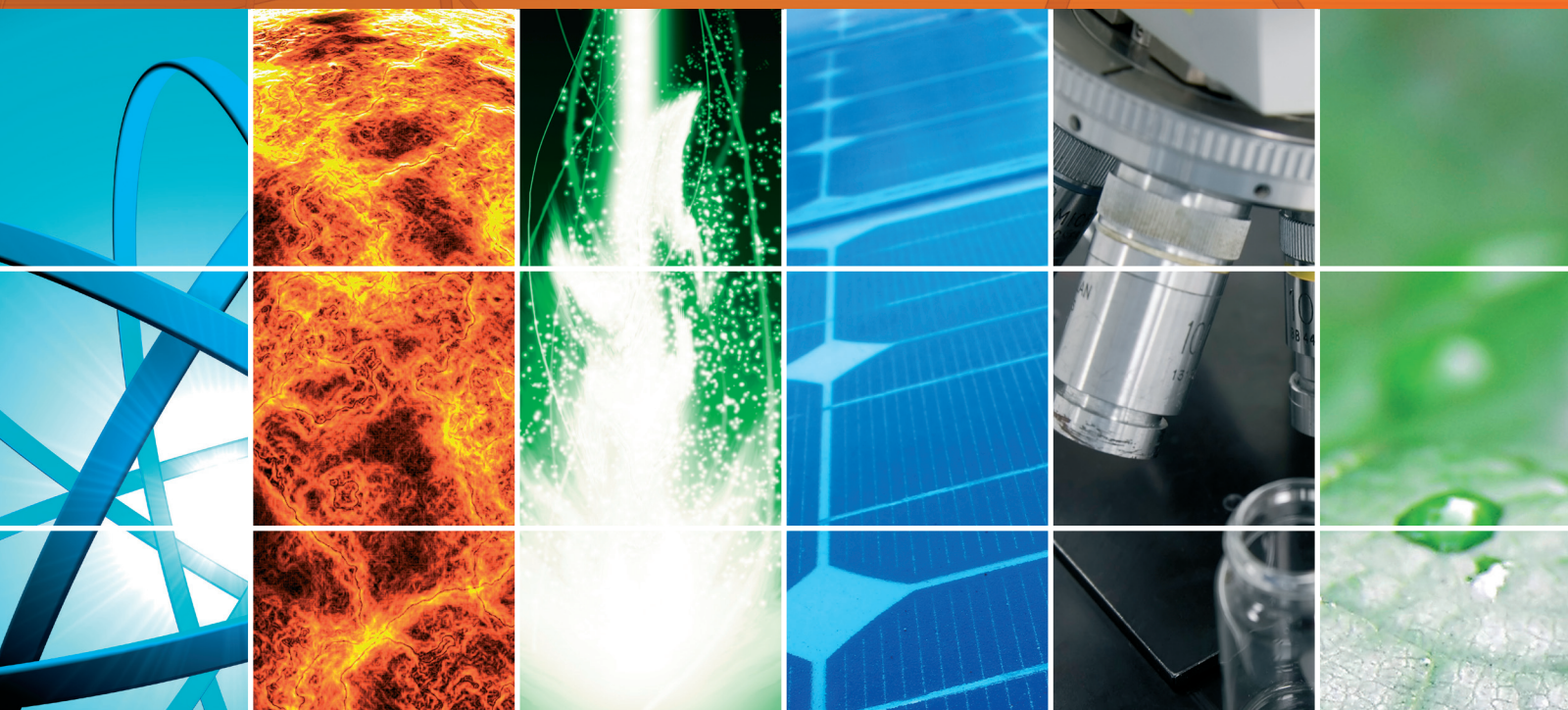


Photovoltaic Materials and Devices 2016

Guest Editors: Bhushan Sopori, Prakash Basnyat, and Vishal Mehta





Photovoltaic Materials and Devices 2016

International Journal of Photoenergy

Photovoltaic Materials and Devices 2016

Guest Editors: Bhushan Sopori, Prakash Basnyat,
and Vishal Mehta



Copyright © 2016 Hindawi Publishing Corporation. All rights reserved.

This is a special issue published in "International Journal of Photoenergy." All articles are open access articles distributed under the Creative Commons Attribution License, which permits unrestricted use, distribution, and reproduction in any medium, provided the original work is properly cited.

Editorial Board

- M. S.A. Abdel-Mottaleb, Egypt
Angelo Albini, Italy
Maan Alkaisi, New Zealand
Xavier Allonas, France
Nicolas Alonso-Vante, France
Alberto Alvarez, Mexico
Wayne A. Anderson, USA
Raja S. Ashraf, UK
Vincenzo Augugliaro, Italy
Detlef W. Bahnemann, Germany
Antonio Barbon, Italy
Valeriy Batoev, Russia
Laura Bellia, Italy
Ignazio Renato Bellobono, Italy
Raghu N. Bhattacharya, USA
Simona Binetti, Italy
Fabio Bisegna, Italy
Thomas M. Brown, Italy
Stephan Buecheler, Switzerland
Gion Calzaferrì, Switzerland
Joaquim Carneiro, Portugal
Carlo S. Casari, Italy
Yatendra S. Chaudhary, India
Chuncheng Chen, China
Věra Cimrová, Czech Republic
Juan M. Coronado, Spain
P. Davide Cozzoli, Italy
Ying Dai, China
Dionysios D. Dionysiou, USA
Abderrazek Douhal, Spain
Miroslav Dramićanin, Serbia
Mahmoud M. El-Nahass, Egypt
Polycarpos Falaras, Greece
Chris Ferekides, USA
Paolo Fornasiero, Italy
Manuel Fuentes Conde, Spain
Hermenegildo García, Spain
Germà García-Belmonte, Spain
David García-Fresnadillo, Spain
Elisa Isabel Garcia-Lopez, Italy
Beverley Glass, Australia
Daniel Glossman-Mitnik, Mexico
Mohammed Ashraf Gondal, KSA
Giulia Grancini, Switzerland
Hidehisa Hagiwara, Japan
Anthony M. Harriman, UK
Michael D. Heagy, USA
Shinya Higashimoto, Japan
Cheuk-Lam Ho, Hong Kong
Wing-Kei Ho, Hong Kong
Jürgen Hüpkès, Germany
Adel A. Ismail, Egypt
Chun-Sheng Jiang, USA
Jurga Juodkazyte, Lithuania
Shahed Khan, USA
Sylvie Lacombe, France
Fernando Langa, Spain
Cooper H. Langford, Canada
Stefan Lis, Poland
Vittorio Loddo, Italy
Gongxuan Lu, China
Wouter Maes, Belgium
Manuel Ignacio Maldonado, Spain
Tapas Mallick, UK
Dionissios Mantzavinos, Greece
Ugo Mazzucato, Italy
Sheng Meng, China
Santolo Meo, Italy
Alberto Mezzetti, France
Claudio Minerò, Italy
Edgar Moctezuma, Mexico
Thomas Moehl, Switzerland
Antoni Morawski, Poland
Franca Morazzoni, Italy
Fabrice Morlet-Savary, France
Mohammad Muneer, India
Ebinazar B. Namdas, Australia
Maria da Graça P. Neves, Portugal
Tebello Nyokong, South Africa
Tsuyoshi Ochiai, Japan
Kei Ohkubo, Japan
Boris Orel, Slovenia
Leonidas Palilis, Greece
Leonardo Palmisano, Italy
Ravindra K. Pandey, USA
Thierry Pauporté, France
Pierre Pichat, France
Philippe Poggi, France
Gianluca Li Puma, UK
Tijana Rajh, USA
Peter Robertson, UK
Leonardo Sandrolini, Italy
Avigdor Scherz, Israel
Elena Selli, Italy
Jinn Kong Sheu, Taiwan
Panagiotis Smirniotis, USA
Bhushan Sopori, USA
Waldemar Stampor, Poland
Zofia Stasicka, Poland
Elias Stathatos, Greece
Jegadesan Subbiah, Australia
Velumani Subramaniam, Mexico
M. Swaminathan, India
Mohamad-Ali Tehfe, Canada
K. R. Justin Thomas, India
Nikolai V. Tkachenko, Finland
Ahmad Umar, KSA
Thomas Unold, Germany
Veronica Vaida, USA
Roel van De Krol, Germany
Mark van Der Auweraer, Belgium
Rienk Van Grondelle, Netherlands
W. G.J.H.M. Van Sark, Netherlands
Sergey Varlamov, Australia
Xuxu Wang, China
David Worrall, UK
Yanfa Yan, USA
Hongtao Yu, USA
Jiangbo Yu, USA
Klaas Zachariasse, Germany

Contents

Photovoltaic Materials and Devices 2016

Bhushan Sopori, Prakash Basnyat, and Vishal Mehta
Volume 2016, Article ID 9427450, 2 pages

Sliding Mode Real-Time Control of Photovoltaic Systems Using Neural Estimators

J. A. Ramos-Hernanz, O. Barambones, J. M. Lopez-Guede, I. Zamora, P. Eguia, and M. Farhat
Volume 2016, Article ID 5214061, 16 pages

A Simple Technique for Sustaining Solar Energy Production in Active Convective Coastal Regions

Moses E. Emetere, Marvel L. Akinyemi, and Etimbuk B. Edeghe
Volume 2016, Article ID 3567502, 11 pages

Wide-Range Enhancement of Spectral Response by Highly Conductive and Transparent $\mu\text{-SiO}_x\text{:H}$ Doped Layers in $\mu\text{-Si:H}$ and $\text{a-Si:H}/\mu\text{-Si:H}$ Thin-Film Solar Cells

Pei-Ling Chen, Po-Wei Chen, Min-Wen Hsiao, Cheng-Hang Hsu, and Chuang-Chuang Tsai
Volume 2016, Article ID 8172518, 8 pages

Preparation of a Textile-Based Dye-Sensitized Solar Cell

Klaus Opwis, Jochen Stefan Gutmann, Ana Rosa Lagunas Alonso, Maria Jesus Rodriguez Henche, Mikel Ezquer Mayo, Fanny Breuil, Enrico Leonardi, and Luca Sorbello
Volume 2016, Article ID 3796074, 11 pages

The Influence of Heating Time and Temperature on the Properties of CIGSSe Solar Cells

Marco Giacomo Flammini, Nicola Debernardi, Maxime Le Ster, Brendan Dunne, Johan Bosman, and Mirjam Theelen
Volume 2016, Article ID 4089369, 7 pages

Accelerated Life Test for Photovoltaic Cells Using Concentrated Light

Daniel Tudor Cotfas, Petru Adrian Cotfas, Dan Ion Floroian, and Laura Floroian
Volume 2016, Article ID 9825683, 7 pages

Investigation of Boron Thermal Diffusion from Atmospheric Pressure Chemical Vapor Deposited Boron Silicate Glass for N-Type Solar Cell Process Application

Ikuo Kurachi and Kentaro Yoshioka
Volume 2016, Article ID 8183673, 8 pages

Data-Driven Photovoltaic System Modeling Based on Nonlinear System Identification

Ayedh Alqahtani, Mohammad Alsaffar, Mohamed El-Sayed, and Bader Alajmi
Volume 2016, Article ID 2923731, 9 pages

Improving the Performance of a Semitransparent BIPV by Using High-Reflectivity Heat Insulation Film

Huei-Mei Liu, Chin-Huai Young, Der-Juinn Horng, Yih-Chearng Shiue, and Shin-Ku Lee
Volume 2016, Article ID 4174216, 15 pages

Energy Storage Requirements for PV Power Ramp Rate Control in Northern Europe

Julius Schnabel and Seppo Valkealahti
Volume 2016, Article ID 2863479, 11 pages

Characterization of Photovoltaic Panels by means of Thermograph Analysis

Noe Samano, José Alfredo Padilla-Medina, and Nimrod Vázquez

Volume 2016, Article ID 8560728, 7 pages

Comparison of Different MPPT Algorithms with a Proposed One Using a Power Estimator for Grid Connected PV Systems

Manel Hlaili and Hfaiedh Mechergui

Volume 2016, Article ID 1728398, 10 pages

Enhanced Light Scattering by Preferred Orientation Control of Ga Doped ZnO Films Prepared through MOCVD

Long Giang Bach, Nam Giang Nguyen, and Van Thi Thanh Ho

Volume 2016, Article ID 1217576, 7 pages

An Efficient Metal-Free Hydrophilic Carbon as a Counter Electrode for Dye-Sensitized Solar Cells

Mojgan Kouhnavard, Norasikin Ahmad Ludin, Babak Vazifehkhah Ghaffari, Kamaruzzaman Sopian, Norshazlinah Abdul Karim, and Mikio Miyake

Volume 2016, Article ID 5186762, 7 pages

A Power Case Study for Monocrystalline and Polycrystalline Solar Panels in Bursa City, Turkey

Ayşegül Taşcıoğlu, Onur Taşkın, and Ali Vardar

Volume 2016, Article ID 7324138, 7 pages

New 1,3,4-Oxadiazole Based Photosensitizers for Dye Sensitized Solar Cells

Umer Mehmood, Ibnelwaleed A. Hussein, and Muhammad Daud

Volume 2015, Article ID 637652, 8 pages

Editorial

Photovoltaic Materials and Devices 2016

Bhushan Sopori,¹ Prakash Basnyat,¹ and Vishal Mehta²

¹National Renewable Energy Laboratory, 1617 Cole Boulevard, Lakewood, CO 80401, USA

²Mechanical Engineering Department, Ohio Northern University, 525 S Main St, Ada, OH 45810, USA

Correspondence should be addressed to Bhushan Sopori; bhushan.sopori@nrel.gov

Received 9 August 2016; Accepted 14 August 2016

Copyright © 2016 Bhushan Sopori et al. This is an open access article distributed under the Creative Commons Attribution License, which permits unrestricted use, distribution, and reproduction in any medium, provided the original work is properly cited.

Photovoltaic energy continues to grow with about 59 GW of solar PV installed in 2015. While most of the PV production (about 93%) was Si wafer based, both CdTe and CI(G)S are growing in their shares. There is also continued progress at the laboratory scale in OPV and dye sensitized solar cells. As the market grows, emphasis on reducing the cost of modules and systems continues to grow. This is the fourth special issue of this journal that is dedicated to gathering selected papers on recent advances in materials, devices, and modules/PV systems. This issue contains sixteen papers on various aspects of photovoltaics. These fall in four broad categories of novel materials, device design and fabrication, modules, and systems. A brief description and salient results of these papers are given below. We hope that readers enjoy this issue.

Novel Materials. The paper “Enhanced Light Scattering by Preferred Orientation Control of Ga Doped ZnO Films Prepared through MOCVD” by L. G. Bach et al. explores effective approach by employing low temperature ZnO buffer layer prior to high temperature GZO film growth that can make pyramidal surface structure of GZO film for effective light trapping. U. Mehmood et al.’s paper “New 1,3,4-Oxadiazole Based Photosensitizers for Dye Sensitized Solar Cells (DSSCs)” explores the fabrication and characterization of 1,3,4-oxadiazole photosensitizers for photovoltaic application. The paper by M. Kouhnavard et al. entitled “An Efficient Metal-Free Hydrophilic Carbon as a Counter Electrode for Dye-Sensitized Solar Cells” introduces new method for the production of metal-free and cost-effective counter electrode for dye sensitized solar cell by using doctor blading method. P.-L. Chen et al.’s paper “Wide-Range Enhancement of Spectral Response by Highly Conductive and Transparent $\mu\text{c-SiOx:H}$ Doped Layers in $\mu\text{c-Si:H}$ and

$\text{a-Si:H}/\mu\text{c-Si:H}$ Thin-Film Solar Cells” explores the increase of light absorption in thin film silicon solar cells by p- and n-type $\mu\text{c-SiOx:H}$ layers by using spectral response method.

Device Design and Fabrication. Research paper “Investigation of Boron Thermal Diffusion from Atmospheric Pressure Chemical Vapor Deposited Boron Silicate Glass for N-Type Solar Cell Process Application” by I. Kurachi and K. Yoshioka reveals the thermal boron diffusion from the BSG film and process stability for device surface properties by using newly developed boron diffusion simulator. The paper by K. Opwis et al. entitled “Preparation of a Textile-Based Dye-Sensitized Solar Cell” presents textile fabrics based new dye sensitized solar cell and deposition techniques of different layers for large area device to achieve low weight, flexibility, and mechanical strength structure. M. G. Flammini et al.’s paper “The Influence of Heating Time and Temperature on the Properties of CIGSSe Solar Cells” explains the effect of heat treatment of CIGSSe modules at different temperature for different time.

Modules and Systems. J. Schnabel and S. Valkealahti’s paper entitled “Energy Storage Requirements for PV Power Ramp Rate Control in Northern Europe” illustrates the simulations results that explain the behavior of the PV power fluctuation in northern European climatic conditions and requirements for sizing the energy storage system to compensate for the fluctuations. N. Samano et al.’s paper “Characterization of Photovoltaic Panels by means of Thermograph Analysis” explains the thermal behavior, defect monitoring, and process control of multicrystalline module by use of thermograph analysis. The paper by A. Alqahtani et al. entitled “Data-Driven Photovoltaic System Modeling Based on Non-linear System Identification” deals with the documentation

of a PV system characteristics with a switch mode power convertor which can contribute to the future design and implementation of nonlinear control strategies. The paper “Improving the Performance of a Semitransparent BIPV by Using High-Reflectivity Heat Insulation Film” by H.-M. Liu et al. explains the influence of the different heat insulation solar glass structure on the building integrated photovoltaic systems in Taiwan. J. A. R. Hernanz et al.’s paper “Sliding Mode Real Time Control of Photovoltaic Systems Using Neural Estimators” explores the novel control for tracking maximum power point while a Boost DC/DC convertor is used in a photovoltaic module. The paper by D. T. Cotfas et al. entitled “Accelerated Life Test for Photovoltaic Cells Using Concentrated Light” introduces new method for the life testing of photovoltaic cells by using light and temperature from a concentrated light solar simulator. M. Hlaili and H. Mechergui’s paper “Comparison of Different MPPT Algorithms with a Proposed One Using a Power Estimator for Grid Connected PV Systems” compares several widely adopted MPPT algorithms and proposes one effective method of injecting the high quality sinusoidal current to the grid. M. Emeter et al.’s paper “A Simple Technique for Sustaining Solar Energy Production in Active Convective Coastal Regions” studies the issue of solar radiation irregularities due to solar shading in the coastal region and proposes a mathematical model to explain the collective solar radiation over a massive coastal area. The paper by A. Taşçıoğlu et al. entitled “A Power Case Study for Monocrystalline and Polycrystalline Solar Panels in Bursa City, Turkey” introduces study of time dependent power performance and power values that can be generated from mono- and polycrystalline solar panels at the existing environmental condition of Bursa city in Turkey.

*Bhushan Sopori
Prakash Basnyat
Vishal Mehta*

Research Article

Sliding Mode Real-Time Control of Photovoltaic Systems Using Neural Estimators

**J. A. Ramos-Hernanz,¹ O. Barambones,² J. M. Lopez-Guede,²
I. Zamora,³ P. Eguia,³ and M. Farhat⁴**

¹Electrical Engineering Department, Faculty of Engineering Vitoria-Gasteiz, University of the Basque Country, Nieves Cano 12, 01006 Vitoria-Gasteiz, Spain

²Systems Engineering and Automatic Control Department, Faculty of Engineering Vitoria-Gasteiz, University of the Basque Country, Nieves Cano 12, 01006 Vitoria-Gasteiz, Spain

³Electrical Engineering Department, Faculty of Engineering, University of the Basque Country, Alameda Urquijo, s/n, 48013 Bilbao, Spain

⁴Department of Electrical, Electronics and Communications Engineering, American University of Ras Al Khaimah, Sheikh Saqr Bin Khalid Rd., Ras Al Khaimah, UAE

Correspondence should be addressed to J. A. Ramos-Hernanz; josean.ramos@ehu.es

Received 15 April 2016; Revised 13 June 2016; Accepted 28 June 2016

Academic Editor: Prakash Basnyat

Copyright © 2016 J. A. Ramos-Hernanz et al. This is an open access article distributed under the Creative Commons Attribution License, which permits unrestricted use, distribution, and reproduction in any medium, provided the original work is properly cited.

The maximum power point tracking (MPPT) problem has attracted the attention of many researchers, because it is convenient to obtain the maximum power of a photovoltaic module regardless of the weather conditions and the load. In this paper, a novel control for a boost DC/DC converter has been introduced. It is based on a sliding mode controller (SMC) that takes a current signal as reference instead of a voltage, which is generated by a neuronal reference current generator. That reference current indicates the current (I_{MPP}) at the maximum power point (MPP) for given weather conditions. In order to test the designed control system, a photovoltaic module model based on a second artificial neuronal network (ANN) has been obtained from experimental data gathered during 18 months in the Faculty of Engineering Vitoria-Gasteiz (Spain). We have analyzed the performance of such model and we found that it is very accurate (MSE = 0.062 A and $R = 0.991$ with test dataset). We also have tested the performance of the overall SMC design with both simulated and real tests, concluding that it guarantees that the power in the output of the converter is very close to the power of the photovoltaic module output.

1. Introduction

In the recent Paris Conference [1], we can find important initiatives for supporting green energies. With regard to photovoltaic energy, two main initiatives stand out: the former, the creation of the “Alliance for Solar Energy” promoted by the Government of India and signed by 120 countries, and the latter, the creation of the “Global Solar Council,” mainly composed by associations devoted to renewable and solar energy from the five continents. The council was created with the aim of promoting photovoltaic energy worldwide through a unique interlocutor of the sector with the international

organizations, increasing collaboration between different countries and supporting emerging solar markets.

Due to its simplicity of operation, robustness, and cheapness, photovoltaic solar energy is a very appropriate source of energy, especially for emerging countries, where the construction of large electrical infrastructures is infeasible in some areas. Moreover, in recent years, great progress in this area, better efficiency, and improved performance of photovoltaic modules have been achieved. These factors, along with the advancement of electronic technology, make this type of energy even more valued.

The optimal operation of a photovoltaic system depends on two types of variables; the first type is those that are imposed and depend on weather conditions, that is, irradiance and temperature. The second type of variables is those that can be modified to search for the desired performance of the system, given the weather conditions. This is the case that we are facing in this paper, that is, working at the maximum power point. In order to get it, it is mandatory to get an appropriate performance of the converter.

The search of control algorithms for improving converters performance in photovoltaic systems has a considerable significance for many researchers [2, 3]. Among different control algorithms, the sliding mode control is successful due to its many advantages [4–6], the most outstanding being its easy implementation, simplicity, robustness, and high performance in many fields such as robotics [7] or photovoltaic energy [8].

When a sliding mode controller is tuned by scientists or practitioners, it is desired to have a model of the photovoltaic module to control in order to carry out preliminary analytic or simulated tests instead of using the actual module. In the literature, there are a number of models of different complexities to explain the electrical behavior of photovoltaic modules. In order to clarify such variety, we can make a first division into theoretical and empirical models. Theoretical models use a characteristic equation [9] (see Section 2.1), among them being a number of models which use different degrees of freedom; that is, some of them are very complete but in other cases researchers determine/approximate them in several practical ways in order to get these models being useful.

The most complete model used in the literature is based on a double diode equivalent circuit which leads to a 7-parameter model, that is, a_1 , a_2 , R_S , R_{SH} , I_{01} , I_{02} , and I_{PH} . Two-diode model has been used around the fifties [10, 11]. Later, Gow and Manning, using the same model, adjusted the parameters through Levenberg-Marquardt and Newton-Raphson algorithms [12]. This model is still being used in more recent literature [13, 14].

In [15], the approach used by Villalva et al. is to modify the value of R_S and R_{SH} and adjust them by means of an iterative algorithm to fit the theoretical curve to experimental data in the MPP, implementing the complete model under Simulink-SimPowerSystem assisted by Simulink. De Soto et al. used this 5-parameter approach building three versions: from a basic model with two approximations of five magnitudes to a model where they are calculated [16]. They compared the results generated by this model with experimental data obtained from a facility by other researchers and studied the effect of changing R_S and R_{SH} .

A number of researchers make some approximations of the characteristic parameters. The most usual of them is to assume that $R_{SH} = \infty$, so $I_{SH} = 0$ A and the third term of the characteristic equation is discarded leading to a 4-parameter model. In [17, 18], this simplification is carried out when the model of the exact same module is built following almost the same procedure. These works are quite similar to [19]. However, there are several differences: the first calculates the temperature coefficient k_0 used to calculate the short circuit

current I_{SC} , while the last one uses the value provided by the manufacturer; and the used numeric value of ideality factor of the diode is different between [17, 18] and [19]. A model where the ideality factor can be varied to fit it to different PV technologies is proposed in [20]. As a last 4-parameter model, Bayrak and Cebeci formulate a distinct model from the previous ones and develop the model of a microgrid facility and hybrid PV and fuel system [21].

Ramos-Hernanz et al. use polynomial interpolation and describe a model which allows obtaining only the IV and PV curves and provides further insight into the behavior of the photovoltaic module, but it is suited only for a range of temperatures and irradiances [22].

Another approach to the empirical methods is modeling the behavior of the photovoltaic elements by means of artificial neuronal networks [23]. In [24], an interesting review of different approaches is presented, while [25, 26] developed a practical model, but with very narrow amplitudes for irradiance and temperature. Lopez-Guede et al. are seeking to expand these limits [27], but in spite of expanding the range of magnitudes, they still obtain partial models with data captured during quite small time range (two months). Bonanno et al. use RFB neural networks to generate two models [28]. The former is to obtain I_{PV} from irradiance and voltage and uses 5,600 real samples. The second one is devoted to obtain P_{PV} , again from irradiance and voltage using 4,600 real samples.

Researchers reported a relative MSE of 2% and 1%, respectively, but the test has been done with training data, so in fact they have reported the training accuracy. In this paper, a new sliding mode controller (SMC) for maximum power point tracking in a photovoltaic module is introduced, and its performance is demonstrated in a real installation. Its main characteristic is that as reference generator it uses an artificial neural network which will seek for a reference current I_{REF} corresponding to the maximum power operating point (I_{MPP}). Gow and Manning have been developing works related to this paper; for example, in [12], they have used the facilities with a different photovoltaic module to design a control system that uses a voltage reference generator implemented through a polynomial equation.

In order to design the SMC controller, we have carried out several tasks related to the three main elements of the autonomous photovoltaic system (photovoltaic module, converter, and load):

- (i) A model of the Mitsubishi Electric PV-TD185MF5 185 W photovoltaic module has been developed based on neural networks, using actual measurements taken during 18 months, with an approximate average duration of ten minutes for each measure. A total of 62,912 samples (I_{PV} , V_{PV} , temperature T , and irradiance G) have been obtained, covering a broad number of different weather situations.
- (ii) These real data have been used to draw the characteristic curves of the module and calculate the MPP in each one of them. These points were learned by a second artificial neural network in order to obtain the reference current at which that the module operates

at its optimum point, given the power supplied by the module and the temperature. That is, a neuronal reference current generator implementation has been obtained.

- (iii) A SMC has been designed, so that, given a reference current, the photovoltaic module will work at its point of maximum power.
- (iv) And finally, the joint behavior of all these components has been validated through simulated and real tests using the installation that is at the Faculty of Engineering Vitoria-Gasteiz (University of the Basque Country, Spain).

The document is structured as follows: in Section 2, we give a short background on some basic concepts used in this paper as photovoltaic generators, characteristic curves of photovoltaic modules, boost converters DC/DC, artificial neural networks, and sliding mode control. Section 3 describes how the model of a photovoltaic module has been obtained using artificial neural networks. In Section 4, we describe the sliding mode control, as well as the modeling process of the reference current generator, while the results obtained are discussed in Section 5. Finally, Section 6 gives our main conclusions.

2. Background

2.1. Photovoltaic Generator. A solar cell can be modeled as a PN semiconductor junction which when exposed to light converts light energy into electrical energy, generating a DC current which will mainly depend on the existing solar irradiance and temperature.

Electric generators are usually classified as current or voltage sources. A photovoltaic device shows a functional mixed behavior, which is a source of current or voltage depending on the operating point in which the device is working.

Most manufacturers provide few experimental data on the performance of solar cells working at ideal operating conditions. These data are typically provided in Standard Test Conditions (STC) (1,000 W/m², 25° (±2)°C, AM 1.5 according to EN 6090-4). There are manufacturers that also provide these data for other conditions (800 W/m², Nominal Operating Cell Temperature (NOCT), AM 1.5). Usually the provided data are short circuit current (I_{SC}), open circuit voltage (V_{OC}), current at the maximum power point (I_{MPP}), voltage at the maximum power point (V_{MPP}), temperature coefficient of open circuit voltage V_{OC} (K_V) [%/K], and temperature coefficient of short circuit current I_{SC} (K_I) [%/K].

The basic model of a photovoltaic generator is a photovoltaic cell. The cell can be modeled as a diode, usually made of silicon and designed to maximize the absorption of photons and to minimize the reflection, converting a part of the received solar energy to electric energy. The ideal cell model is presented in the dotted area of Figure 1.

However, there are some recombination phenomena in the material, specifically in the depletion layer of the

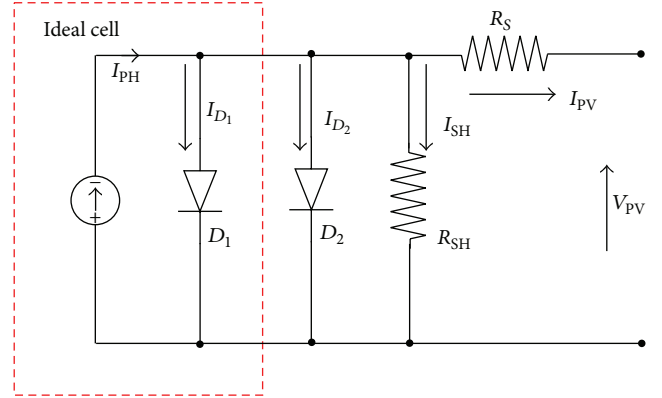


FIGURE 1: Two-diode model of a photovoltaic cell.

semiconductor which can be modeled through a second diode, leading to a two-diode model. The typical two-diode equivalent circuit of a photovoltaic cell is shown in Figure 1.

Analyzing the schema of Figure 1, we define the following equations:

$$I = I_{PV} = I_{PH} - I_{D1} - I_{D2} - I_{SH}$$

$$I = \left[\begin{array}{c} \frac{I_{PH}}{I_{PH}} - \frac{I_{D1}}{I_{01} \cdot \left(e^{q(V+IR_S)/akT} - 1 \right)} \\ - \frac{I_{D2}}{I_{02} \cdot \left(e^{q(V+IR_S)/akT} - 1 \right)} \\ - \frac{I_{SH}}{(V + IR_S)} \\ \frac{I_{SH}}{R_{SH}} \end{array} \right], \quad (1)$$

where I_{01} is a saturation current of diode 1 (A), I_{02} is a saturation current of diode 2 (A), V is a cell voltage (V), q is the charge of an electron (1.6×10^{-19} C), a is the diode ideality constant, k is Boltzmann's constant 1.38×10^{-23} (J/K), and T is the cell temperature.

Many researchers use some simplifications obtaining equations that define the model of a single diode [17–20] due to its simplicity and reliability.

Analyzing the schema of Figure 2, we define the following equations:

$$I = I_{PV} = I_{PH} - I_D - I_{SH}, \quad (2)$$

$$I = \frac{I_{PH}}{I_{PH}} - \frac{I_D}{I_0 \cdot \left(e^{q(V+IR_S)/akT} - 1 \right)} - \frac{I_{SH}}{(V + IR_S)} \frac{I_{SH}}{R_{SH}}. \quad (3)$$

There are a number of data which cannot be found in data sheets as series resistance (R_S), shunt resistance (R_{SH}), diode ideality constant (a), and saturation current of the diode (I_0).

Both (2) and (3) are similar, but (3) has been expanded representing the output current generated by the module (I_{PV}) which depends on the voltage of the photovoltaic module (V_{PV}) and on solar radiation and temperature on the photovoltaic module.

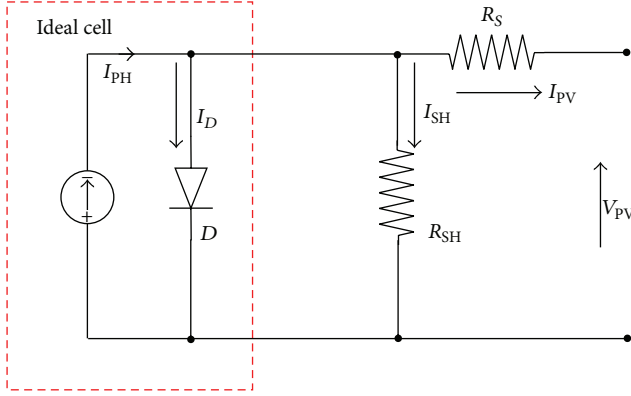


FIGURE 2: One-diode model of a photovoltaic cell.

We define the current produced between electrodes of a photocell as the photogenerated current or photocurrent according to

$$I_{PH} = \left(\frac{G}{G_{REF}} \right) (I_{SC,REF} + K_{I_{sc}} (T - T_{REF})), \quad (4)$$

where G is working irradiance (W/m^2), G_{REF} is the reference irradiance (usually $1,000 W/m^2$), $I_{SC,REF}$ is the short circuit current of reference (A), $K_{I_{sc}}$ is the temperature coefficient of short circuit current ($\%/^{\circ}C$), T is the cell temperature ($^{\circ}C$), and T_{REF} is the reference temperature (usually $25^{\circ}C$).

Moreover, the reverse saturation current of the diode (I_0) can be defined as shown:

$$I_{0,REF} = \frac{I_{SC,REF}}{e^{(qV_{OC,REF}/akT_{REF})-1}} \quad (5)$$

$$I_0 = I_{0,REF} \left(\frac{T}{T_{REF}} \right)^3 e^{[(qE_g/ak)((1/T)-(1/T_{REF}))]},$$

where $V_{OC,REF}$ is the open circuit reference voltage and E_g is the band gap energy (for silicon it has a value of $1.11 eV$ at $300^{\circ}K$).

In order to apply these concepts to the development of a solar cell model, we have chosen the PV-Mitsubishi TD1185MF5 PV module for its modeling. This module has 50 polycrystalline cells connected in series. Its main characteristics are specified in Table 1.

2.2. Characteristic Curves. One of the best tools to describe the operation of a photovoltaic module is the current-voltage (I - V) relationship, that is, the I - V , P - V , and P - I characteristic curves. The IV curve of an ideal solar cell is superimposing the I - V curve of the diode and the photogenerated current. These curves result from mathematical expressions that describe the behavior of the photovoltaic cells which constitute the module.

Conceptually, the I - V curve represents the current and voltage combinations in which the cell might work if the irradiance and cell temperature could be maintained constant. The same applies to P - I curves (power-current) and P - V (power-voltage).

TABLE 1: Key specifications of the Mitsubishi PV module.

Manufacturer	Mitsubishi
Model	PV-TD185-MF5
Cell type	Polycrystalline
Maximum power [W]	185
Open circuit voltage V_{OC} [V]	30.60
Short circuit current I_{SC} [A]	8.13
Voltage at P_{MPP} [V]	24.40
Current at P_{MPP} [A]	7.58
Temperature coefficient of V_{OC} [$\%/^{\circ}C$]	-0.346
Temperature coefficient of I_{SC} [$\%/^{\circ}C$]	0.057
Nominal operating cell temperature (NOCT) [$^{\circ}C$]	47.5

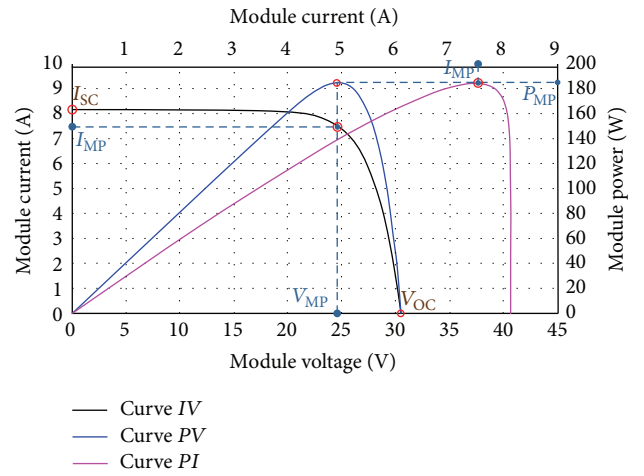


FIGURE 3: Characteristic curves of a photovoltaic module.

In order to evaluate the performance of solar cells and the photovoltaic systems design, we will rely on the electrical characteristics, that is, in the relations of voltage-current of the cells under different levels of radiation and temperatures. This requires understanding how solar radiation, the cell temperature, and electrical loads affect the behavior of the characteristic curves. The particular point of current and voltage of the curve at which the photovoltaic device works is determined by the load to which it is connected. If we have a high knowledge of these curves we can make a correct photovoltaic system design and an appropriate evaluation.

Figure 3 shows the characteristic curves I - V (black), P - V (blue), and P - I (magenta) of a module operating at a given temperature and irradiation. If these factors are changed, the obtained curves will be different. The inferior abscissa axis represents the working voltage (V) of the module and, in the upper one, the current (A). The current (A) is shown in the left ordinate axis, while the obtained power (W) is in the right one.

2.3. Boost DC/DC Converter. A DC converter must provide at its output a regulated DC voltage of a desired value. It must be done in the most efficient way and with as fewer losses as possible.

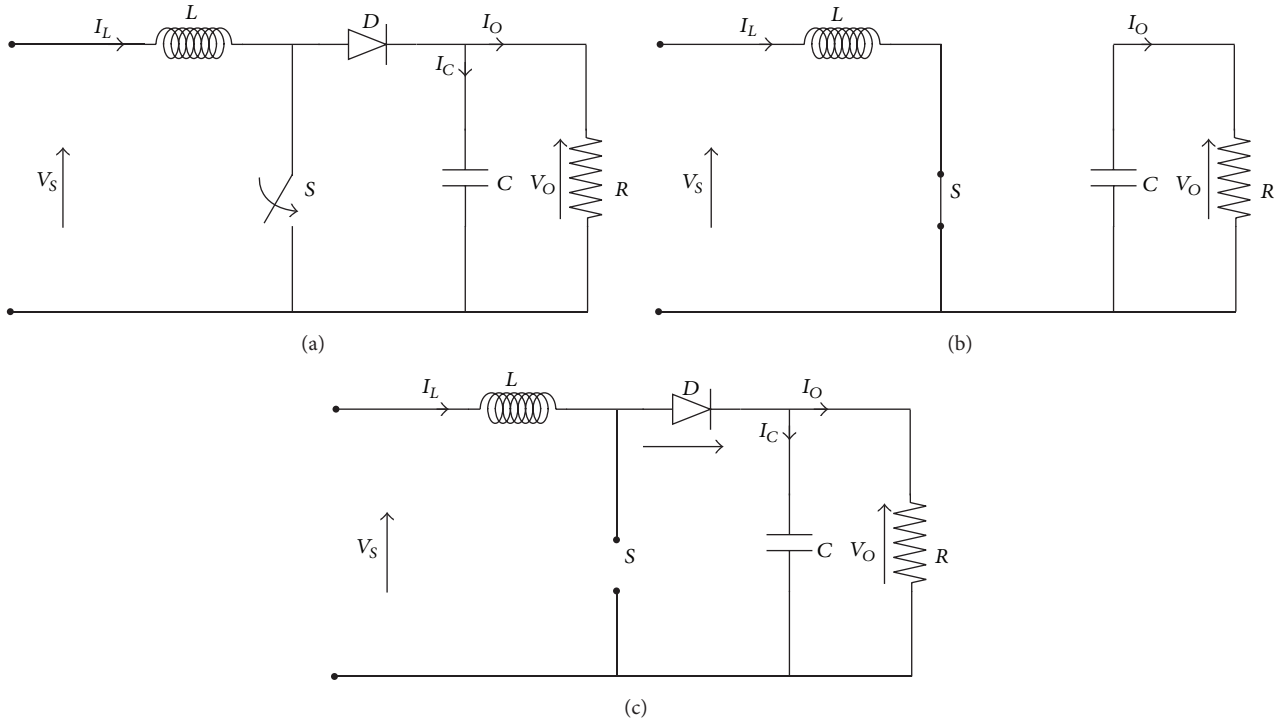


FIGURE 4: BOOST converter.

The most commonly used method to control the output voltage is the pulse width modulation (PWM), which consists in using a constant switching time (T). This time is the sum of driving time (T_{ON}) plus the blocking time (T_{OFF}), and varying the driving time (T_{ON}), it is possible to control the output average voltage.

The power given to the load is a function of the duty cycle (δ), which is defined as the relation between the time in which the converter is driving (T_{ON}) and the switching time ($T = T_{ON} + T_{OFF}$), that is, $\delta = T_{ON}/T$.

In photovoltaic systems, the DC/DC converter is placed between the PV generator and load, being responsible for adapting the energy produced by the generator following a defined control strategy, which usually tries that the system works at the maximum power point to increase the efficiency of the installation.

A concrete type of converter that we have used in our installation due to its characteristics is the boost converter. It provides an average output voltage exceeding the input value. We can see the converter topology in Figure 4(a).

These converters are nonlinear circuits, so in order to study them as linear circuits it is usual to decompose them into two subcircuits. Its linear operation mode depends on the state of the switch (S):

- (i) When the switch (S) is closed (see Figure 4(b)) during T_{ON} , the diode (D) is reverse biased, isolating the input and the output stages. The primary source voltage (V_S) is applied to the coil (L), which causes the (I_L) current to increase and thus the energy is

stored in the coil (L). The load (R_O) is fed only by the capacitor (C).

- (ii) When the switch (S) is open (see Figure 4(c)) during T_{OFF} , the diode is polarized. The voltage of the coil (L) is then added to the voltage of the primary source (V_S), providing at the output a larger voltage (V_O), larger than that of the primary source (V_S) and with the same polarity. In this way, the load (R_O) is fed by the coil (L) and the primary source (V_S).

In the case of a boost converter in continuous driving operating mode, the relations between the input (V_S , I_S , and R_{PV}) and output (V_O , I_O , and R_O) variables are given by

$$\begin{aligned} V_O &= \frac{V_S}{(1 - \delta)}, \\ I_O &= I_S (1 - \delta), \\ R_O &= \frac{R_{PV}}{(1 - \delta)^2}. \end{aligned} \quad (6)$$

Analyzing (6), we can notice that as $\delta \in (0, 1]$, the converter increases the voltage and reduces the current.

The dynamic model of a circuit of a boost converter is defined by

$$\begin{aligned} \frac{dI_L}{dt} &= \frac{V_S}{L} + \frac{1}{L} (u - 1) V_O \\ \frac{dV_O}{dt} &= \frac{1}{C} (I_L - I_O) - \frac{1}{C} u I_L, \end{aligned} \quad (7)$$

where $u \in \{0, 1\}$ represents the operation mode of the circuit when $u = 1$ (Figure 4(b)) and when $u = 0$ (Figure 4(c)). Finally, we can rewrite (7) as

$$\begin{aligned} \dot{x} &= f(x) + g(x)u, \\ x &= \begin{bmatrix} I_L \\ V_O \end{bmatrix}; \\ f(x) &= \begin{bmatrix} \frac{V_S}{L} \\ \frac{1}{C} \left(I_L - \frac{V_O}{R} \right) \end{bmatrix}; \\ g(x) &= \begin{bmatrix} -\frac{V_O}{L} \\ -\frac{I_L}{C} \end{bmatrix}. \end{aligned} \quad (8)$$

2.4. Artificial Neural Networks. Artificial neural networks (ANNs) are based on the operation mode of biological neural networks, although they have different functions and structures. ANNs try to mimic the human brain which is a very complex, nonlinear, and parallel system. In other words, it can perform many simultaneous operations unlike traditional computers, which only can perform one sequential operation at the same time.

The basic component of calculation is usually called neuron, node, or unit. It receives one or more inputs (x_i) from other units or from an external data source. Each input has an associated weight (w_{ij}), which is modified during the training process. The output (y_i) of each unit is a function of the sum of the weighted inputs, as shown in Figure 5:

$$y_i = f \left(\sum_j w_j y_j \right). \quad (9)$$

The main characteristics of the ANNs are the following:

- (i) *Adaptive Learning.* It is the process by which ANN can change their weights in response to input information. They learn to carry out tasks by means of training with examples or by an initial experience. They differentiate patterns by examples and can change their behavior depending on the environment, having a natural suitability to acquire knowledge through experience.
- (ii) *Self-Organization.* They use their learning ability to organize the information that they receive during the learning and/or operation. They can change their internal structure in order to perform a specific task.
- (iii) *Nonlinear Processing.* It allows them to process information from nonlinear phenomena. It increases network capacity to approximate functions and sorting patterns and increase their immunity to noise.
- (iv) *Parallel Processing.* Usually, a large number of processing nodes are used, with a high level of interconnectivity.

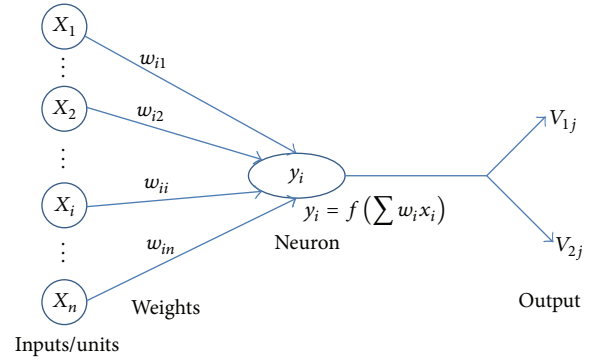


FIGURE 5: Generic artificial neural network structure.

- (v) *High Level of Fault Tolerance.* If a fault occurs even in a small number of neurons, although the system might be influenced, it does not suffer a sudden drop; that is, they can suffer considerable damage and continue to have an acceptable behavior. They have this capability because the information is stored in a distributed way.
- (vi) *Real-Time Operation.* They can face large processes quite quickly because ANNs are perfectly suited due to their parallel implementation.
- (vii) *Easy Insertion into Existing Technologies.* Thanks to the ease and speed that they can be trained and validated, ANNs can be transferred easily to an implementation in specific applications within existing or legacy systems.

2.5. Sliding Mode Control. The sliding mode control (SMC) is defined as using a control signal, switching at high frequency in order to carry the system state to a scalar field. The structure of the controller varies so that a representative point of the system follows a defined trajectory in the state space. It is based on the fact that it is easier to control first-order systems than those of order n . For this purpose, systems of order n are replaced by first-order equivalent systems.

The advantages of SMC are great accuracy, good stability, simplicity, and ruggedness, especially when the dynamics of the system in closed loop slides by the sliding surface, because it remains insensitive to variations in the model parameters and to external perturbations.

2.5.1. Sliding Surface. If in a system there is a sliding mode, the trajectories that intersect the sliding region remain on $S(x)$ except when they reach the end of the sliding surface. If the trajectory goes on the surface, it is said that the system is in sliding mode, as in Figure 6.

In order to analyze this technique, we will consider a nonlinear dynamical system defined by the following equations:

$$\dot{x} = f(x) + g(x)u, \quad x \in \mathfrak{R}^n, \quad u \in \mathfrak{R}, \quad (10)$$

where x is the output of interest, u is the discontinuous control input which can take the values 0 and 1 (their discontinuity points correspond with the shape changes of

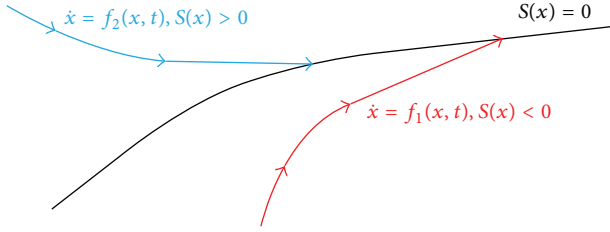


FIGURE 6: Sliding surface.

the converter), $X = [x, \dot{x}, \dots]^T$ is the state vector, $f(X)$ is the function that describes the system, and $g(X)$ is the control gain.

The variable sliding surface in time domain is defined in the state space \mathfrak{R}^n by the equation $S(X) = 0$ in which

$$S(X) = \left(\frac{d}{dt} + \lambda \right)^{(n-1)} e(X), \quad (11)$$

where λ is a strictly positive constant corresponding to the bandwidth of the control system, n is the number of times that must be derived to the surface to gain control, and $e(X) = (x^* - x)$, where x is the control variable and x^* its reference value.

The purpose of the control is to keep the surface to zero. This is a linear differential equation whose unique solution is $e(X) = 0$ for a proper choice of λ regarding the convergence condition.

We define the following control signal:

$$u(t) = \begin{cases} u = 0 \iff S(X) < 0 \iff \frac{dS}{dt} > 0, \\ u = 1 \iff S(X) > 0 \iff \frac{dS}{dt} \leq 0. \end{cases} \quad (12)$$

We say that the converter is controlled in sliding mode when the law described by (12) is enforced and there is a region where there is a sliding mode. Then S is a sliding region.

If the dynamics of the system are out of the sliding region and they are above it, the control will switch to the value $u = 1$ in order to bring the system dynamics into the sliding region $S(X)$. Otherwise, if they are below the sliding region, the control system changes to the value $u = 0$ to bring again the system dynamics to the sliding surface.

The execution of the control law to get the system to slide across the surface means that the switching frequency is infinite, which is physically impossible. Therefore, we will use a modified control law expressed in

$$u(t) = \begin{cases} u = 0 \iff S(X) \leq -\Delta \\ u = 1 \iff S(X) \geq \Delta, \end{cases} \quad (13)$$

where Δ is a positive constant. When Δ tends to zero, it is said that the system tends to ideal sliding dynamics. The switching frequency is not kept constant, but changes could be finite when it does on the surface.

2.5.2. Invariance Conditions. The sliding surface is characterized by the following conditions of invariance or ideal sliding dynamics of (14), and the state trajectories evolve on it:

$$\begin{aligned} S(X) &= 0, \\ \frac{dS(X)}{dt} &= 0. \end{aligned} \quad (14)$$

These conditions guarantee that the trajectory of the system state is addressed to the sliding surface ($S = 0$) and slides on it.

System stability can be analyzed using the method of Lyapunov stability. The Lyapunov function is a scalar positive function. The desired function is one that ensures monitoring of the variable to control the reference value. We define the positive function of the form V in

$$V = \frac{1}{2} S^2 > 0. \quad (15)$$

If the function is derived, (16) is obtained:

$$\dot{V} = S \cdot \frac{dS}{dt} = S \cdot \dot{S}. \quad (16)$$

The function decreases if the derivative is negative.

A system meets the slip condition when the scalar $S(X)$ is zero and it met the condition of

$$\frac{d}{dt} S^2 \leq -\eta |S|, \quad (17)$$

where η is a strictly positive constant indicating the force of attraction of the path to the sliding surface. Once the system is on the surface, the system trajectories remain on it.

3. Module Developed

This section will describe the steps taken for modeling the Mitsubishi PV-TD185-MF5 module. It is located on the roof of the Faculty of Engineering of Vitoria-Gasteiz (University of the Basque Country, Spain). The model is obtained from experimental data (32,916 samples), taken during 18 months. The measurements were made randomly with an approximate average duration of ten minutes, during which four magnitudes were measured (temperature, irradiance, current, and voltage) varying the load resistance.

3.1. Data Acquisition. Figure 7 shows a schematic diagram with all the devices involved to capture the four relevant magnitudes, that is, V_{PH} , I_{PH} , temperature T , and irradiance G in the surroundings of the photovoltaic module. The voltmeter is placed in parallel with the module to obtain V_{PH} , while the ampere meter is placed in series to obtain I_{PH} .

Besides, there is a variable resistance to act as a variable load and obtain different pairs of voltage and current with the same irradiance and temperature. The variable resistance value is controlled according to our convenience, but the temperature and the irradiance depend on the climatological conditions.

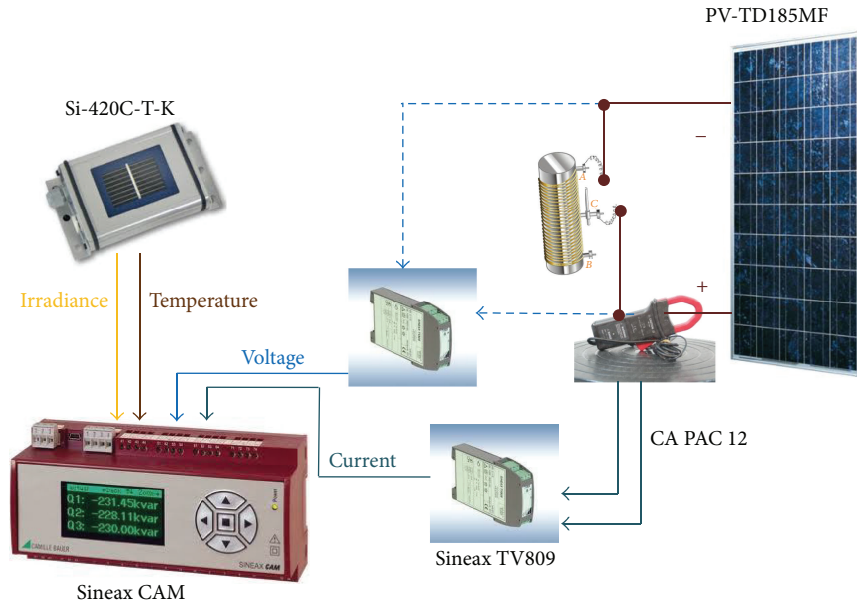


FIGURE 7: Scheme of measurement elements for data logging.

The involved measurement elements for data logging are the following:

- (i) *Irradiance and Temperature Sensor (Si-420TC-T-K)*. This sensor provides the irradiance (W/m^2) and the temperature ($^{\circ}\text{C}$) of its cell (placed next to the photovoltaic module) along the duration of the data acquisition process, which usually is not long. Once the sensor acquires a stable working temperature, both irradiance and temperature values have usually a very small variation; therefore, they are assumed as constants by manufacturers when providing the I - V and P - V characteristic curves of their photovoltaic modules. The sensor provides its output expressed as current. With regard to the accuracy of the device, it is $\pm 5\%$ when it measures irradiance and $\pm 1.5^{\circ}\text{C}$ when it measures temperature.
- (ii) *Clamp Current Chauvin Arnoux PAC 12*. The current clamp is used to measure the direct current provided by the photovoltaic module, providing at its output a voltage proportional to the measured current. This clamp has two working scales: one with a narrow input range (0.4 to 60 A DC) but more accurate readings (precision $\pm 1.5\%$) and a second one with a broader input range (0.5 to 600 A DC) but with less accurate readings (precision $\pm 2\%$). Since the expected value of I_{PV} is less than 10 A, we have chosen the first working mode, which leads to measurements with a maximum error of ± 150 mA.
- (iii) *Programmable Amplifier with Insulation SINEAX TV809*. The functions of this device are to isolate electrically the input/output signals and amplify and/or convert the signal level or type (current to voltage or vice versa) of the input DC signals. In the

experiments described in this paper, we have used two independent devices. Since the value of both V_{PV} and the output of the current clamps I_{PV} are expressed in volts, and the used data logger only can read currents at its input, it is mandatory to use two independent devices to transform these magnitudes into current values. The configuration of the transformations to carry out is done through the TV800plus (V1.11) software, and the main function of both amplifiers is to convert the voltage and current signals of the photovoltaic module into a 4–20 mA current signal proportional to the input. The accuracy of this device is $\pm 0.2\%$ of the maximum value of the input. In the case of V_{PV} , the maximum value is set to 50 V, leading to maximum error of ± 0.1 V, while the maximum value of I_{PV} is set to 10 A, leading to maximum error of ± 20 mA.

- (iv) *SINEAX CAM Data Logger*. This device is devoted to collect and register the four physical magnitudes that later will be used to elaborate the datasets to obtain different approximations as realistic as possible, that is, irradiance, temperature, V_{PH} , and I_{PH} . It is designed for long-term measurements in industrial installations, and it allows continuous measurement and recording of data. In our case, the logging frequency was set to 0.5 Hz. The data logger is supplied with the CB-Manager software, which integrates several useful functions to configure the I/O interface according to specific requirements and to display the measured values. The accuracy of this device is $\pm 0.1\%$ of the maximum value of the input configuration (full scale) which is set to 20 mA, so the measurement error is negligible.

The data measured and recorded using the CB-Manager are saved in plain ASCII files. After some minor modifications as changing decimal sign (. by ,) and separator (, by ;) and eliminating unnecessary data, these files are imported into a Microsoft Excel file in order to obtain graphics which allow detecting outliers or corrupted data, so that a single file with 62,916 samples of measured data (current I_{PV} , voltage V_{PV} , irradiance G , and temperature T) is obtained.

3.2. Obtaining Photovoltaic Module Model. We import these data into the MathWorks Matlab environment and generate four vectors, one for each measured magnitude. Since we will use an artificial neural network to generate the model, with these vectors we form the network input and output, in such a way that the generated neural network will have three-dimensional input patterns (T , G , and V_{PV}) and a single output value I_{PV} associated with each combination of inputs. Once we have defined the model to learn, we must fix the structure of the ANN and train and validate the learned model.

During the structure design phase, we heuristically chose a one-layer feed-forward artificial neural network composed of three inputs, one output, and 15 nodes in the hidden layer. Once the network architecture was designed, we proceed to train it to learn the desired behavior defined through the input and output correspondences. In this phase, the ANN calculates its predictions and compares them with the actual values of the variable that had tried to predict them, so that the network learns that there were erroneous predictions and modifies the synaptic weights in order to reduce that error. This process is driven by a training algorithm, which presents sequentially the training data at the input layer of the ANN. In this case, the Levenberg-Marquardt algorithm has been used. We call “epoch” to a complete presentation of all training data during the learning process. Learning occurs epoch to epoch until the weights and thresholds are stabilized and the error criterion on the complete training set converges to a minimum value following a metric, in our case, the Mean Square Error (MSE).

After training phase, it is expected that the ANN shows a behavior similar to the actual photovoltaic module, even when new inputs are presented at its input layer.

Of the total number of 62,916 samples of experimental data obtained, we use 44,042 samples pairs for training (70%), 9,437 for validation (15%), and the remaining 9,437 for test (15%). The network was trained with backpropagation Levenberg-Marquardt algorithm during 1000 epochs, obtaining a network with a Mean Squared Error (MSE) of 6.1553×10^{-2} A and with a training correlation coefficient $R = 0.99075$, as shown in Figure 8.

3.3. Validation of the Model. In Figure 9, there are the characteristic I - V curves of three different days in different weather conditions: the experimental values (blue) and the predicted values by the ANN-based model (red). We can see that the model provides a prediction very similar to the actual values obtained through experimental measurements.

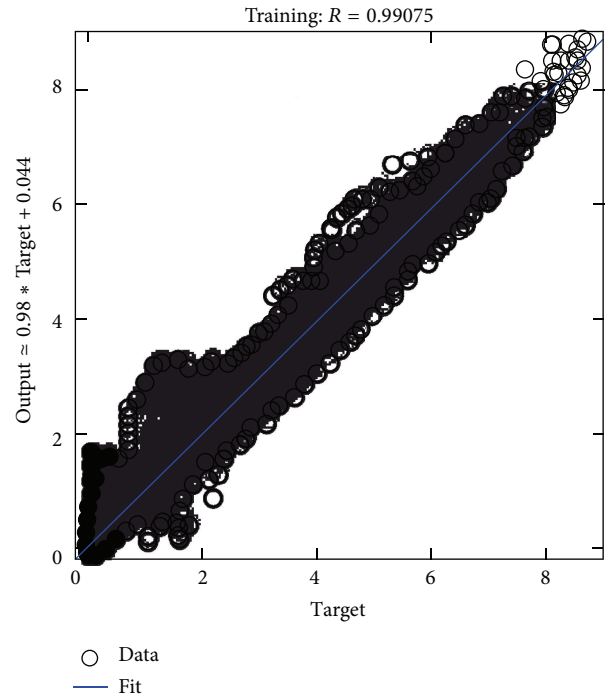


FIGURE 8: Training correlation coefficient.

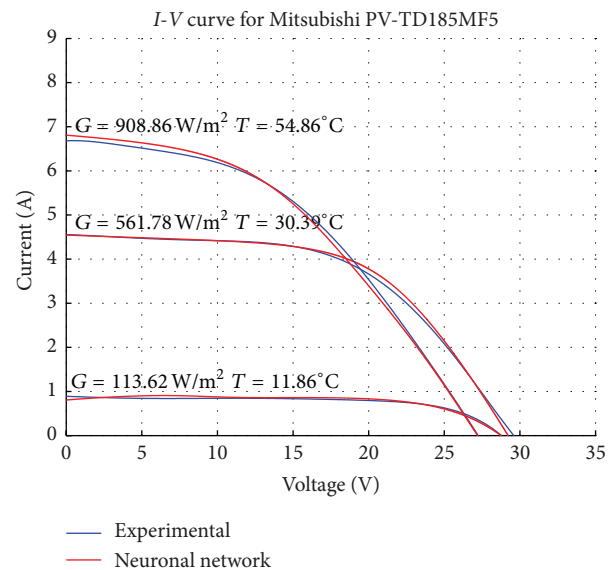


FIGURE 9: Model validation.

Moreover, using a test dataset of 9,437 samples a test correlation coefficient $R = 0.99069$ has been achieved as shown in Figure 10.

With these results, we can state that the model is accurate enough to be used in those studies where the Mitsubishi PV-TD185MF module is implied.

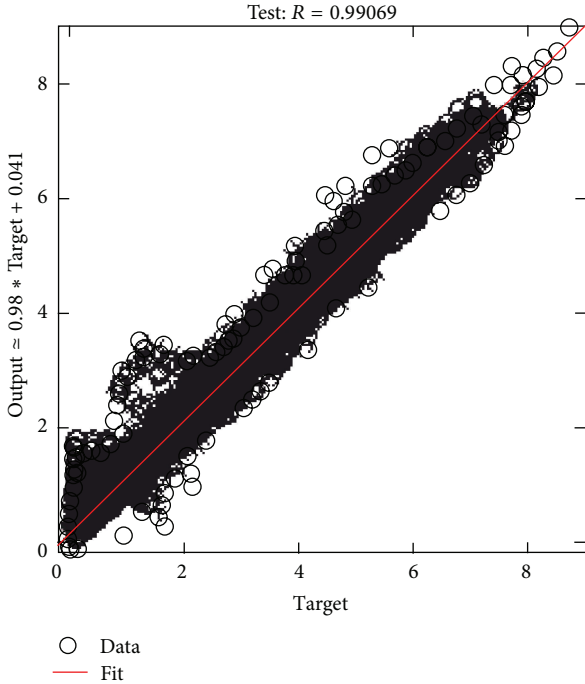


FIGURE 10: Test correlation coefficient.

4. Sliding Mode Control

4.1. Reference Current Generator. Boost converter function is to take the output of the photovoltaic module and transform it to obtain the maximum power. The behavior of the converter depends on the sliding control which obtains the reference (δ) necessary for the IGBT inverter to find the maximum power point. In turn, the sliding mode controller needs a reference current (I^*) to compare with the current of the photovoltaic generator and to obtain such pulse (δ). The reference current generator is which is going to give us this reference current I^* .

In order to obtain the reference current generator (I_{REF}), we rely on the $P-I$ characteristic curve. As can be seen in Figure 11, maximum power points at different irradiance conditions form a straight blue line, instead of the quadratic equation that results if $P-V$ characteristic curve is used.

Knowing this line, for any power value, it is straight to know which current value, at the maximum power point, that should be used as reference current. Since the power generated by the module also depends on the temperature, it is necessary to obtain these straight lines at different temperature values.

4.2. Experimental Current Reference Generator Design. In order to design the reference current generator, we will use the same experimental data used to obtain the model of the photovoltaic module in Section 3.

In this case, the 62,192 samples will be divided into groups of temperature of 5°C, going from 5°C to 50°C. Each one of these groups is divided again into irradiance groups with values from 100 to 1,000 W/m² and step 100 W/m². With

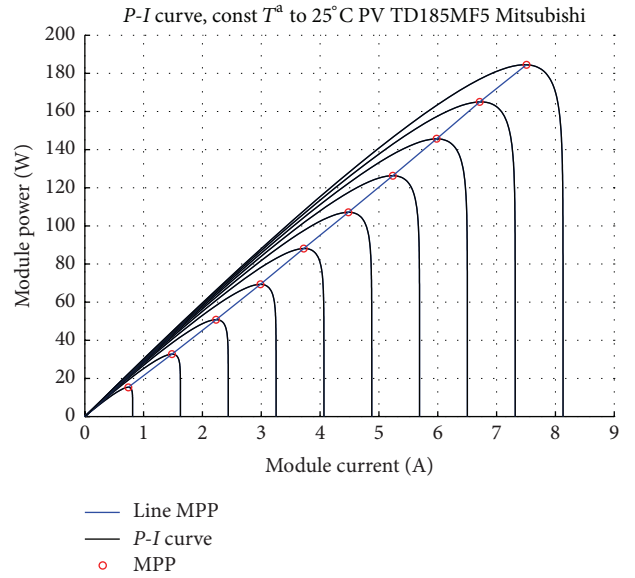


FIGURE 11: $P-I$ characteristic curves of the module at different irradiance conditions.

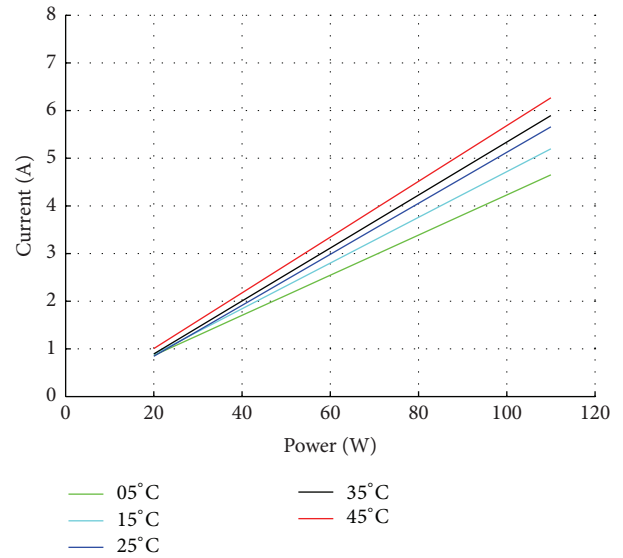
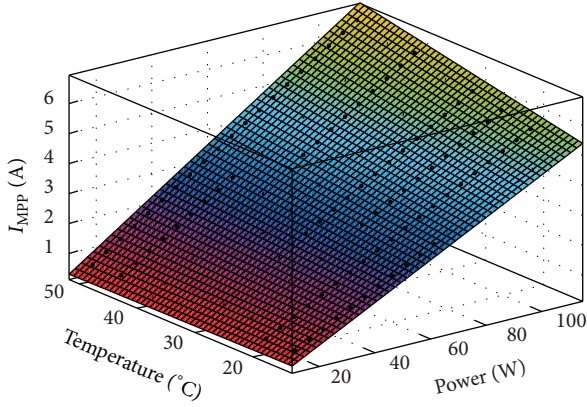


FIGURE 12: Lines of MPP for different temperatures (°C).

the values of each group (combination of temperature and irradiance), the characteristic curves $P-I$ have been obtained and their MPPs have been found. For example, Figure 11 shows a characteristic curve $P-I$ for each irradiance, all of them at a constant temperature of 25°C. With all the MPP points of Figure 11, a curve of Figure 12 has been created using interpolation, specifically the curve corresponding to 25°C. That is, each curve of Figure 12 contains the MPPs for all irradiances (implicitly as one moves in the abscissa axis) of a given temperature, expressing it as $I_{MPP} = f(G)$. With the triplets (I_{MPP} , P_{MPP} , and T), an interpolation is carried out in order to obtain a function $I_{MPP} = f(P_{MPP}, T)$ that gives the value of the current at the MPP for given values of power


 FIGURE 13: P - T - I characteristic surface of the MPPs.

and temperature. Finally, Figure 13 is created interpolating the curves shown in Figure 12 and it gives us the reference current for the maximum power point at given temperature and irradiance.

With these values, we trained an ANN to learn the function $I_{MPP} = F(P_{MPP}, T)$. The process to obtain the neural network is similar to that followed when learning the photovoltaic module model carried out in Section 3.2, taking into account that in this case it has two inputs (P_{MPP}, T) and one output (I_{MPP} or I_{REF}).

We obtained the maximum power points data to carry out the ANN training calculating them for power values ranging from 15 to 110 W with step of 5 W, while for temperature values range from 15 to 50°C with step of 5°C. In this way, we got a set of 160 triplets (P_{MPP}, T , and I_{MPP}), of which 112 samples were used for training (70%), 24 for validation (15%), and the remaining 24 for the test (15%).

An ANN of four hidden nodes was trained with back-propagation Levenberg-Marquardt algorithm. After 489 iterations, a network with a Mean Squared Error (MSE) of 2.036×10^{-3} A and a training correlation coefficient $R = 0.99992$ was achieved as shown in Figure 14, while its test correlation coefficient was $R = 0.99986$, as shown in Figure 15. So, we can state that the ANN has learned properly the behavior of the sliding mode controller.

4.3. Stability Demonstration. As we have seen in the previous section, the neural network will help us determine currents of reference required by the system at all times; then the converter will force the photovoltaic system to work with the reference value obtained and thus in the area of the maximum power

$$\begin{aligned} S &= e = I_{REF} - I_p, \\ u &= \int_0^t k \cdot \text{sign}(S(t)) dt. \end{aligned} \quad (18)$$

In order to limit the control signal of operating range for the duty cycle of our DC/DC converter, the integral of the control signal is limited between 0.1 and 0.9.

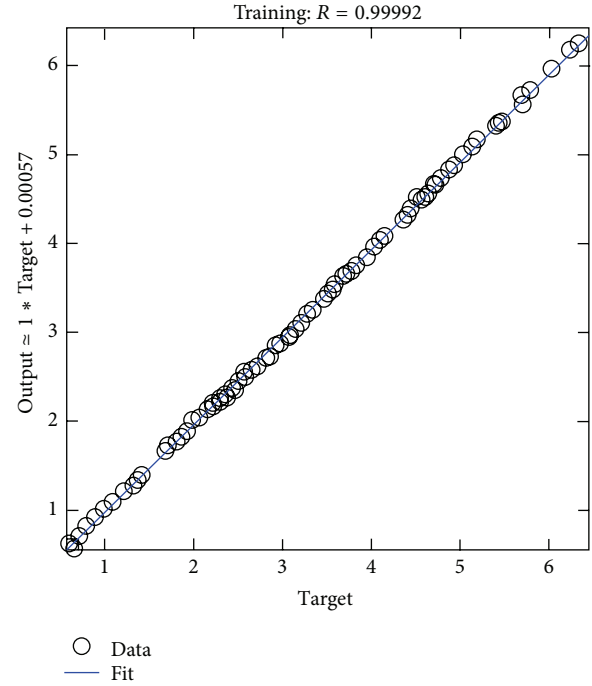


FIGURE 14: Train correlation coefficient.

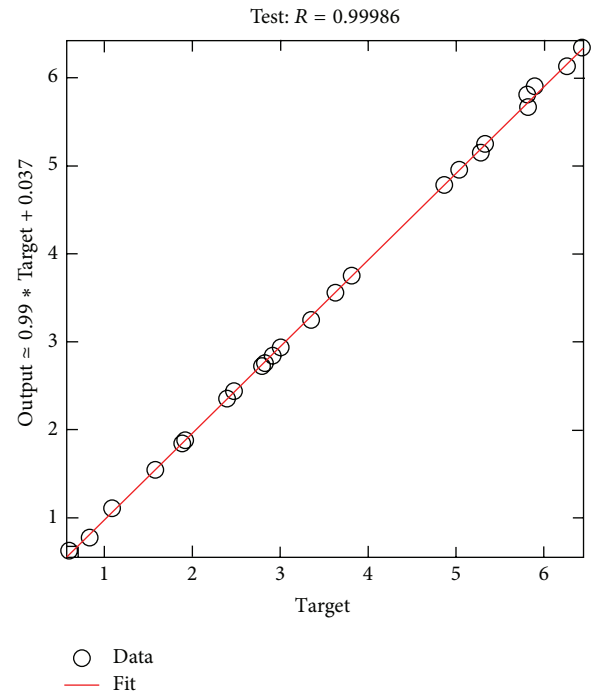


FIGURE 15: Test correlation coefficient.

The demonstration of stability of the proposed controller is based on the theory of Lyapunov stability. For this purpose a Lyapunov function is defined by

$$V = \frac{1}{2} S^2 > 0, \quad (19)$$

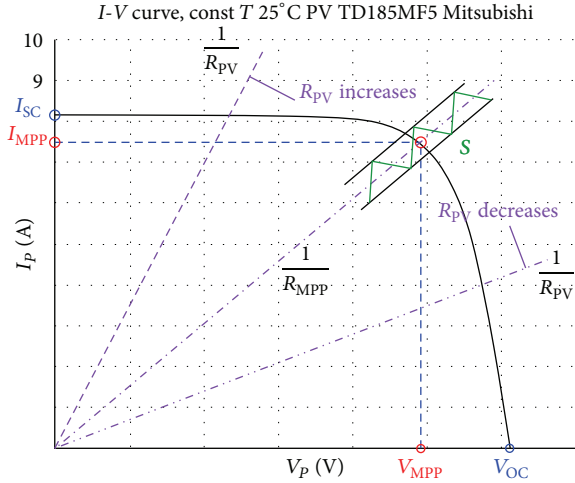


FIGURE 16: Behavior of the R_{pV} related to the characteristic curve.

whose derivative with respect to time is given by

$$\dot{V} = S \frac{dS}{dt} = S \cdot \dot{S} < 0. \quad (20)$$

Taking into account the expression of

$$\begin{aligned} S &= e = I_{MPP}^* - I_{PV} \\ \dot{S} &= \dot{e} = -\dot{I}_{PV} \end{aligned} \quad (21)$$

and using Lyapunov stability theory, it can be shown that when $\dot{V} < 0$, the value of S tends to zero and therefore the system state converges to MPP.

When $S > 0$. It means that the reference current provided by the reference generator is larger than the current provided by the module. For this reason and to make the tracking error be zero ($S = 0$), I_{PV} has to increase and therefore, the V_{pV} must decrease. For this purpose, R_{pV} has to decrease, which is achieved increasing the duty cycle (δ) as we can deduce from (6). In Figure 16, we see the behavior of the R_{pV} magnitude.

We check stability because if I_{pV} increases, \dot{S} will be negative and also the product $S \cdot \dot{S} < 0$, which implies that the system is stable and converges to the maximum power point.

When $S < 0$. Using the same procedure, we have $I_{REF} < I_p$ and then \dot{S} is positive and the product $S \cdot \dot{S} < 0$, which implies that the system is stable and converges to the maximum power point.

For this reason and to make the tracking error be zero ($S = 0$), I_{pV} current has to decrease and therefore V_{pV} must increase. For this purpose, R_{pV} has to increase, which is achieved by decreasing the duty cycle (δ), as we can deduce from (6).

5. Results

In this section, we present our results divided into two subsections attending to their nature:

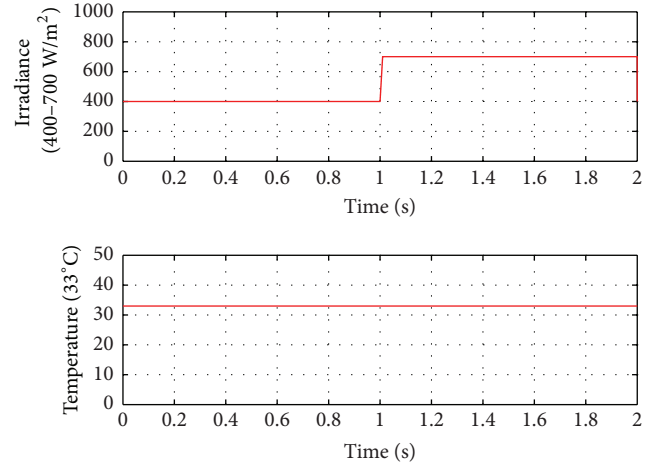


FIGURE 17: Temperature (constant) and irradiance (step) input values.

- Simulation Results.* They are obtained using the photovoltaic module model in the MathWorks Matlab/Simulink environment. Due to the ease to change the weather dependent parameters, we tested the operation of the controller when abrupt changes in irradiance and temperature.
- Experimental Results.* They are obtained operating on the actual system making real measurements. In this case, we present the operation of the controller when there are load variations.

5.1. Simulation Results. The first test carried out in order to test the performance of the controller analyzes its response when there are sudden irradiance changes. As shown in Figure 17, we have used a constant temperature of 33°C and an irradiance step from 400 to 700 W/m² after two seconds of simulation.

As we can see in Figure 18, the obtained power at the output of the converter (blue line), that is, the power absorbed by the load, follows the power value of the output of the module (red line). This shows that the controller has a good performance when dealing with irradiance changes.

The second test is devoted to study the behavior of the controller when there are sudden temperature changes. In this case, the irradiance is constant (800 W/m²), while the temperature changes suddenly from 10 to 45°C, as shown in Figure 19.

In this case, we also can see in Figure 20 that the converter output power (blue line) again follows the power value of the output of the module (red line). So we can state that the converter has a good performance when dealing with temperature changes.

5.2. Experimental Results. In this section, we will analyze the behavior of the proposed controller under real conditions.

In order to carry out the experiments, we used a real-time digital sign processor (DSP) model dSPACE DSP1104 integrated with MathWorks Matlab/Simulink through its

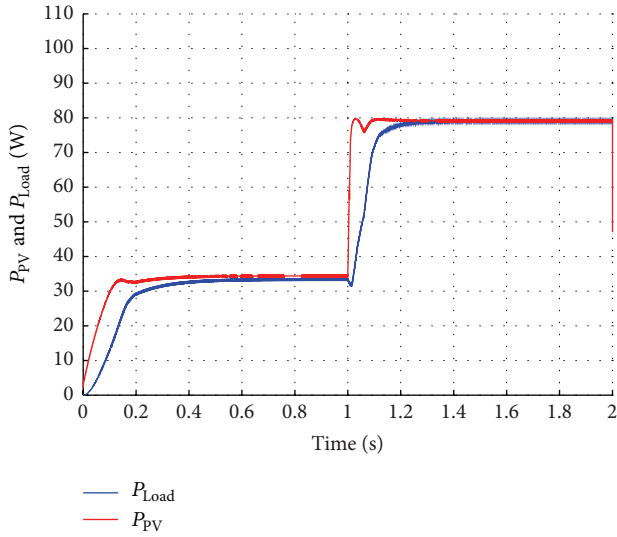


FIGURE 18: Power response when sudden irradiance changes.

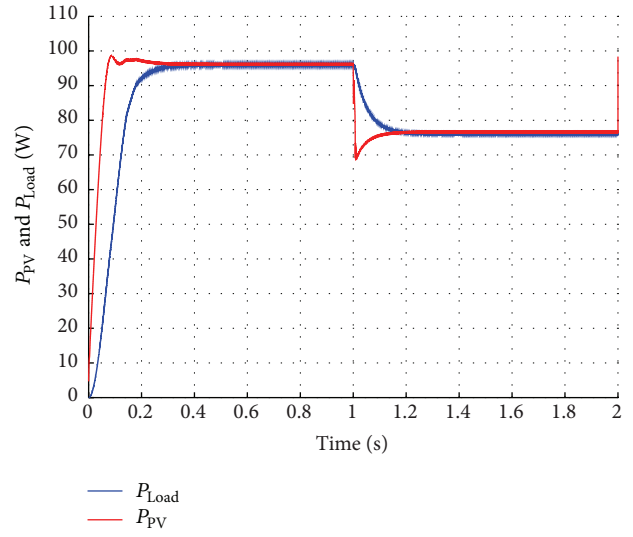


FIGURE 20: Power response when sudden temperature changes.

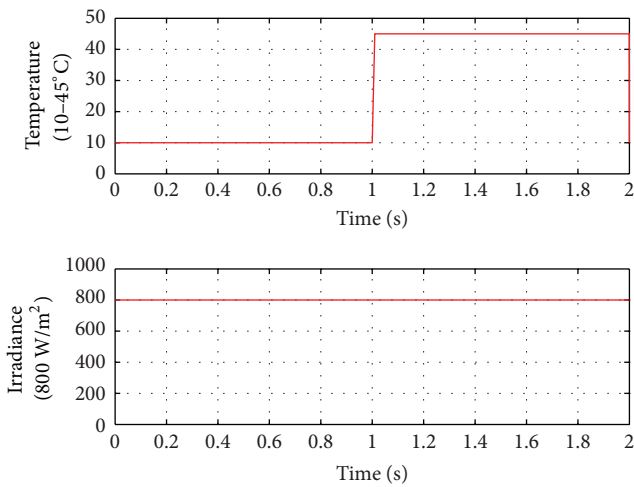


FIGURE 19: Temperature (step) and irradiance (constant) input values.

toolbox for real-time work and Real-Time Interface (RTI). This is widely used in industry and research because it reduces the time gap between the simulation and the development of real implementation, profiting from its capability to simulate failures and to analyze the behavior of the real system.

The installation in which the experiments have been carried out consists of the Mitsubishi PV-TD185MF5 photovoltaic module, a boost converter, a DSP model dSPACE DSP1104, a variable load, and a personal computer for data storage, as shown in the schematics of Figure 21, while Figures 22(a) and 22(b) show the actual installation. The used boost converter has been designed and manufactured by the TEP 192 Research Group of the University of Huelva (Spain), and its specifications are shown in Table 2.

The communication between the DSP and the computer has been done using the ControlDesk Next Generation 5.1

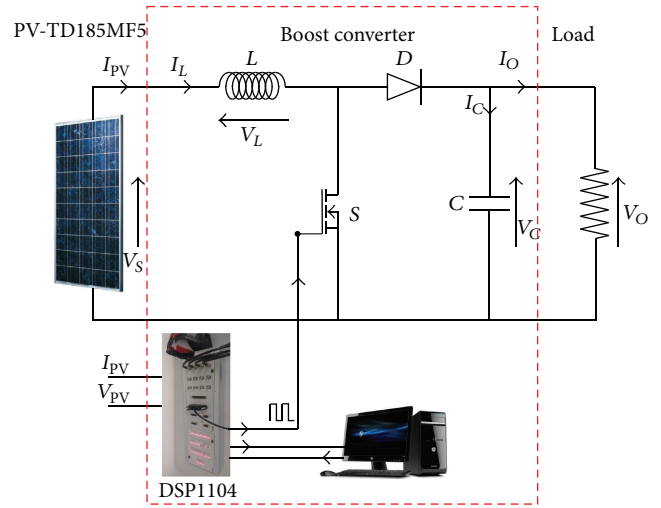


FIGURE 21: System block diagram.

TABLE 2: Boost converter parameters.

Boost converter		
Schottky	2x MURF1560GT	600 V, 15 A, 0.4 V to 10 A/150°C
IGBT	1x HGT40N60B3	600 V, 40 A, 1.5 V to 150°C
L	6x PCV-2-564-08	560 μH, 7 A, 42 mΩ
C	2x TK Series	1500 μF, 250 V

software, which allows display on the screen and manipulating real-time system variables through a graphical user interface.

Once the experimental setup is fixed, the first step is to find out which is the maximum power point for the actual conditions in which the system is working. For this purpose, the variable load is connected directly to the photovoltaic module and its value is varied from its minimum to its maximum value (0–47 Ω) gathering pairs of (P, I) points



FIGURE 22: Picture of the actual installation.

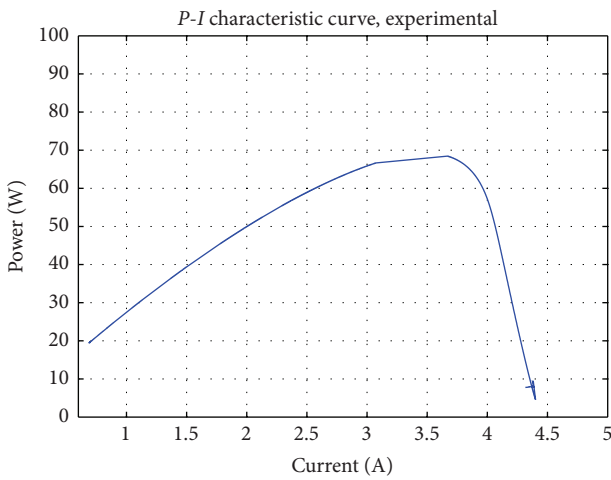


FIGURE 23: P - I characteristic curve from experimental data.

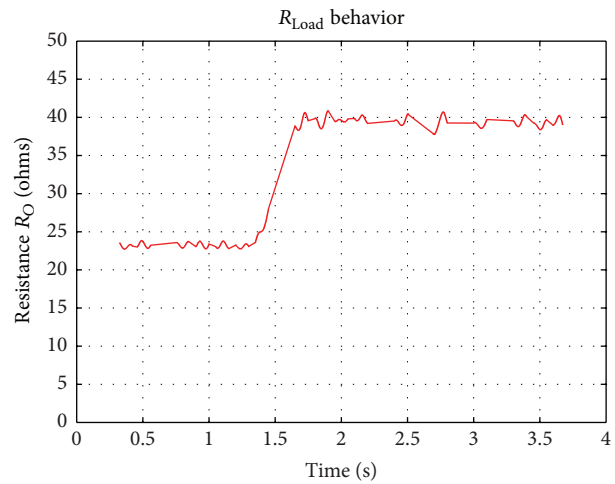


FIGURE 24: Behavior of the load resistance R_{Load} .

with which the P - I characteristic curve is obtained (see Figure 23) and locates the maximum power point. In this real experiment case, that point corresponded to a current I_{MPP} of 3.6 A and a P_{MPP} power of approximately 68 W.

Now that the value that the converter should follow is known, the installation is prepared to make the measurements.

The experiment is to vary the load and check that the power supplied to the load by the converter follows the power given by the photovoltaic module, in such a way that although the load varies, the converter continues operating at the maximum power point under the existing irradiance and temperature conditions at each moment.

During the experiment the load was manually varied from 23 Ω to 39 Ω , so the change is not immediate as can be seen in Figure 24 because the load needs some time to move from one value to other.

During the experiment, the temperature (blue line) and the irradiance (red line) are quite stable due to its short duration, remaining on approximate values of 33°C and 635 W/m^2 as can be seen in Figure 25.

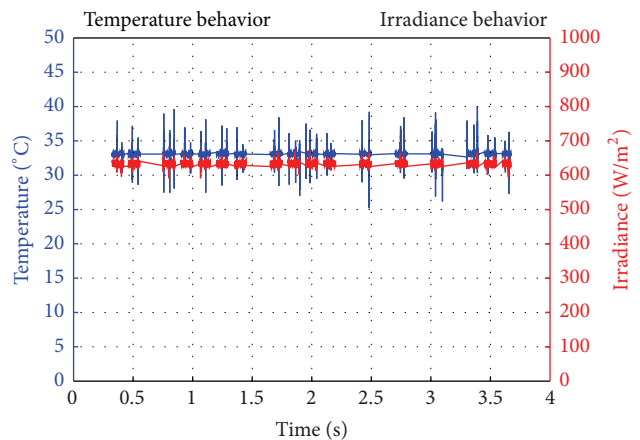


FIGURE 25: Behavior of temperature (T) and irradiance (G).

Figure 26 shows the behavior of the power at the output of the converter (or in load) and at the output of the photovoltaic module which are compared, being very close and remaining around a mean value of 68.5 W. This value is approximately

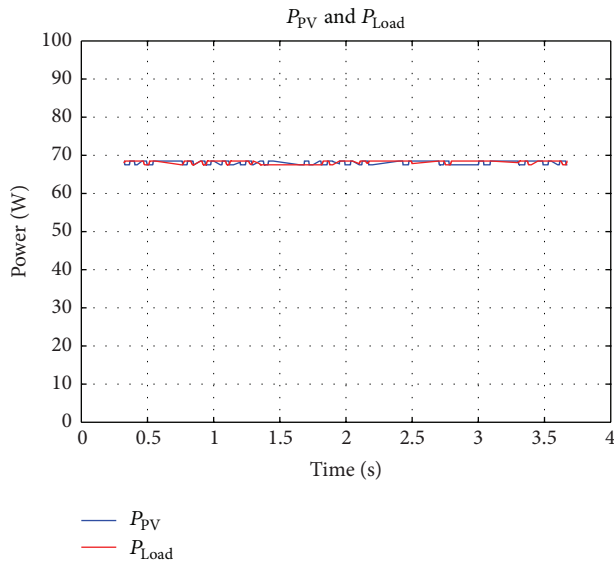


FIGURE 26: P_{PV} behavior versus P_{Load} .

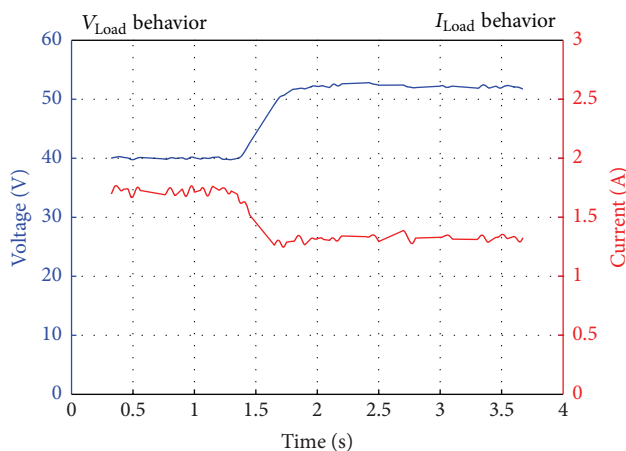


FIGURE 27: Behavior of load voltage V_{Load} and load current I_{Load} .

the same that the MPP provided the P - I characteristic curve as shown in Figure 23.

Finally, the voltage and current values in the load can be seen in Figure 27. It must be noted that the change of the load value implies a value change in these two variables, the product of both of them being the value of the power given to the load, which should be kept constant (as seen in Figure 27).

After this real experiment, we can state that the designed converter has also a good performance when the load value is changed.

6. Conclusions

In this paper, we have addressed one of the more outstanding problems when dealing with photovoltaic modules, that is, the maximum power point tracking problem when a boost DC/DC converter is used.

In the first part of the paper, we have given a short background on some key topics regarding the paper, as the basic description of a photovoltaic generator and its characteristic curves, boost DC/DC converters, artificial neuronal networks, and sliding mode control.

Later, we have detailed all the components of a real photovoltaic installation placed at the Faculty of Engineering Vitoria-Gasteiz (Basque Country University, Spain). That installation has been used to acquire data about the real operation of the Mitsubishi Electric PV-TD185MF5 185 W photovoltaic module. We have explained how the data have been gathered and the process used to train an artificial neural network to learn the behavior of the real module, obtaining a very accurate model with $MSE = 0.062$ A and $R = 0.991$ when tested with a new dataset. So, the first finding of this paper is a very accurate neuronal model obtained from real data.

Once we have got a validated model of the photovoltaic module, which allows us to make simulations, we design the sliding mode controller. The controller generates a pulse signal to control the boost DC/DC converter, but in turn, it needs a reference signal. In this work, we have used as reference a current signal, more specifically, the current at which the module gives maximum power for a given temperature and irradiance conditions. That information was obtained from the real gathered data and since we are dealing with a sliding mode controller, it has represented as a sliding surface.

Finally, we have carried out several tests in order to validate the controller and its robustness when there are sudden changes in temperature, irradiance, and load. Simulated and real tests have shown that the controller that provides a good overall performance guaranteeing that the power in the output of the converter is very close to the power of the photovoltaic module output, this one being the second main contribution of the paper.

Competing Interests

The authors declare that they have no competing interests.

Acknowledgments

The authors are very grateful to the UPV/EHU for its support through Projects GIU13/41 and UFI11/07.

References

- [1] United Nations Climate Change Conference, Paris, France, 2015, <http://www.cop21.gouv.fr/en/>.
- [2] T. Logeswaran and A. SenthilKumar, "A review of maximum power point tracking algorithms for photovoltaic systems under uniform and non-uniform irradiances," *Energy Procedia*, vol. 54, pp. 228–235, 2014.
- [3] V. Salas, E. Olías, A. Barrado, and A. Lázaro, "Review of the maximum power point tracking algorithms for stand-alone photovoltaic systems," *Solar Energy Materials and Solar Cells*, vol. 90, no. 11, pp. 1555–1578, 2006.
- [4] A. H. Alqahtani and V. I. Utkin, "Self-optimization of photovoltaic system power generation based on sliding mode control,"

- in *Proceedings of the 38th Annual Conference on IEEE Industrial Electronics Society (IECON '12)*, pp. 3468–3474, IEEE, Montreal, Canada, October 2012.
- [5] Y. Levron and D. Shmilovitz, “Maximum power point tracking employing sliding mode control,” *IEEE Transactions on Circuits and Systems I: Regular Papers*, vol. 60, no. 3, pp. 724–732, 2013.
 - [6] J. J. Slotine and W. Li, *Applied Nonlinear Control*, Prentice-Hall, Englewood Cliffs, NJ, USA, 1991.
 - [7] A. Cid-Pastor, L. Martinez-Salamero, A. El Aroudi, R. Giral, J. Calvente, and R. Leyva, “Synthesis of loss-free resistors based on sliding-mode control and its applications in power processing,” *Control Engineering Practice*, vol. 21, no. 5, pp. 689–699, 2013.
 - [8] F. Zhang, J. Maddy, G. Premier, and A. Guwy, “Novel current sensing photovoltaic maximum power point tracking based on sliding mode control strategy,” *Solar Energy*, vol. 118, pp. 80–86, 2015.
 - [9] A. Luque and S. Hegedus, Eds., *Handbook of Photovoltaic Science and Engineering*, John Wiley & Sons, 2011.
 - [10] M. Wolf and H. Rauschenbach, “Series resistance effects on solar cell measurements,” *Advanced Energy Conversion*, vol. 3, no. 2, pp. 455–479, 1963.
 - [11] D. S. H. Chan and J. C. H. Phang, “Analytical methods for the extraction of solar-cell single- and double-diode model parameters from I–V characteristics,” *IEEE Transactions on Electron Devices*, vol. 34, no. 2, pp. 286–293, 1987.
 - [12] J. A. Gow and C. D. Manning, “Development of a photovoltaic array model for use in power-electronics simulation studies,” *IEE Proceedings—Electric Power Applications*, vol. 146, no. 2, pp. 193–200, 1999.
 - [13] M. R. AlRashidi, K. M. El-Naggar, and M. F. AlHajri, “Parameters estimation of double diode solar cell model,” *International Journal of Electrical, Computer, Energetic, Electronic and Communication Engineering*, vol. 7, no. 2, pp. 118–121, 2013.
 - [14] A. M. Humada, M. Hojabri, S. Mekhilef, and H. M. Hamada, “Solar cell parameters extraction based on single and double-diode models: a review,” *Renewable and Sustainable Energy Reviews*, vol. 56, pp. 494–509, 2016.
 - [15] M. G. Villalva, J. R. Gazoli, and E. Ruppert Filho, “Modeling and circuit-based simulation of photovoltaic arrays,” in *Proceedings of the Brazilian Power Electronics Conference (COBEP '09)*, pp. 1244–1254, Bonito-Mato Grosso do Sul, Brazil, October 2009.
 - [16] W. De Soto, S. A. Klein, and W. A. Beckman, “Improvement and validation of a model for photovoltaic array performance,” *Solar Energy*, vol. 80, no. 1, pp. 78–88, 2006.
 - [17] F. M. González-Longatt, “Model of photovoltaic module in Matlab,” in *2do Congreso Iberoamericano de Estudiantes de Ingeniería Eléctrica, Electrónica y Computación (II CIBELEC '05)*, vol. 2005, pp. 1–5, Puerto la Cruz, Venezuela, 2005.
 - [18] G. Walker, “Evaluating MPPT converter topologies using a MATLAB PV model,” *Journal of Electrical and Electronics Engineering*, vol. 21, no. 1, pp. 49–55, 2001.
 - [19] A. Oi, *Design and simulation of photovoltaic water pumping system [Ph.D. thesis]*, California Polytechnic State University, San Luis Obispo, Calif, USA, 2005.
 - [20] H. L. Tsai, C. S. Tu, and Y. J. Su, “Development of generalized photovoltaic model using MATLAB/SIMULINK,” in *Proceedings of the World Congress on Engineering and Computer Science*, vol. 2008, pp. 1–6, October 2008.
 - [21] G. Bayrak and M. Cebeci, “Grid connected fuel cell and PV hybrid power generating system design with Matlab Simulink,” *International Journal of Hydrogen Energy*, vol. 39, no. 16, pp. 8803–8812, 2014.
 - [22] J. A. Ramos-Hernanz, J. M. Lopez-Guede, I. Z. Belder et al., “Modelling of a photovoltaic panel based on their actual measurements,” *International Journal on Technical and Physical Problems of Engineering*, vol. 6, no. 4, pp. 37–41, 2014.
 - [23] M. Ameziane, B. Sefriti, J. Boumhidi, and K. Slaoui, “Neural network sliding mode control for a photovoltaic pumping system,” *Journal of Electrical Systems*, vol. 9, no. 3, pp. 380–391, 2013.
 - [24] S. Kalogirou and A. Sencan, “Artificial intelligence techniques in solar energy applications,” in *Solar Collectors and Panels, Theory and Applications*, R. Manyala, Ed., chapter 15, pp. 315–340, InTech, Rijeka, Croatia, 2010.
 - [25] F. Almonacid, L. Hontoria, J. Aguilera, and G. Nofuentes, “Una nueva aproximación para la caracterización de módulos fotovoltaicos basada en redes neuronales,” *Boletín del Instituto de Estudios Giennenses* 192, 2005.
 - [26] F. Almonacid, C. Rus, L. Hontoria, and F. J. Muñoz, “Characterisation of PV CIS module by artificial neural networks. A comparative study with other methods,” *Renewable Energy*, vol. 35, no. 5, pp. 973–980, 2010.
 - [27] J. M. Lopez-Guede, J. A. Ramos-Hernanz, E. Zulueta, and U. Fernandez-Gamiz, “Towards a systematic neural network based modelization of photovoltaic modules,” in *Proceedings of the 3rd European Conference on Renewable Energy Systems (ECRES '15)*, E. Kurt, Ed., October 2015.
 - [28] F. Bonanno, G. Capizzi, G. Graditi, C. Napoli, and G. M. Tina, “A radial basis function neural network based approach for the electrical characteristics estimation of a photovoltaic module,” *Applied Energy*, vol. 97, pp. 956–961, 2012.

Research Article

A Simple Technique for Sustaining Solar Energy Production in Active Convective Coastal Regions

Moses E. Emeteri, Marvel L. Akinyemi, and Etimbuk B. Edeghe

Department of Physics, Covenant University, Canaanland, PMB 1023, Ota, Nigeria

Correspondence should be addressed to Moses E. Emeteri; emeteri@yahoo.com

Received 19 March 2016; Accepted 17 July 2016

Academic Editor: Vishal Mehta

Copyright © 2016 Moses E. Emeteri et al. This is an open access article distributed under the Creative Commons Attribution License, which permits unrestricted use, distribution, and reproduction in any medium, provided the original work is properly cited.

The climatic factors in the coastal areas are cogent in planning a stable and functional solar farm. 3D simulations relating the surface temperature, sunshine hour, and solar irradiance were adopted to see the effect of minute changes of other meteorological parameters on solar irradiance. This enabled the day-to-day solar radiation monitoring with the primary objective to examine the best technique for maximum power generation via solar option in coastal locations. The month of January had the highest turbulent features, showing the influence of weather and the poorest solar radiance due to low sunshine hour. Twenty-year weather parameters in the research area were simulated to express the systematic influence of weather of PV performance. A theoretical solar farm was illustrated to generate stable power supply with emphasis on the longevity of the PV module proposed by introducing an electronic concentrator pillar (CP). The pictorial and operational model of the solar farm was adequately explained.

1. Introduction

The quest to meet the energy budget of a growing economy [1] is of utmost importance. The energy option from fossil and nuclear sources has been reported severally to be dangerous because of the massive release of anthropogenic pollution [2–4] from automobiles, multipurpose generators, and industrial machinery. Extensively, anthropogenic gas emissions into the atmosphere may initiate climate change [5, 6], global warming, and so forth. Hence, the promotion of clean renewable energy source is the only way of curbing air pollution in the environment. Solar energy is described as the cleanest renewable energy whose source is the sun. The sun and its numerous events (known as solar activity) have been reported to be the main driver of climate change [7]. The solar activity in the tropical regions is quite high (compared to the polar region) to drive the global energy and convective processes. In the tropics, high solar activity is advantageous in operating a successful solar farm. The annual global radiation in tropical and subtropical regions is about 1600–2200 kWh/m². Solar farms in the tropic have capacities of generating electric power, ranging from 10 (Megawatts) MW to 150 MW [8]. In the coastal area of the tropics, an increased

solar activity culminates into an increased convective updraft and downdraft, cloud formation, frequent cloud movement [9], and so forth. These events in the coastal areas engender a process known as atmospheric shading. Atmospheric shading occurs when the cloud movement cast its shadow on the earth surface. Atmospheric shade is inimical to solar power generation because the solar cell is designed in such a way that little shade on one panel can gradually shut down solar power production. The bypass diodes assist in minimizing the effects of partial shading by preventing damage from reverse bias on partially shaded cell or cells. Bypass diodes allow the flow of electricity from nonshaded parts to pass by the shaded part of the module. However, the failure of the bypass diode has been reported [10]. It causes great power loss during large shading, hence, causing the module's performance to drop by 1/3 instantly. The failure of the bypass diode is evident when probed by Signal Transmitter Device.

A major advantage of the coastal areas is the high precipitation level which helps to clean the surface of the solar panel for effective photoemission. Solar energy operators in the coastal areas are faced with challenges ranging from climate change, inefficient solar panel, durability of the solar panel, poor energy budget, and so forth. The estimated solar power

reaching the earth is little above 1000 W/m^2 [13]. In Nigeria, about 1,770 TW h/year of solar energy falls on the entire land area of Nigeria [14]. By this estimation, if 10% of the solar energy can be harvested, the energy generation would be about 200 times more than the total energy obtained from fossil and hydroelectricity. This means that if solar energy is judiciously harvested, solar option is capable of meeting the energy needs of the whole world. An efficient harvest of the solar radiation within the tropics and specifically coastal areas depends on the efficiency of the solar panel used. The improvement of the PV farm is of utmost interest in the quest of maximizing the utilization of solar energy. The PV metamorphosis includes dye-sensitized solar cells with 11% efficiency, organic photovoltaic known as plastic solar cells with 8% efficiency, and III-V multijunction solar cells with over 40% efficiency. The PV technologies mentioned above do not yet contribute to the PV market, hence, the emergence of the concentrating solar power (CSP) technology. The CSP technology is presently enhanced by the smart grid concept to eliminate uncertainty and intermittency of solar generation.

Solar panels are made up of solar cells, that is, an array of photovoltaic (PV) cells. The primary requirement for a material to be used for solar cell application is its band gap. The band gap of the solar material is expected to be between 1.1 eV and 1.7 eV [15]. Solar cells are classified based on its inherent band gap. Types of solar cell include silicon solar cells, III-V group solar cells, and thin film solar cells. PV modules do not only convert solar irradiation directly into electric but also produce plenty of waste heat, which can be recovered for thermal use [16]. Materials used to fabricate the PV panels are monocrystalline silicon, polycrystalline silicon, microcrystalline silicon, copper indium selenide, and cadmium telluride [17]. The technology behind solar panels varies with respect to the manufacturer. Recently, the production of solar cell from silicon semiconductor is one of the latest inventions of the PV technologies. The concentrating solar power (CSP) technology is another recent technique for improving the functionality of the PV module. A typical CSP plant consists of three main subsystems: solar collector field, solar receiver, and a power conversion system [18]. The CSP option includes the collector and the receiver, parabolic trough, solar tower or central receiver, linear Fresnel, and dish Stirling [19]. The efficiency of the CSP is high in the tropical region. However, the efficiency of the CSP is greatly reduced in coastal region which is characterized by high convective activity and solar shading. Already advanced control techniques have been applied to concentrating solar power systems to overcome the problems caused by the sporadic nature of solar radiation [20]. Another way scientists sought to solve the irregular solar radiation problem is the use of storage systems [21]. Researchers have suggested the incorporation of the thermal energy storage (TES) system to the solar farm. This idea enables an efficient utilization of fluctuating solar energy on a continuous basis [22–24]. Recent research [25] has shown that the success of the TES depends on the type of fluid used to convey heat from the solar collector to the TEM. Gnaneswar Gude et al. [26] have shown that low temperature desalination systems are very efficient for TES.

This paper seeks to solve the challenges of solar radiation irregularities due to solar shading in the coastal region. It examines a comparative functional analysis of two types of PV solar panel randomly chosen. The PV solar panel was tested in a changing solar radiation noticed in the south west region of Nigeria. A model was propounded to mathematically represent the challenges of solar energy operators in coastal areas. Solution was proffered via adopting of electronic concentrator pillars in a prototype solar farm.

2. Location of Study Area

The study area is located on a narrow coastal plain of the Bight of Benin, specifically on the south west of Nigeria. It lies approximately on longitude 2.48°E and 3.26°E , respectively, and latitude 6.24°N and 6.25°N (as shown in Figures 1 and 2). The detail of the location is expressed by Emetere and Akinyemi [27]. Coastal regions are influenced by geomorphological and oceanographical factors, for example, storm event and open-ocean convection intensity that controls the seasonal variability of the hydrology, hydrodynamics, and biogeochemistry [28].

3. Methodology

The theories used in the methodology have been propounded by Emetere and Akinyemi [27]. The dataset used for this study was obtained from Giovanni, Nigerian Meteorological Agency, and Davis weather station. The field work comprises primarily two PV modules from different producers, that is, SolarWorld and Sharp Solar as established in [27].

The voltage form is measured directly from the PV module, that is, using a multimeter set to direct current DC voltage. A manual data logger was used to obtain readings. The readings were collected every ten minutes every day between the hours of twelve noon and three in the afternoon (3 pm) when the sun is believed to be at its peak.

The experiment was performed in the active days of December, 2013. The choice of December was as a result of the following:

- (i) One-year data collected by the Davis weather station shows an average solar radiance in the months (Figure 3).
- (ii) The peak days of December were captured using the Davis weather station (Figure 4).

The meteorological effect (ME) on the performance of the PV module will be established in the succeeding section. The varying solar radiation shows the clear evidence of ME in coastal areas. We propose that the coastal regions are characterized by solar sectional shading (SSS). Solar sectional shading is an atmospheric event due to cloud movements and formation over area, leading to physical shades over a region during solar radiation [27]. The evidence of weather on solar farm was done using 3D simulation of sunshine hour, solar irradiance, and surface temperature.



FIGURE 1: Location of study area in the enclave of Nigeria.



FIGURE 2: Location of study coastal area.

4. Evidence of Weather Effect on Solar Farm Setup

A twenty-year dataset (1993–2012) obtained from Nigerian Meteorological Agency for the research site was used to investigate the weather effect on solar farms in the coastal

area. The weather parameters are sunshine hour, solar irradiance, and surface temperature. The 3D representation of the weather parameter was articulated via the “surfer 8” software (see Figures 5–7). The shape enabled the instability of the weather parameters within two decades. For example, the months of January, February, March, May, July, September,

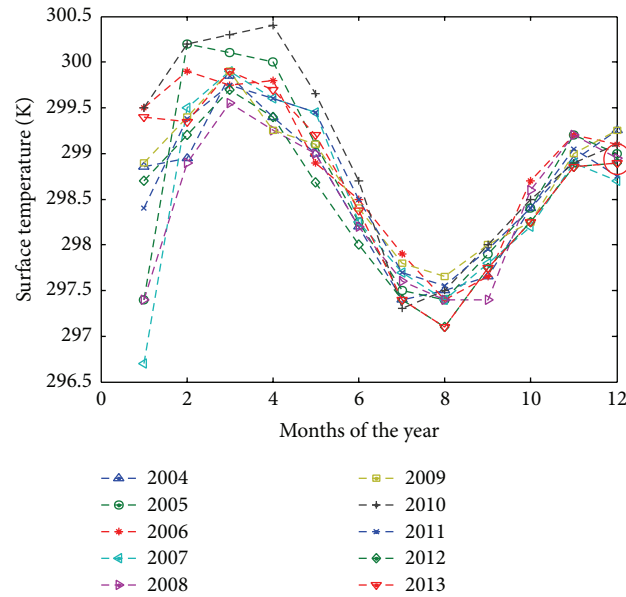


FIGURE 3: Monthly surface temperature data (2004–2013).

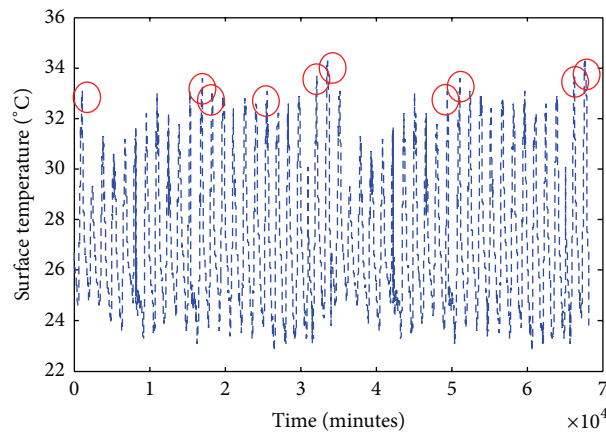


FIGURE 4: Ten-year surface temperature data (2004–2013).

October, November, and December showed massive instabilities over two decades while larger part of the months of April, June, and August showed stability.

5. Field-Work Results

The voltage-time graph of the four PV thin film module groups and temperature-time graph from the Davis weather station for active days of December are shown in Figure 9. The specific solar radiation trends were selected and discussed [27]. The undulating surface temperature which is a direct influence of solar radiation [29, 30] is captured in the voltage output. All groups responded to the first surface trough above 30°C (see the red arrow in Figures 8 and 9). The arrows show that there was a small voltage difference between the clean and dusty sharp PV modules. Also it is important to note that the coincidental intercepts between the clean and dusty PV modules are due to a basic principle; that is, the open-circuit

voltage V_{oc} is inversely proportional to the temperature; that is, as the temperature increases, the voltage decreases. All the solar panels in each group responded differently to subsequent drop of solar radiation. Sometimes, CSW and DSW recover their sinusoidal form, that is, in accordance with the prevailing solar radiation.

A comparative study between Figures 8 and 9 shows a fluctuation between 140 and 180 minutes. Also, it can be interpreted that the fluctuation was as a result of temperature drop due to solar shading. Another kind of solar irradiance trend on the efficiency of the PV module is the affirmation of the two kinds of temperature rise, that is, an undulating temperature rise and a fair temperature rise. An undulating temperature rise is characterized by slant crest and trough. A fair temperature rise is neither linear nor parabolic. It is characterized by uniform or constant regions within its rise. Both groups of SolarWorld PV modules seem to perform better in a fair temperature rise. The sharp PV thin film module

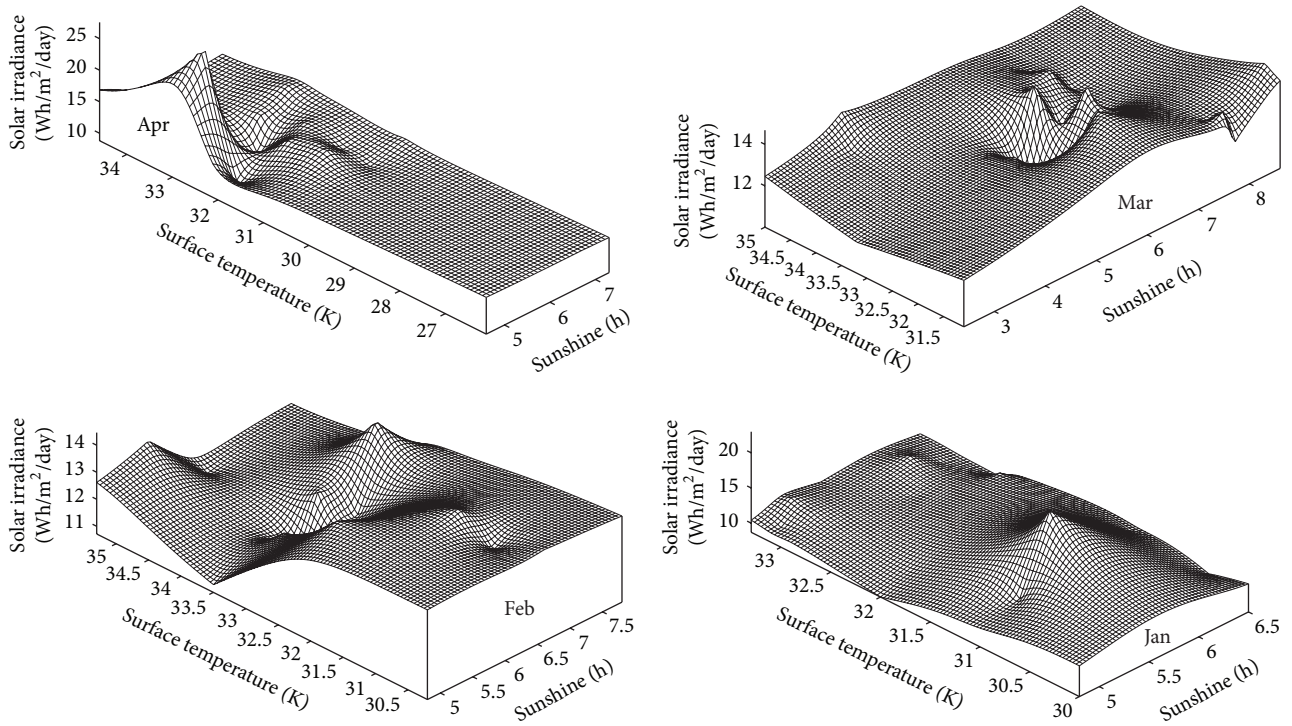


FIGURE 5: Weather parameter trend for January–April.

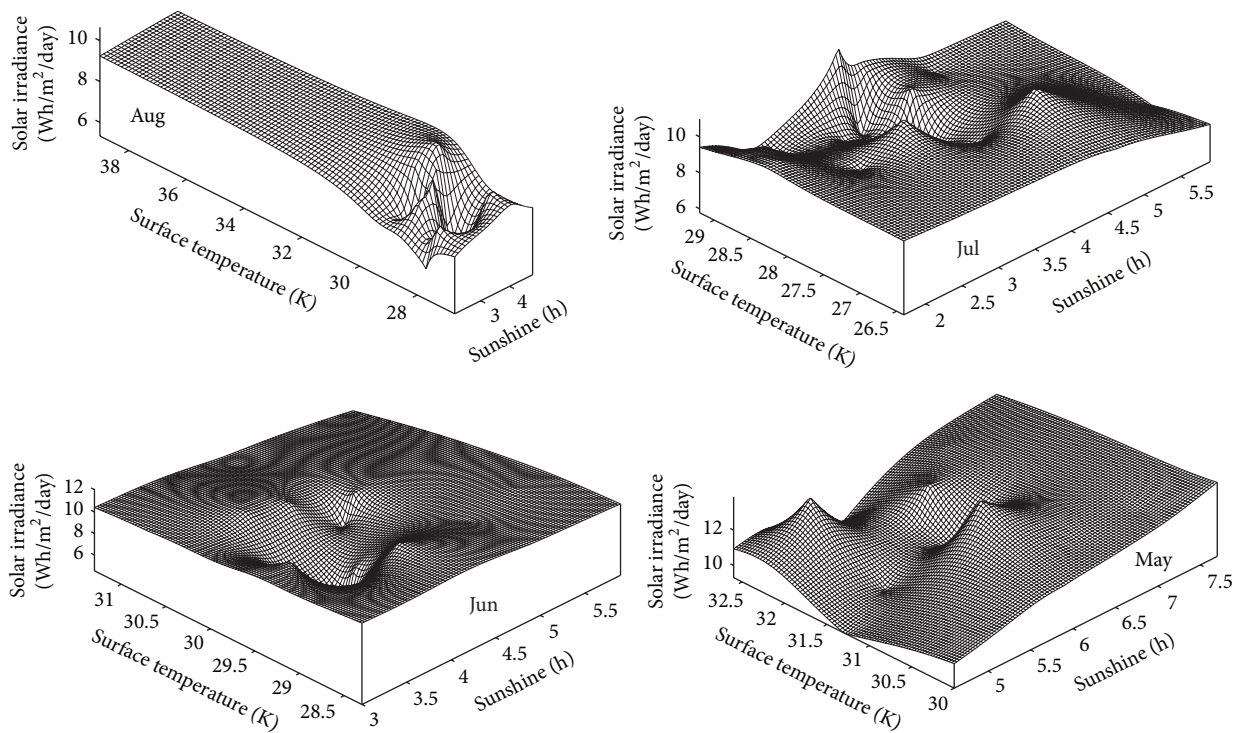


FIGURE 6: Weather parameter trend for May–August.

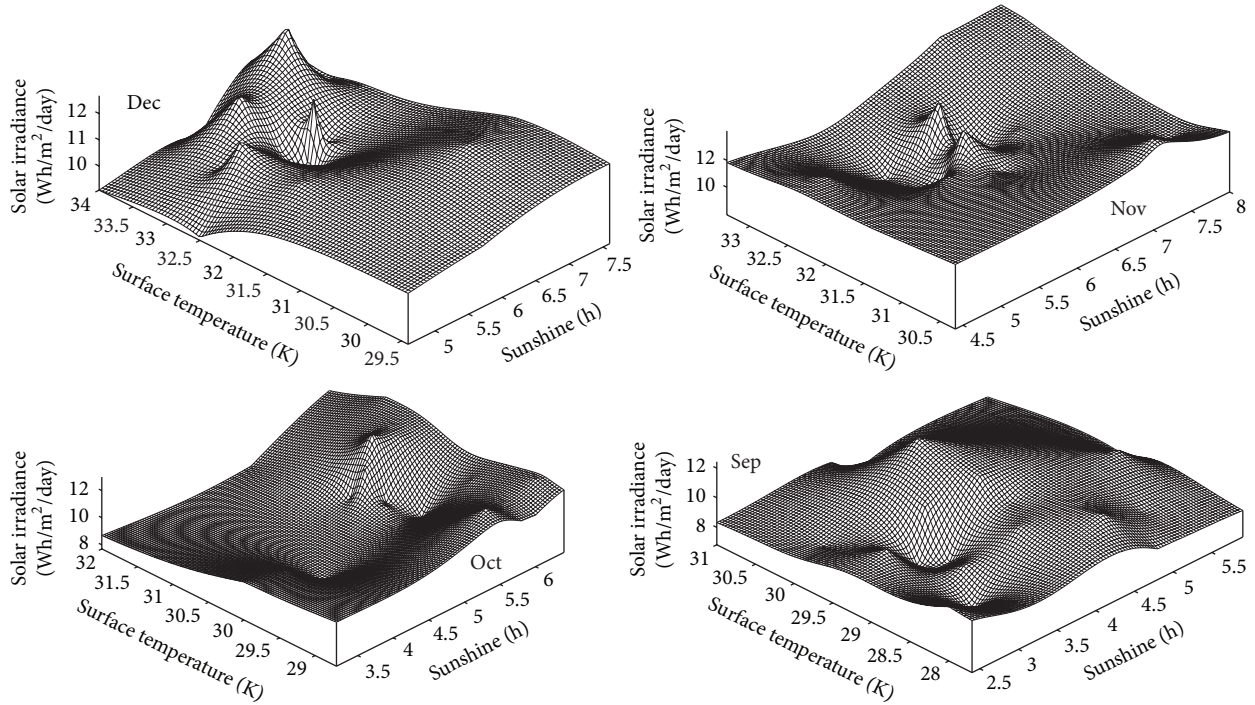


FIGURE 7: Weather parameter trend for September–December.

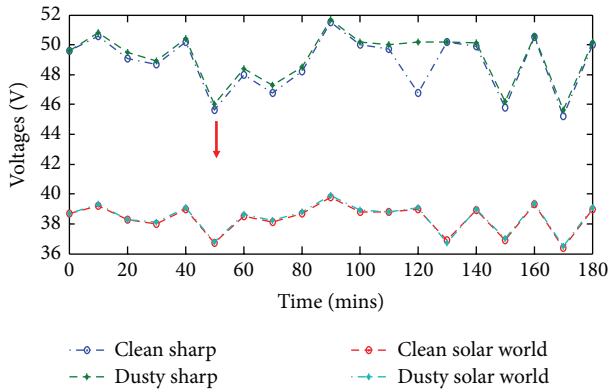


FIGURE 8: Voltage-time on day four (12:00–15:00 daily).

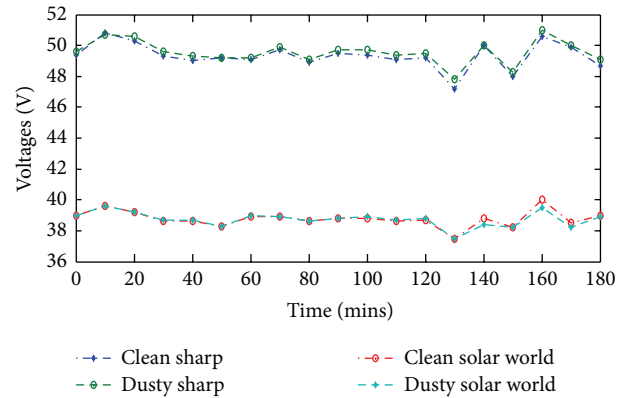


FIGURE 10: Voltage-time on day six (12:00–15:00 daily).

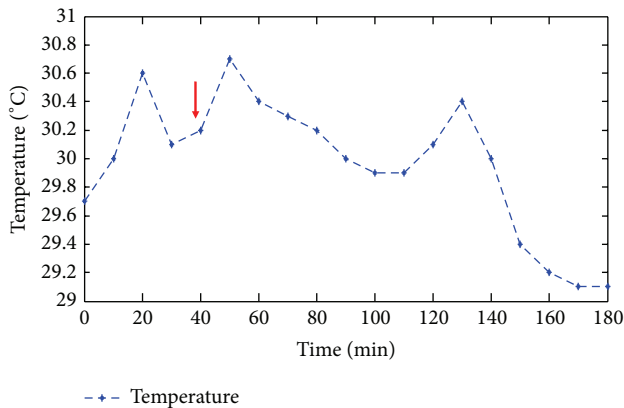


FIGURE 9: Temperature-time on day four (12:00–15:00 daily).

does not easily recover from sudden drop in temperature. SolarWorld PV module is more stable at this point. Also, the solar radiation may mimic a Gaussian distribution (see Figure 11). Its output as seen in Figure 10 supports a fairly stabilized voltage output.

6. The Theoretical Solar Farm Suggested for Coastal Areas

PV panels mounted in coastal region (as illustrated in the previous sections) can sometimes be inefficient in harvesting all available energy from sunlight because of the SSS, shape of PV module, and varying solar intensity throughout the day. Therefore, the results shown in previous sections are very

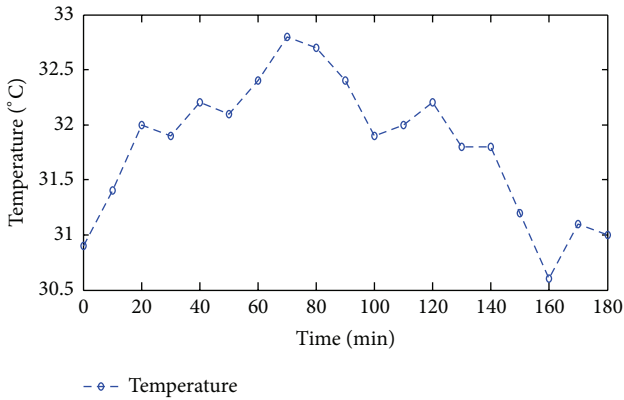


FIGURE 11: Temperature-time on day six (12:00-15:00 daily).

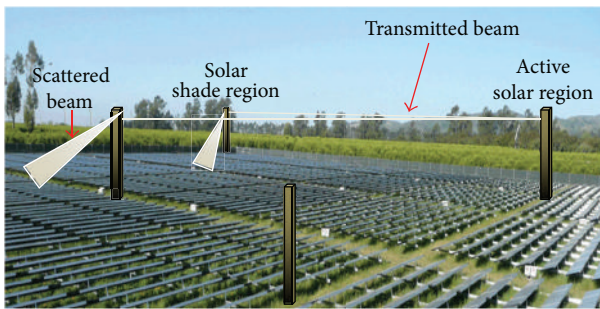


FIGURE 12: Solar farm with concentrator pillars at SSS boundaries.

important in planning a solar farm for coastal region. We maintain the basic parameters for setting up a solar farm. The only improvement proposed for the solar farm setup is the inclusion of the electronic concentrator pillars (CP) which are expected to provide uniform solar radiation for the PV modules. Solar concentrators are efficient in tropic region except for its coast plain. The size of the SSS may be large over an area. This is due to formation of cloud forms. When the size of the SSS is large, the solar tracker (which mounts the concentrator) may be inefficient in a solar farm. The technique suggested in this research is hinged on two assumptions; that is, the solar farm must occupy a fairly large area for the electronics concentrator to keep track of the position of the sun; the mirrors and transmitting lens should be mounted on different solar tracker. On a smaller solar farm, the success of this technique lies in the expertise of personnel to determine of the SSS boundaries so as to locate the concentrator pillars (CP) as shown in Figure 12. The CP is made up of majorly transmitting lens, mirrors, solar radiation relays, and switching integrated circuit. All the electronic CP are configured to operate at almost equal voltage output. When there is SSS in some part, there is a drastic drop in the voltage supply of the particular CP, that is, within the circuitry of the CP. This action initiates the transmitting lens of the CP in the active solar region to switch on and transmits radiation to other neighboring CP. We propose that this technique could maintain an almost uniform solar radiation (see Figure 12) during the active hours of the day.

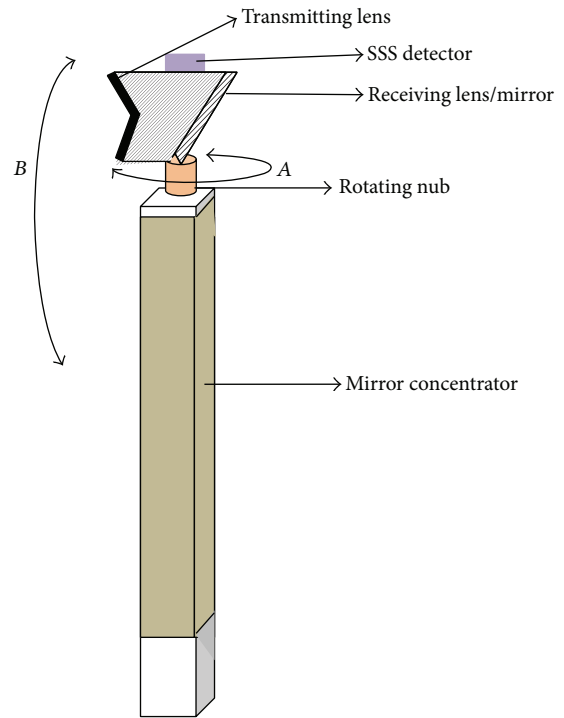


FIGURE 13: Pictorial model of a concentrator pillar.

We gave a pictorial model for the electronic CP (Figure 13). The electronics diagram was not reported to allow for ingenuity by researchers or manufacturers.

The electronic concentrator pillar is made up of a mirror wall for reflectivity rebound. An improved mirror may be used, that is, mirror symmetrical dielectric totally internally reflecting concentrator (MSDTIRC). Davis [31] and Muhammad-Sukki et al. [30] recently highlighted the advantages of the MSDTIRC, that is, increasing the electrical output of a solar photovoltaic (PV) system and reducing the amount of the PV cell material needed, hence minimizing the production cost of the system. The rotating nub enables both zenith and azimuth rotation to locate the nearest transmitting CP (see “A” in Figure 13). The casing of the transmitting lens is designed to provide a continuous radiating guide. This process is almost synonymous to the fundamental principles of a wave guide or resonating cavity. The transmitting lens has a vertical/zenith rotation (see “B” in Figure 13) whose stability depends on the solar sensors of neighboring CP. The solar sensor on the transmitting CP works on the principle of back-scattering. This process enables it to detect the radiational magnitude of the nearest receiving CP. The transmitting CP trips off as soon as solar detector receives a back-scattered solar radiation that is equal or nearly equal to SSS detector. This process repeats itself if any SSS detector switches off. The sensors of the electronic CP are programmed to operate at similar magnitude. If the radiational magnitude of any CP falls below others, the rotating nub of the nearest receiving and transmitting CP rotates to detect each of them.

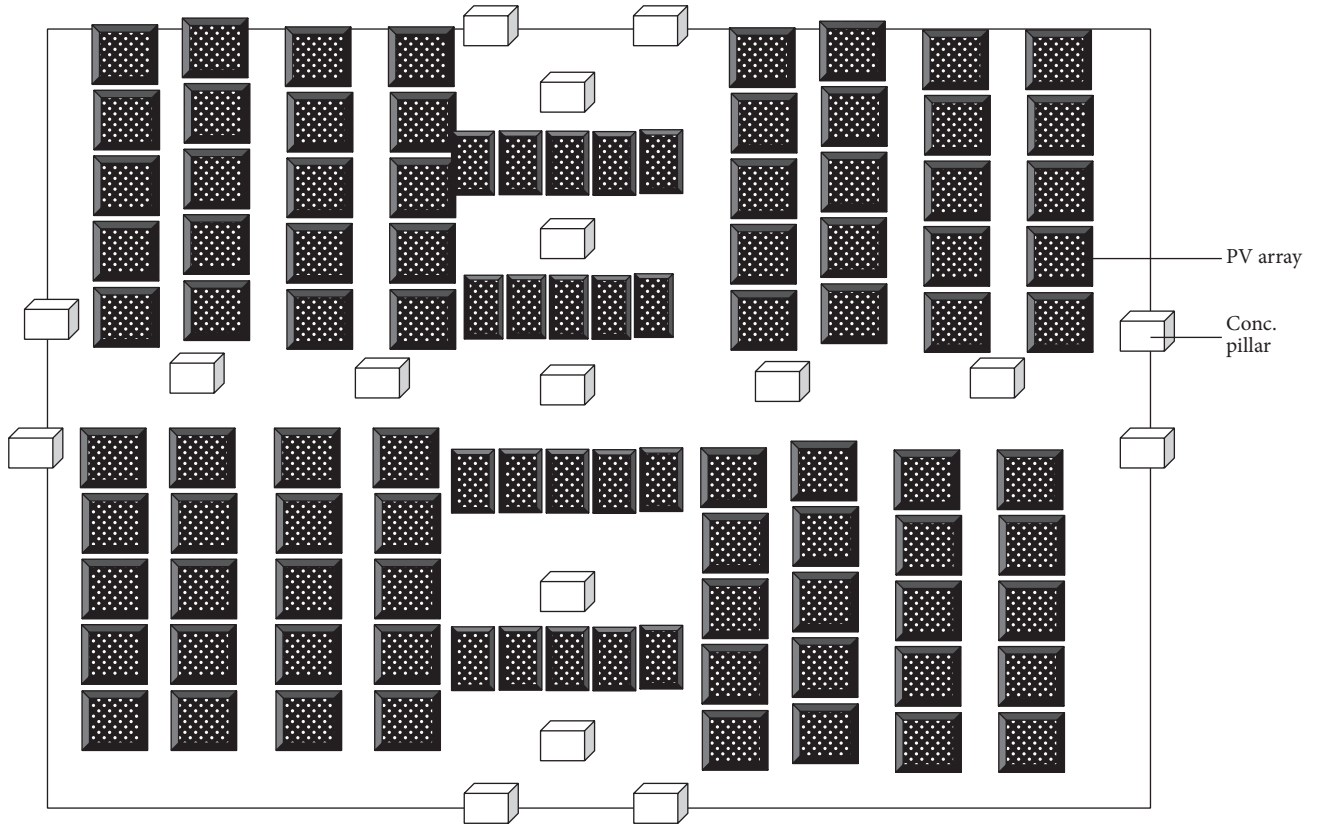


FIGURE 14: Aerial view of the solar farm.

Further calculations are required for maximum application of this technique. The aerial view of the solar farm is shown in Figure 14.

The concentrator pillars at the boundaries are used to correct the shades created by the concentrator pillar within the solar farm. The economic viability of this project is dependent on the quality of the material used. Hence, the cost may vary due to availability of material or components used to build the concentrator pillars.

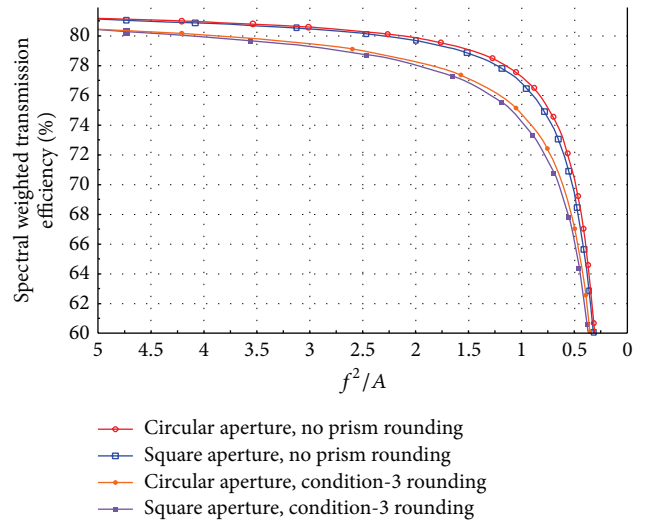
The validity of the CP technology to improve the PV module efficiency is evident in its transmittance and energy yield. The transmittance may be surface reflection (T_{sr}) or geometry loss (T_{gl}). This can be expressed mathematically:

$$T_{sr} = \left(\frac{n_t \cos \theta_t}{2n_i \cos \theta_i} \right) (t_{\perp}^2 + t_{\parallel}^2). \quad (1)$$

Here n_i is the index of refraction for the ray in the incident media, n_t is the index of refraction for the ray in the transmitted media, and θ_i and θ_t are incident and refracted angles. Consider

$$T_{gl} = 1 - \left(\frac{s-b}{d} \right). \quad (2)$$

Here s is the radius loss distance, b is the projected draft, and d is the transmission distance. Since geometry loss arises from the draft surface and prism tip rounding of the lens facets,

FIGURE 15: Circular versus square lens aperture transmittance comparison when plotted on an axis of squared focal ratio f^2/A . Reference [11].

the prospect of the lens array design in Figure 11 to improve the efficiency of the PV had been expressed in Figure 15.

The spectra weighted transmission efficiency for square lens aperture is lower than circular lens. This means that when rays are transmitted from the CP onto the PV module, the tendency of geometry loss is lower than the circular lens.

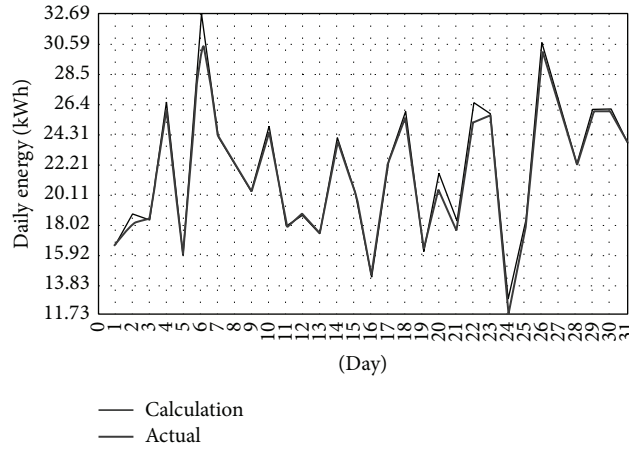


FIGURE 16: Daily energy output from polycrystalline PV module. Reference [12].

The validity of the energy yield prediction of a PV model has been expressed in [12] shown in Figure 16.

The energy yield of the PV module is given as [32]

$$E = a_1H + a_2HT_{\max}^{-2} + a_3T_{\max}. \quad (3)$$

Here H is the direct normal irradiation, T is the temperature, and a_1 , a_2 , and a_3 are regression coefficients. The three terms on the right hand side give linear trend lines, that is, the first two for each installation (CP and PV module) and the third for both installations. Hence, CP installation can be modeled linearly and rarely generate energy at very low levels of irradiation [10]; hence, the performance ratio (PR) is expressed as

$$PR = \frac{0.85E}{H}. \quad (4)$$

We propose that “ n ” is number of hours per day; then

$$PR = \frac{0.85E}{H}n. \quad (5)$$

Since performance ratio is the ratio of production energy to expected energy and the regression coefficient is negligible due to the CP, then the expected energy yield can be written as

$$E_e = \frac{T_{\max}}{PR - (0.85n + 0.85nT_{\max}^{-2})}. \quad (6)$$

The second term of the denominator was discarded because it is not dependent on temperature. This term becomes the source of error when the system is at its minimum energy generation at very low levels of irradiation; hence,

$$E_e = \frac{T_{\max}}{PR - 0.85nT_{\max}^{-2}}. \quad (7)$$

Equation (5) was analyzed at various performance ratios, that is, 0.5, 0.85, and 1.5 (Figure 17).

From the above simulation, the minimum energy expectation is 65 KWh at a performance ratio, that is, unity. The expected energy yield rises as the duration of the CP installation increases. From Figure 17, the linearity of the CP installation was affirmed. Hence if we intend to generate twice the production energy (PR = 0.5), the maximum expected energy yield would be 135 KWh.

7. Conclusion

It was analytically and numerically proven that climatic factors influence solar radiation in coastal regions. This means that solar PV efficiency would be greatly affected. The day-to-day solar radiation pattern experiment was performed in the tropical coastal areas. The solar radiation pattern is characterized by undulating rise, fair rise, and Gaussian distribution. The danger of the irregular solar radiation features can be seen to mitigate individual performance of the solar cells and its lifecycle. The reason for irregular solar radiation was adduced to solar sectional shading because it is prevalent in the coastal region and triggers the type of solar pattern for the day/month/year. The SSS is an atmospheric event which occurs due to cloud formation and movements over coastal area. A mathematical model was propounded to explain the collective solar radiation over a massive coastal area. The surface temperature or the solar intensity is inversely proportional to the area. The practical solution for enhancing solar PV efficiency in the coastal areas was suggested via the introduction of electronic concentrator pillars in a proposed solar farm. The pictorial and operational model was adequately explained.

Competing Interests

The authors declare no conflict of interests.

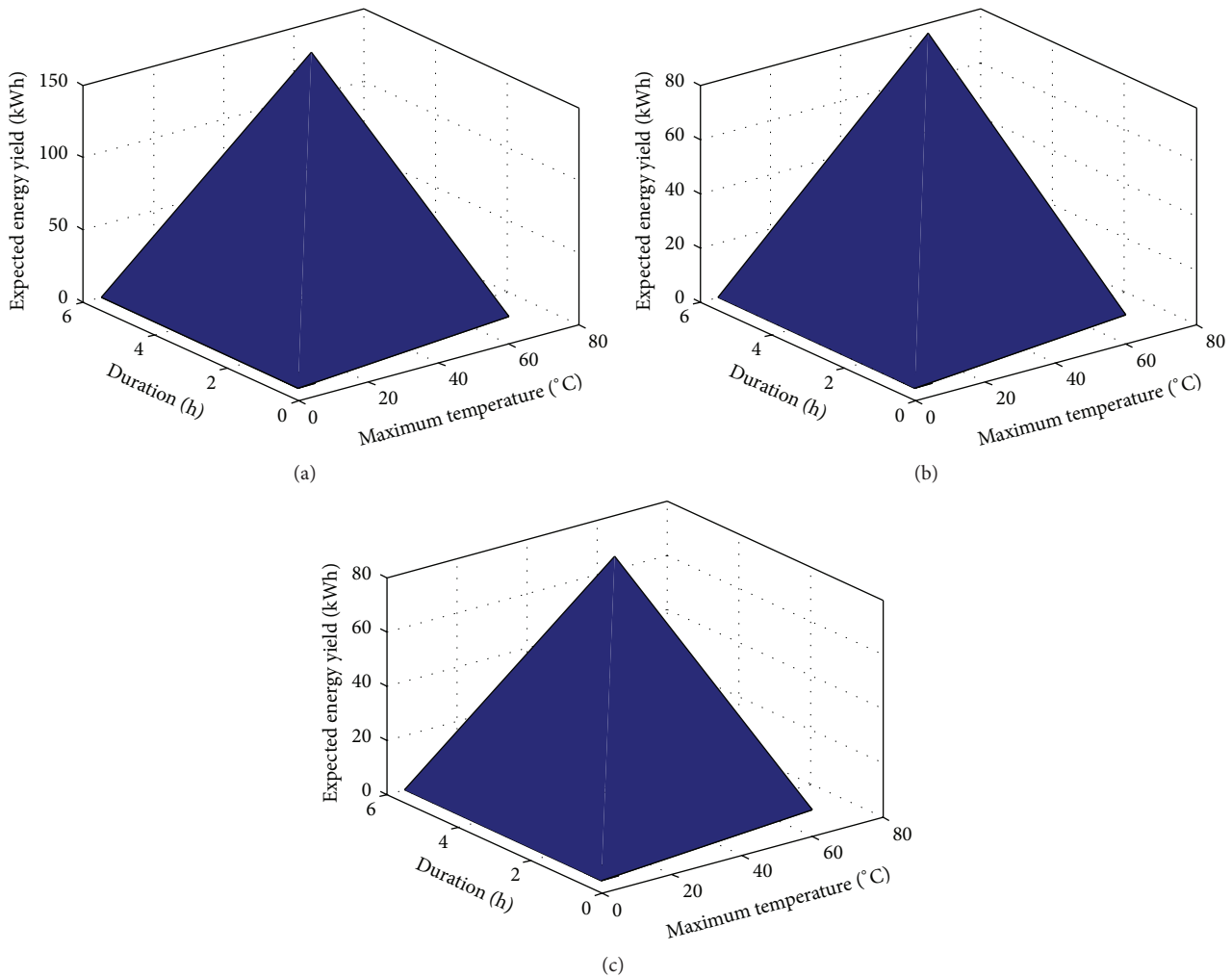


FIGURE 17: (a) Energy yield when PR = 0.5. (b) Energy yield when PR = 0.85. (c) Energy yield when PR = 1.

Acknowledgments

The authors appreciate the host institution for their partial sponsorship. The authors appreciate the contributions of Jennifer Emeter.

References

- [1] V. Devabhaktuni, M. Alam, S. Shekara Sreenadh Reddy Depuru, R. C. Green II, D. Nims, and C. Near, "Solar energy: trends and enabling technologies," *Renewable and Sustainable Energy Reviews*, vol. 19, pp. 555–564, 2013.
- [2] M. E. Emeter and M. L. Akinyemi, "Modeling of generic air pollution dispersion analysis from cement factory," *Analele Universitatii din Oradea—Seria Geografie*, no. 1, Article ID 231123-628, pp. 181–189, 2013.
- [3] M. E. Emeter, "Modeling of particulate radionuclide dispersion and deposition from a cement factory," *Annals of Environmental Science*, vol. 7, no. 6, pp. 71–77, 2013.
- [4] A. Brown, "Aerosol choices matter," *Nature Climate Change*, vol. 2, pp. 75–79, 2012.
- [5] A. Tsikalakis, T. Tomtsi, N. D. Hatzigaryriou et al., "Review of best practices of solar electricity resources applications in selected Middle East and North Africa (MENA) countries," *Renewable and Sustainable Energy Reviews*, vol. 15, no. 6, pp. 2838–2849, 2011.
- [6] S. Keleş and S. Bilgen, "Renewable energy sources in Turkey for climate change mitigation and energy sustainability," *Renewable and Sustainable Energy Reviews*, vol. 16, no. 7, pp. 5199–5206, 2012.
- [7] K. G. McCracken, J. Beer, and F. Steinhilber, "Evidence for planetary forcing of the cosmic ray intensity and solar activity throughout the past 9400 years," *Solar Physics*, vol. 289, no. 8, pp. 3207–3229, 2014.
- [8] M. Jacobson, "Review of solutions to global warming, air pollution, and energy security," Tech. Rep., Stanford University, Stanford, Calif, USA, 2008.
- [9] M. E. Emeter, "Forecasting hydrological disaster using environmental thermographic modeling," *Advances in Meteorology*, vol. 2014, Article ID 783718, 9 pages, 2014.
- [10] C. Greacen and D. Green, "The role of bypass diodes in the failure of solar battery charging stations in Thailand," *Solar Energy Materials and Solar Cells*, vol. 70, no. 2, pp. 141–149, 2001.

- [11] A. M. Omar, M. Z. Hussin, S. Shaaria, and K. Sopianb, "Energy yield calculation of the grid connected photovoltaic power system," in *Computer Applications in Environmental Sciences and Renewable Energy*, pp. 162–167, WSEAS Press, 2014.
- [12] E. Skoplaki and J. A. Palyvos, "On the temperature dependence of photovoltaic module electrical performance: a review of efficiency/power correlations," *Solar Energy*, vol. 83, no. 5, pp. 614–624, 2009.
- [13] E. Hoff and M. Cheney, "The idea of low cost photovoltaic," *Energy Journal*, vol. 93, article 17, 2000.
- [14] S. Olayinka Oyedepo, "Energy and sustainable development in Nigeria: the way forward," *Energy, Sustainability and Society*, vol. 2, no. 1, article 15, pp. 1–17, 2012.
- [15] V. V. Tyagi, S. C. Kaushik, and S. K. Tyagi, "Advancement in solar photovoltaic/thermal (PV/T) hybrid collector technology," *Renewable and Sustainable Energy Reviews*, vol. 16, no. 3, pp. 1383–1398, 2012.
- [16] Y. Tian and C. Y. Zhao, "A review of solar collectors and thermal energy storage in solar thermal applications," *Applied Energy*, vol. 104, pp. 538–553, 2013.
- [17] T. M. Razykov, C. S. Ferekides, D. Morel, E. Stefanakos, H. S. Ullal, and H. M. Upadhyaya, "Solar photovoltaic electricity: current status and future prospects," *Solar Energy*, vol. 85, no. 8, pp. 1580–1608, 2011.
- [18] M. S. Jamel, A. Abd Rahman, and A. H. Shamsuddin, "Advances in the integration of solar thermal energy with conventional and non-conventional power plants," *Renewable and Sustainable Energy Reviews*, vol. 20, pp. 71–81, 2013.
- [19] X. Py, Y. Azoumah, and R. Olives, "Concentrated solar power: current technologies, major innovative issues and applicability to West African countries," *Renewable and Sustainable Energy Reviews*, vol. 18, pp. 306–315, 2013.
- [20] E. F. Camacho, F. R. Rubio, M. Berenguel, and L. Valenzuela, "A survey on control schemes for distributed solar collector fields. Part II: advanced control approaches," *Solar Energy*, vol. 81, no. 10, pp. 1252–1272, 2007.
- [21] U. Desideri and P. E. Campana, "Analysis and comparison between a concentrating solar and a photovoltaic power plant," *Applied Energy*, vol. 113, pp. 422–433, 2014.
- [22] J. J. Navarrete-González, J. G. Cervantes-de Gortari, and E. Torres-Reyes, "Exergy analysis of a rock bed thermal storage system," *International Journal of Exergy*, vol. 5, no. 1, pp. 18–30, 2008.
- [23] I. M. Michaelides, S. A. Kalogirou, I. Chrysis et al., "Comparison of performance and cost effectiveness of solar water heaters at different collector tracking modes in Cyprus and Greece," *Energy Conversion and Management*, vol. 40, no. 12, pp. 1287–1303, 1999.
- [24] S. Karsli, "Performance analysis of new-design solar air collectors for drying applications," *Renewable Energy*, vol. 32, no. 10, pp. 1645–1660, 2007.
- [25] F. Cavallaro, "Fuzzy TOPSIS approach for assessing thermal-energy storage in concentrated solar power (CSP) systems," *Applied Energy*, vol. 87, no. 2, pp. 496–503, 2010.
- [26] V. Gnanaswar Gude, N. Nirmalakhandan, S. Deng, and A. Maganti, "Low temperature desalination using solar collectors augmented by thermal energy storage," *Applied Energy*, vol. 91, no. 1, pp. 466–474, 2012.
- [27] M. E. Emetere and M. L. Akinyemi, "Weather effect on photovoltaic module adaptation in coastal areas," *International Journal of Renewable Energy Research*, vol. 5, no. 3, pp. 821–825, 2015.
- [28] M. Stabholz, X. Durrieu de Madron, M. Canals et al., "Impact of open-ocean convection on particle fluxes and sediment dynamics in the deep margin of the Gulf of Lions," *Biogeosciences*, vol. 10, no. 2, pp. 1097–1116, 2013.
- [29] H. van Loon, G. A. Meehl, and J. M. Arblaster, "A decadal solar effect in the tropics in July-August," *Journal of Atmospheric and Solar-Terrestrial Physics*, vol. 66, no. 18, pp. 1767–1778, 2004.
- [30] F. Muhammad-Sukki, S. H. Abu-Bakar, R. Ramirez-Iniguez et al., "Mirror symmetrical dielectric totally internally reflecting concentrator for building integrated photovoltaic systems," *Applied Energy*, vol. 113, pp. 32–40, 2014.
- [31] A. Davis, "Raytrace assisted analytical formulation of Fresnel lens transmission efficiency," in *Novel Optical Systems Design and Optimization XII*, vol. 7429 of *Proceedings of SPIE*, pp. D1–D12, San Diego, Calif, USA, August 2009.
- [32] F. J. Gómez-Gil, X. Wang, and A. Barnett, "Analysis and prediction of energy production in concentrating photovoltaic (CPV) installations," *Energies*, vol. 5, no. 3, pp. 770–789, 2012.

Research Article

Wide-Range Enhancement of Spectral Response by Highly Conductive and Transparent $\mu\text{c-SiO}_x\text{:H}$ Doped Layers in $\mu\text{c-Si:H}$ and a-Si:H/ $\mu\text{c-Si:H}$ Thin-Film Solar Cells

Pei-Ling Chen, Po-Wei Chen, Min-Wen Hsiao, Cheng-Hang Hsu, and Chuang-Chuang Tsai

Department of Photonics, National Chiao Tung University, 1001 University Road, Hsinchu 30010, Taiwan

Correspondence should be addressed to Pei-Ling Chen; daphnechen0822orama@gmail.com

Received 15 April 2016; Accepted 12 July 2016

Academic Editor: Vishal Mehta

Copyright © 2016 Pei-Ling Chen et al. This is an open access article distributed under the Creative Commons Attribution License, which permits unrestricted use, distribution, and reproduction in any medium, provided the original work is properly cited.

The enhancement of optical absorption of silicon thin-film solar cells by the p- and n-type $\mu\text{c-SiO}_x\text{:H}$ as doped and functional layers was presented. The effects of deposition conditions and oxygen content on optical, electrical, and structural properties of $\mu\text{c-SiO}_x\text{:H}$ films were also discussed. Regarding the doped $\mu\text{c-SiO}_x\text{:H}$ films, the wide optical band gap (E_{04}) of 2.33 eV while maintaining a high conductivity of 0.2 S/cm could be obtained with oxygen incorporation of 20 at.%. Compared to the conventional $\mu\text{c-Si:H(p)}$ as window layer in $\mu\text{c-Si:H}$ single-junction solar cells, the application of $\mu\text{c-SiO}_x\text{:H(p)}$ increased the V_{OC} and led to a significant enhancement in the short-wavelength spectral response. Meanwhile, the employment of $\mu\text{c-SiO}_x\text{:H(n)}$ instead of conventional ITO as back reflecting layer (BRL) enhanced the external quantum efficiency (EQE) of $\mu\text{c-Si:H}$ single-junction cell in the long-wavelength region, leading to a relative efficiency gain of 10%. Compared to the reference cell, the optimized a-Si:H/ $\mu\text{c-Si:H}$ tandem cell by applying p- and n-type $\mu\text{c-SiO}_x\text{:H}$ films achieved a V_{OC} of 1.37 V, J_{SC} of 10.55 mA/cm², FF of 73.67%, and efficiency of 10.51%, which was a relative enhancement of 16%.

1. Introduction

Over the past decade, silicon-based thin-film solar cell technology has become a viable approach for mass production due to its characteristics such as large-scale production, low temperature process, and abundant storage of silicon in the earth crust [1, 2]. However, compared with the mainstream of photovoltaics, the conversion efficiency of silicon-based thin-film solar cells still needs to be improved. One of the approaches is to fabricate multijunction solar cells comprising subcells with absorbers having different band gaps to convert broad-band solar energy into electricity. Among various silicon-based materials, the hydrogenated microcrystalline silicon ($\mu\text{c-Si:H}$) has been reported as a promising candidate for the absorber of middle or bottom cells in multijunction cells. The $\mu\text{c-Si:H}$ has the advantages of higher optical absorption coefficients at the infrared region and less light-induced degradation than the hydrogenated amorphous silicon (a-Si:H) [3]. Intensive researches have focused on the development of a-Si:H/ $\mu\text{c-Si:H}$ tandem solar

cells [4–6]. The band gap combination of a-Si:H (~1.8 eV) and $\mu\text{c-Si:H}$ (~1.1 eV) provides a great benefit of utilizing broad sunlight spectrum [6]. However, the absorber thickness of $\mu\text{c-Si:H}$ is relatively thick (~1–3 μm) compared with a-Si:H owing to its nature of indirect band gap. To further improve the efficiency of $\mu\text{c-Si:H}$ solar cells without increasing the thickness of the absorbers, the light management of the solar cells is a critical factor.

Studies have reported that the p- and n-type $\mu\text{c-Si:H}$ are commonly used as doped layers in $\mu\text{c-Si:H}$ solar cells due to its properties of low activation energy and high conductivity, which increased the built-in field and reduced the series resistance of solar cells [7, 8]. However, the optical band gap (E_{04} , the photon energy at which the absorption coefficient is 10⁴ cm⁻¹) could only be adjusted in a small range of 1.9–2.1 eV for the doped $\mu\text{c-Si:H}$ layers [9, 10]. Besides, the parasitic absorption of the doped $\mu\text{c-Si:H}$ layers contributes to the loss in photocurrent. To further improve the optical properties of the doped layers, hydrogenated microcrystalline silicon oxide ($\mu\text{c-SiO}_x\text{:H}$) has been developed for thin-film solar cells. The

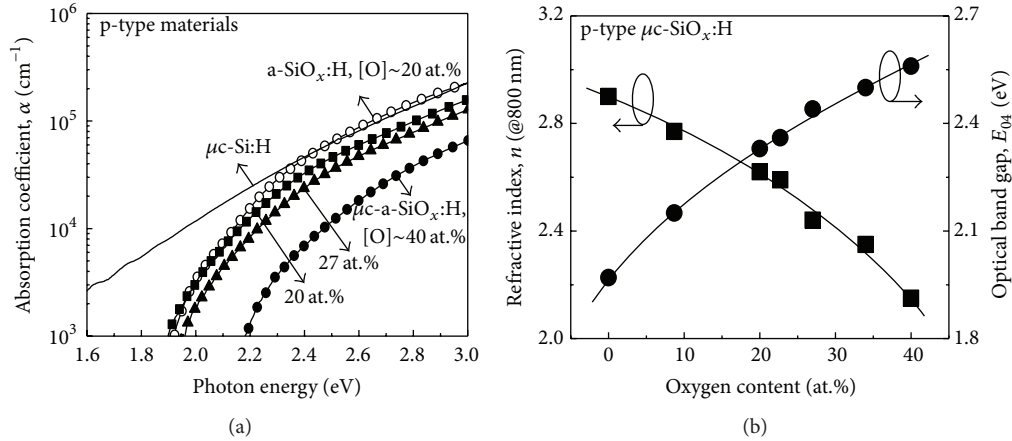


FIGURE 1: (a) Absorption coefficient of a-SiO_x:H, μc-Si:H, and μc-SiO_x:H with varied oxygen content [O] and (b) the refractive index (n) and the optical band gap (E_{04}) of μc-SiO_x:H with varied oxygen content [O].

μc-SiO_x:H has been proposed to be a mixed-phase material comprising a-SiO_x:H phase and μc-Si:H phase [11, 12]. The oxygen-rich amorphous phase supplied low refractive index and high E_{04} , while the conductive doped μc-Si:H phase provided the low-resistance pathway for carrier transport [12]. The incorporation of oxygen in the silicon network effectively widened the E_{04} and reduced the refractive index. As a result, the doped μc-SiO_x:H can be used as doped layers as well as intermediate reflecting layer (IRL), tunneling recombination junction (TRJ) layer, and back reflecting layer (BRL), owing to its tunable optical and electrical properties [13–17].

Nevertheless, excessive oxygen content in μc-SiO_x:H film significantly suppressed the crystallization, which adversely affected the electrical property. Reports have shown that compared to μc-Si:H having conductivity of 10~10² S/cm and E_{04} of 1.9~2.1 eV, the conductivity of the doped μc-SiO_x:H films degraded to 10⁻³~10⁻⁴ S/cm as the E_{04} was as high as 2.3 eV [18, 19]. Therefore, to further improve the electrical and optical property by optimizing the deposition conditions were needed for enabling the extensive applicability of the μc-SiO_x:H films.

This work aims to efficiently enhance the light absorption in solar cells. The optoelectrical properties of the doped μc-SiO_x:H materials as the window and the back reflector layers employed in μc-Si:H single-junction and a-Si:H/μc-Si:H tandem solar cells were investigated.

2. Experimental Details

Silicon-based thin-films were prepared with a single chamber process in multichamber plasma-enhanced vapor deposition (PECVD) system equipped with 27.12 MHz RF power and NF₃ in situ plasma cleaning. Gas mixture of SiH₄, CO₂, B₂H₆, PH₃, and H₂ was used as source gases. The μc-SiO_x:H(p) and μc-SiO_x:H(n) films were deposited onto Corning EAGLE XG glass substrate at approximately 190°C. The incorporation of oxygen was achieved by introducing CO₂ in highly H₂-diluted SiH₄. The oxygen content, [O], of μc-SiO_x:H films was

examined by an X-ray photoelectron spectroscopy (XPS). The crystalline volume fraction (X_C) of μc-SiO_x:H was calculated from the ratio of the integrated intensities of deconvoluted peaks centered at 480, 510, and 520 cm⁻¹ from a Raman spectrum with a probe laser of 488 nm excitation. The optical band gap (E_{04}) was obtained by an ultraviolet-visible-near-infrared spectrophotometer. The refractive indices were estimated from an ellipsometry measurement by applying Fresnel equation. The dark conductivity (σ_d) was measured with coplanar Ag electrodes at room temperature.

The μc-Si:H solar cells were deposited in a superstrate configuration on textured SnO₂:F glass substrate. The structure of μc-Si:H single-junction solar cells was glass/SnO₂:F/μc-SiO_x:H(p)/μc-Si:H(i)/μc-SiO_x:H(n)/Ag with 1.4 μm thick μc-Si:H absorber. The thicknesses of the absorbers of a-Si:H and μc-Si:H component cells were 240 nm and 1.4 μm, respectively. The Ag electrode was prepared by thermal evaporator with the area of 0.25 cm² defined by the shadow mask. The cells were characterized by an AM1.5G illuminated J - V measurement system and an external quantum efficiency (EQE) instrument.

3. Results and Discussion

3.1. Electrical and Optical Properties of Doped μc-SiO_x:H Thin-Films. The absorption coefficients of the p-type μc-SiO_x:H as a function of [O] are shown in Figure 1(a). Compared to the a-SiO_x:H(p), the μc-SiO_x:H(p) exhibited lower absorption coefficient owing to the indirect band gap of μc-Si:H phase while the oxygen content was 20 at.% in both cases. In addition, the optical absorption coefficient of μc-SiO_x:H(p) shifted toward higher photon energy as the oxygen content was increased from 0 (μc-Si:H(p)) to 40 at.%, which was attributed to the increased a-SiO_x:H phase in the films [11]. The n-type μc-SiO_x:H layers showed similar trends [20].

The refractive index (n , at the wavelength of 800 nm) and the E_{04} versus the oxygen content are demonstrated in Figure 1(b). As the [O] was increased from 0 (μc-Si:H(p)) to 40 at.%, the E_{04} was increased from 1.97 to 2.56 eV. This can be

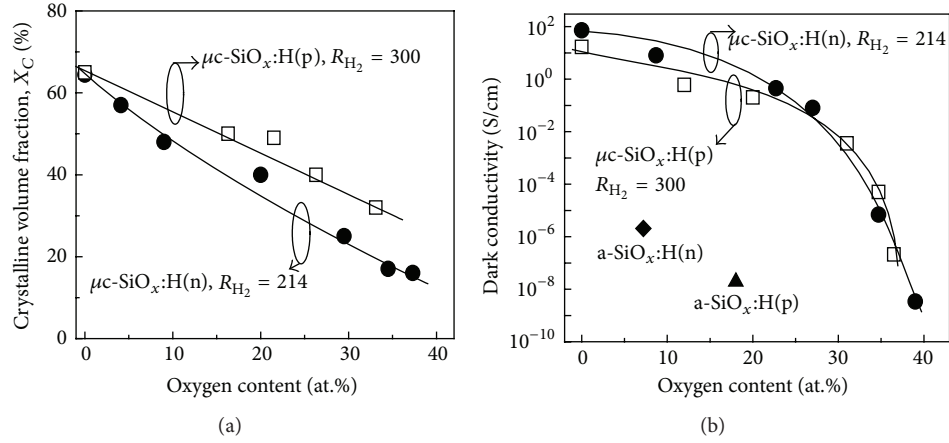


FIGURE 2: (a) Crystalline volume fraction (X_C) of $\mu\text{c-SiO}_x\text{:H(p)}$ and $\mu\text{c-SiO}_x\text{:H(n)}$ films versus the oxygen content [O]. (b) Dependence of the dark conductivity (σ_d) on the oxygen content [O] for $\mu\text{c-SiO}_x\text{:H(p)}$ and $\mu\text{c-SiO}_x\text{:H(n)}$ films.

ascribed to the increased Si-O bond in a-SiO_x:H phase since the bonding energy of Si-O bond was higher than that of Si-Si and Si-H bonds in a-SiO_x:H phase. On the other hand, the refractive index was decreased from 2.90 to 2.15 accordingly. The tunable refractive index was beneficial when employing $\mu\text{c-SiO}_x\text{:H}$ doped layers as the index-matching layer, IRL, and BRL.

The electrical properties of $\mu\text{c-SiO}_x\text{:H}$ doped layers mainly depended on X_C and doping, which was significantly affected by the deposition conditions in the PECVD system. The dependence of X_C of $\mu\text{c-SiO}_x\text{:H(p)}$ and $\mu\text{c-SiO}_x\text{:H(n)}$ films on [O] is shown in Figure 2(a). In the case of $\mu\text{c-SiO}_x\text{:H(p)}$ with H₂-to-SiH₄ flow ratio (R_{H_2}) of 300, X_C was decreased from 65 to 32% when the [O] was increased from 0 to 33 at.%. Similarly, in the case of $\mu\text{c-SiO}_x\text{:H(n)}$ with R_{H_2} of 214, as the [O] was increased from 0 to 37 at.%, X_C was decreased from 64% to 16%. This suggested that the incorporation of oxygen into $\mu\text{c-Si}$:H network suppressed the formation of crystalline phase due to the oxygen-induced defects [21]. It should be noted that R_{H_2} of $\mu\text{c-SiO}_x\text{:H(p)}$ under similar X_C was higher than that of $\mu\text{c-SiO}_x\text{:H(n)}$, which can be ascribed to the boron that had more impact on disrupting the crystalline structure than that of phosphorus [22]. It has been reported that the energy-favorable configuration of phosphorus atoms in the Si matrix was tetrahedral, which made phosphorus act as the crystallization centers [23]. In contrast, the boron may adopt other energy-favorable configurations that were not tetrahedral. The inactive boron atoms could segregate to the grain boundaries, which hindered the crystalline formation [24]. Therefore, R_{H_2} of $\mu\text{c-SiO}_x\text{:H(p)}$ was higher than that of $\mu\text{c-SiO}_x\text{:H(n)}$ in order to assist the crystallization in our case.

The dependence of σ_d on the [O] for $\mu\text{c-SiO}_x\text{:H(p)}$ and $\mu\text{c-SiO}_x\text{:H(n)}$ films was shown in Figure 2(b). In the case of $\mu\text{c-SiO}_x\text{:H(p)}$, the decreasing trend on σ_d from 16.7 to 2.1×10^{-7} S/cm with the increase [O] from 0 to 36 at.% was observed. In comparison, in the case of $\mu\text{c-SiO}_x\text{:H(n)}$, σ_d was decreased from 72.4 to 3.4×10^{-9} S/cm as [O] was increased from 0 to 39 at.%. The reduced σ_d can be attributed

to the decreased X_C arising from the increased defect density by the oxygen incorporation into the films. Moreover, the doping efficiency was reduced with the decrease in X_C [25], which further degraded σ_d at high [O]. In Figure 2(b), the p-type and n-type a-SiO_x:H were also shown for comparison. Regarding p-type layers, it can be seen that σ_d of $\mu\text{c-SiO}_x\text{:H}$ with [O] of 20 at.% was higher than that of a-SiO_x:H with [O] of 18 at.%. Similarly, $\mu\text{c-SiO}_x\text{:H(n)}$ with [O] of 8 at.% exhibited higher σ_d than a-SiO_x:H(n) with [O] of 7 at.%. The significantly enhanced σ_d was due to the crystalline structure of $\mu\text{c-SiO}_x\text{:H}$ layer which facilitated the carrier transport and the higher doping efficiency in $\mu\text{c-Si}$:H phase of $\mu\text{c-SiO}_x\text{:H}$ films compared with the a-SiO_x:H doped layers. As a result, $\mu\text{c-SiO}_x\text{:H(p)}$ with [O] of 20 at.%, E_{04} of 2.33 eV, and the high σ_d of 0.2 S/cm were obtained. Regarding the $\mu\text{c-SiO}_x\text{:H(n)}$, high σ_d of 0.08 S/cm was obtained as [O] was 27 at.% with lower refractive index of 2.55 (n at 800 nm). $\mu\text{c-SiO}_x\text{:H(p)}$ and $\mu\text{c-SiO}_x\text{:H(n)}$ with tunable optical and electrical properties were applied as window layer and BRL in silicon thin-film solar cells, respectively.

3.2. Application of $\mu\text{c-SiO}_x\text{:H(p)}$ as Window Layer in $\mu\text{c-Si}$:H Solar Cells. The $\mu\text{c-SiO}_x\text{:H(p)}$ with varied [O] were utilized in $\mu\text{c-Si}$:H single-junction solar cells. The EQE and cell reflection are illustrated in Figure 3. With the [O] increased from 0 ($\mu\text{c-Si}$:H(p)) to 31 at.%, the short-wavelength spectral response was enhanced significantly. This was due to the reduced parasitic absorption loss by using wide-band gap $\mu\text{c-SiO}_x\text{:H(p)}$ and the increased light-incoupling owing to graded refractive index [26]. The decreased cell reflection in the short-wavelength range with the increasing oxygen content corresponded to the increased EQE in the short-wavelength range. This indicated that the refractive index of $\mu\text{c-SiO}_x\text{:H(p)}$ ($n = 2.7$ at 800 nm) in between the front TCO ($n \sim 2$) and the $\mu\text{c-Si}$:H absorber ($n \sim 3.6$) may act as an antireflection layer by the graded refractive index. The corresponding cell performance of $\mu\text{c-Si}$:H single-junction solar cells is summarized in Table 1. With the [O] increase from 0 to 31 at.%, the short-circuit current density (J_{SC}) was

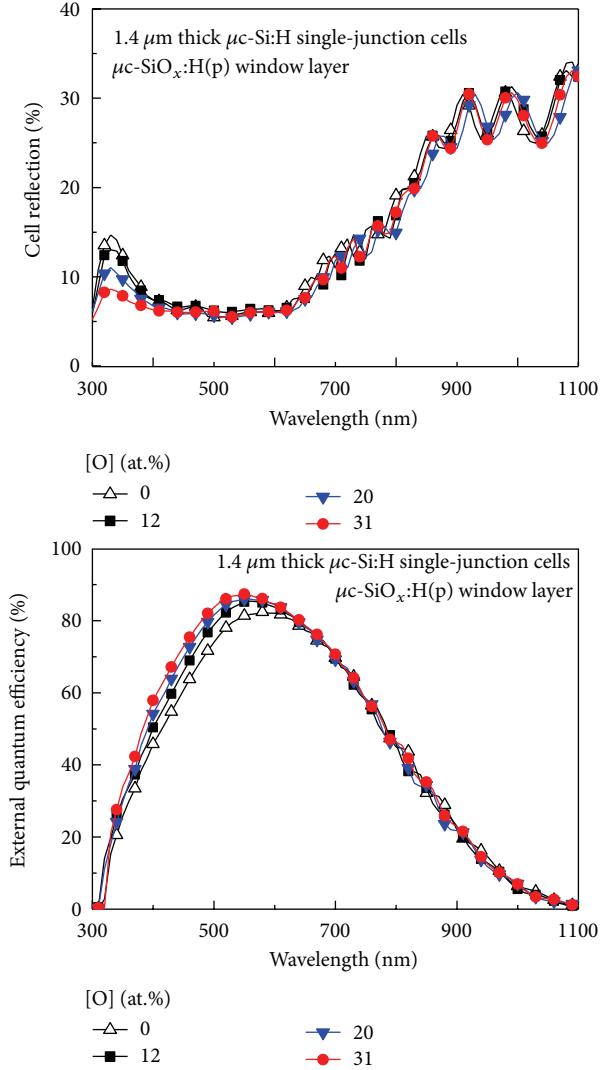


FIGURE 3: External quantum efficiency of $\mu\text{c-Si:H}$ single-junction solar cells employed $\mu\text{c-SiO}_x\text{:H(p)}$ with varied oxygen content [O] as window layer and cell reflectance as a function of oxygen content.

increased from 19.73 to 21.62 mA/cm^2 . Compared with the cell using $\mu\text{c-Si:H(p)}$ ([O] = 0%), the cell employing $\mu\text{c-SiO}_x\text{:H(p)}$ with [O] of 12 at.% and 20 at.% exhibited enhancement in fill factor (FF). This can be attributed to the shunt quenching effect by $\mu\text{c-SiO}_x\text{:H(p)}$ layer which suppressed the carrier recombination at the p/i interface [12, 27]. With [O] increased from 0 to 20 at.%, the open-circuit voltage (V_{OC}) was increased from 0.49 to 0.51 V, which were due to the increase in band gap of $\mu\text{c-SiO}_x\text{:H(p)}$ window layer. In addition, the utilization of wide-band gap p-layer presented a potential barrier on the conduction band, which suppressed the diffusion of electron across the p/i interface and reduced the carrier recombination in bulk region or at p/i interface, leading to an improved V_{OC} [18]. Further increase in the [O] to 31 at.% resulted in the decrease in V_{OC} and FF, which can be attributed to the increase in oxygen-induced defect states existing near the p/i interface and the decrease in σ_d of

TABLE 1: Performance of $\mu\text{c-Si:H}$ single-junction solar cells employed $\mu\text{c-SiO}_x\text{:H(p)}$ with varied oxygen content [O] as window layer.

[O] (at.%)	V_{OC} (V)	J_{SC} (mA/cm^2)	FF (%)	η (%)
0	0.49	19.73	67.4	6.67
12	0.50	20.37	70.0	7.05
20	0.51	21.37	68.5	7.33
31	0.50	21.62	64.5	6.98

$\mu\text{c-SiO}_x\text{:H(p)}$ layer. In our case, the cell efficiency of 7.33% was obtained by employing the $\mu\text{c-SiO}_x\text{:H(p)}$ window layer with [O] of 20 at.% in $\mu\text{c-Si:H}$ single-junction solar cell.

3.3. Application of Different Back Reflecting Layers in $\mu\text{c-Si:H}$ Solar Cells. The back reflector comprising the BRL and metal contact is critical to reflect unabsorbed photons back into the absorber, resulting in the improved long-wavelength absorption and cell performance. The role of BRL was to reduce the parasitic absorption loss of the back reflector. We employed three BRLs in $\mu\text{c-Si:H}$ single-junction solar cells, whose schematic structures are shown in Figure 4.

Figure 5(a) shows the EQE and cell absorbance of $\mu\text{c-Si:H}$ solar cells. Compared to the cell using $\mu\text{c-Si:H(n)}$ as BRL, the cell employing the sputtered ITO as BRL exhibited the lower cell absorbance but slightly higher EQE at wavelengths from 600 to 700 nm. This can be ascribed to the less plasmonic absorption loss by employing ITO than that employing $\mu\text{c-Si:H(n)}$ as BRL [28, 29]. The ITO layer has lower refractive index ($n \sim 2$) than $\mu\text{c-Si:H(n)}$ ($n = 3.1$ at 800 nm), which shifted the plasmonic absorption to short-wavelength region, resulting in the enhanced optical reflection of back reflector. This led to the increase in J_{SC} from 18.95 to 20.01 mA/cm^2 as shown in Table 2. Similar effect was found by using $\mu\text{c-SiO}_x\text{:H(n)}$ ($n = 2.55$ at 800 nm) as BRL. Compared with the cell employing $\mu\text{c-Si:H(n)}$ as BRL, the cell with $\mu\text{c-SiO}_x\text{:H(n)}$ exhibited significantly improved EQE from 500 to 1000 nm, which was due to the reduction in plasmonic absorption loss. J_{SC} was significantly increased from 18.95 to 20.83 mA/cm^2 . On the other hand, in comparison to the cell employing the ITO layer as BRL, the cell using $\mu\text{c-SiO}_x\text{:H(n)}$ as BRL ([O] of 27 at.%) exhibited higher absorbance and EQE. This enhancement in EQE was likely due to the improved interface quality by the in situ fabrication process, which avoided the sputtering damage and reduced the formation of native oxide at the interface [11, 30].

In order to have a clear picture on the carrier collection of $\mu\text{c-Si:H}$ solar cells by employing different BRLs, the internal quantum efficiency (IQE) of $\mu\text{c-Si:H}$ solar cells is demonstrated in Figure 5(b). The IQE denoted the ratio of the collected charge carriers to the absorbed photons by the solar cells. Compared to the case using $\mu\text{c-Si:H(n)}$ as BRL, the enhancement of IQE from 600 to 750 nm was due to the reduction in the parasitic absorption loss near the BRL/Ag interface, which led to the more photons being reflected back to the absorber.

Similar to the case using ITO layer, the cell with $\mu\text{c-SiO}_x\text{:H(n)}$ as BRL exhibited significantly enhanced IQE

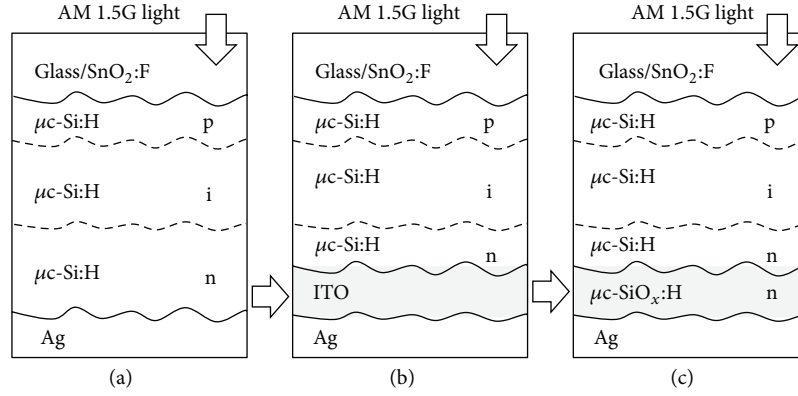


FIGURE 4: Structures of $\mu\text{c-Si:H}$ single-junction solar cells with different BRLs showing (a) the reference cell with $\mu\text{c-Si:H(n)}$ as n-layer and BRL, (b) the cell employing ITO as BRL, and (c) the cell using $\mu\text{c-SiO}_x\text{:H(n)}$ as a replacement for ITO as BRL.

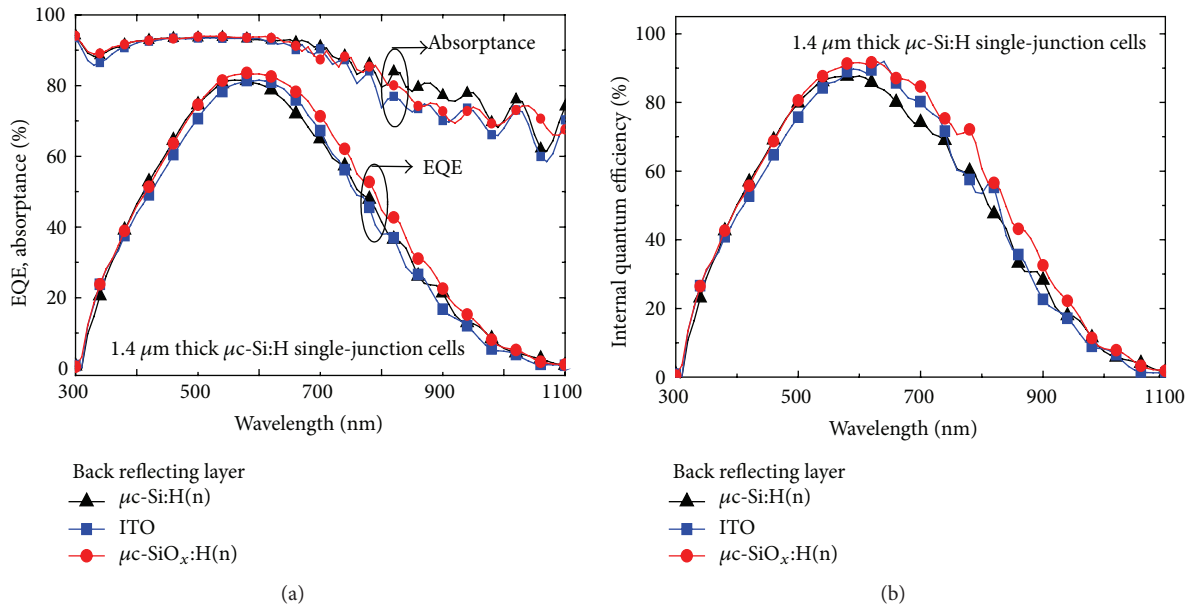


FIGURE 5: (a) External quantum efficiency and absorbance. (b) Internal quantum efficiency of $\mu\text{c-Si:H}$ single-junction solar cells with different BRLs.

TABLE 2: Performance of $\mu\text{c-Si:H}$ single-junction solar cells with different BRLs.

BRL	V_{OC} (V)	J_{SC} (mA/cm ²)	FF (%)	η (%)
$\mu\text{c-Si:H(n)}$	0.48	18.95	68.2	6.27
ITO	0.48	20.01	68.2	6.55
$\mu\text{c-SiO}_x\text{:H(n)}$	0.50	20.83	70.0	7.20

compared with the cell using $\mu\text{c-Si:H(n)}$. This was due to the reduction in parasitic absorption loss by shifting the plasmonic absorption to the less-critical spectral range. In addition, by replacing ITO with $\mu\text{c-SiO}_x\text{:H(n)}$ as BRL, the IQE was enhanced at the wavelength ranging from 450 to 1100 nm. This manifested that the carrier collection was improved owing to the removal of sputtering damage and the contamination during the air exposure. In our case, the optimized cell efficiency of 7.2% with V_{OC} of 0.5 V, J_{SC} of

20.83 mA/cm² and FF of 70.0% was obtained by employing the $\mu\text{c-SiO}_x\text{:H(n)}$ as BRL in $\mu\text{c-Si:H}$ single-junction solar cell.

3.4. Optimization of a-Si:H/ $\mu\text{c-Si:H}$ Solar Cells by Employing Different p-Layer and Back Reflecting Layer in Bottom Cell.

The schematic structures of a-Si:H/ $\mu\text{c-Si:H}$ tandem cells with different p-layers and BRLs in $\mu\text{c-Si:H}$ bottom cells are shown in Figure 6. The EQE of a-Si:H/ $\mu\text{c-Si:H}$ tandem cell employing different p-layers and BRLs in the bottom cell are illustrated in Figure 7. As can be seen, compared to the tandem cell using $\mu\text{c-Si:H(n)}$ as BRL, the cell employing the sputtered ITO as BRL exhibited higher spectral response in wavelengths ranging from 600 to 1000 nm. This was coincided with the results shown in Figure 5, which was due to the decreased plasmonic absorption loss by employing the ITO layer. Therefore, J_{SC} of bottom cell was increased from 9.78 to 10.62 mA/cm² as shown in Table 3. The employment

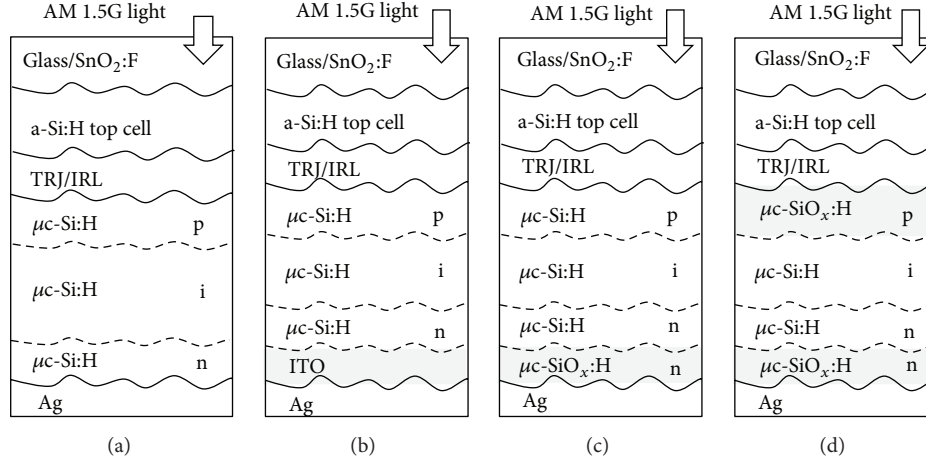


FIGURE 6: Structures of a-Si:H/ μ c-Si:H tandem solar cells with different p-layers of bottom cell and BRLs showing (a) the reference cell with μ c-Si:H(p) and μ c-Si:H(n) in bottom cell, (b) the cell employing ITO as BRL, (c) the cell using μ c-SiO_x:H(n) as a replacement for ITO as BRL, and (d) the cell using μ c-SiO_x:H(p) as a replacement for μ c-Si:H(p).

TABLE 3: Comparison of the cell performances of a-Si:H/ μ c-Si:H tandem cell with different p-layers of bottom cell and BRLs.

p-layer (bottom cell)	BRL	V_{OC} (V)	J_{SC} (mA/cm ²)	$J_{QE,top}$ (mA/cm ²)	$J_{QE,bot}$ (mA/cm ²)	$J_{QE,total}$ (mA/cm ²)	FF (%)	η (%)
μ c-Si:H(p)	μ c-Si:H(n)	1.34	9.70	11.47	9.78	21.25	69.9	9.06
μ c-Si:H(p)	ITO	1.35	10.11	11.45	10.62	22.07	71.1	9.94
μ c-Si:H(p)	μ c-SiO _x :H(n)	1.35	10.62	11.52	11.58	23.10	71.9	10.27
μ c-SiO _x :H(p)	μ c-SiO _x :H(n)	1.37	10.55	11.57	13.08	24.65	73.7	10.51

of μ c-SiO_x:H(n) ([O] of 27 at.%) as BRL exhibited similar effect as the case of ITO. Compared to μ c-Si:H(n) as BRL, the tandem cell employing μ c-SiO_x:H(n) as BRL had a significant enhancement in the spectral response of long-wavelength range, which led to the increase in J_{SC} of bottom cell from 9.78 to 11.58 mA/cm². In addition, compared to the sputtered ITO as BRL, the replacement of μ c-SiO_x:H(n) as BRL showed higher spectral response from 600 to 1000 nm. The increase of J_{SC} in the bottom cell from 10.62 to 11.58 mA/cm² was more likely because of the decreased plasmonic losses by the μ c-SiO_x:H(n) as BRL. Another factor could ascribe to the all in situ PECVD process which reduced the interface defects [31].

In addition, the cell with μ c-SiO_x:H(p) as the replacement of μ c-Si:H(p) of the bottom cell is shown for comparison. The significant enhancement in spectral response of long-wavelength range can be ascribed to two factors. First, the absorption coefficient of μ c-SiO_x:H(p) is lower than that of μ c-Si:H(p), which resulted in the reduced parasitic absorption loss by the p-layer. Second, the replacement of μ c-Si:H(p) by μ c-SiO_x:H(p) could increase the built-in field due to the higher optical band gap of μ c-SiO_x:H(p), resulting in the increased V_{OC} and the enhanced carrier collection in long-wavelength region. These two factors led to the advanced optical absorption in long-wavelength range, contributing in the significantly enhanced J_{SC} of bottom cell from 11.58 to 13.08 mA/cm².

The performance of tandem cell with μ c-SiO_x:H(p) replacing μ c-Si:H(p) of the bottom cell is shown in Table 3. The increased FF from 71.9 to 73.7% can be ascribed to the

shunt quenching effect by the μ c-SiO_x:H(p) layer, which led to reduced leakage current of the cell [32]. In addition, the carrier recombination in tunneling recombination junction (TRJ) may be enhanced by replacing μ c-Si:H(p) with μ c-SiO_x:H(p), resulting in the increase in V_{OC} and FF [33]. Combining the effects discussed above, the a-Si:H/ μ c-Si:H tandem solar cell employing the μ c-SiO_x:H(p) as p-layer of bottom cell and μ c-SiO_x:H(n) as BRL with efficiency of 10.51%, V_{OC} of 1.37 V, J_{SC} of 10.55 mA/cm², and FF of 73.67% was obtained.

4. Conclusion

The p-type and the n-type μ c-SiO_x:H with varied [O] have been prepared and employed as window layer and back reflecting layer, respectively, in μ c-Si:H single-junction solar cells. Regarding the μ c-SiO_x:H films, the decreased refractive index accompanied with the wider E_{04} with increasing [O] can be ascribed to the increased Si-O bond in amorphous silicon oxide phase, while structural defects could disrupt crystalline structure, resulting in the degraded X_C and σ_d .

By utilizing μ c-SiO_x:H(p) with increasing [O] in μ c-Si:H single-junction solar cell, the short-wavelength spectral response enhanced. However, too much oxygen incorporation induced defects in μ c-SiO_x:H(p) which could decrease the V_{OC} and FF. Meanwhile, ITO in μ c-Si:H single-junction cell was replaced by the highly conductive μ c-SiO_x:H(n) with [O] of 27 at.%. The employment of μ c-SiO_x:H(n) enhanced spectral response and increased FF, which were due to the

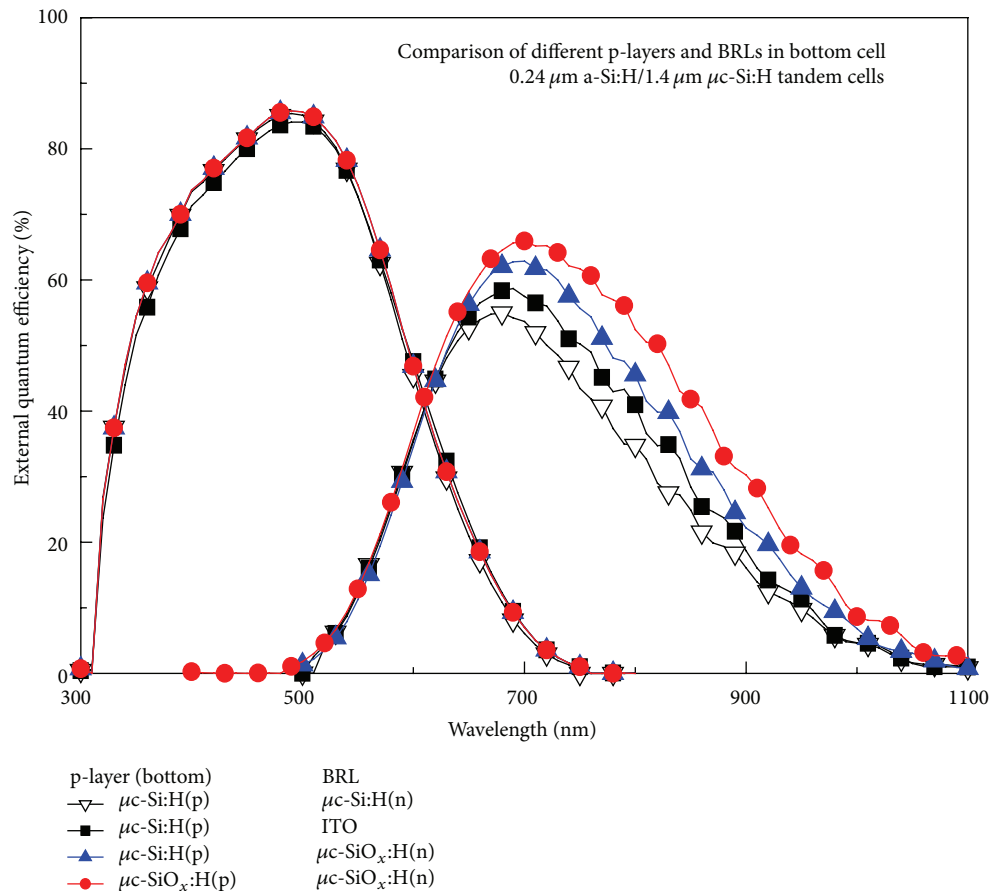


FIGURE 7: External quantum efficiency of a-Si:H/ $\mu\text{c-Si:H}$ tandem solar cells employing different p-layers of bottom cell and BRLs.

elimination of ex-situ ITO sputtering step and the unavoidable sputtering damage at the $\mu\text{c-Si:H(n)}$ /ITO interface. Finally, further replacing $\mu\text{c-Si:H(p)}$ by $\mu\text{c-SiO}_x\text{:H(p)}$ as p-layer of bottom cell enhanced FF and V_{OC} , which might result from the increased carrier recombination between TRJ layers. In addition, the higher J_{SC} of bottom cell can be ascribed to the less parasitic absorption loss of $\mu\text{c-SiO}_x\text{:H(p)}$ than that of $\mu\text{c-Si:H(p)}$. Compared to the reference cell, the optimized cell efficiency by employing $\mu\text{c-SiO}_x\text{:H(p)}$ and $\mu\text{c-SiO}_x\text{:H(n)}$ achieved cell efficiency from 9.06 to 10.51%, with V_{OC} of 1.37 V, J_{SC} of 10.55 mA/cm^2 , and FF of 73.67%, which had a relative efficiency enhancement of 16%.

Competing Interests

The authors do not have any competing interests concerning the content of the paper.

Acknowledgments

This work was sponsored by Ministry of Science and Technology in Taiwan under Grant no. 103-3113-P-008-001. Besides, the authors gratefully thank Hung-Jung Hsu for continuous support and encouragement.

References

- [1] K. L. Chopra, P. D. Paulson, and V. Dutta, "Thin-film solar cells: an overview," *Progress in Photovoltaics: Research and Applications*, vol. 12, no. 2-3, pp. 69–92, 2004.
- [2] A. V. Shah, H. Schade, M. Vanecek et al., "Thin-film silicon solar cell technology," *Progress in Photovoltaics: Research and Applications*, vol. 12, no. 2-3, pp. 113–142, 2004.
- [3] A. V. Shah, J. Meier, E. Vallat-Sauvain et al., "Material and solar cell research in microcrystalline silicon," *Solar Energy Materials & Solar Cells*, vol. 78, no. 1–4, pp. 469–491, 2003.
- [4] H. Keppner, J. Meier, P. Torres, D. Fischer, and A. Shah, "Microcrystalline silicon and micromorph tandem solar cells," *Applied Physics A: Materials Science and Processing*, vol. 69, no. 2, pp. 169–177, 1999.
- [5] K. Yamamoto, A. Nakajima, M. Yoshimi et al., "A thin-film silicon solar cell and module," *Progress in Photovoltaics: Research and Application*, vol. 13, no. 6, pp. 489–494, 2005.
- [6] K. Ding, T. Kirchartz, B. E. Pieters et al., "Characterization and simulation of a-Si:H/ $\mu\text{c-Si:H}$ tandem solar cells," *Solar Energy Materials and Solar Cells*, vol. 95, no. 12, pp. 3318–3327, 2011.
- [7] R. E. Hollingsworth and P. K. Bhat, "Doped microcrystalline silicon growth by high frequency plasmas," *Applied Physics Letters*, vol. 64, no. 5, pp. 616–618, 1994.
- [8] S. C. Saha and S. Ray, "Development of highly conductive n-type $\mu\text{c-Si:H}$ films at low power for device applications," *Journal of Applied Physics*, vol. 78, no. 9, pp. 5713–5720, 1995.

- [9] J. K. Rath and R. E. I. Schropp, "Incorporation of p-type microcrystalline silicon films in amorphous silicon based solar cells in a superstrate structure," *Solar Energy Materials and Solar Cells*, vol. 53, no. 1-2, pp. 189–203, 1998.
- [10] S. C. Saha, A. K. Barua, and S. Ray, "The role of hydrogen dilution and radio frequency power in the formation of microcrystallinity of n-type Si:H thin film," *Journal of Applied Physics*, vol. 74, no. 9, pp. 5561–5568, 1993.
- [11] G. Lucovsky, J. Yang, S. S. Chao, J. E. Tyler, and W. Czubytyj, "Oxygen-bonding environments in glow-discharge-deposited amorphous silicon-hydrogen alloy films," *Physical Review B*, vol. 28, no. 6, pp. 3225–3233, 1983.
- [12] P. Cuony, M. Marending, D. T. L. Alexander et al., "Mixed-phase p-type silicon oxide containing silicon nanocrystals and its role in thin-film silicon solar cells," *Applied Physics Letters*, vol. 97, no. 21, Article ID 213502, 2010.
- [13] L. V. Mercaldo, P. Delli Veneri, I. Usatii, E. M. Esposito, and G. Nicotra, "Properties of mixed phase n-doped silicon oxide layers and application in micromorph solar cells," *Solar Energy Materials and Solar Cells*, vol. 119, pp. 67–72, 2013.
- [14] A. Sarker, C. Banerjee, and A. K. Barua, "Preparation and characterization of n-type microcrystalline hydrogenated silicon oxide films," *Journal of Physics D: Applied Physics*, vol. 35, no. 11, pp. 1205–1209, 2002.
- [15] V. Smirnov, W. Böttler, A. Lambertz, H. Wang, R. Carius, and F. Finger, "Microcrystalline silicon n-i-p solar cells prepared with microcrystalline silicon oxide ($\mu\text{c-SiO}_x\text{:H}$) n-layer," *Physica Status Solidi (C) Current Topics in Solid State Physics*, vol. 7, no. 3-4, pp. 1053–1056, 2010.
- [16] T. Krajangsang, S. Kasashima, A. Hongsingthong, P. Sichanugrist, and M. Konagai, "Effect of p- $\mu\text{c-Si}_{1-x}\text{O}_x\text{:H}$ layer on performance of hetero-junction microcrystalline silicon solar cells under light concentration," *Current Applied Physics*, vol. 12, pp. 515–520, 2012.
- [17] A. Lambertz, T. Grundler, and F. Finger, "Hydrogenated amorphous silicon oxide containing a microcrystalline silicon phase and usage as an intermediate reflector in thin-film silicon solar cells," *Journal of Applied Physics*, vol. 109, no. 11, Article ID 113109, 2011.
- [18] C. Zhang, M. Meier, A. Lambertz et al., "Optical and electrical effects of p-type c-SiO_x:H in thin-film silicon solar cells on various front textures," *International Journal of Photoenergy*, vol. 2014, Article ID 176965, 10 pages, 2014.
- [19] V. Smirnov, A. Lambertz, S. Tillmanns, and F. Finger, "p- and n-type microcrystalline silicon oxide ($\mu\text{c-SiO}_x\text{:H}$) for application in thin film silicon tandem solar cells," *Canadian Journal of Physics*, vol. 92, pp. 932–935, 2014.
- [20] S. W. Liang, *Development and optimization of microcrystalline silicon thin-film solar cells with microcrystalline silicon oxide as N-type and back reflecting layer and its application in multi-junction devices [Ph.D. thesis]*, Department of Photonics and Institute of Electro-Optical Engineering, National Chiao Tung University, 2014.
- [21] D. Das, M. Jana, and A. K. Barua, "Characterization of undoped $\mu\text{c-SiO:H}$ films prepared from ($\text{SiH}_4+\text{CO}_2+\text{H}_2$)-plasma in RF glow discharge," *Solar Energy Materials & Solar Cells*, vol. 63, no. 3, pp. 285–297, 2000.
- [22] F. Demichelis, C. F. Pirri, and E. Tresso, "Influence of doping on the structural and optoelectronic properties of amorphous and microcrystalline silicon carbide," *Journal of Applied Physics*, vol. 72, no. 4, pp. 1327–1333, 1992.
- [23] D. Adler, "Density of states in the gap of tetrahedrally bonded amorphous semiconductors," *Physical Review Letters*, vol. 41, no. 25, pp. 1755–1758, 1978.
- [24] T. Hamasaki, M. Ueda, Y. Osaka, and M. Hirose, "Preferential segregation of dopants in $\mu\text{c-Si:H}$," *Journal of Non-Crystalline Solids*, vol. 59-60, no. 2, pp. 811–814, 1983.
- [25] L. Xiao, O. Astakhov, R. Carius, A. Lambertz, T. Grundler, and F. Finger, "Defects and structure of $\mu\text{c-SiO}_x\text{:H}$ deposited by PECVD," *Physica Status Solidi C*, vol. 7, no. 3-4, pp. 941–944, 2010.
- [26] K. Schwanitz, S. Klein, T. Stolley, M. Rohde, D. Severin, and R. Trassl, "Anti-reflective microcrystalline silicon oxide p-layer for thin-film silicon solar cells on ZnO," *Solar Energy Materials and Solar Cells*, vol. 105, pp. 187–191, 2012.
- [27] R. Biron, C. Pahud, F.-J. Haug, J. Escarré, K. Söderström, and C. Ballif, "Window layer with p doped silicon oxide for high V_{OC} thin-film silicon n-i-p solar cells," *Journal of Applied Physics*, vol. 110, no. 12, Article ID 124511, 2011.
- [28] U. Palanchoke, V. Jovanov, H. Kurz, P. Obermeyer, H. Stiebig, and D. Knipp, "Plasmonic effects in amorphous silicon thin film solar cells with metal back contacts," *Optics Express*, vol. 20, no. 6, pp. 6340–6347, 2012.
- [29] F.-J. Haug, T. Söderström, O. Cubero, V. Terrazzoni-Daudrix, and C. Ballif, "Plasmonic absorption in textured silver back reflectors of thin film solar cells," *Journal of Applied Physics*, vol. 104, no. 6, Article ID 064509, 2008.
- [30] T. Söderström, F.-J. Haug, X. Niquille, and C. Ballif, "TCOs for Nip thin film silicon solar cells," *Progress in Photovoltaics: Research and Applications*, vol. 17, no. 3, pp. 165–176, 2009.
- [31] B. Demareux, S. De Wolf, A. Descoedres, Z. C. Holman, and C. Ballif, "Damage at hydrogenated amorphous/crystalline silicon interfaces by indium tin oxide overlayer sputtering," *Applied Physics Letters*, vol. 101, no. 17, Article ID 171604, 2012.
- [32] M. Despeisse, C. Battaglia, M. Boccard et al., "Optimization of thin film silicon solar cells on highly textured substrates," *Physica Status Solidi A*, vol. 208, no. 8, pp. 1863–1868, 2011.
- [33] B. Bills, X. Liao, D. W. Galipeau, and Q. H. Fan, "Effect of tunnel recombination junction on crossover between the dark and illuminated current-voltage curves of tandem solar cells," *IEEE Transactions on Electron Devices*, vol. 59, no. 9, pp. 2327–2330, 2012.

Research Article

Preparation of a Textile-Based Dye-Sensitized Solar Cell

**Klaus Opwis,¹ Jochen Stefan Gutmann,¹ Ana Rosa Lagunas Alonso,²
Maria Jesus Rodriguez Henche,² Mikel Ezquer Mayo,² Fanny Breuil,³
Enrico Leonardi,⁴ and Luca Sorbello⁴**

¹Deutsches Textilforschungszentrum Nord-West gGmbH, 47798 Krefeld, Germany

²Centro Nacional de Energías Renovables, 31621 Sarriguren, Spain

³Eurecat Centro Tecnológico de Cataluña, 08301 Mataró, Spain

⁴Dyesol Italia, 00187 Rome, Italy

Correspondence should be addressed to Klaus Opwis; opwis@dtw.de

Received 29 March 2016; Revised 8 July 2016; Accepted 12 July 2016

Academic Editor: Vishal Mehta

Copyright © 2016 Klaus Opwis et al. This is an open access article distributed under the Creative Commons Attribution License, which permits unrestricted use, distribution, and reproduction in any medium, provided the original work is properly cited.

Solar energy conversion is an object of continuous research, focusing on improving the energy efficiency as well as the structure of photovoltaic cells. With efficiencies continuously increasing, state-of-the-art PV cells offer a good solution to harvest solar energy. However, they are still lacking the flexibility and conformability to be integrated into common objects or clothing. Moreover, many sun-exposed surface areas are textile-based such as garments, tents, truck coverings, boat sails, and home or outdoor textiles. Here, we present a new textile-based dye-sensitized solar cell (DSC) which takes advantage from the properties inherent to fabrics: flexibility, low weight, and mechanical robustness. Due to the necessary thermostability during manufacturing, our DSC design is based on heat-resistant glass-fiber fabrics. After applying all needed layers, the overall structure was covered by a transparent and simultaneously conductive protective film. The light and still flexible large-area devices (up to 6 cm² per individual unit) are working with efficiencies up to 1.8% at 1/5 of the sun. Stability tests assure no loss of photovoltaic activity over a period of at least seven weeks. Therefore, our technology has paved the way for a new generation of flexible photovoltaic devices, which can be used for the generation of power in the mentioned applications as well as in modern textile architecture.

1. Introduction

The conversion of sunlight into electric energy is the most environmentally friendly and nonhazardous alternative to fossil and fissionable resources. Along with the aim to increase the efficiency, former and present R&D focuses on the optimization of photovoltaic (PV) structures and the development of new photoactive materials.

Currently, most photovoltaic devices are still fabricated for large-scale electric power generation either in centralized solar parks or as building integrated photovoltaics (BIPV). For these applications, rigid, weather-proof, and long-term stable devices are desired. The common material of choice is monocrystalline or multicrystalline silicon, which have high average energy-conversion efficiencies in the range of 18 to 26 percent. Besides silicon, other semiconducting alternative materials have been developed and tested within the previous

decades, which differ strongly in terms of production costs on the one hand and the efficiency on the other hand. Well-described types are III-V (GaAs, InP, and GaInP), chalcogenide (CIGS, CdTe, and CZTS), and multijunction cells with up to five different p-n-junctions. Furthermore, in recent years organic, dye-sensitized, and perovskite solar cells have proven their large potential within the present and future photovoltaic market [1–3]. In particular, the dye-sensitized solar cell (DSC), which was introduced by O'Regan and Grätzel in the early 1990s, seems to be the most promising candidate for an enduring launch into several commercial products. Compared to other types of solar cells, DSC are much less sensitive to the angle of incidence of radiation, shadowing, and ambient temperature changes. They perform over the most extensive range of light conditions enabling the energy production even in the early morning, in the late

afternoon, or on cloudy days. They combine high energy-conversion efficiencies and sufficient robustness towards environmental impact and, therefore, sufficient life-time. The base materials are comparatively inexpensive. In addition, the layer thickness of the used direct semiconductors can be reduced on micron or even nanoscale. This allows the use of cost-effective thin-layer and/or printing technologies and the integration of lightweight and flexible DSC structures into countless commercial products of our day-to-day life [3–8].

Besides plastics and film applications [3, 9–11], which have already arrived to a commercial level, photovoltaic textiles have attracted increasing attention in recent years since they are often exposed directly to sunlight and represent ideal substrates for the conversion of solar energy into electricity. We refer to outdoor textiles such as blinds, tents, tarpaulins, sails, and last but not least the important increasing market of textile architecture, which has an outstanding potential to form the basis for flexible, lightweight, and robust PV structures.

As a result, a large effort has been put into research activities focusing on innovative concepts for textile-based DSC. The major challenge is to combine properties and demands of the photovoltaic concept (and processing) with inherent properties of fibrous substrates (and typical textile processing).

In literature, several successful DSC designs on fibrous materials such as paper, wires, fibers, strings, or textiles are listed [12–23]. However, in most cases these approaches are aimed at the production of single fibers or wires with photovoltaic activity, concealing the need of additional sensitive processing steps afterwards, for example, weaving, which could impair the cell performance dramatically. Furthermore, the length of those one-dimensional cells is limited to a certain extent. This impedes the (textile) processing additionally. On contrary to the most common single-fiber approaches, our investigations are focused on already woven textile structures taking advantage from the properties inherent to fabrics: flexibility, low weight, and mechanical robustness. We report on the preparation of a two-dimensional textile-based dye-sensitized solar cell and the used deposition techniques of all further needed conductive, photoactive, and protective layers to achieve flexible, light, mechanically strong, and comparatively large-area devices.

2. Experimental

2.1. Production of Textile-Based DSC. A commercial high flexible glass-fiber fabric (Interglas, Germany) with the following characteristics was used as basic substrate for the deposition of the DSC structure: mass per unit area 107 g/m^2 , thickness 0.09 mm , tensile strength (warp) 250 N/cm , tensile strength (weft) 235 N/cm , thermostability (short-time) 600°C , and thermostability (permanent) 500°C . Afterwards the glass-fiber fabric was covered with a thin polyamide film by roll-to-roll procedure followed by electron beam deposition or sputtering of a titanium layer. Titanium dioxide DSL-18NR-AO (Dyesol) was deposited by screen-printing. The cured material (500°C for 5 min) was sensitized by various

ruthenium-based dyestuffs. As a transparent counter electrode, a commercial PEN + ITO film was selected (CPFilms). The film has a thickness of $125 \mu\text{m}$ with a transparency of 75% at 550 nm . The sheet resistance amounts to $15 \Omega/\text{sq}$. On the ITO side of the film, the catalyst layer was deposited by the chemical reduction of H_2PtCl_6 at room temperature resulting in homogeneous Pt clusters on the substrate surface. After the adding of the electrolyte (EL-HSE, Dyesol), the textile part (glass-fiber fabric + PA layer + Ti + dye-sensitized TiO_2) was covered with the counter electrode part (PEN + ITO + Pt) yielding the flexible textile-based DSC. The overall structure was sealed by the use of special epoxy and thermoplastic foils (DuPont, Dyesol) to achieve the final textile-based DSC.

2.2. Analytics/Characterization. After the Ti deposition, the samples were characterized by means of optical microscopy and mechanical profilometry. Surface resistances of the electrodes were measured via 4-point probe.

The electrical characterization of the samples was performed at Standard Test Conditions (STC) in accordance with the standard IEC:60904-1-Ed.2:2006, under irradiation with a steady-state class A solar simulator according to IEC:60904-9-Ed.2:2007. The *IV*-curves at STC (1000 W/m^2 , 25°C , AM 1.5G spectrum) and at various values of irradiance were measured. During the measurement, the samples were kept at a constant temperature using a vacuum chuck.

The spectral mismatch, caused by the deviation of the simulator spectrum from the standard solar spectrum AM1.5G (IEC:60904-3-Ed.2:2008) in combination with the different spectral responses of reference cell and device under test, was calculated according to the standard IEC:60904-7-Ed.3:2008 and corrected consequently.

For the spectral mismatch correction, the spectral distribution of the solar simulator was measured with a calibrated spectroradiometer, and the spectral response of the solar cell was measured with a filter monochromator according to IEC:60904-8-Ed.2:1998.

In order to study the influence of the temperature on the electrical behavior of the cells, CENER carried out *IV*-curve measurements at different temperatures, maintaining the irradiance value constant at 830 W/m^2 .

Outdoor *IV*-curve measurements were carried out on a sunny day, placing the PV cells on a solar tracker perfectly sun-oriented. The global irradiance was measured using a calibrated pyranometer, and the cell temperature was monitored with a calibrated thermocouple.

The spectral response measurements were performed using a filter monochromator based system according to the procedure established in the IEC:60904-8:2008 standard. The frequency of the chopper was around 4 Hz, and the bias light used was a white light with an intensity value around 100 W/m^2 . For complementary information, the measurement of the spectral reflectance of the cells was carried out using a calibrated spectroradiometer and an integrating sphere.

In the first part of the stability study, textile-based DSC were irradiated with a constant intensity of 830 W/m^2 , and the temperature of the cell was maintained almost

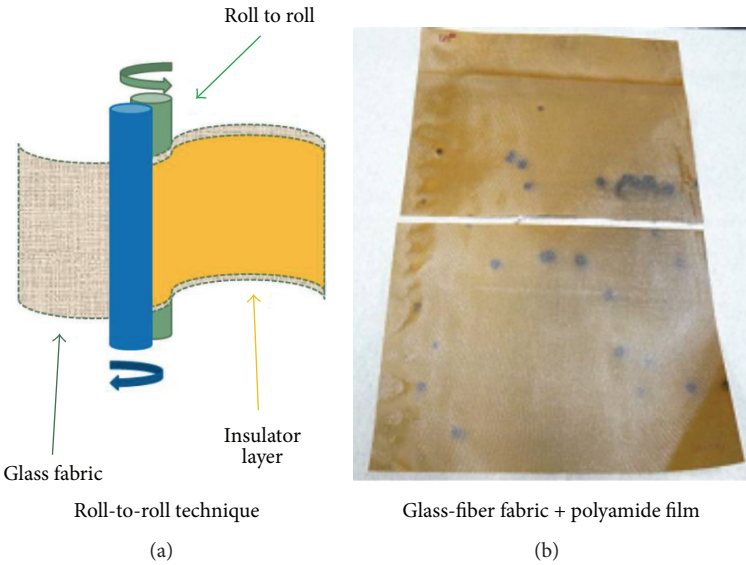


FIGURE 1: Roll-to-roll technique used (a) to cover the glass-fiber fabric with a polyamide film (b).

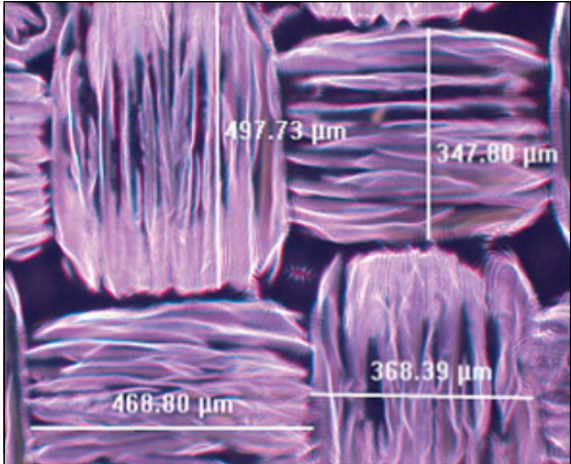
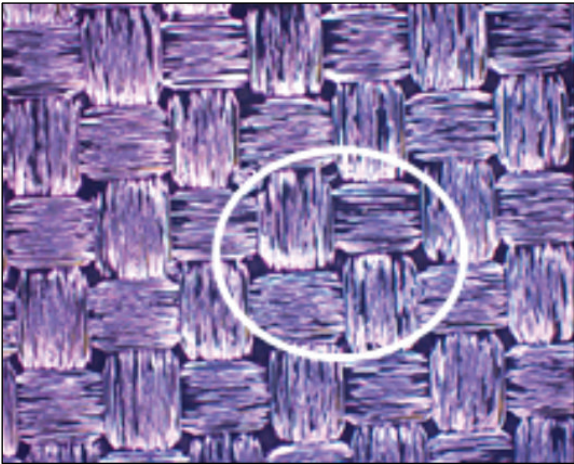
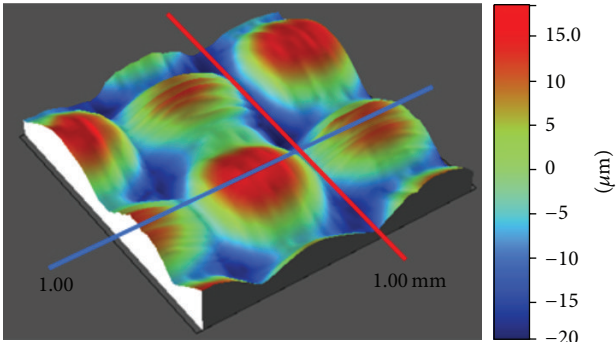


FIGURE 2: Optical characterization of Ti layers deposited on the polyamide covered glass-fiber fabric by eBeam.

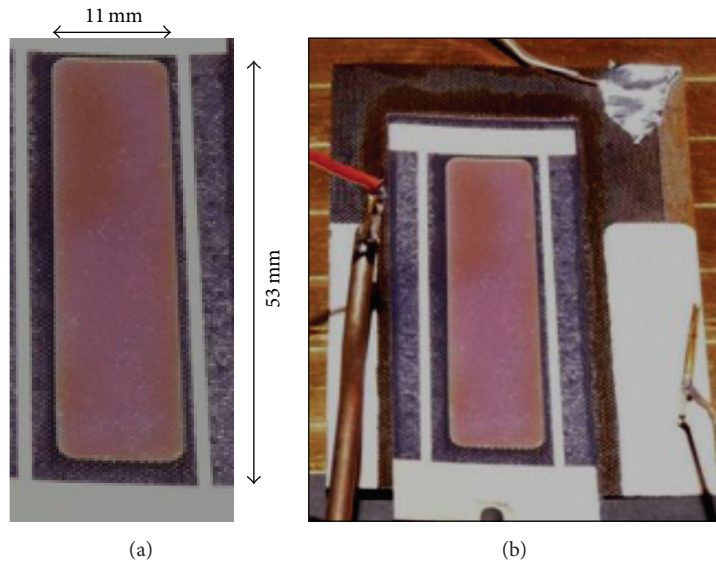
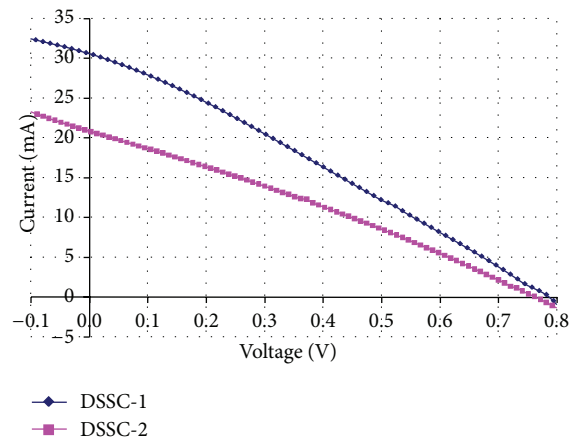


FIGURE 3: Final textile-based DSC (a) and 4-point configuration used in the IV -curve measurement (b).



Solar cell	V_{oc} (V)	I_{sc} (mA)	P_{max} (mW)	V_{max} (V)	I_{max} (mA)	FF (%)	Area (cm^2)	Ef (%)
DSC-1	0.79	30.6	6.6	0.37	17.6	27.4	6.0	1.10
DSC-2	0.75	20.8	4.5	0.35	13.0	28.7	6.0	0.75

FIGURE 4: IV -curves of two samples of textile-based DSC under STC.

constantly between $30^{\circ}C$ and $31^{\circ}C$. In order to study the stability/durability of the electrical behavior of the cells over time, IV -curves (irradiance: $830 W/m^2$; temperature: $25^{\circ}C$) of the DSC cells were measured in 3 consecutive days and 45 days after the first measurement. The PV cells were stored in dark conditions between measurements. In addition, the open circuit voltage, the current density, and the fill factor of the DSC samples were measured over a period of 7 weeks.

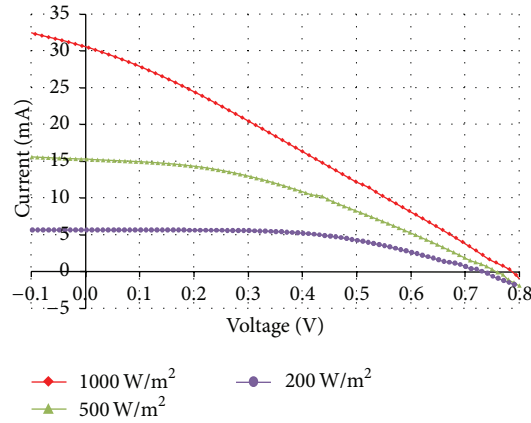
3. Results and Discussion

3.1. Structure of Textile-Based DSC. In accordance to typical DSC, our textile-based DSC structure is a composite of several materials. The layer-by-layer structure (schematically

shown in Table 1) consists of the textile substrate (1), which serves as a flexible, lightweight but mechanically strong support for all the following layers. Each layer shows material-specific characteristics and must fulfill DSC requirements in terms of thermostability, roughness, adhesion, conductivity, photovoltaic activity, transparency, barrier properties, and flexibility. In addition, the overall structure must be liquid-proof to avoid leakage of the electrolyte.

To achieve a flat, thermostable, and liquid-proof substrate, the glass-fiber fabric was covered with a thin polyamide film (2) by a simple roll-to-roll procedure (Figure 1).

On this improved material, a titanium layer (3) was deposited to turn the fiber glass into a conductive substrate, which can act as the bottom electrode. The Ti films were



Irradiance (W/m ²)	V _{oc} (V)	I _{sc} (mA)	P _{max} (mW)	V _{max} (V)	I _{max} (mA)	FF (%)	Area (cm ²)	Ef (%)
1000	0.79	30.6	6.6	0.37	17.6	27.4	6.0	1.10
500	0.75	15.3	4.5	0.42	10.7	39.3	6.0	1.51
200	0.71	5.7	2.2	0.46	4.8	54.1	6.0	1.83

FIGURE 5: IV-curves at 3 different irradiance levels for DSC-1.

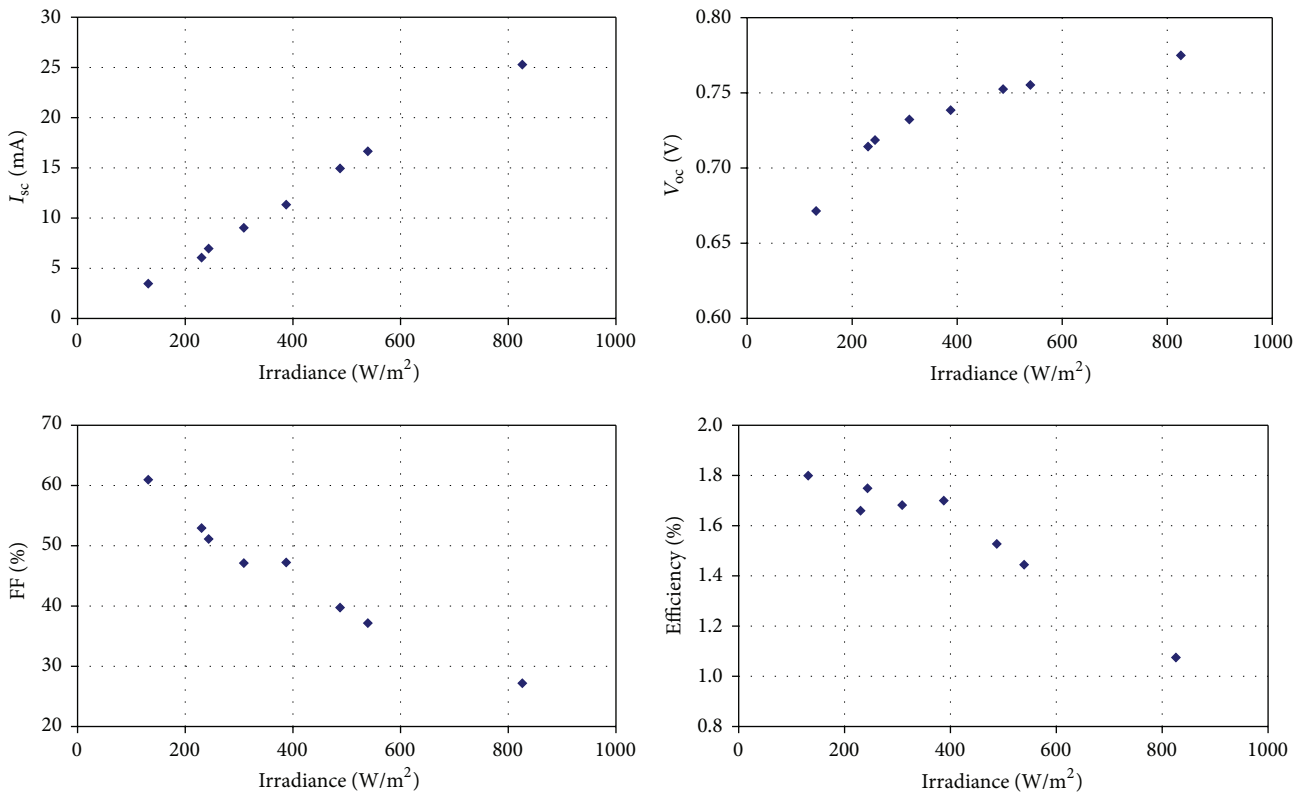


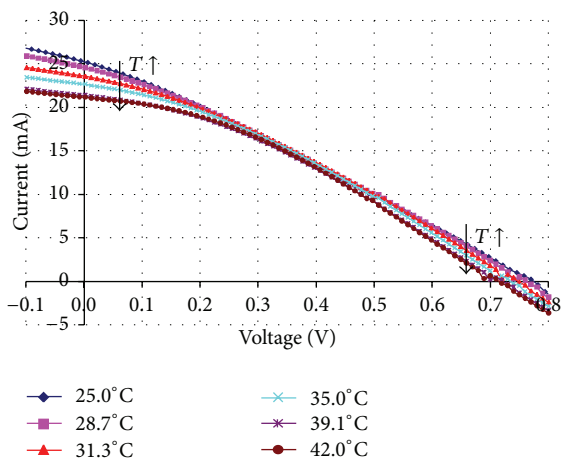
FIGURE 6: Variation of the main electrical parameters of DSC-1 with the irradiance level.

grown by two different deposition techniques: electron beam (eBeam) and sputtering. After the Ti deposition, the samples were characterized by means of optical microscopy and mechanical profilometry. Exemplarily, Figure 2 shows images of the materials after eBeam deposition of Ti. Independently

from the Ti deposition technique used, the sample surfaces maintained the substrate topography. Moreover, both technologies lead to quite homogeneous films with good adherence to the substrate. Surface resistances lower than 3 Ω/sq were found indicating sufficient conductivity.

TABLE 1: Textile-based DSC device structure and essential requirements of the layers.

Layer	Material used	Properties/requirements
8	Cover	Special epoxy and thermoplastic foils
7	Upper electrode	Thin PEN/ITO film
6	Catalyst	Pt
5	Electrolyte	Γ/I_3^-
4	Active layer	TiO_2 and dyestuff
3	Bottom electrode	Ti
2	Smoothing layer	Polyamide coating
1	Substrate	Glass-fiber fabric
		Sun light
		Transparency and impermeability towards the electrolyte
		Conductivity and transparency
		Good adhesion
		Conductivity, thermoresistance, high flexibility, and good adhesion
		Thermoresistance, impermeability towards the electrolyte, high flexibility, and good adhesion
		Thermoresistance, high flexibility, being light, and mechanical strength

FIGURE 7: DSC-1 IV -curves measured at 6 different temperatures at an irradiance value of 830 W/m^2 .

In the following step, titanium dioxide DSL-18NR-AO was deposited by screen-printing and cured for 5 minutes at 500°C to achieve a nanoporous structure of the titania, which allows a high uptake of various ruthenium-based dyestuffs. The dye-sensitized titania forms the photoactive layer (4) that absorbs the sun light yielding electric charges. This short-term but high-temperature curing step clarifies the necessity of all previous layers to be thermostable in the range of 500°C for a certain time. In the field of conventional textile materials, only glass-fiber fabrics fulfill this essential requirement.

A commercial PEN-ITO film (7) was selected as a transparent counter electrode. The film has a thickness of $125 \mu\text{m}$ with a transparency of 75% at 550 nm. The sheet resistance of $15 \Omega/\text{sq}$ is sufficient.

On the ITO side of the film, the catalyst layer (6) was deposited by the chemical reduction of H_2PtCl_6 at room temperature resulting in homogeneous Pt clusters on the substrate surface. After adding the electrolyte (5), the textile part (glass-fiber fabric + PA layer + Ti + dye-sensitized TiO_2) was covered with the counter electrode part (PEN + ITO + Pt) yielding the flexible textile-based DSC. The overall structure was sealed by a special epoxy and thermoplastic foils (8) to

protect the structure from environmental conditions. Our textile-based DSC device with the size of nearly 6 cm^2 is shown in Figure 3(a).

3.2. Photovoltaic Performance of Textile-Based DSC

3.2.1. IV -Curve Measurement under Standard and Nonstandard Test Conditions. In order to characterize the textile-based DSC electrically in terms of its photovoltaic performance, we started with IV -curve measurement under Standard Test Conditions (STC) using the configuration shown in Figure 3(b) providing the results summarized in Figure 4. The DSC devices show a significant photovoltaic activity with an average efficiency of nearly 1.0%.

Solar cells normally present a different electrical behavior depending on the irradiance level, and the photovoltaic efficiency of the cells can change significantly depending on the irradiance value. As a consequence of this and in addition to the STC measurements, we measured the IV -curve of the DSC-1 cell at different irradiance values, maintaining the AM1.5G spectrum and the 25°C temperature. As an example, in Figure 5, the IV -curves obtained for 3 representative levels of irradiance (1000 W/m^2 , 500 W/m^2 , and 200 W/m^2) are shown to have joined to the electrical parameters extracted from them. The represented IV -curves were obtained by applying the correction value due to the spectral mismatch factor.

As can be seen in Figure 5, the electrical behavior of the cell presents a clear dependency with the irradiance level. The efficiency of the cell improves significantly when the irradiance decreases, mainly due to the significant increase of the Fill Factor (FF) at low irradiance levels.

Figure 6 shows the variation of the main electrical parameters (V_{oc} , I_{sc} , FF, and efficiency) as a function of the irradiance level. All the represented values are extracted from the IV -curves measured at different irradiances, taking into account the spectral mismatch factor.

The value of the I_{sc} increases linearly with the irradiance level. This fact is completely reasonable because, normally, the I_{sc} value is directly proportional to the irradiance value. In addition, V_{oc} increases with the irradiance level due to the increasing electron injection into titania at higher illumination, which pushes the Fermi level up.

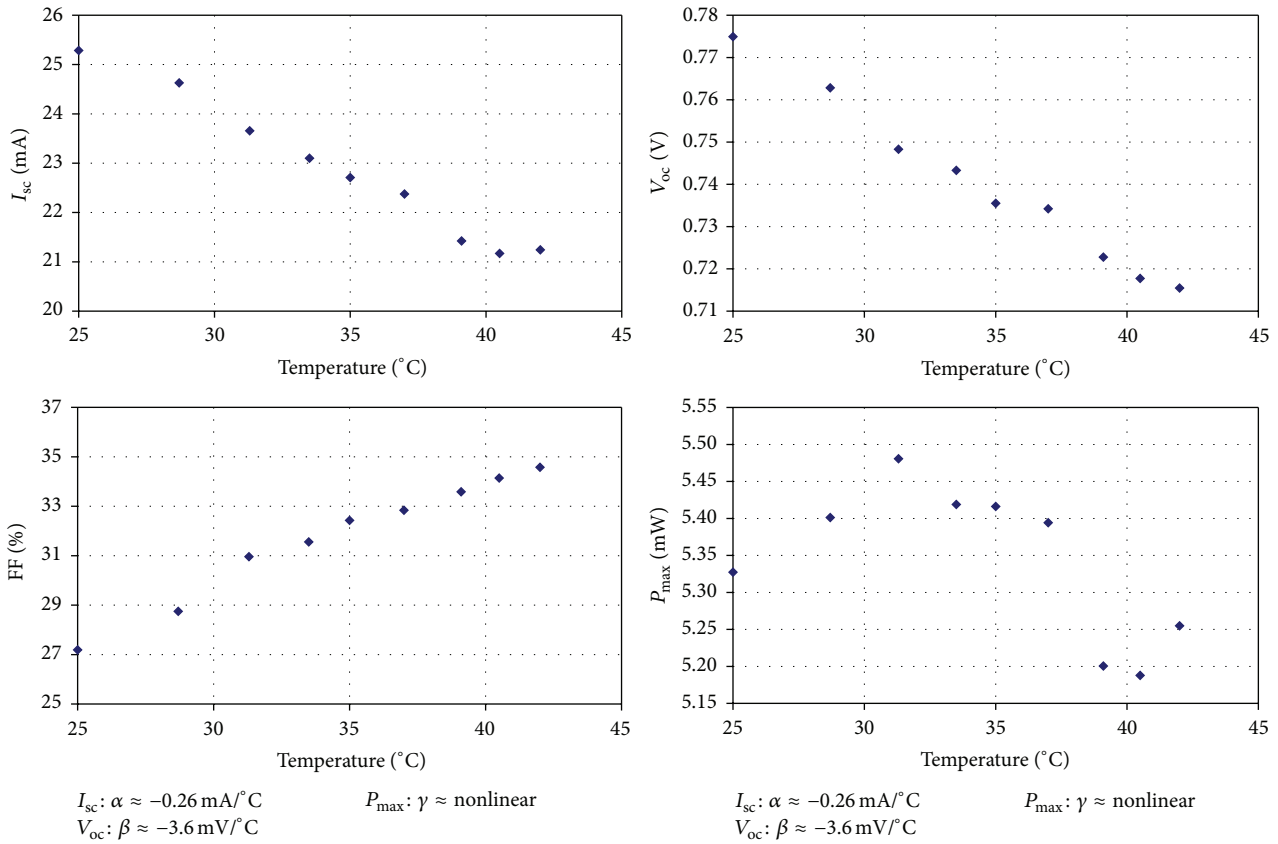
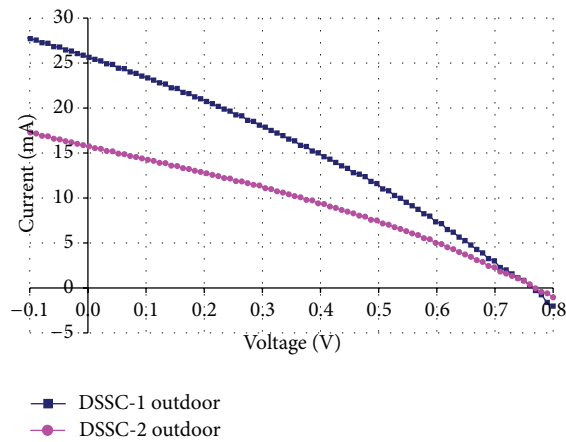


FIGURE 8: Variation of the main electrical parameters of DSC-1 with the temperature, at an irradiance value of 830 W/m².



Solar cell	V_{oc} (V)	I_{sc} (mA)	P_{max} (mW)	V_{max} (V)	I_{max} (mA)	FF (%)	Area (cm ²)	Ef (%)
DSC-1	0.76	25.7	6.09	0.38	15.9	31.0	6.0	1.01
DSC-2	0.77	15.8	3.91	0.41	9.5	32.3	6.0	0.65

FIGURE 9: Outdoor IV-curves of DSC-1 and DSC-2 (38°C, 1015 W/m²).

The most important data, extracted from these measurements, is the large improvement of the fill factor when the irradiance value decreases. Apparently, the dependency of the FF with the irradiance level follows a linear tendency. The slope of said tendency is so considerable that, as an example,

the value of the FF at 200 W/m² is practically double compared to the value at 1000 W/m².

Finally, despite the I_{sc} and V_{oc} tendency, the electrical efficiency of the cell improves notably when irradiance decreases, due to the significant improvement of the FF

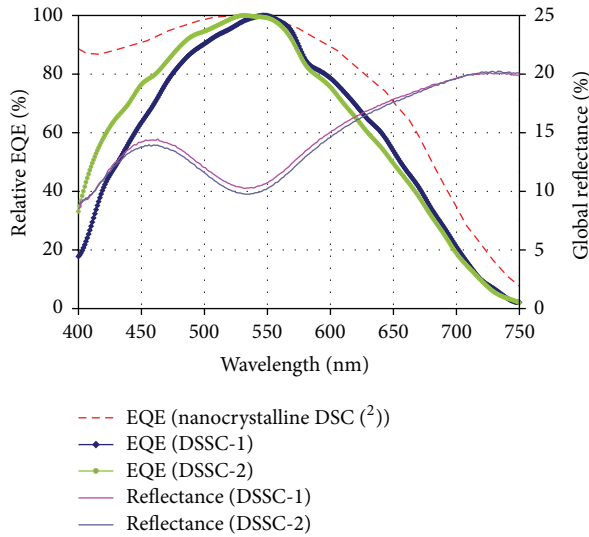


FIGURE 10: Relative External Quantum Efficiency (EQE) and global reflectance of DSC-1 and DSC-2 and EQE measurement of a reference dye-sensitized cell.

at low irradiance levels. Under 1/5 of sun conditions, the efficiency increases to a remarkable 1.8%. As demonstrated here, DSC devices are known to perform well under difficult light conditions such as low illumination or diffuse/indirect illumination, under which 1st- and 2nd-generation PV technologies tend to suffer a loss of performance.

3.2.2. Temperature Coefficients of the Main Electrical Parameters. In order to study the influence of the temperature on the electrical behavior of the textile-based DSC, we carried out some *IV*-curve measurements at different temperatures, maintaining the irradiance value constant at 830 W/m^2 . Figure 7 shows the *IV*-curves measured at 6 different temperatures at constant irradiance level (830 W/m^2) for DSC-1.

As presented in Figure 7, *IV*-curve shape changes significantly with temperature variation. Figure 8 shows the variation of I_{sc} , V_{oc} , FF, and P_{max} with the cell temperature for the case of the DSC-1. The keys of the figure show the value of the temperature coefficients for I_{sc} , V_{oc} , and P_{max} parameters.

As can be seen in Figure 8, I_{sc} and V_{oc} parameters show a negative variation with temperature, meaning that their value decreases when temperature increases. Nevertheless, the most important information extracted from this data is the improvement of the FF parameter when temperature increases. Simultaneously as I_{sc} and V_{oc} decrease, the maximum power (P_{max}) remains practically constant with the temperature variation. This represents a very important advantage for these types of cells in comparison to other PV technologies as crystalline silicon based solar cells, which suffer significant P_{max} reduction with increasing temperature.

3.2.3. Outdoor *IV*-Curve Measurement. As a complementary study of the measurements carried out in the solar simulator, *IV*-curve measurements were also performed outdoors to test the electrical behavior of the cell under real conditions. The

main advantage of the outdoor measurement is that the data does not require any spectral mismatch correction, but the disadvantage is the inability to control the irradiance level. Both irradiance and cell temperature were also measured during the test.

The *IV*-curves were measured on a sunny day by placing the PV cells on a solar tracker, perfectly adjusted to the sun. The global irradiance during the *IV*-curve measurements varied between 1010 W/m^2 and 1020 W/m^2 , and the cell temperature fluctuated between 37°C and 39°C . The measurements obtained for both DSC samples are shown in Figure 9. As shown from Figure 9, the results of the outdoor measurements are quite similar to the results obtained in the solar simulator.

3.2.4. Spectral Response and Global Reflectance Measurement. The measurement of the spectral response of dye-sensitized solar cells is not a trivial matter. The time response of these cells is quite slow compared to other technologies and, as a consequence, very low frequencies must be used in the chopping process of the light during the spectral response measurement. Besides this fact, the spectral response of the cells presents a clear dependence with the bias light intensity used to polarize the cell during the measurement.

Figure 10 shows the relative External Quantum Efficiency (EQE) measured for both cells (DSC-1 and DSC-2). The global reflectance as a function of the wavelength is also included in the graph. Finally, as a comparison, the EQE measurement of a similar dye-sensitized cell (deposited on glass) is also included.

As can be seen in Figure 10, the relative spectral response of both cells (DSC-1 and DSC-2) is quite similar. The photo-generation wavelength range of these cells goes from 400 nm to 750 nm and shows a maximum around 550 nm. Comparing these results with the EQE values extracted from the bibliography for similar dye-sensitized solar cells (deposited on glass), it can be said that the spectral response is quite similar, with a slight worse performance, especially in the short wavelength range ($<550 \text{ nm}$).

3.2.5. Stability Study. In order to complete the electrical characterization of the textile-based DSC, a study of the stability of their electrical response with the increase of the exposition time was carried out. In the first part of this stability study, DSC-2 was irradiated with a constant intensity of 830 W/m^2 , and the temperature of the cell was maintained practically constant between 30°C and 31°C . Different *IV*-curves were measured during the exposition time. Figure 11 shows the evolution of the electrical parameters (I_{sc} , V_{oc} , FF, and P_{max}) as a function of the exposure time.

All electrical parameters show a slight variation with the exposure time: I_{sc} and V_{oc} exhibit a slight improvement with exposure time. The behavior of the FF is just the opposite of its value decreasing with the exposure time. The variation of the FF provokes that the maximum power (P_{max}) of the cell also decreases when exposure time increases. Independently of the tendency, the progress of the 4 parameters is quite similar. They show a rapid change in the first minutes of exposure (≈ 15

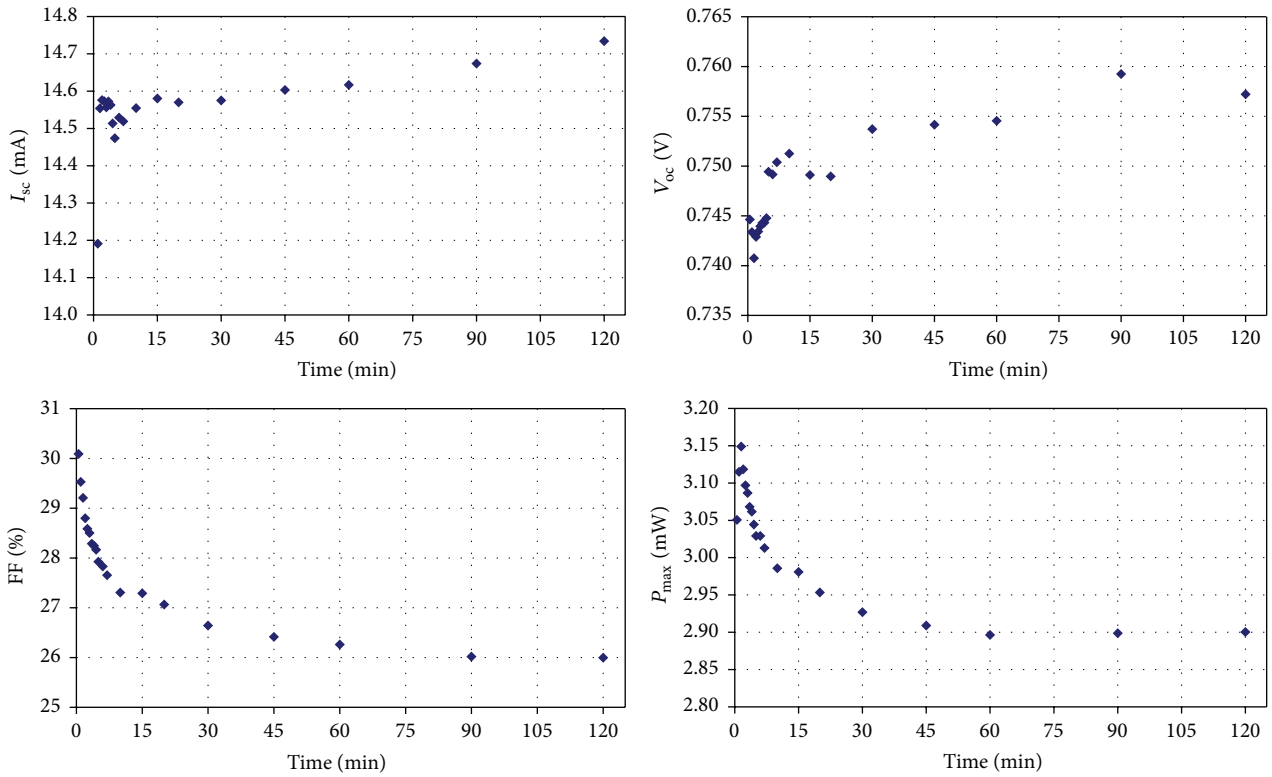
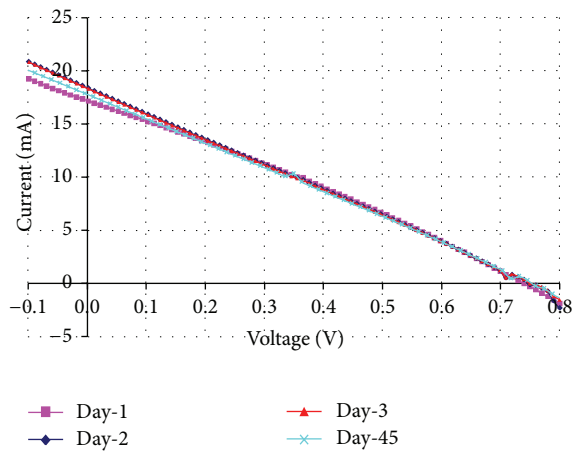


FIGURE 11: Evolution of the main electrical parameters with exposure time at 830 W/m^2 at $30\text{-}31^\circ\text{C}$.



Day	V_{oc} (V)	I_{sc} (mA)	P_{max} (mW)	V_{max} (V)	I_{max} (mA)	FF (%)	Area (cm^2)	Ef (%)
1	0.74	17.2	3.6	0.37	10.0	28.7	6.0	0.61
2	0.75	18.4	3.7	0.36	10.4	26.8	6.0	0.61
3	0.75	18.4	3.7	0.36	10.4	26.8	6.0	0.61
45	0.75	17.7	3.6	0.35	10.3	27.1	6.0	0.60

FIGURE 12: IV -curves measured in 4 different days for DSC-2. (Irradiance: 830 W/m^2 , Temperature: 25°C .)

minutes) and, after this period of time, the variation with time slows down. After 2 hours of exposure, the efficiency remains almost stable.

Finally, we studied the stability/durability of the textile-based DSC over time. Figure 12 shows the IV -curves of

DSC-2 obtained after 3 consecutive days and 45 days after the first experiment, and the electrical parameters were extracted from them. The figure demonstrates the stability of the electrical behavior of our DSC, at least in dark-stored conditions.

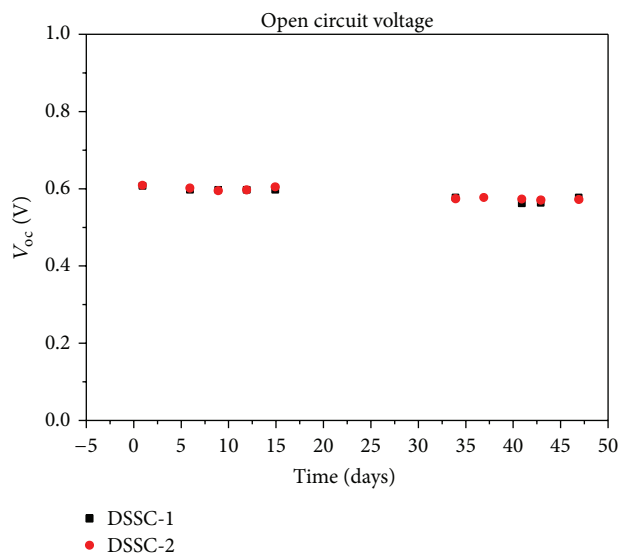


FIGURE 13: Characterization of V_{oc} over a period of 7 weeks.

In addition, the open circuit voltage, the current density, and the fill factor of the DSC samples were measured over a period of 7 weeks. All parameters show no significant loss of cell performance over the investigated period (data for V_{oc} exemplarily shown in Figure 13).

4. Conclusions

Solar energy conversion is an object of continuous research, focusing on improving the energy efficiency as well as the structure of photovoltaic cells. With efficiencies continuously increasing, state-of-the-art PV cells offer a good solution to harvest solar energy. However, it is important to understand that available, inflexible PV structures cannot be integrated in many common products, and especially textiles, although they are often directly exposed to sunlight and represent ideal substrates for the conversion of solar energy. Outdoor textiles such as blinds, tents, tarpaulins, and sails, and finally the increasing market of textile architecture, exhibit an outstanding potential to form the basis for flexible, lightweight, and robust PV structures.

Compared to conventional silicon based photovoltaic technology, DSC technology promises a lower cost in manufacture. Because of greatly reduced sensitivity to angle of incidence of radiation and shadowing, DSC produces electricity more efficiently, including low light conditions. In addition, they can be directly incorporated into buildings by replacing conventional glass panels rather than taking up roof or extra land area. Moreover, advantages include not necessitating the use of high-priced raw materials, a manufacturing process that does not produce toxic emissions, and the potential for a rapid efficiency enhancement.

We demonstrated successfully the development of a new two-dimensional textile-based dye-sensitized solar cell, which exploits the typical inherent properties of fabrics such as flexibility, low weight, and mechanical robustness. We apply our DSC design on a heat-resistant glass-fiber fabric

due to the necessity of high-temperature processes during the manufacture and report on all further needed conductive, photoactive, and protective materials and their deposition techniques to achieve flexible, light, and mechanically strong textile-based DSC. Our produced large-area devices (up to 6 cm^2 per individual unit) show efficiencies up to 1.8% at 1/5 of the sun. Stability tests assure no loss of photovoltaic activity of the noncorrosive and liquid-proof devices over a period of at least seven weeks.

Therefore, our technology has paved the way for a new generation of flexible photovoltaic devices, which can be used for the generation of power in the mentioned applications as well as in modern textile architecture. This can be considered as a “breakthrough” in textile DSC technology and will promise a quick launch into market after some aspects on the durability in the day-to-day life are assured by various stress tests and the efficiency is improved to a level of >3%. In the near future, further research should be focused on the development of new titanium inks, low temperature curing processes, and the implementation of solid-state or quasi-solid-state electrolytes, which enables the use of other typical fiber forming polymers such as polyesters and polyamides as textile substrates for textile-based DSC.

Competing Interests

The authors declare that there are no competing interests regarding the publication of this paper.

Acknowledgments

The authors would like to thank the European Commission for the financial support of the FP7, NMP project NMP2-SE-2008-214459 “DEPHOTEX-Development of Photovoltaic Textiles based on novel fibres.”

References

- [1] R. W. Miles, G. Zoppi, and I. Forbes, “Inorganic photovoltaic cells,” *Materials Today*, vol. 10, no. 11, pp. 20–27, 2007.
- [2] M. A. Green, K. Emery, Y. Hishikawa, W. Warta, and E. D. Dunlop, “Solar cell efficiency tables (version 47),” *Progress in Photovoltaics: Research and Applications*, vol. 24, no. 1, pp. 3–11, 2016.
- [3] M.-E. Ragoussi and T. Torres, “New generation solar cells: concepts, trends and perspectives,” *Chemical Communications*, vol. 51, no. 19, pp. 3957–3972, 2015.
- [4] B. O’Regan and M. Grätzel, “A low-cost, high-efficiency solar cell based on dye-sensitized colloidal TiO_2 films,” *Nature*, vol. 353, no. 6346, pp. 737–740, 1991.
- [5] H. S. Jung and J.-K. Lee, “Dye sensitized solar cells for economically viable photovoltaic systems,” *Journal of Physical Chemistry Letters*, vol. 4, no. 10, pp. 1682–1693, 2013.
- [6] S. Mathew, A. Yella, P. Gao et al., “Dye-sensitized solar cells with 13% efficiency achieved through the molecular engineering of porphyrin sensitizers,” *Nature Chemistry*, vol. 6, no. 3, pp. 242–247, 2014.
- [7] M. Grätzel, “Perspectives for dye-sensitized nanocrystalline solar cells,” *Progress in Photovoltaics*, vol. 8, no. 1, pp. 171–185, 2000.

- [8] M. Grätzel, "Recent advances in sensitized mesoscopic solar cells," *Accounts of Chemical Research*, vol. 42, no. 11, pp. 1788–1798, 2009.
- [9] H. Lindström, A. Holmberg, E. Magnusson, S.-E. Lindquist, L. Malmqvist, and A. Hagfeldt, "A new method for manufacturing nanostructured electrodes on plastic substrates," *Nano Letters*, vol. 1, no. 2, pp. 97–100, 2001.
- [10] C. Longo, J. Freitas, and M.-A. De Paoli, "Performance and stability of TiO₂/dye solar cells assembled with flexible electrodes and a polymer electrolyte," *Journal of Photochemistry and Photobiology A: Chemistry*, vol. 159, no. 1, pp. 33–39, 2003.
- [11] D. Zhang, T. Yoshida, T. Oekermann, K. Furuta, and H. Minoura, "Room-temperature synthesis of porous nanoparticulate TiO₂ films for flexible dye-sensitized solar cells," *Advanced Functional Materials*, vol. 16, no. 9, pp. 1228–1234, 2006.
- [12] S. I. Cha, Y. Kim, K. H. Hwang, Y.-J. Shin, S. H. Seo, and D. Y. Lee, "Dye-sensitized solar cells on glass paper: TCO-free highly bendable dye-sensitized solar cells inspired by the traditional Korean door structure," *Energy and Environmental Science*, vol. 5, no. 3, pp. 6071–6075, 2012.
- [13] Y. Fu, Z. Lv, S. Hou et al., "TCO-free, flexible, and bifacial dye-sensitized solar cell based on low-cost metal wires," *Advanced Energy Materials*, vol. 2, no. 1, pp. 37–41, 2012.
- [14] X. Fan, F. Wang, Z. Chu, L. Chen, C. Zhang, and D. Zou, "Conductive mesh based flexible dye-sensitized solar cells," *Applied Physics Letters*, vol. 90, no. 7, Article ID 073501, 2007.
- [15] H. Dai, Y. Zhou, L. Chen et al., "Porous ZnO nanosheet arrays constructed on weaved metal wire for flexible dye-sensitized solar cells," *Nanoscale*, vol. 5, no. 11, pp. 5102–5108, 2013.
- [16] H. Wang, Y. Liu, H. Huang et al., "Low resistance dye-sensitized solar cells based on all-titanium substrates using wires and sheets," *Applied Surface Science*, vol. 255, no. 22, pp. 9020–9025, 2009.
- [17] X. Fan, Z. Z. Chu, F. Z. Wang et al., "Wire-shaped flexible dye-sensitized solar cells," *Advanced Materials*, vol. 20, no. 3, pp. 592–595, 2008.
- [18] K. Cherenack, C. Zysset, T. Kinkeldei, N. Münzenrieder, and G. Tröster, "Woven electronic fibers with sensing and display functions for smart textiles," *Advanced Materials*, vol. 22, no. 45, pp. 5178–5182, 2010.
- [19] T. Chen, L. Qiu, Z. Cai et al., "Intertwined aligned carbon nanotube fiber based dye-sensitized solar cells," *Nano Letters*, vol. 12, no. 5, pp. 2568–2572, 2012.
- [20] Z. Lv, J. Yu, H. Wu et al., "Highly efficient and completely flexible fiber-shaped dye-sensitized solar cell based on TiO₂ nanotube array," *Nanoscale*, vol. 4, no. 4, pp. 1248–1253, 2012.
- [21] H. Sun, H. Li, X. You et al., "Quasi-solid-state, coaxial, fiber-shaped dye-sensitized solar cells," *Journal of Materials Chemistry A*, vol. 2, no. 2, pp. 345–349, 2014.
- [22] Y. Fu, Z. Lv, S. Hou et al., "Conjunction of fiber solar cells with groovy micro-reflectors as highly efficient energy harvesters," *Energy and Environmental Science*, vol. 4, no. 9, pp. 3379–3383, 2011.
- [23] M. Peng, S. Hou, H. Wu et al., "Integration of fiber dye-sensitized solar cells with luminescent solar concentrators for high power output," *Journal of Materials Chemistry A*, vol. 2, no. 4, pp. 926–932, 2014.

Research Article

The Influence of Heating Time and Temperature on the Properties of CIGSSe Solar Cells

Marco Giacomo Flammini,^{1,2} Nicola Debernardi,^{1,2} Maxime Le Ster,^{2,3} Brendan Dunne,⁴ Johan Bosman,^{2,3} and Mirjam Theelen^{1,2}

¹TNO, Thin Film Technology, High Tech Campus 21, 5656 AE Eindhoven, Netherlands

²Solliance, High Tech Campus 21, 5656 AE Eindhoven, Netherlands

³ECN, Solar Energy, Thin Film PV Technologies, High Tech Campus 21, 5656 AE Eindhoven, Netherlands

⁴NEXCIS, 190 avenue Célestin Coq, 13790 Rousset Cedex, France

Correspondence should be addressed to Marco Giacomo Flammini; marco.flammini@hotmail.it

Received 15 April 2016; Revised 16 June 2016; Accepted 12 July 2016

Academic Editor: Prakash Basnyat

Copyright © 2016 Marco Giacomo Flammini et al. This is an open access article distributed under the Creative Commons Attribution License, which permits unrestricted use, distribution, and reproduction in any medium, provided the original work is properly cited.

Nonencapsulated CIGSSe solar cells, with a silver grid, were exposed to different temperatures for various periods in order to measure the effect of the heat exposure in CIGSSe modules. The heat treatment time and temperature were varied during the experiments, which were executed at atmospheric conditions. In all the cases, after reaching a temperature of about 300°C, the *IV* measurement showed a reduction of 2-3% in terms of V_{OC} and J_{SC} . This is confirmed, respectively, by Raman and EQE measurements as well. The efficiency drop was -7%, -29%, and -48%, respectively, for 30 seconds, 300 seconds, and 600 seconds of exposure time. With temperatures larger than 225°C, the series resistance starts to increase exponentially and a secondary barrier becomes visible in the *IV* curve. This barrier prevents the extraction of electrons and consequently reducing the solar cells efficiency. Lock-in thermography demonstrated the formation of shunts on the mechanical scribes only for 300 and 600 seconds exposure times. The shunt resistance reduction is in the range of 5% for all time periods.

1. Introduction

In the recent years, CIGS technology has shown notable progress in terms of performance and reliability. The research center ZSW (Zentrum für Sonnenenergie- und Wasserstoff) has achieved the world record efficiency of $21.7 \pm 0.7\%$ on a CIGS sample of 0.5 cm^2 deposited on glass substrate [1]. This development confirms the remarkable technological potential of thin film technology, which could lead to a further cost reduction in the manufacturing process of solar cells. Many researchers are focusing their attention on damp degradation mechanisms involved in $\text{Cu}(\text{In,Ga})(\text{S,Se})_2$ in order to increase the lifetime and, consequently, to scale up the penetration into the market. On the other hand, less studies focus on heat treatment of the whole solar cells, which could give further information to what extend CIGS is able to withstand critical environment conditions. Ramanathan

et al. [2] investigated the effect of high temperatures, and they found that CIGS samples did not show any changes in external quantum efficiency (EQE) when heated up to 360°C for 30 minutes. Secondary Ion Mass Spectrometry (SIMS) results indicated that the diffusion of Cadmium into the CIGS layer occurred after heating at 400°C and concluded that the deterioration in terms of cell performance was attributable to the excess of Cd in the absorber layer and that CIGS devices are stable below 350°C. Kijima and Nakada [3] have conducted heat treatments on CIGS in air environments and have revealed significant changes already at a temperature of 250°C, in both the optical and electrical properties. They observed a reduction of the buffer layer thickness which led to an improved EQE response in the short wavelength spectrum. The increase in bandgap was explained by migration of sulfur, which was confirmed by SIMS measurements. Figure 1 collects literature data of nonencapsulated CIGS solar cells

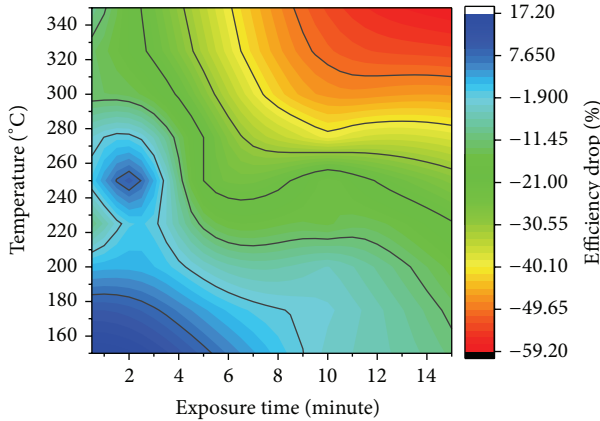


FIGURE 1: Effects on the efficiency of CIGS solar cells for different heat treatment conditions, as a function of time and temperature [2–7].

(initial efficiency: 7–15%) exposed to noncumulative heat treatment, at room condition. The solar cells were exposed to different temperature conditions in atmospheric air.

It was observed that both exposure time and temperature have a large influence on the efficiency changes in these solar cells. It can be observed that for low temperatures and/or exposure times, the CIGS solar cells performance were improved by maximum 15%. The critical temperature for CIGS solar cells were observed to be around 250°C for a heat treatment of at least 300 seconds. Moreover, exposure to elevated temperature can also be also important for tandem cells, in which CIGS is used as a bottom cell, as well as for the deposition of module packaging, like the encapsulation layer. In general, this reference gives an excellent overview regarding CIGS in inert ambient but only a few experiments have been conducted in atmosphere air environment. Therefore, the aim of this study is to investigate the effects of high temperature exposure on $\text{Cu}(\text{In,Ga})(\text{S,Se})_2$, in the range of 150–300°C and for a period of 30 seconds to 600 seconds, in order to understand the possible next processing temperature for TCO deposition, back-end interconnection, and encapsulation. Back-end processes that involve laser scribing are very likely to increase the local sample temperature at the positions where the laser beam hits the solar sample. Based on Finite Element Modeling we estimate that these temperature increments can go up to a few hundred degrees Celsius in the CIGS material in the direct vicinity of the scribe in case of insufficient ablation. In addition, this research could give valuable information regarding the ideal temperature for isolating and Ag sintering used for solar cells interconnections. This research can help to understand the feasibility of applying CIGS as a bottom cell in a tandem structure; indeed it will give an indication of the maximum temperature at which different layers can be deposited on top of CIGS. The aim of these experiments is to understand the influence of temperature for a certain amount of time on $\text{Cu}(\text{In,Ga})(\text{S,Se})_2$ solar cells.

TABLE 1: Temperatures and time at which cells are exposed.

Samples	Number of cells	Temperature (°C)	Time (seconds)
A	3	—	—
B	3	150, 200, 225, 250, 275, 300	30
C	3	150, 200, 225, 250, 275, 300	300
D	6	150, 200, 225, 250, 275, 300	600

2. Materials and Methods

The CIGS solar cells structure is composed by molybdenum (Mo) back contact/two-stage CIGS absorber layer/Cadmium sulfide (CdS) as buffer layer/intrinsic zinc oxide (i-ZnO)/aluminum doped zinc oxide (ZnO:Al) as transparent conductive layer and a silver grid is screen-printed on top of the stack. The solar cells all have a surface area of 1 cm² and are cut from one 10 cm × 10 cm slide. This slide was obtained from the large scale production facilities of NEXCIS in France. Therefore, all samples are expected to be very similar. Silver ink has been applied on top of the Mo back contact in order to avoid Mo oxidation during heat treatment. Table 1 lists the samples used in the experiment and the exposure conditions applied. Sample A was used as a reference sample; meanwhile samples B, C, and D have been, respectively, exposed for 30, 300, and 600 seconds, to all the temperatures mentioned in Table 1.

The samples B, C, and D were analyzed before being subjected to any heat treatment. Once the characterization was done, the solar cells were exposed to 150°C for different time periods. After the heat treatment the solar cells were analyzed again and the results compared. Once Step 2 was completed the solar cells were heated again at a higher temperature (200°C) and the same characterization techniques were used again iteratively. Figure 2 indicates the process cycle for each temperature. The oven was heated to the required temperature.

Step 1 (warm-up of the oven). For each experiment the heating phase took about 20 minutes in order to stabilize the oven temperature. The relative humidity percentage was estimated to be below 10%. Cells were then exposed to this temperature for the stated time. After analysis, the same samples were heated to the next temperature. This means that when we speak about the sample at 300°C, it has already been cumulatively heated at 150°C, 200°C, 225°C, 250°C, 275°C, and 300°C for 30 seconds each time in the case of group B.

Step 2 (measurements). In this phase the samples B, C, and D were analyzed with current-voltage measurements (OAI TriSol solar Simulator). Series and shunt resistance, shown in Table 2, were obtained from the slope determination of the light current-voltage curves. Moreover, samples were analyzed by spectral response, LIT (ImageIR camera and Sunfilm IR lens from Infratec), optical microscopy, SIMS (Cameca IMS 7f), and SEM (Jeol/JSM-6010LA Intouch-Scope) images of back contact, grid, and samples surfaces.

TABLE 2: Values of V_{OC} , J_{SC} , FF , η , R_S , and R_{SH} at 25°C, 225°C, and 300°C.

	25°C				225°C			300°C		
	A	B	C	D	B	C	D	B	C	D
V_{OC} (mV)	603 ± 3	603 ± 4	602 ± 2	601 ± 2	600 ± 4	587 ± 2	591 ± 2	598 ± 4	592 ± 1	585 ± 2
J_{SC} (mA/cm ²)	36.1 ± 0.2	35.7 ± 0.1	36.3 ± 0.2	35.9 ± 0.2	36.4 ± 0.1	36.5 ± 0.1	36.1 ± 0.3	35.9 ± 0.1	36.2 ± 0.2	34.7 ± 0.9
FF (%)	66 ± 1	68.1 ± 1	68.1 ± 1	66 ± 1	65 ± 1	65 ± 2	59 ± 1	64 ± 1	50 ± 1	37 ± 1
Efficiency (%)	14.3 ± 0.1	14.6 ± 0.2	14.9 ± 0.3	14.3 ± 0.3	14.2 ± 0.1	14.0 ± 0.4	12.8 ± 0.1	13.6 ± 0.2	10.6 ± 0.2	7.5 ± 0.1
R_S (Ωcm^2)	3.1 ± 0.1	2.8 ± 0.1	2.7 ± 0.2	3.1 ± 0.2	3.2 ± 0.1	2.9 ± 0.3	4.3 ± 0.2	3.6 ± 0.1	9.8 ± 0.8	27.1 ± 1.0
R_{SH} (Ωcm^2)	1334 ± 82	1203 ± 192	1211 ± 30	1115 ± 293	1078 ± 95	1067 ± 28	1114 ± 139	1143 ± 71	1132 ± 43	1003 ± 91

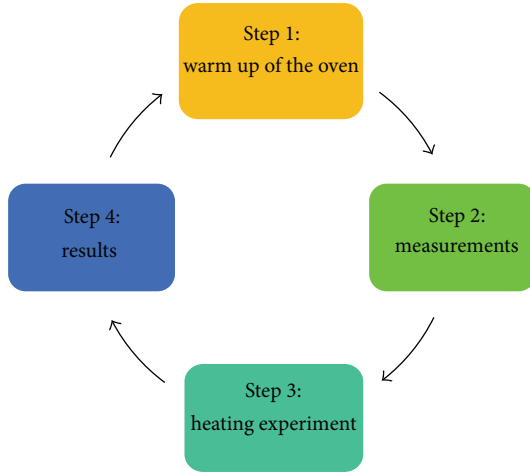


FIGURE 2: Cyclic steps for the heating experiments.

All these experiments gave an overview in terms of electrical, compositional, and visual aspects of the samples before they are exposed to heat treatment. Once this phase has been completed the cells are inserted in the oven and phase 3 begins.

Step 3 (heating experiment). The heating phase lasted, respectively, for 30 seconds, 300 seconds, and 600 seconds for the sample of groups B, C, and D. The temperature of the oven was monitored with a thermocouple located near the samples holder with an uncertainty of 5°C. The samples were not preheated but directly inserted at the set temperature, at 1 bar, and in air atmosphere.

Step 4 (results). Once the heat treatment has been completed (for 30 seconds, 300 seconds, or 600 seconds), the samples were measured again with the same techniques of Step 1 and the results analyzed. The heat, due to this thermal mechanism, was accumulated after each cycle in the solar cell, so the same cells are exposed to the next temperature, and so on. Once the results are analyzed Step 1 starts again and the oven is warmed up till the next temperature.

3. Experimental Results

3.1. Electrical Changes. Before the heat treatment all the solar cells gave similar values of efficiency, FF , V_{OC} , J_{SC} , and series

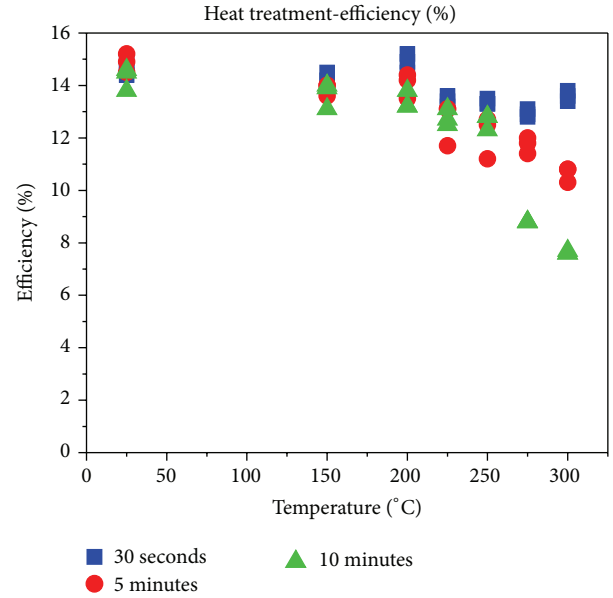


FIGURE 3: Efficiency evolution for different heat treatment condition. The 30 seconds (in blue), the 300 seconds (in red), and the 600 seconds (in green).

and shunt resistances, listed in Table 2. Below the critical temperature of 225°C barely any changes could be observed even for exposure of 600 seconds. The IV measurements results, shown in Figure 3, point out that the efficiency reduction, after the exposure to 300°C for 30 seconds was limited to 2-3%; meanwhile in the cases of 300 seconds and 600 seconds it dropped by 30% and 50%, respectively. Figure 4 shows the current-voltage curves for samples exposed to 300°C for 30, 300, and 600 seconds.

The IV curves of the solar cells exposed to 300°C for 30 seconds (blue), 300 seconds (red), and 600 seconds (green) are plotted in Figure 4. The comparison of the IV curve slope between the initial IV slope and the final slope indicates the formation of a barrier for the cells exposed at 300 and 600 seconds. The barrier partly prevents the electrons' extraction.

The CIGSSe solar cells exposed for 30 seconds did not show any barrier formation in the IV curve. The barrier formation, observable in Figure 4, firstly occurred at 225°C, for samples heated for 300 and 600 seconds, and become more and more evident by increasing the exposure temperature. The J_{SC} and V_{OC} before and after the heat treatment were

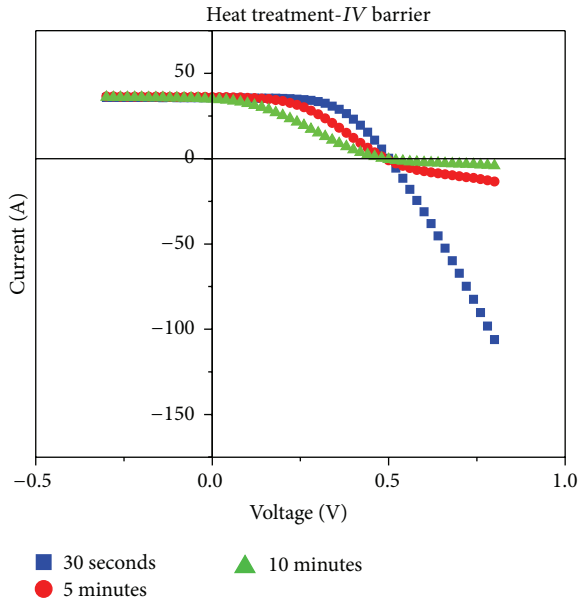


FIGURE 4: *IV* curve barrier formation for heat treatment for 30 (in blue), 300 (in red), and 600 (in green) seconds after being exposed to 300°C.

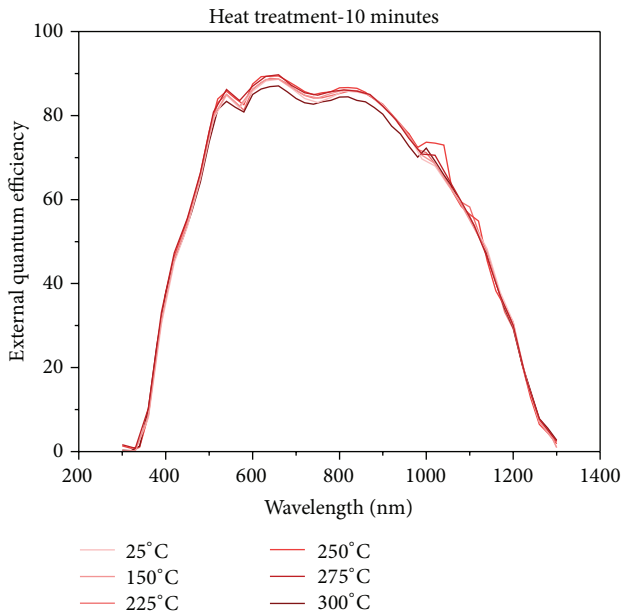


FIGURE 5: EQE of samples D heated for 600 seconds. The darker the color the more the heat treatment.

similar, which means that the electrons are still generated but not optimally extracted; this indicates the formation of a secondary barrier in the solar cell.

The EQE measurement, shown in Figure 5, indicated that, in the case of 600-second exposure time, the solar cells exposed to 300°C showed a global reduction in J_{SC} by maximum 2-3%. These results confirmed the *IV* measurements and are consistent with literature results, where a high EQE drop has been identified for temperature above 350°C [2, 6, 7].

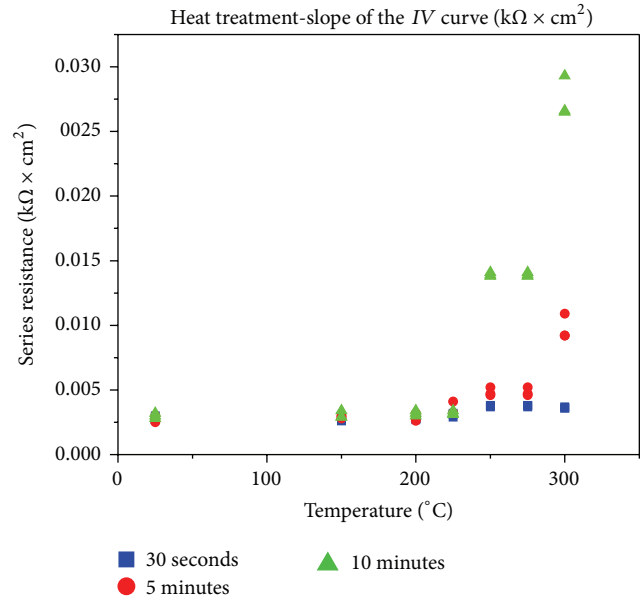


FIGURE 6: The slope of the *IV* curve is a method to estimate the series resistance increase and consequently the barrier formation. In squares exposure of 30 seconds, in circles 300 seconds, and in triangles 600 seconds.

The EQE showed changes in the heated samples mainly in the region of 500–1000 nm wavelength. These changes could be caused by modification in the transparency of TCO or due to improvement in carrier collection. Figure 6 illustrates the slope of the *IV* curve which represents the series resistance and/or the barrier evolution. The slope drastically increases after 225°C due to the barrier formation that bends the *IV* curve and influences the series resistance calculation. The V_{OC} reduction was limited to a maximum value of 4% in all cases. Concerning the shunt resistance, the reduction was in the range of 5% in all the three time periods; meanwhile the increase in series resistance was negligible for the 30-second exposure. In order to observe the evolution of the barrier, Figure 6 shows the slope of the *IV* curve after the V_{OC} point. The value of the *IV* curve slope is a simple method to estimate the effect of the series resistance on the performance of the solar cells. The barrier formation bends the *IV* curve and heavily modifies the slope of the *IV* curve and consequently the series resistance values. The main cause of the efficiency reduction is the barrier formation; indeed, it reduces the extraction of electrons. In case of 300- and 600-second exposure time, the series resistance increase followed an exponential trend, with the increase in the exposure temperature, which was the main cause for high drops in terms of fill factor (50%). In general, the results indicated that up to a temperature of 225°C the CIGS solar cells performance was not affected by the heat treatment.

Figure 7 illustrates the effect of applying different filters between the light source and the solar cells when performing *IV* measurements in order to learn more about the cause of the barrier. The J_{SC} was corrected in order to properly compare the results. In the case of the blue filter, it is evident

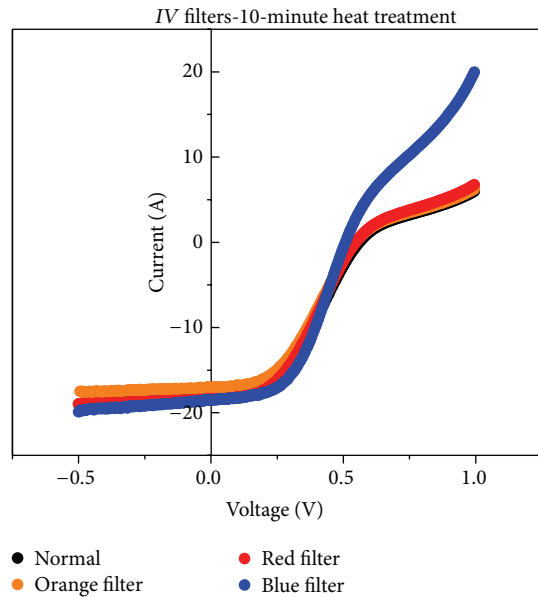


FIGURE 7: *IV* curve measurements under filters with a different color of the solar cells heated till 300°C for 600 seconds.

that the barrier is reduced and current is better extracted. The *IV* curve produced by the use of the blue filter also indicates that the shape is not completely normal, but is closer to the expected behavior. A blue filter let only blue light pass through, meaning that CdS is excited and a normal behavior of the CIGSSe is observed. This could indicate that the barrier issue is more related to the front contact region rather than the back contact or CIGSSe absorber layer. In order to localize the observed shunting, lock-in thermography was used. The measurements are shown in Figure 8 and indicated the formation of shunts on the P3 mechanically scribes surrounding the 1 cm² cells (white dashed lines). P3 lines were scribed mechanically when creating the interconnected cells. Those lines are visible in Figure 8, where we can notice shunt formation in vicinity of the scribes due to heat treatment. The shunts increase with the increasing in the exposure time. The blue line in Figure 8 represents the Ag grid of the solar cells. The figure shows the sample B ((a) exposed for 30 seconds), sample C ((b) exposed for 300 seconds), and sample D ((c) exposed for 600 seconds) after being exposed at a temperature of 300°C. The increase in white color in the sample exposed for 600 seconds at 300°C indicate the degradation of the P3 line and consequently the increase in shunt resistance.

3.2. Compositional Changes. The compositional changes of the samples were studied by SEM-EDX and SIMS. The reference sample A was compared, by cross-sectional SEM-EDX, with sample D. The latter is chosen because it showed the strongest barrier behavior since it was exposed for the longest time to the highest temperature. In general, no diffusion or migration of elements was observed, apart for aluminum (detected with the use of SIMS). It was striking that Cadmium diffusion, as was observed by Ramanathan et

al. after heating the solar cells at 400°C, was not observed [2]. SIMS measurement demonstrated a possible migration of aluminum from the front contact layer to the CIGSSe absorber layer (Figure 9). Chirila et al. [8] also observed Al diffusion; indeed they used an Al flexible substrate and a migration of Al from this flexible layer to CIGSSe layer has been detected with SEM-EDX and SIMS. Even if a possible Al diffusion has been observed, the reduction of Al from the AZO layer has a small effect on the solar cell performance.

4. Discussion on Barrier Formation

IV and EQE measurements indicate almost no variations in terms of J_{SC} and V_{OC} . The filters experiment, plotted in Figure 7, can indicate that the *IV* barrier, which produces difficulties related to the electrons extraction, is likely present in the p-n junction region. By combining the filter experiments with the results of SIMS and cross-sectional SEM and with the information from the literature [8] one possible explanation of the barrier can be derived. Chirila et al. [8] observed a diffusion of Al from the substrate to the CIGSSe absorber layer and described that Al could act as a trap point in the absorber.

In our heating experiment an opposite diffusion of Al has been detected: the Al diffusion observed with SIMS was from the front contact to the CIGSSe absorber layer. The aluminum present in the absorber layer could produce traps point which provoked recombination of electrons-holes pairs. These effects could affect the extraction of electrons from the solar cells and by doing this reduction of the performance of them is affected. The Al diffusion could therefore be the cause for the *IV* barrier, while the diffusion from the front contact to the CIGSSe absorber layer could have a second effect: it could decrease the conductivity of the front contact layer, and by doing so it influences the series resistance of the solar cells [8].

5. Conclusions and Outlook

The CIGSSe solar cells exposed for 30 seconds did not show any barrier formation in the *IV* curve (Figure 5). Moreover, only in the case of 30 seconds no shunts on the mechanical scribe lines (Figure 8) were observed. Regarding the efficiency, the reduction after an exposure of 300°C for 30 seconds was limited to 2-3% (Figure 3). On the other hand, in the cases of 300 and 600 seconds the efficiency dropped by 29% and 48%, respectively. Furthermore, for the last two cases lock-in thermography indicated a formation of shunts on the P3 scribed lines. The electrical properties, analyzed with EQE and *IV* measurements, showed almost no changes in J_{SC} and V_{OC} . Concerning the shunt resistance, the reduction was in the range of 5% for all the three time periods. The series resistances could not be easily calculated, since the slopes of the curves were affected by the barrier, which led to bending of the *IV* curve. The *IV* slope increase around open circuit conditions was negligible for the 30 seconds; meanwhile for the 300 and 600 seconds the increase was almost exponential and it was the main cause for the high drops in terms of fill factor (50%). The results demonstrate that CIGSSe solar cells

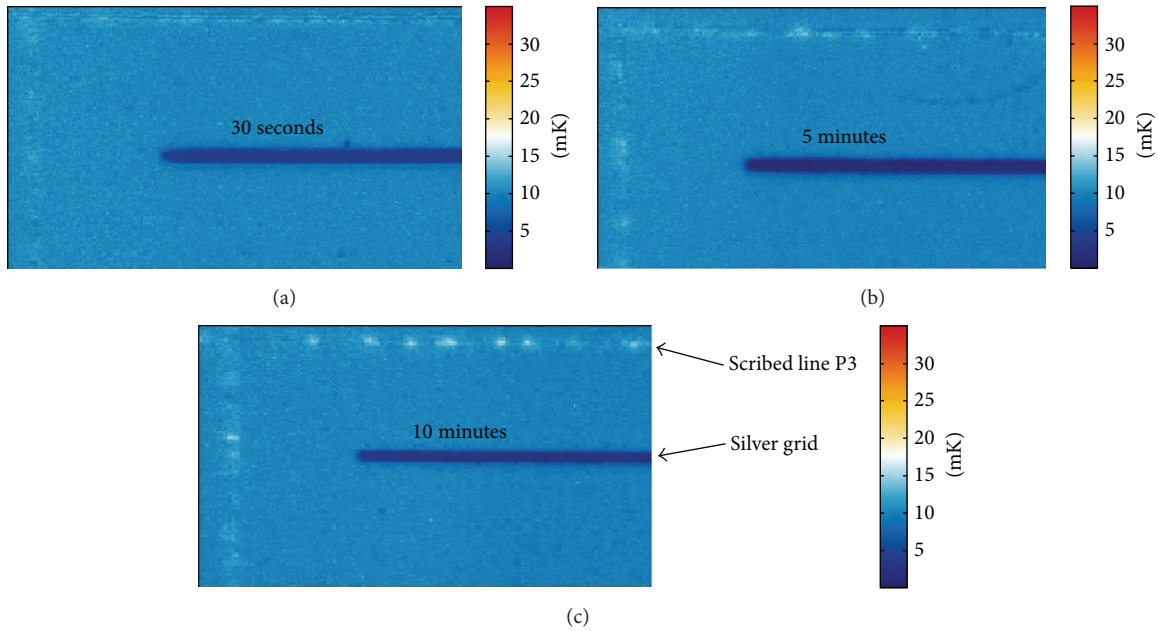


FIGURE 8: LIT images of sample heated for 30 seconds (a), 300 seconds (b), and 600 seconds (c) after being exposed to 300°C.

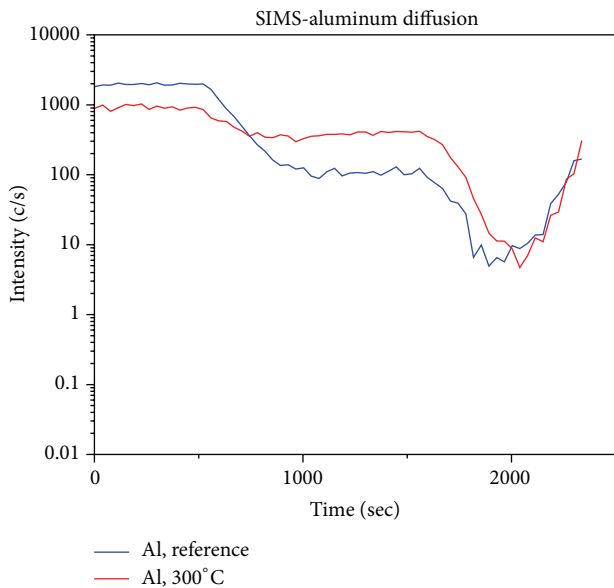


FIGURE 9: SIMS measurements showing Al diffusion from front contact to CIGSse absorber layer. In blue the reference sample and in red the sample at 300°C for 600 seconds.

were able to withstand until 225°C in air atmosphere even for 600 seconds. At higher temperatures IV barrier which reduced the extraction of carriers and reduced the solar cell performance was observed. Future experiments should focus on noncumulative heat treatment as well. Moreover, it would be interesting to heat the solar cells under vacuum or inert conditions, in order to understand the influence of air on the degradation of the solar cells.

Competing Interests

The authors declare that they have no competing interests.

Acknowledgments

The authors would like to thank Klaas Bakker and Henk Steijvers (TNO) for the fruitful discussions. Also, many thanks goes to Bertil Okkerse (Philips Innovation Services) and Denis Mangin (Université de Lorraine) for their assistance with the measurements or analysis.

References

- [1] M. A. Green, K. Emery, Y. Hishikawa, W. Warta, and E. D. Dunlop, "Solar cell efficiency tables (version 47)," *Progress in Photovoltaics: Research and Applications*, vol. 24, no. 1, pp. 3–11, 2016.
- [2] K. Ramanathan, M. A. Contreras, J. R. Tuttle et al., "Effect of heat treatments and window layer processing on the characteristics of CuInGaSe₂ thin film solar cells," in *Proceedings of the 25th IEEE Photovoltaic Specialists Conference*, pp. 837–840, May 1996.
- [3] S. Kijima and T. Nakada, "High-temperature degradation mechanism of Cu(In,Ga)Se₂-based thin film solar cells," *Applied Physics Express*, vol. 1, no. 7, Article ID 075002, 2008.
- [4] D. S. Chen, J. Yang, F. Xu et al., "Effect of rapid thermal annealing on the compositional ratio and interface of Cu(In,Ga)Se₂ solar cells by XPS," *Applied Surface Science*, vol. 264, pp. 459–463, 2013.
- [5] X. Wang, S. S. Li, W. K. Kim et al., "Investigation of rapid thermal annealing on Cu(In,Ga)Se₂ films and solar cells," *Solar Energy Materials and Solar Cells*, vol. 90, no. 17, pp. 2855–2866, 2006.

- [6] J.-H. Wi, T. G. Kim, J. W. Kim et al., “Photovoltaic performance and interface behaviors of Cu(In,Ga)Se₂ solar cells with a sputtered-Zn(O,S) buffer layer by high-temperature annealing,” *ACS Applied Materials and Interfaces*, vol. 7, no. 31, pp. 17425–17432, 2015.
- [7] F. Liu, Y. Sun, Q. He, and Z. Zhou, “Rapid thermal annealing on dS/Cu(In, Ga)Se₂-based solar cells,” in *Proceedings of the International Conference on Materials for Renewable Energy and Environment (ICMREE '13)*, pp. 143–146, Chengdu, China, August 2013.
- [8] A. Chirila, S. Buecheler, F. Pianezzi et al., “Highly efficient Cu(In,Ga)Se₂ solar cells grown on flexible polymer films,” *Nature Materials*, vol. 10, no. 10, pp. 857–861, 2011.

Research Article

Accelerated Life Test for Photovoltaic Cells Using Concentrated Light

Daniel Tudor Cotfas, Petru Adrian Cotfas, Dan Ion Floroian, and Laura Floroian

Electrical Engineering and Computer Science Faculty, Transilvania University of Brasov, 500036 Brasov, Romania

Correspondence should be addressed to Daniel Tudor Cotfas; dtcotfas@unitbv.ro

Received 14 April 2016; Revised 7 June 2016; Accepted 3 July 2016

Academic Editor: Prakash Basnyat

Copyright © 2016 Daniel Tudor Cotfas et al. This is an open access article distributed under the Creative Commons Attribution License, which permits unrestricted use, distribution, and reproduction in any medium, provided the original work is properly cited.

This paper presents a new method developed to significantly reduce the necessary time for the ageing tests for different types of photovoltaic cells. Two ageing factors have been applied to the photovoltaic cells: the concentrated light and the temperature. The maximum power of the photovoltaic cells was monitored during the ageing process. The electrical dc and ac parameters of the photovoltaic cells were measured and analyzed at 1 sun irradiance, before and after the test stress. During the test, two photovoltaic cells are kept at maximum power point and the other two are kept at open circuit voltage point. The method is validated through the results obtained for the monocrystalline silicon solar cell.

1. Introduction

The reliability and durability are two important factors for the new photovoltaic cells and panels, today perhaps at least as important for them as the price per watt. The lifetime of new photovoltaic cells such as, but not only, the multijunction cells used in concentrated light whose efficiency is 46% [1] and the very promising perovskite solar cells whose efficiency increases very quickly at 20.1% [2], is not known.

Therefore, a predictive model for the lifetime and the behavior of the new photovoltaic cells and panels is very important for producers as well as for customers. The accelerated ageing test for the photovoltaic cells and panels is one of the main analyses which are the base of the predictive model [3, 4].

There are several methods to realize the accelerated ageing test for photovoltaic cells and panels indoors, such as

- (i) Damp Heat Test (DH): the ageing factors are the temperature and the relative humidity; the values for these two factors are 85°C and 85%; the time for the ageing test is over 2000 hours [5];
- (ii) Highly Accelerated Stress Test (HAST): the ageing factors are the temperature and the relative humidity, but their values grow in comparison to DH, so the

temperature can be 110°C, 130°C, or 150°C, and the humidity can be 85% or 100%; the increasing of the ageing factors values leads to the decrease of the time for the ageing test; in this case the time for the ageing test is around 400 hours;

- (iii) step-stress accelerated ageing tests: the ageing factors are the temperature and the injected current to emulate constant illumination; the temperature can be 130°C, 150°C, or 170°C and the value of the current is equal to the value of the short circuit current, I_{sc} , at 1 sun multiplied with 700 or 1050; the test being made for multijunction solar cells [6];
- (iv) thermal cycling test: this method uses the variation of the temperature between -40°C and 85°C and the injected current to emulate constant illumination; the amount of the cycling varies in function of the upper limit of the temperature, 500 for 110°C, 1000 for 85°C, or 2000 for 65°C; the injected current in the solar cell is equal to $1.25 \times I_{sc} \times \text{no. of suns}$ [7];
- (v) potential induced degradation (PID): the ageing factors for the photovoltaic modules are the external bias voltage, the temperature, and the relative humidity; their values are 1000 V, 50°C, and 50% [5] or 600 V, 65°C, and 85% [8].

The lifetime for the Si photovoltaic panels now is known and it is over 25 years [9]. The failure criterion is when its maximum power decreases with at least 20% from the initial maximum power [10].

Núñez et al. had defined a degradation failure criterion for the multijunction cells [11]. The failure limit is when the maximum power decreases with at least 2.5% from the initial maximum power. Núñez et al. considered that a power loss of up to 20% is generated by the other elements of the concentrator photovoltaic system.

The degradation failure criterion for the silicon photovoltaic cell corresponds to losing 10% of the maximum power through light-induced power degradation, occurrence of microcracks, increase in series resistance, decrease of shunt resistance, and so forth [12–14].

2. Method

The main goal of the accelerated life test is to reduce the testing time under simulated working conditions. In DH test the necessary time is around 2000 h and the target of the new methods is tens or some hundreds of hours.

There are many methods to perform the accelerated life test, but there is scarce research using light as ageing factor, because the majority use a climatic chamber and therefore the concentrated light is difficult to use [11]. The researchers had emulated the work conditions in concentrated light by injection of the forward current equivalent to the photogenerated current by the photovoltaic cell at the level of the desired concentration [11, 15]. In this case the stress produced on the photovoltaic cells by the high concentrated light cannot be taken into consideration.

The paper presents a new method for the accelerated life test using the concentrated light obtained from a solar simulator with a xenon lamp (called ALTCL). Due to working conditions there are two stress factors: light and temperature.

The experiment set-up to apply the new method consists of the solar simulator, the photovoltaic cells, the measurement system, and the photovoltaic cells support cooled with water, which is provided with a variable flow of water [16].

2.1. Solar Simulator. The experiments were performed at Solar Technology Laboratory of Paul Scherrer Institute (PSI), Villigen, Switzerland, using the high-flux solar simulator (HFSS), which has ten xenon arc lamps cooled with high pressure water, Figure 1. The highly concentrated light, similar to the solar radiation, is obtained in the focal plane using the lamps.

The lamp reflector is designed as a truncated ellipsoid [17, 18]. The accelerated ageing test was performed using only one of the ten xenon arc lamps, which works at 10.6 kW. The electric power of the lamp was maintained quasi-constant using an automatic system.

2.2. Photovoltaic Cells' Water Cooled Support. The photovoltaic cells' water cooling support allows the mounting of the four PV cells in different configurations and the maintaining

of the PV cells temperature quasi-constant during the measurements under concentrated light [16]; see Figure 2.

The facility of the various mounting of the photovoltaic cells is necessary to have the PV cells illuminated with the same or with the different levels of the concentrated light.

The temperature of the photovoltaic cells can be adjusted using the levels of illumination and also the variable water flow which can be assured by the automatic pump system. The distribution of the illumination levels obtained with one xenon lamp at PSI is presented in Figure 3.

The photovoltaic cells were positioned so all of them are uniformly illuminated, with the same radiative flux, 190 suns. The shutter of the solar simulator was gradually opened until the temperature of the photovoltaic cells was $150^{\circ}\text{C} \pm 2^{\circ}\text{C}$.

2.3. Measurement System. The measurements were performed in concentrated light and under illumination at 1 sun.

The measurements in concentrated light were performed at PSI using a system based on cRIO from National Instruments and a module developed by our team which allows measuring the current voltage characteristics, I - V , for all four photovoltaic cells simultaneously and also their temperature. The photovoltaic cells' temperature was measured using a thermocouple for each of them. The maximum power can be determined by measuring I - V characteristic of the photovoltaic cells. For measuring the current and voltage on the photovoltaic cells the NI 9227 and NI 9215 modules were used. The first module is used to measure the current through the photovoltaic cells and the second one is used for measuring their output voltage. These modules allow measuring all four channels at the same time. The dynamic load used for measuring I - V characteristics of the photovoltaic cell is based on a large capacitor. The solar cell temperatures are measured with a NI 9211 module which allows sampling simultaneously for all four channels. The DIO (Digital Input Output) NI 9401 module is used for starting I - V characteristic measurements. Between measurements of two consecutive I - V characteristics a load can be applied to the photovoltaic cells. The applied load is based on a MOSFET which is controlled using the four analog outputs of the NI 9269 module. Some of the studied photovoltaic cells were maintained in the maximum power point regime while the others were maintained in the open circuit regime.

The measurements under 1-sun illumination were performed using the Autolab PGSTAT100. This system allows measuring I - V characteristic under illumination using the potentiostat mode and also plotting and fitting the Nyquist diagram using the Fra (Frequency Response Analyzer) module.

2.4. Photovoltaic Cells. The photovoltaic cells chosen for the experiment are commercial monocrystalline silicon cells and InGaP/InGaAs/Ge multijunction cells. Four photovoltaic cells were tested, two of each type. In each pair of photovoltaic cells one of them was measured with load and one without load.

The reason of the choosing the monocrystalline silicon cells is that the lifetime is known. The monocrystalline silicon

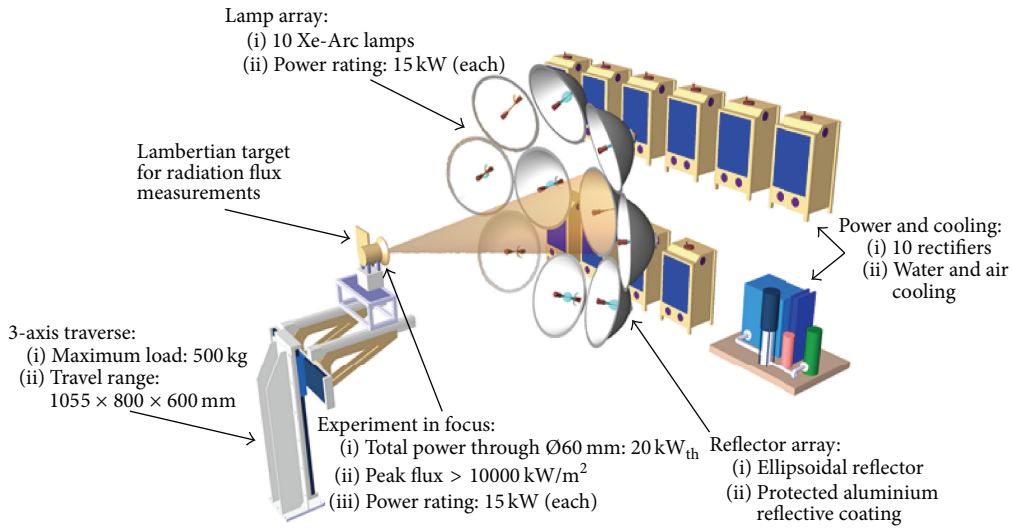


FIGURE 1: Schema of the solar simulator.



FIGURE 2: The photovoltaic cells' water cooled support with four PV cells.

photovoltaic cells were cut at 0.5 cm/0.5 cm because the system can measure up to 5 A and for a good uniformity of the illumination. The short circuit current measured at 190 suns is 1.65 A and the open circuit voltage is 0.668 V.

InGaP/InGaAs/Ge photovoltaic cells are made to work in concentrated light. Their structure is triple junction and the dimensions are 1 cm/1 cm. The short circuit current measured at 190 suns is 2.67 A and the open circuit voltage is 2.82 V.

3. Results and Discussion

The desired temperature for the test, 150°C, was obtained and maintained quasi-constant using only the concentrated light and the cooling system.

Núñez et al. [11] proposed two criteria for reliability of the photovoltaic cell: catastrophic failure, instant drop in power of the photovoltaic cells, and degradation failure, the power decreasing with more than 2.5% for the multijunction

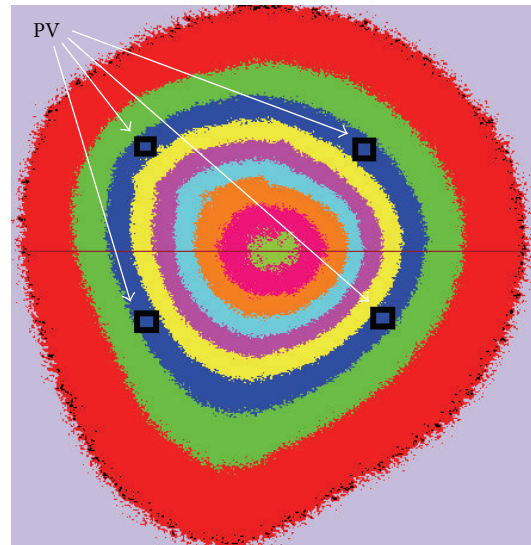


FIGURE 3: The radiative flux map and the positioning of the photovoltaic cells.

photovoltaic cells which work in concentrated light and more than 10% for the silicon photovoltaic cells.

The photovoltaic cells were subjected to 190-sun concentrated light and 150°C for 35 hours and 7 hours per day and in the rest of day they were kept in darkness and at room temperature. After five days only the second criterion was observed.

The result of the accelerated ageing test of the monocrystalline silicon photovoltaic cell without load during the experiment is presented in Figure 4. The normalized power

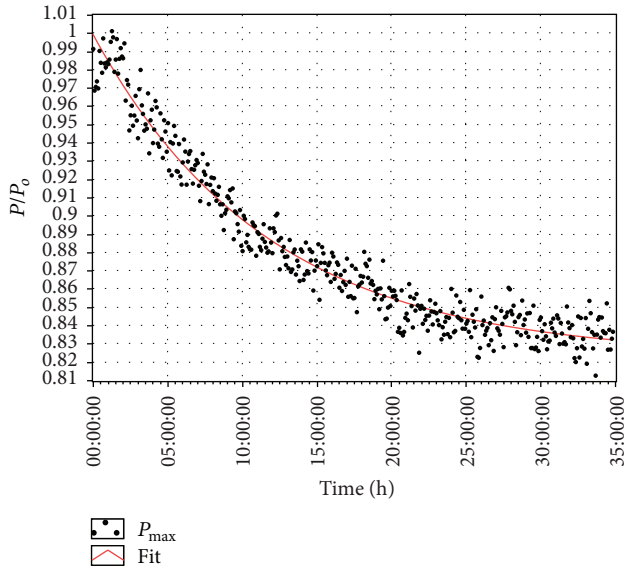


FIGURE 4: The normalized power of the monocrystalline photovoltaic cell without load evolution over time.

P/P_0 , which is the ratio between the maximum power P determined during the experiment and the initial maximum power P_0 of the photovoltaic cell at 190 suns and 150°C , is represented over the time. The maximum power of the photovoltaic cell was determined using I - V characteristic which was measured every five minutes.

The normalized power of the monocrystalline silicon photovoltaic cell without load decreases exponentially; see the red fitting curve from Figure 4, and the degradation failure criterion is reached after 10 hours. After 20 hours, an asymptotic decrease is observed in the normalized power. The normalized power after 35 hours is 0.83, which means a decrease of 17%; see Figure 4.

The normalized power InGaP/InGaAs/Ge multijunction photovoltaic cell without load decreases very slowly and after 35 hours it decreases only by 1.5%.

The decreasing ratio of the normalized power for the photovoltaic cells with load during the ageing test, after 35 hours, was lower, 6% for the monocrystalline silicon (see Figure 5), and negligible for the multijunction photovoltaic cell.

The photovoltaic cells were analyzed in static regime, dc, and dynamic regime, ac, before and after the accelerated ageing test.

I - V characteristics and power voltage, P - V , characteristics are measured for each photovoltaic cell. The measurements were realized with Autolab, under illumination at 1000 W/m^2 irradiance (1 sun) and at this time the temperature of the photovoltaic cells is maintained constant with thermostat at $25^\circ\text{C} \pm 0.5^\circ\text{C}$.

Figure 6 shows I - V and P - V characteristics measured for the monocrystalline silicon photovoltaic cell without load before and after the accelerated test. By analyzing the results it is observed that the short circuit current, I_{sc} , decreases with $3.9\% \pm 0.1\%$, the open circuit voltage decreases with $5.4 \pm 0.1\%$, and the maximum power decreases with $18.2\% \pm 0.2\%$.

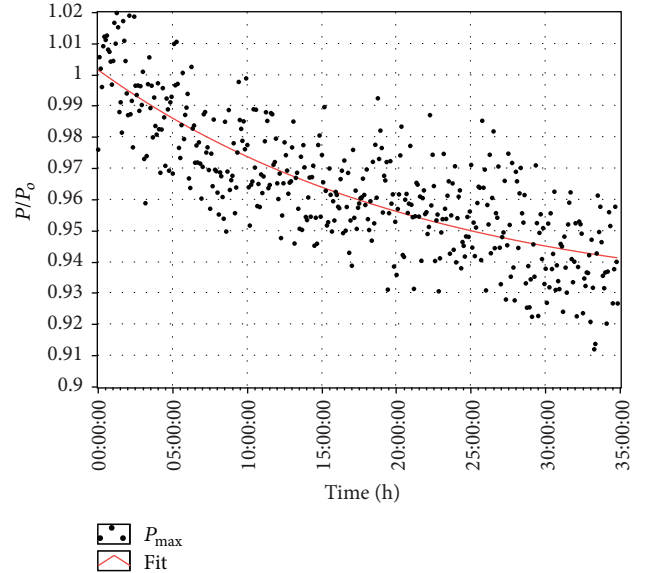


FIGURE 5: The normalized power of the monocrystalline photovoltaic cell with load evolution over time.

The shape of I - V characteristic around the knee (the maximum power point), for the aged photovoltaic cell, shows an important modification. This can be explained by the increasing of the series resistance, R_s , and the decreasing of the shunt resistance, R_{sh} .

I - V and P - V characteristics measured for the InGaP/InGaAs/Ge multijunction photovoltaic cell without load before and after the accelerated test are presented in Figure 7. The maximum power decreases with $1.5\% \pm 0.1\%$, whereas I_{sc} and V_{oc} remain quasi-constant after the ageing process. The shape of I - V characteristic measured after the ageing process remains almost unchanged, only the effect of the slight increase in the series resistance being observed.

The impedance spectroscopy [19, 20] with the frequency domain technique is used to analyze the parameters of the photovoltaic cells in dynamic regime before and after the ageing process. An ac pure sinusoidal signal with amplitude smaller than the thermal voltage, (kT/e) , is superposed on the dc bias signal. The measurements were performed at bias voltage equal to V_{max} , the voltage corresponding to the maximum power point. The photovoltaic cells were maintained at $25^\circ\text{C} \pm 0.5^\circ\text{C}$ and were illuminated at 1 sun.

The Nyquist diagrams, before and after the ageing process, for the monocrystalline silicon photovoltaic cell without load are presented in Figure 8 and those for the InGaP/InGaAs/Ge multijunction photovoltaic cell without load are presented in Figure 9. The important ac parameters of the photovoltaic cells are obtained using the fitting procedure with the equivalent ac circuit and they are presented in Table 1.

The results obtained for the ac parameters of the photovoltaic cells confirm analysis for the behavior of the photovoltaic cells in static regime. The series resistance strongly increases for the monocrystalline silicon photovoltaic cell,

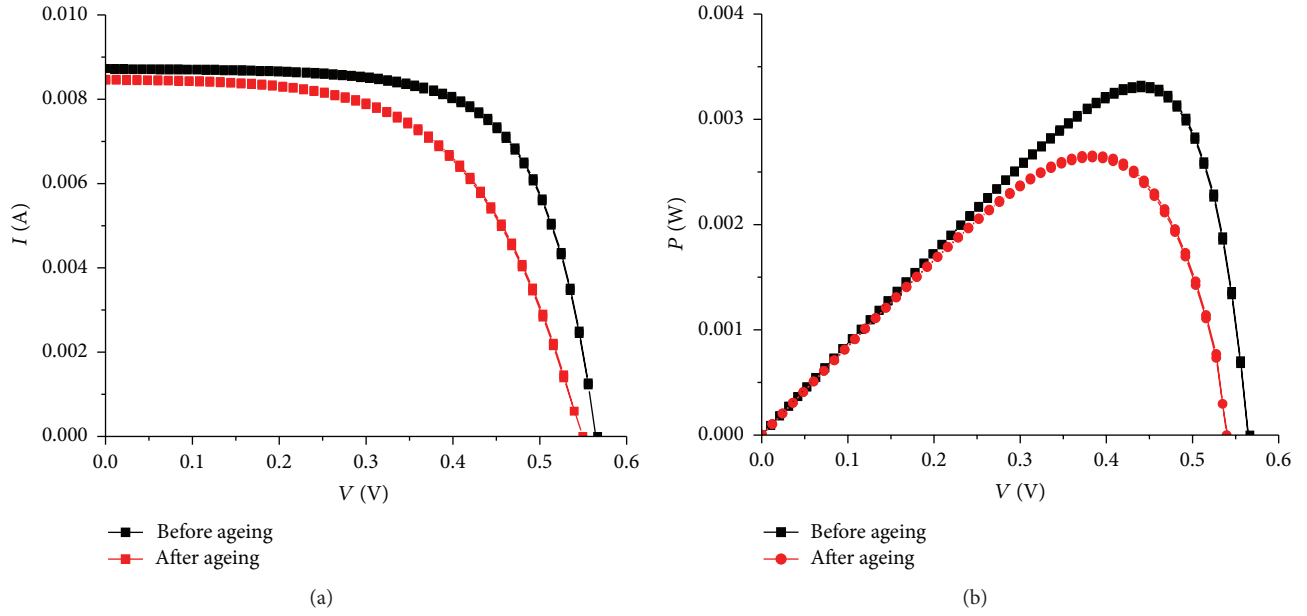


FIGURE 6: The monocrystalline silicon photovoltaic cell without load before and after ageing process. (a) I - V characteristics; (b) P - V characteristics.

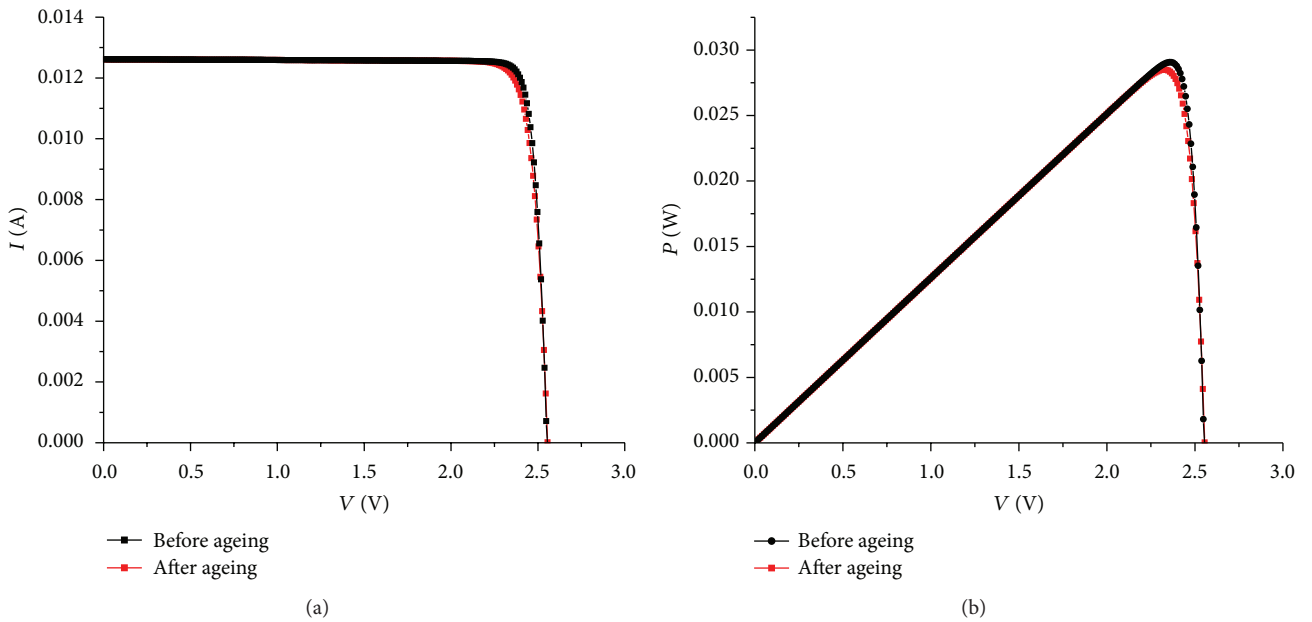


FIGURE 7: The InGaP/InGaAs/Ge multijunction photovoltaic cell without load before and after ageing process. (a) I - V characteristics; (b) P - V characteristics.

TABLE 1: The ac parameters of the photovoltaic cells at 1000 W/m^2 and 25°C .

Type of photovoltaic cell	Ageing test	R_s [Ω]	R_p [Ω]	C [nF]
Monocrystalline silicon without load	Before	0.23 ± 0.01	49.67 ± 0.2	644.3 ± 3.5
	After	0.76 ± 0.01	$24,23 \pm 0.16$	432.4 ± 2.5
Monocrystalline silicon with load	Before	0.22 ± 0.01	49.71 ± 0.2	642.3 ± 3.5
	After	0.45 ± 0.01	$38,23 \pm 0.16$	552.4 ± 2.5
InGaP/InGaAs/Ge without load	Before	0.87 ± 0.012	18.42 ± 0.12	$(19.43 \pm 0.1) * 10^3$
	After	0.881 ± 0.012	18.39 ± 0.12	$(19.42 \pm 0.1) * 10^3$

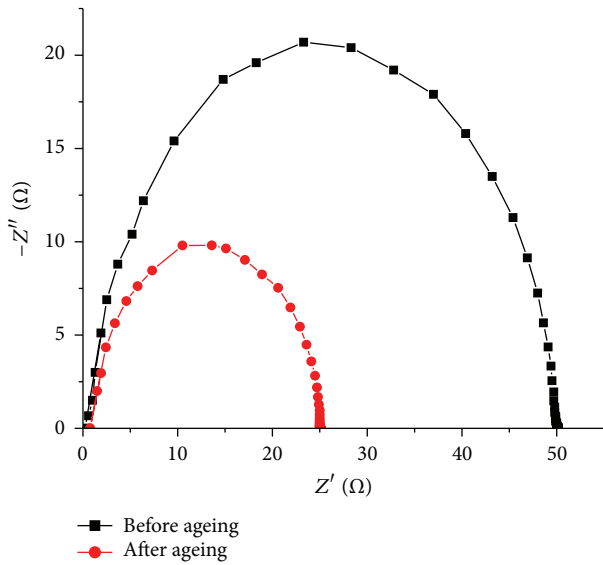


FIGURE 8: Nyquist plot of the monocrystalline silicon photovoltaic cell without load before and after ageing process.

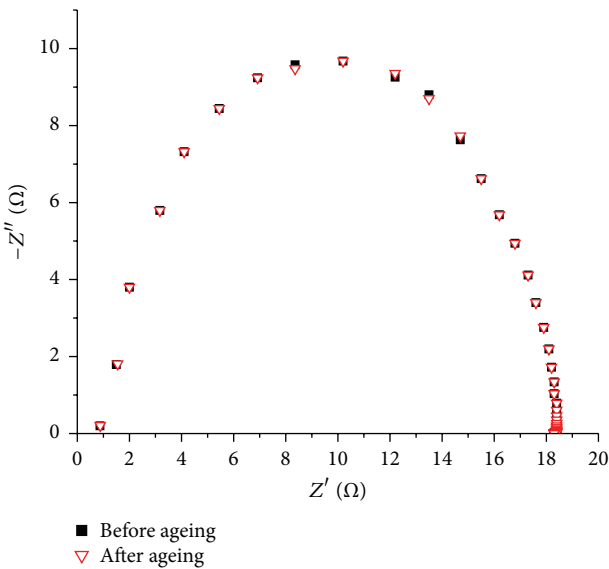


FIGURE 9: Nyquist plot of the InGaP/InGaAs/Ge multijunction photovoltaic cell without load before and after ageing process.

whereas for the multijunction photovoltaic cell it slightly increases. The same behavior is determined for the decrease of the shunt resistance and for the capacitance.

4. Conclusions

A new method for the accelerated life test of the photovoltaic cells was developed and verified. The novelty of the method is the use of only concentrated light and the cooling system so as to have two ageing factors: the light and the temperature.

The duration of the life test is reduced considerably, for example, 10–20 hours for the monocrystalline silicon

photovoltaic cells without load at 190 suns. For monocrystalline silicon cell with load the degradation after 35 h at the same illumination is 6%. The maximum power of InGaP/InGaAs/Ge multijunction cell without load at 190 suns after 35 hours decreases with 1.5%, which means it does not reach the limit of the degradation failure.

The maximum power of the photovoltaic cells with load decreases slightly than the maximum power of the photovoltaic cells without load, which proves that lifetime of the photovoltaic panels increases if they work in load.

The parameters of the photovoltaic cells were analyzed in static and dynamic regime at 1 sun and 25°C using I - V and P - V characteristics and the Nyquist diagrams. The behavior of the short circuit current, open circuit voltage, maximum power, series and parallel resistance, and capacitance before and after the ageing process was studied.

The future research will consist of increasing the duration of the life test for the multijunction photovoltaic cells until the limit of the degradation failure criterion is reached and also we will apply the method validated by present work to test other type of photovoltaic cells.

Competing Interests

The authors declare that they have no competing interests.

Acknowledgments

Financial support by the Access to Research Infrastructures activity in the 7th Framework Programme of the EU (SFERA 2 Grant Agreement no. 312643) is gratefully acknowledged. The authors are thankful to Y. Baeuerle, D. Wuillemin, and C. Wieckert as well as further coworkers from the Solar Technology Laboratory of Paul Scherrer Institute, Villigen, Switzerland, where all the measurements in concentrated light were performed. They hereby acknowledge the structural funds project PRO-DD (POS-CCE, O.2.2.1., ID 123, SMIS 2637, no. 11/2009) for providing a part of the infrastructure used in this work.

References

- [1] M. A. Green, K. Emery, Y. Hishikawa, W. Warta, and E. D. Dunlop, "Solar cell efficiency tables (version 44)," *Progress in Photovoltaics: Research and Applications*, vol. 23, pp. 1–9, 2015.
- [2] M. I. Ahmed, A. Habib, and S. S. Javaid, "Perovskite solar cells: potentials, challenges, and opportunities," *International Journal of Photoenergy*, vol. 2015, Article ID 592308, 13 pages, 2015.
- [3] US Department of Energy, Sandia, and NREL, "Accelerated aging testing and reliability in photovoltaics. Solar energy technology program," 2008.
- [4] D. C. Jordan and S. R. Kurtz, "Photovoltaic degradation rates—an analytical review," *Progress in Photovoltaics: Research and Applications*, vol. 21, no. 1, pp. 12–29, 2013.
- [5] A. Phinikarides, N. Kindyni, G. Makrides, and G. E. Georghiou, "Review of photovoltaic degradation rate methodologies," *Renewable and Sustainable Energy Reviews*, vol. 40, pp. 143–152, 2014.

- [6] J. R. González, M. Vázquez, N. Núñez, C. Algora, I. Rey-Stolle, and B. Galiana, "Reliability analysis of temperature step-stress tests on III-V high concentrator solar cells," *Microelectronics Reliability*, vol. 49, no. 7, pp. 673–680, 2009.
- [7] G. J. Lin, L. J. Wang, J. Q. Liu, W. P. Xiong, M. H. Song, and Z. H. Wu, "Accelerated aging tests of high concentration multi-junction solar cells," *Procedia Environmental Sciences*, vol. 11, pp. 1147–1152, 2011.
- [8] C. R. Osterwald, T. J. McMahon, and J. A. del Cueto, "Electrochemical corrosion of $\text{SnO}_2:\text{F}$ transparent conducting layers in thin-film photovoltaic modules," *Solar Energy Materials and Solar Cells*, vol. 79, no. 1, pp. 21–33, 2003.
- [9] E. Kaplani, "Detection of degradation effects in field-aged c-Si solar cells through IR thermography and digital image processing," *International Journal of Photoenergy*, vol. 2012, Article ID 396792, 11 pages, 2012.
- [10] M. Vázquez and I. Rey-Stolle, "Photovoltaic module reliability model based on field degradation studies," *Progress in Photovoltaics: Research and Applications*, vol. 16, no. 5, pp. 419–433, 2008.
- [11] N. Núñez, J. R. González, M. Vázquez, C. Algora, and P. Espinet, "Evaluation of the reliability of high concentrator GaAs solar cells by means of temperature accelerated aging tests," *Progress in Photovoltaics: Research and Applications*, vol. 21, no. 5, pp. 1104–1113, 2013.
- [12] M. Paggi, I. Berardone, A. Infuso, and M. Corrado, "Fatigue degradation and electric recovery in Silicon solar cells embedded in photovoltaic modules," *Scientific Reports*, vol. 4, article 4506, pp. 1–7, 2014.
- [13] D. De Graaff, R. Lacerda, and Z. Campeau, "Degradation mechanisms in Si module technologies observed in the field; their analysis and statistics," in *Proceedings of the NREL Photovoltaic Module Reliability Workshop*, Golden, Colo, USA, February 2011.
- [14] P. Basnyat, B. Sopori, S. Devayajanam et al., "Experimental study to separate surface and bulk contributions of light-induced degradation in crystalline silicon solar cells," *Emerging Materials Research*, vol. 4, no. 2, pp. 239–246, 2015.
- [15] C. Algora, "Reliability of III-V concentrator solar cells," *Microelectronics Reliability*, vol. 50, no. 9–11, pp. 1193–1198, 2010.
- [16] D. T. Cotfas, P. A. Cotfas, D. Floroian, L. Floroian, and M. Cernat, "Ageing of photovoltaic cells under concentrated light," in *Proceedings of the 2015 Intl Aegean Conference on Electrical Machines & Power Electronics (ACEMP '15) and Intl Conference on Optimization of Electrical & Electronic Equipment (OPTIM) & 2015 Intl Symposium on Advanced Electromechanical Motion Systems (ELECTROMOTION '15)*, Side, Turkey, September 2015.
- [17] J. Petrasch, P. Coray, A. Meier et al., "A novel 50 kW 11,000 suns high-flux solar simulator based on an array of xenon arc lamps," *ASME Journal of Solar Energy Engineering*, vol. 129, no. 4, pp. 405–411, 2007.
- [18] I. Alkneit and H. Schmit, "Spectral characterization of PSI's high-flux solar simulator," *Journal of Solar Energy Engineering*, vol. 134, no. 1, Article ID 011013, 2012.
- [19] M. Toivola, J. Halme, L. Peltokorpi, and P. Lund, "Investigation of temperature and aging effects in nanostructured dye solar cells studied by electrochemical impedance spectroscopy," *International Journal of Photoenergy*, vol. 2009, Article ID 786429, 15 pages, 2009.
- [20] D. T. Cotfas, P. A. Cotfas, and S. Kaplanis, "Methods and techniques to determine the dynamic parameters of solar cells: review," *Renewable and Sustainable Energy Reviews*, vol. 61, pp. 213–221, 2016.

Research Article

Investigation of Boron Thermal Diffusion from Atmospheric Pressure Chemical Vapor Deposited Boron Silicate Glass for N-Type Solar Cell Process Application

Ikuo Kurachi¹ and Kentaro Yoshioka²

¹*D&S Inc., Tokyo 193-0834, Japan*

²*AMAYA Co., Ltd., Saitama 343-0822, Japan*

Correspondence should be addressed to Ikuo Kurachi; i_kurachi@mtg.biglobe.ne.jp

Received 9 April 2016; Accepted 7 June 2016

Academic Editor: Prakash Basnyat

Copyright © 2016 I. Kurachi and K. Yoshioka. This is an open access article distributed under the Creative Commons Attribution License, which permits unrestricted use, distribution, and reproduction in any medium, provided the original work is properly cited.

An atmospheric pressure chemical vapor deposition (AP-CVD) system has been newly developed for boron silicate glass (BSG) film deposition dedicating to solar cell manufacturing. Using the system, thermal boron diffusion from the BSG film is investigated and confirmed in terms of process stability for surface property before BSG deposition and BSG thickness. No degradation in carrier lifetime is also confirmed. A boron diffusion simulator has been newly developed and demonstrated for optimization of this process. Then, the boron thermal diffusion from AP-CVD BSG is considered to be the suitable method for N-type silicon solar cell manufacturing.

1. Introduction

In development of advanced solar cell, improvement of efficiency and reliability with maintaining low manufacturing cost is one of crucial issues. To achieve the high efficiency and reliability, the N-type silicon solar cell is the most likely candidate although the P-type silicon solar cell is now industrial standard [1, 2]. Indeed, the P-type silicon cell has a reliability problem which is efficiency degradation due to light illumination, which is called light induced degradation (LID) caused by formation of boron and interstitial oxygen pairs [3–5]. On the other hand, the N-type silicon cell which uses the phosphorus doped silicon wafer has no such LID and higher immunity to metallic contaminations comparing to the P-type silicon cell [6]. In order to manufacture the N-type silicon cell, a P⁺ diffusion layer which is usually a boron doped layer has to be formed. Thus, many boron diffusion processes have been proposed and used to fabricate the N-type silicon solar cell. Open-tube liquid source diffusion of BBr₃ [7, 8] must be a common industrial standard process but the number of process steps increases because of diffusion protection film formation on the opposite side. Ion

implantation is the most advanced process and has precise controllability of the dopants [9]. However, crystal defects are induced by the implantation and thermal annealing after the implantation required for recovering of the crystal defects. In addition, low throughput of the implantation is also one of the problems. On the other hand, boron thermal diffusion from a deposited boron silicate glass (BSG) film is a simple and well matured method [10–12]. Particularly, the BSG film deposition using atmospheric pressure chemical vapor deposition (AP-CVD) is a cost-effective process because of the simple machine composition. In this paper, characteristic stability for process variation of the boron thermal diffusion from the BSG film deposited by newly developed AP-CVD system has been investigated. For optimization of the process, boron diffusion simulator has been developed and demonstrated for prediction of the solar cell performance.

2. Experimental Procedure

Czochralski- (CZ-) grown n-type (100)-oriented silicon wafers were used as starting materials. The dopant of silicon

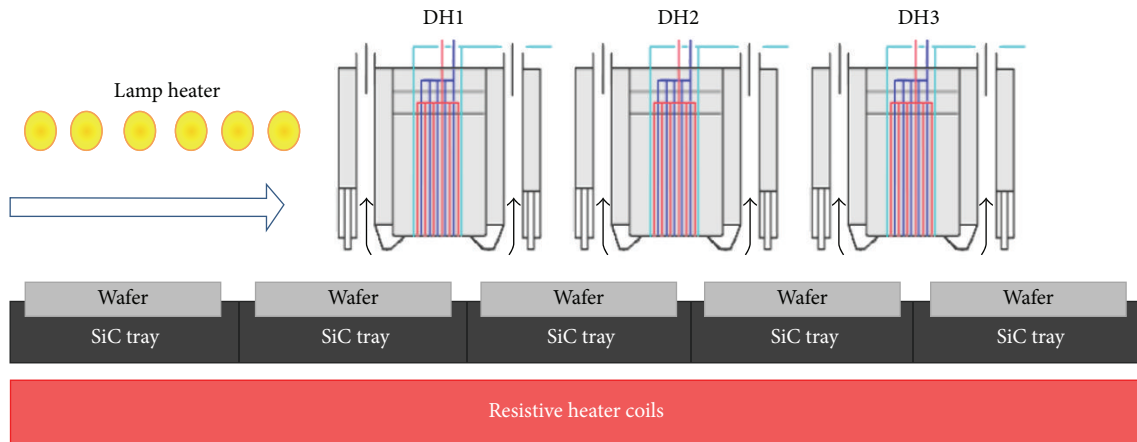


FIGURE 1: A schematic of newly developed AP-CVD system. Deposited wafers are carried by SiC trays underneath the multideposition gas dispersion heads (DH1–3). The wafers are also heated by resistive heater coils and lamp heaters at the predeposition zone.

wafer is phosphorus with 6–9 ohm cm in resistivity. The wafer thickness is 675 μm for the boron diffusion experiments. We compared the boron diffusion profiles between 675 μm and 180 μm thick wafers which are usually used in solar cell manufacturing but no difference was observed in the boron diffusion profiles. For the other experiments such as lifetime measurements, the 180 μm thick wafers were used. Prior to a BSG film deposition, the wafers were cleaned by diluted hydrofluoric acid (DHF) to remove native oxide on the wafers. To study the variation of diffusion process, some wafers were dipped in $\text{HCl}/\text{H}_2\text{O}_2$ solution after the DHF cleaning to make chemical oxide on the wafer surface. The wafers with a 5 nm CVD oxide film on the surface were also prepared. The BSG film was deposited by the AP-CVD system with $\text{SiH}_4/\text{O}_2/\text{B}_2\text{H}_6$ gases at 430°C. The BSG film thickness and boron concentration were varied from 40 to 80 nm by controlling tray speed and 1.19×10^{21} to $1.37 \times 10^{22} \text{ cm}^{-3}$ by controlling gas flow ratio of B_2H_6 to SiH_4 , respectively. A 50 nm undoped silicate glass (USG) film was also deposited on the BSG film to prevent out-diffusion of boron during the subsequent thermal diffusion. The thermal diffusion was performed by furnace annealing in N_2 ambient with varying time from 20 to 60 min and temperature from 900 to 1050°C. The stand-by temperature of the furnace was 800°C and ramping up and down rates are 10 and 3°C/min, respectively. After the diffusion, USG and BSG films were removed using DHF solution for sheet resistance and boron depth profile measurements. To inspect the generation of boron-rich layer (BRL), wafer surface property that was hydrophobic or hydrophilic was examined during this process. The sheet resistance of diffused layer was measured by conventional four-terminal measurement. The boron depth profiles were measured by secondary ion mass spectroscopy (SIMS) using O_2 as primary ions.

3. AP-CVD BSG Deposition System

The newly developed AP-CVD BSG deposition system consists of multigas dispersion heads (DH1, DH2, and DH3), SiC trays, resistive heaters, and predeposition lamp heaters

as shown schematically in Figure 1 [13]. To deposit the BSG film, thermal decomposition of SiH_4 , O_2 , and B_2H_6 gases is used. These gases are delivered through the dispersion heads to the wafer surface. The wafers are automatically loaded and unloaded from the wafer carriers to the SiC trays. The wafers are heated by the resistive heaters. The resistive heaters are covered with quartz glass underneath the SiC trays. The SiC trays move from the wafer loading portion to the unloading portion and carry the wafers through the oxide deposition zones under the dispersion heads. The predeposition heaters prevent wafer bending especially for thin wafers. We set the important factors of system development for the solar cell manufacturing which are (i) boron concentration uniformity within a wafer and between wafers, (ii) suppression of metallic contamination, and (iii) better Cost of Ownership (CoO). Owing to the dispersion heads designed by a process simulation, good sheet resistance uniformity within 10% after the thermal diffusion is realized as shown in Figure 2. Because the wafers contact only with the trays, the SiC trays prevent metallic contamination during the process. Previous AP-CVD tools commonly use Inconel mesh belts to transfer wafers underneath the deposition head zone which means that there is possibility of metallic contaminations such as Nickel, Iron, and Chrome in the wafers. The metallic contamination in the wafers makes the problems of solar cell performance degradation. Less footprint and simple machine composition with no vacuum system is feasible for better CoO. In addition, because of the multihead concept, a stacked film such as undoped silicate glass (USG)/BSG is easily deposited by one path. The oxide is deposited only on the surface of wafers, which is suitable for the codiffusion process [14–16] and the manufacturing cost reduction. In this process, deposited BSG film thickness and boron concentration have to be controlled. The deposited film thickness can be controlled by the tray speed as well as the deposition temperature and the SiH_4/O_2 gas flow rate. The BSG boron concentration is controlled by the gas flow ratio of B_2H_6 to SiH_4 . The relation between the gas flow ratio and the BSG boron concentration which was measured by SIMS is shown in Figure 3.

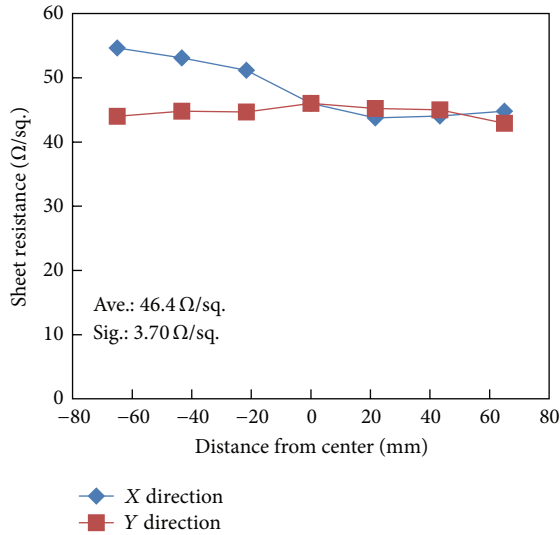


FIGURE 2: Sheet resistance uniformity within a wafer after diffusion. BSG boron concentration is $6.72 \times 10^{21} \text{ cm}^{-3}$. Diffusion was performed at 950°C for 20 min. The BSG film was deposited on a $156 \times 156 \text{ mm}^2$ pseudo square silicon wafer.

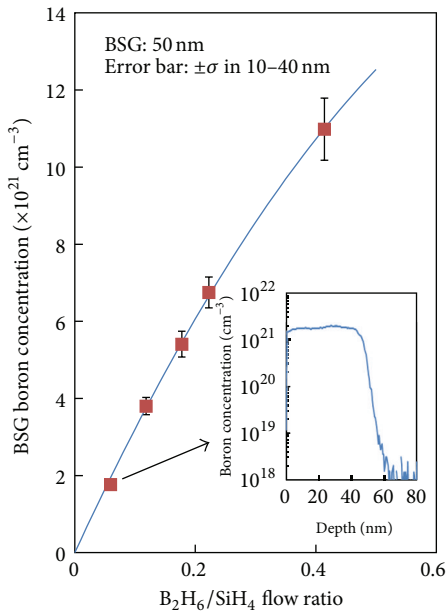


FIGURE 3: BSG boron concentration measured by SIMS as a function of flow ratio of B_2H_6 to SiH_4 . The inset graph shows the boron concentration profile in BSG measured by SIMS as an example. The BSG boron concentration can be varied by changing the gas flow ratio of B_2H_6 to SiH_4 .

4. Results and Discussion

4.1. Effect of Native Oxide Underneath BSG for Boron Diffusion. With consideration of the stable boron diffusion layer formation, queue time control between precleaning and BSG deposition is one of the key manufacturing parameters. When the queue time is long, the native oxide must be formed on the silicon surface. Thus, there is a possibility to alternate

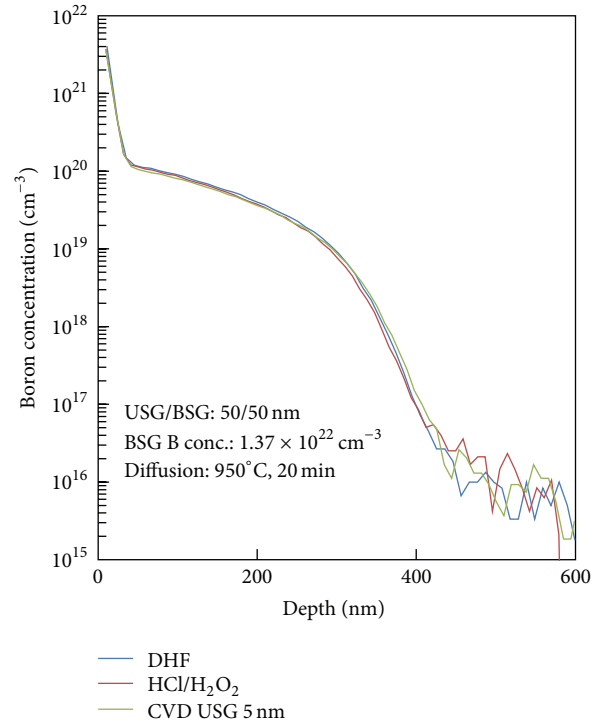


FIGURE 4: Boron profiles for the sample with DHF preclean (blue line), $\text{HCl}/\text{H}_2\text{O}_2$ preclean (red line), and CVD USG 5 nm on the silicon surface (green line). In the case of HF preclean, there must be no oxide between BSG and silicon. In the case of $\text{HCl}/\text{H}_2\text{O}_2$ preclean, around 1-2 nm chemical oxide exists between BSG and silicon. Even though the chemical or 5 nm CVD oxide exists, the profiles are identical to no oxide case.

the boron diffusion profiles due to existence of the native oxide. We have investigated the boron profiles after the thermal diffusion by SIMS when there is no oxide, chemical oxide, or CVD oxide between the BSG film and the silicon surface. The precleaning by DHF just before the BSG deposition was used to obtain the “no oxide” sample. To make chemical oxide on the surface, $\text{HCl}/\text{H}_2\text{O}_2$ precleaning was used and the thickness of the chemical oxide was estimated to be 1-2 nm. The sample with a 5 nm CVD oxide film on the surface was also prepared. After these surface treatments, a 50 nm BSG film was deposited. The boron diffusion profiles for these samples annealed for 20 min at 950°C are shown in Figure 4. As shown in the figure, the profiles are almost identical. It can be concluded that such chemical or CVD oxide film does not affect boron diffusion from BSG. Thus, this process has enough stability for the queue time control between the precleaning and the BSG deposition which is a superior point for the production control.

4.2. Effect of BSG Thickness for Boron Diffusion. During the thermal boron diffusion, the BSG film should work as an infinite boron diffusion source. To confirm this, 40 nm or 80 nm BSG deposited wafers were prepared and annealed for 20 min at 950°C . The thickness of 40 nm is the thinnest for the stable BSG film deposition with consideration of incubation time

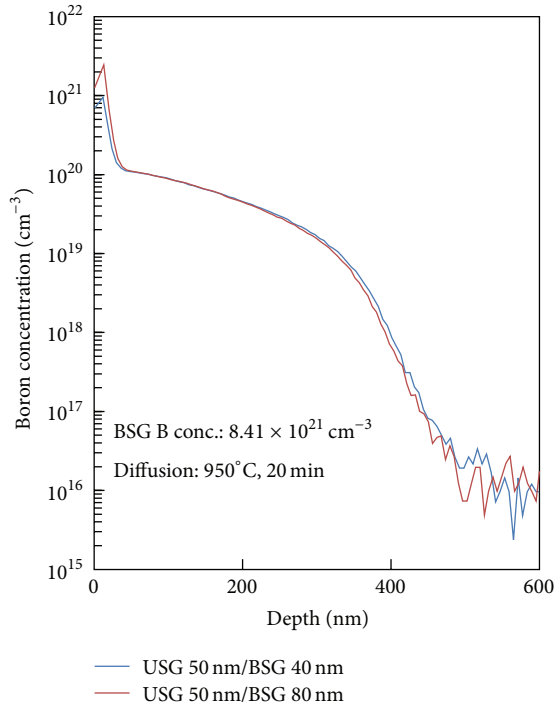


FIGURE 5: Boron profiles for USG 50 nm/BSG 40 nm (blue line) and USG 50 nm/BSG 80 nm (red line). For both cases, the profiles are almost identical.

control. The BSG boron concentration of both samples is $8.41 \times 10^{21} \text{ cm}^{-3}$. The boron profiles after the diffusion are shown in Figure 5. There is no difference in the boron profiles. The BSG thickness of 40 nm is confirmed to be enough to make the infinite diffusion source of boron in this diffusion condition. Furthermore, no thickness dependence in the diffusion profile is another superior point for the production control.

4.3. BSG Boron Concentration Dependency. In this process, the P^+ layer sheet resistance can be controlled by changing the BSG boron concentration and/or thermal diffusion conditions such as temperature and time. Figure 6 shows the P^+ sheet resistance as a function of the BSG boron concentration with the different diffusion temperatures. The diffusion time was fixed at 20 min. As shown in this figure, the sheet resistance decreases with the BSG boron concentration up to certain BSG boron concentrations and then slightly increases. From this minimum sheet resistance point, BRL is starting to form at the surface. With the BSG boron concentration increasing, the surface boron concentration also increases. When the surface concentration reaches the solid solubility limit, BRL is formed on the surface of silicon. Because BRL consists of silicon borides, the crystal structure changes. Thus, BRL existence on the surface affects boron diffusion as described in [17]. To manipulate and predict the boron diffusion profile, a simulator to calculate the boron profile after the diffusion is indispensable because the diffusion mechanism is quite complicated [18, 19]. Then, we have made the boron diffusion simulator by solving diffusion equation

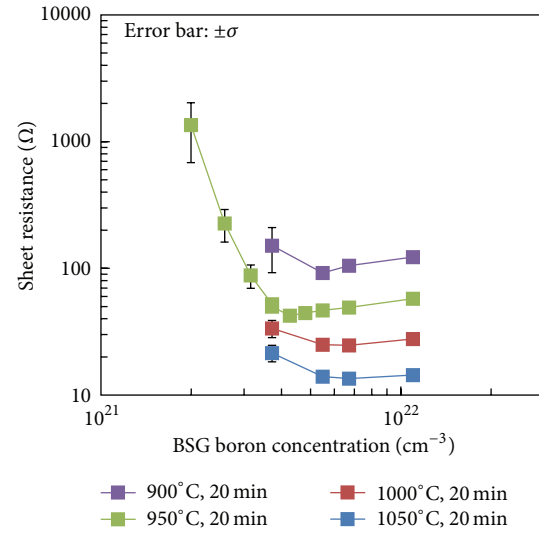


FIGURE 6: Sheet resistance dependence on BSG boron concentration as a parameter of diffusion temperatures. The sheet resistance can be controlled by the BSG boron concentration and diffusion conditions such as temperature and time. BRL is formed when the BSG concentration is higher than the concentration at the minimum sheet resistance.

numerically and the boron diffusion model of this simulation will be explained in the next section.

4.4. Carrier Lifetime after Boron Diffusion. Another important issue to apply the process to solar cell manufacturing is the effect on the carrier lifetime. It is reported that the open-tube liquid source BBr_3 diffusion induces the crystal defects and the carrier lifetime degradation due to the formation of BRL at the surface [7, 20]. On the contrary, it is also reported that the formation of BRL improves the lifetime owing to metallic impurity gettering of BRL [21]. To investigate the effect on the lifetime using this process and existence of BRL on the surface, the BSG films were deposited on both sides of 156 mm square $180 \mu\text{m}$ thick silicon wafers with two different boron concentrations, $3.72 \times 10^{21} \text{ cm}^{-3}$ and $6.72 \times 10^{21} \text{ cm}^{-3}$, which are without and with BRL after the diffusion, respectively. In addition, both side USG deposited Si wafers are also prepared as references. The carrier lifetimes after diffusion at different temperatures for 20 min are measured by microwave photoconductive decay (μ -PCD). Before the measurements, the P^+ diffusion layers were etched off by a mixed solution of HNO_3 and HF. After RCA precleaning, the surfaces of wafers were chemically passivated by iodine to reduce the effect of surface recombination in the lifetime measurements. The lifetime was measured on area of whole wafer and averaged values were used. The results are shown in Figure 7 including the lifetime of a starting Si wafer without annealing. In the case of no existence of BRL on the surface ($3.72 \times 10^{21} \text{ cm}^{-3}$), the lifetimes decrease with the diffusion temperature. The lifetimes are, however, almost the same as those of the USG deposited samples. This means that the decrease of lifetimes is not due to the boron diffusion. When BRL is formed on the

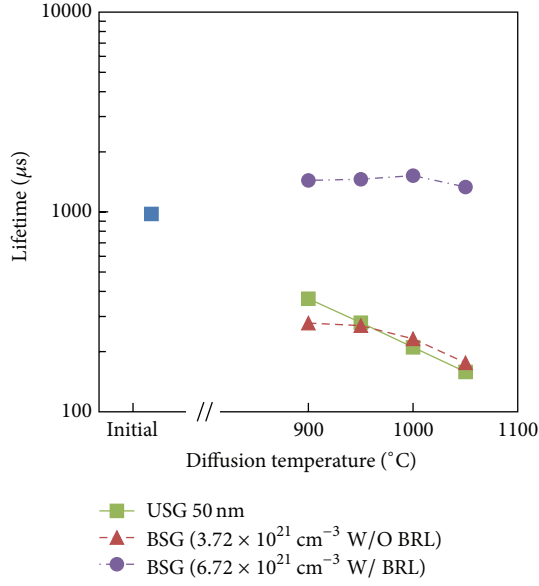


FIGURE 7: Carrier lifetimes as a function of diffusion temperature. The lifetimes of low BSG boron concentration decrease with diffusion temperature but almost the same as that of USG deposited samples. The lifetimes of samples with BRL are higher than that of the initial silicon wafer.

surface ($6.72 \times 10^{21} \text{ cm}^{-3}$), the lifetimes are more than 1 ms which is higher than that for the initial Si wafer. From this result, the gettering effect by BRL is confirmed in this process. It is also concluded that the thermal boron diffusion from AP-CVD BSG does not affect the carrier lifetime. This process was also applied to N-type silicon solar cell fabrication instead of BBr_3 diffusion. We got 19.35% in efficiency using this process with comparing to 19.13% for the BBr_3 diffusion. This result also supports that the boron diffusion from AP-CVD BSG does not induce any crystal defect.

5. Boron Diffusion Profile Prediction Simulator

The boron thermal diffusion simulator called DADiS (D&S AMAYA Diffusion Simulator) has been newly developed to predict the diffusion profile using process parameters which are the BSG boron concentration, the thermal diffusion temperature profile including stand-by temperature, ramping up and down rate, and diffusion temperature and time. In this simulator, the diffusion equation,

$$\frac{\partial c}{\partial t} = \frac{\partial}{\partial x} \left(D \frac{\partial c}{\partial x} \right), \quad (1)$$

where c is the boron concentration in silicon, D is the diffusivity of boron in silicon, x is the depth from the surface, and t is the diffusion time, is solved numerically with the constant surface boron concentration because the BSG film is the finite boron diffusion source. The important factor

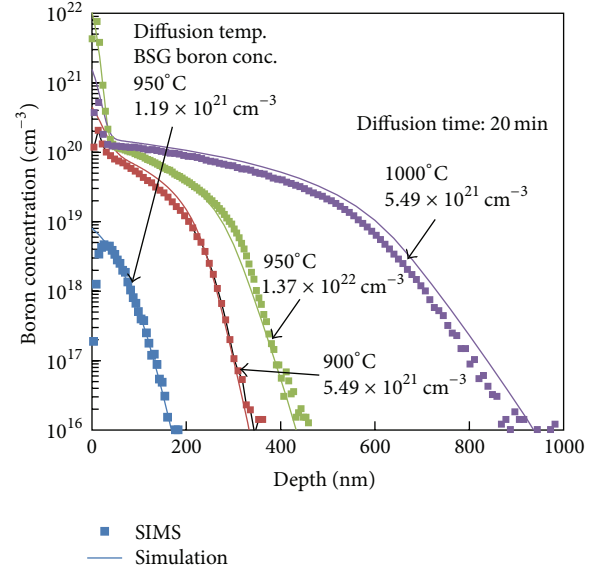


FIGURE 8: Examples of comparison between measured and simulated boron profiles after diffusion by DADiS. The simulated profiles including surface BRL area agree well with the measured profiles for wide range of the BSG boron concentrations and diffusion temperatures.

to predict the profile is the accurate diffusivity model. The diffusivity model in this simulator is used as

$$D = D_i \frac{c}{2n_i} \left(1 + \sqrt{1 + 4 \frac{n_i^2}{c^2}} \right), \quad (2)$$

where D_i is the intrinsic diffusivity showing BSG boron concentration dependence and n_i is the intrinsic carrier concentration at the diffusion temperature [22]. The intrinsic diffusivity has temperature dependence with the activation energy E_a as

$$D_i = D_{i,\text{ref}} \exp \left[\frac{-E_a}{k} \left(\frac{1}{T} - \frac{1}{T_{\text{ref}}} \right) \right], \quad (3)$$

where k is the Boltzmann constant, T is the diffusion temperature, and $D_{i,\text{ref}}$ is the intrinsic diffusivity at the reference temperature T_{ref} . To extract the diffusion activation energy, E_a , boron profiles of different diffusion temperatures are used. After the extraction of E_a , the $D_{i,\text{ref}}$ dependence on BSG boron concentration is empirically modeled based on the boron profiles of different BSG boron concentration samples. The surface boron concentration equations as a function of the BSG boron concentration were also modeled. The boron profile in BRL is assumed to be a complimentary error function with fitting parameters. Detail explanation of the model is found in [23]. Examples of comparison between measured and DADiS simulated boron profiles are shown in Figure 8. Figure 9 shows the errors of DADiS in depth to measured values at given boron concentrations. The errors are almost within 15% for the ranges of 1.18 to $13.69 \times 10^{21} \text{ cm}^{-3}$ in the BSG boron concentration, 900 to 1050°C in

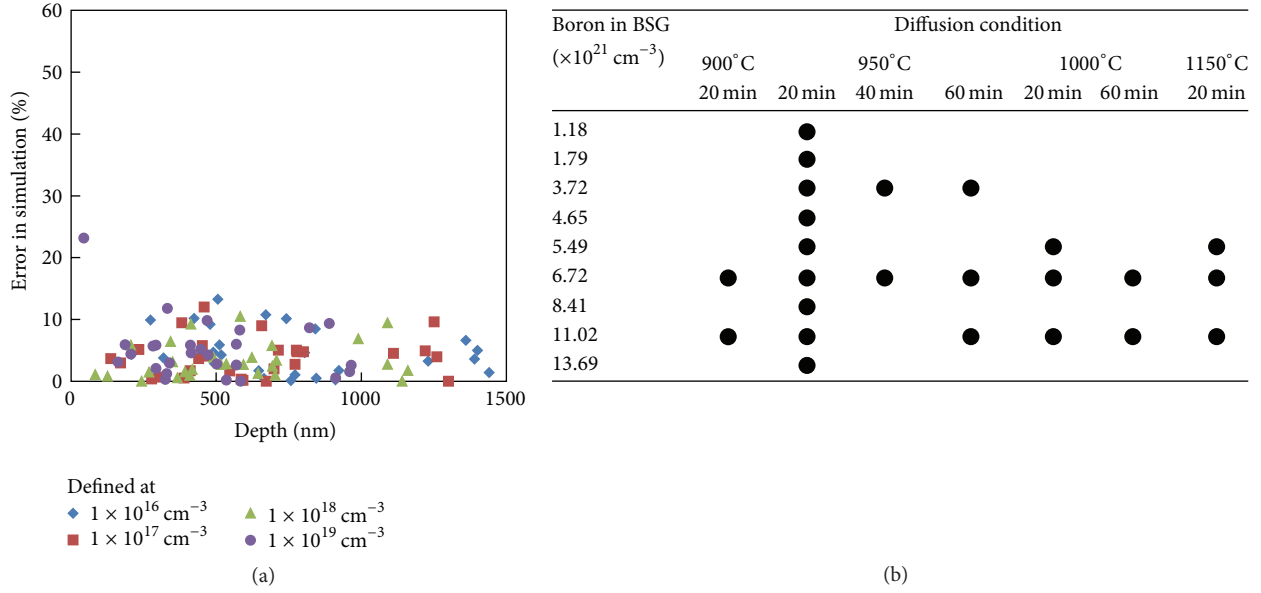


FIGURE 9: (a) Simulation error in depth at the same boron concentration. (b) is a list of examined BSG boron concentration, diffusion temperature, and time. Even though wide range of the conditions was used, the error is almost within 15%. It is confirmed that the simulator DADiS is accurate and useful for the boron diffusion analysis.

the diffusion temperature, and 20 to 60 min in the diffusion time which are covered commonly used process conditions. Another important prediction by the simulator is the sheet resistance after the diffusion because the sheet resistance is commonly used for monitoring of the boron diffusion in the solar cell manufacturing. When the boron diffusion profile is known, the sheet resistance R_s is given as

$$R_s = \frac{1}{q\mu N_{\text{boron}}} = \frac{1}{q\mu \int_0^{\infty} c dx}, \quad (4)$$

where q is the elementary electric charge, μ is the mobility of holes, and N_{boron} is the number of boron atoms in the diffusion layer [24]. It is well known that the mobility has impurity concentration dependence and is empirically given as

$$\mu = \alpha_1 - \alpha_2 \ln(c), \quad (5)$$

where α_1 and α_2 are the fitting parameters [25]. Using the boron profile calculated by DADiS, (4), and (5), R_s can be predicted when the BSG boron concentration and the diffusion conditions are known. Figure 10 shows the comparison between measured and simulated R_s by DADiS [26]. The simulated R_s agrees well with the measured R_s for a wide range of 30 to 2000 $\Omega/\text{sq.}$ and the error in resistance is within 20%. The boron profiles and sheet resistance after the thermal diffusion are accurately predicted by DADiS with conditions of the BSG boron concentration and thermal diffusion temperature profiles. Owing to the accuracy of DADiS, the optimization of diffusion process can be achieved with less experiment [27].

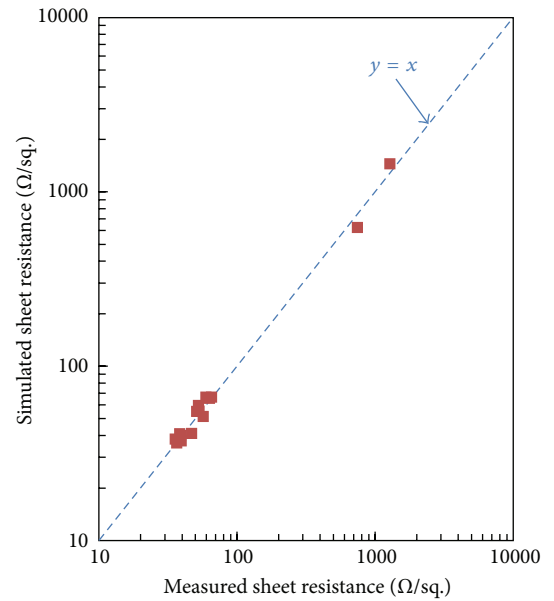


FIGURE 10: Comparison between measured and DADiS simulated sheet resistance. The error of simulation in the sheet resistance is within 20%.

6. TCAD Simulation for Prediction of Solar Cell Characteristics

Using DADiS and well-known solar cell simulator, PCID [28], the solar cell characteristics such as J_{sc} , V_{oc} , and efficiency can be easily simulated as a function of the BSG boron concentration or diffusion conditions. The boron diffusion profiles calculated by DADiS can be used as input files of

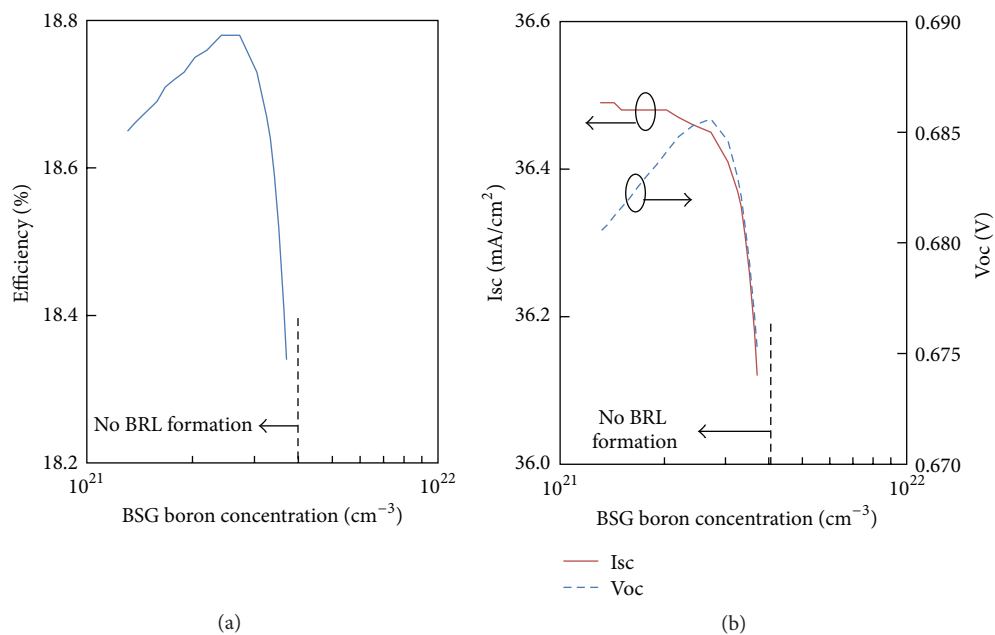


FIGURE 11: Simulated (a) efficiency, (b) short circuit current, and open circuit voltage using PCID with DADiS as a function of BSG boron concentration. The evaluated BSG boron concentration range is lower than $4 \times 10^{21} \text{ cm}^{-3}$ and no BRL is formed. The maximum point in efficiency is observed at around $3 \times 10^{21} \text{ cm}^{-3}$.

PCID to simulate the solar cell characteristics. This method, which is so called technology computer aided design (TCAD) for the solar cell, reduces the development time and cost. For example, the optimized condition of the BSG boron concentration must exist for the solar cell efficiency. The simulation results using DADiS and PCID are shown in Figure 11. We can find out the optimized condition as shown in the figure. It is indicated that the TCAD simulation can accelerate solar cell development speed and reduce developing cost greatly.

7. Conclusion

The AP-CVD system to deposit the BSG films has been newly developed for boron diffusion layer formation in the N-type silicon solar cell manufacturing. This system has good performance for manufacturing with less CoO. Using this system, the process stability of thermal boron diffusion is investigated. It is found that the boron diffusion profiles are almost identical even though there is 5 nm CVD oxide between the BSG film and silicon or BSG thickness is changed from 40 nm to 80 nm, which indicates stable productivity by the system. The boron diffusion profiles can be manipulated by the BSG boron concentration or thermal diffusion conditions such as diffusion temperature and time. It is also confirmed that this process does not affect carrier lifetime. Because the boron diffusion mechanism is complicated, the boron diffusion profile prediction simulator, DADiS, has been developed and demonstrated for the optimization of BSG boron concentration with PCID. It is concluded that the P⁺ diffusion layer formation by thermal boron diffusion from AP-CVD BSG is the suitable method for the N-type silicon solar cell manufacturing.

Competing Interests

The authors declare that they have no competing interests.

References

- [1] Y. Wan, C. Samundsett, T. Kho et al., "Towards industrial advanced front-junction n-type silicon solar cells," in *Proceedings of the 40th IEEE Photovoltaic Specialist Conference (PVSC '14)*, pp. 862–865, Denver, Colo, USA, June 2014.
- [2] J. Benick, B. Steinhauser, R. Muller et al., "High efficiency n-type PERT and PERL solar cells," in *Proceedings of the 40th IEEE Photovoltaic Specialist Conference (PVSC '14)*, pp. 3637–3640, Denver, Colo, USA, June 2014.
- [3] J. Schmidt, A. G. Aberle, and R. Hezel, "Investigation of carrier lifetime instabilities in CZ-grown silicon," in *Proceedings of the 26th IEEE Photovoltaic Specialists Conference (PVSC '97)*, pp. 13–18, Anaheim, Calif, USA, October 1997.
- [4] S. W. Glunz, S. Rein, J. Y. Lee, and W. Warta, "Minority carrier lifetime degradation in boron-doped Czochralski silicon," *Journal of Applied Physics*, vol. 90, no. 5, pp. 2397–2404, 2001.
- [5] P. Basnyat, B. Sopori, S. Devayajanam et al., "Experimental study to separate surface and bulk contributions of light-induced degradation in crystalline silicon solar cells," *Emerging Materials Research*, vol. 4, no. 2, pp. 239–246, 2015.
- [6] D. Macdonald and L. J. Geerligs, "Recombination activity of interstitial iron and other transition metal point defects in p- and n-type crystalline silicon," *Applied Physics Letters*, vol. 85, no. 18, pp. 4061–4063, 2004.
- [7] M. A. Kessler, T. Ohrdes, B. Wolpensinger, R. Bock, and N.-P. Harder, "Characterisation and implications of the boron rich layer resulting from open-tube liquid source BBR3 boron

- diffusion processes,” in *Proceedings of the 34th IEEE Photovoltaic Specialists Conference (PVSC '09)*, pp. 1556–1561, IEEE, Philadelphia, Pa, USA, June 2009.
- [8] F. Kiefer, C. Ulzhöfer, T. Brendemühl et al., “High efficiency n-type emitter-wrap-through silicon solar cells,” *IEEE Journal of Photovoltaics*, vol. 1, no. 1, pp. 49–53, 2011.
- [9] D. L. Meier, V. Chandrasekaran, H. P. Davis et al., “N-type, ion-implanted silicon solar cells and modules,” *IEEE Journal of Photovoltaics*, vol. 1, no. 2, pp. 123–129, 2011.
- [10] K. M. Whittle and G. L. Vick, “Control of boron diffusion from a pyrolitic borosilicate glass source,” *Journal of the Electrochemical Society*, vol. 116, no. 5, pp. 645–648, 1969.
- [11] B. Bazer-Bachi, C. Oliver, B. Semmache et al., “Co-diffusion from boron doped oxide and POCl₃,” in *Proceedings of the 26th European Photovoltaic Solar Energy Conference and Exhibition*, pp. 1155–1159, Hamburg, Germany, 2011.
- [12] K. O. Davis, *Atmospheric pressure chemical vapor deposition of functional oxide materials for crystalline silicon solar cells [Ph.D. thesis]*, University of Central Florida, Orlando, Fla, USA, 2015.
- [13] <http://www.amaya-cvd.co.jp/en/prod/amax1000s.html>.
- [14] P. Rothhardt, T. Stoffels, R. Keding, U. Belledin, A. Wolf, and D. Biro, “Control of phosphorus doping for co-diffusion processes,” in *Proceedings of the 27th European Photovoltaic Solar Energy Conference and Exhibition*, pp. 1917–1920, Frankfurt, Germany, 2012.
- [15] P. Rothhardt, S. Meier, S. Maier, K. Jiang, A. Wolf, and D. Biro, “Characterization of POCl₃-based codiffusion processes for bifacial N-type solar cells,” *IEEE Journal of Photovoltaics*, vol. 4, no. 3, pp. 827–833, 2014.
- [16] S. P. Phang and D. Macdonald, “Effect of boron codoping and phosphorus concentration on phosphorus diffusion gettering,” *IEEE Journal of Photovoltaics*, vol. 4, no. 1, pp. 64–69, 2014.
- [17] I. Kurachi and K. Yoshioka, “Analytical boron diffusivity model in silicon for thermal diffusion from boron silicate glass film,” *Japanese Journal of Applied Physics*, vol. 54, no. 9, Article ID 096502, 2015.
- [18] I. Kurachi and K. Yoshioka, “Investigation of boron solid-phase diffusion from BSG film deposited by AP-CVD for solar cell application,” in *Proceedings of the 27th European Photovoltaic Solar Energy Conference and Exhibition*, pp. 1873–1876, Frankfurt, Germany, 2012.
- [19] I. Kurachi and K. Yoshioka, “Enhancement and retardation of thermal boron diffusion in silicon from atmospheric pressure chemical vapor deposited boron silicate glass film,” *Japanese Journal of Applied Physics*, vol. 53, no. 3, Article ID 036504, 2014.
- [20] P. J. Cousins and J. E. Cotter, “The influence of diffusion-induced dislocations on high efficiency silicon solar cells,” *IEEE Transactions on Electron Devices*, vol. 53, no. 3, pp. 457–464, 2006.
- [21] S. P. Phang, W. Liang, B. Wolpensinger, M. A. Kessler, and D. Macdonald, “Tradeoffs between impurity gettering, bulk degradation, and surface passivation of boron-rich layers on silicon solar cells,” *IEEE Journal of Photovoltaics*, vol. 3, no. 1, pp. 261–266, 2013.
- [22] M. Miyake, “Diffusion of boron into silicon from borosilicate glass using rapid thermal processing,” *Journal of the Electrochemical Society*, vol. 138, no. 10, pp. 3031–3039, 1991.
- [23] I. Kurachi and K. Yoshioka, “An accurate analytical model of boron diffusion from AP-CVD BSG for solar cell process optimization,” in *Proceedings of the 28th European Photovoltaic Solar Energy Conference and Exhibition*, pp. 1085–1089, Paris, France, 2013.
- [24] S. M. Sze, *Physics of Semiconductor Devices*, John Wiley & Sons, New York, NY, USA, 2nd edition, 1981.
- [25] S. C. Sun and J. D. Plummer, “Electron mobility in inversion and accumulation layers on thermally oxidized silicon surfaces,” *IEEE Transactions on Electron Devices*, vol. 27, no. 8, pp. 1497–1508, 1980.
- [26] I. Kurachi and K. Yoshioka, “Boron diffusion profile estimation using measured sheet resistance for T-CAD solar cell simulation,” in *Proceedings of the 29th European Photovoltaic Solar Energy Conference and Exhibition*, pp. 855–858, Amsterdam, The Netherlands, 2014.
- [27] A. Harada, K. Nakamura, I. Kurachi, K. Yoshioka, N. Ikeno, and A. Ogura, “Emitter layer design by thermal diffusion process for N-type crystalline silicon solar cells,” in *Proceedings of the 29th European Photovoltaic Solar Energy Conference and Exhibition*, pp. 900–903, Amsterdam, The Netherlands, 2014.
- [28] D. A. Clugston and P. A. Basore, “PCID version 5: 32-bit solar cell modeling on personal computers,” in *Proceedings of the 26th IEEE Photovoltaic Specialists Conference*, pp. 207–210, IEEE, Anaheim, Calif, USA, October 1997.

Research Article

Data-Driven Photovoltaic System Modeling Based on Nonlinear System Identification

Ayedh Alqahtani,¹ Mohammad Alsaffar,² Mohamed El-Sayed,² and Bader Alajmi¹

¹Electrical Engineering Department, Public Authority for Applied Education & Training (PAAET), 42325 Kuwait, Kuwait

²Electrical Engineering Department, Kuwait University, 42325 Kuwait, Kuwait

Correspondence should be addressed to Ayedh Alqahtani; a.alqahtani@paaet.edu.kw

Received 11 March 2016; Revised 6 June 2016; Accepted 14 June 2016

Academic Editor: Prakash Basnyat

Copyright © 2016 Ayedh Alqahtani et al. This is an open access article distributed under the Creative Commons Attribution License, which permits unrestricted use, distribution, and reproduction in any medium, provided the original work is properly cited.

Solar photovoltaic (PV) energy sources are rapidly gaining potential growth and popularity compared to conventional fossil fuel sources. As the merging of PV systems with existing power sources increases, reliable and accurate PV system identification is essential, to address the highly nonlinear change in PV system dynamic and operational characteristics. This paper deals with the identification of a PV system characteristic with a switch-mode power converter. Measured input-output data are collected from a real PV panel to be used for the identification. The data are divided into estimation and validation sets. The identification methodology is discussed. A Hammerstein-Wiener model is identified and selected due to its suitability to best capture the PV system dynamics, and results and discussion are provided to demonstrate the accuracy of the selected model structure.

1. Introduction

The modern power system is increasingly taking advantage of renewable energy sources entering the marketplace. Traditional central power stations with their pollution related problems will likely be replaced with cleaner and smaller power plants closer to the loads. The energy generated by the sun is one of the most promising, nonpolluting, free sources of energy [1]. Among their benefits, solar-powered systems are easily expanded. Despite their still relatively high cost, photovoltaic (PV) systems installed worldwide show a nearly exponential increase [2]. A PV cell directly converts sunlight into electricity, and the basic elementary device of PV systems is the PV cell [3]. PV systems have proven that they can generate power to very small electronic devices up to utility-scale PV power plants. The basic building block for PV systems is a PV panel consisting of a number of prewired cells in series [4]. Panels are then connected in series to increase voltage and in parallel to increase current; the product is power. A PV array is formed by series and parallel combinations of panels [5]. Figure 1 represents a generic PV array structure. The performance of a PV system is normally evaluated under the standard test condition (STC),

where an average solar spectrum at 1.5 Air Mass (AM) is used, the irradiance is normalized to 1000 W/m^2 , and the cell temperature is defined as 25°C [6]. However, under real operating conditions (i.e., varying irradiance as well as significant temperature changes), most commercial panels do not necessarily behave as in the specifications given by the manufacturers [7, 8]. In addition, PV panels perform differently according to the location, time of day, and season of the year.

For PV system, the relationship between environmental conditions and electrical output parameters (current and voltage) is highly nonlinear. For this reason, the process of modeling the dynamics of the PV system and identifying the model structure that captures real-life behavior is extremely essential for the purpose of controlling the output power. Another important purpose is to predict future performance of the system for maintenance and troubleshooting.

Modeling and simulation of PV systems have been the subject of many research studies [3, 9–12]. However, the focus of the studies was on the PV panel/array stage without including the power electronics of the complete system—that is, identifying only the nonlinear I - V characteristic of

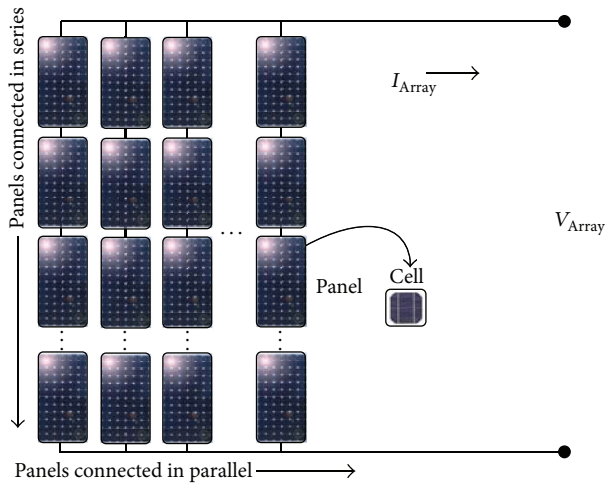


FIGURE 1: Generic PV array structure.

the PV system. In this work, the PV system identification incorporated the entire setup considering a PV system, power converter, maximum power point tracker (MPPT), and a load.

Identification of linear/nonlinear systems became a hot topic in the 1960s, probably because proper models were needed to design good controllers [13]. At this stage, the system identification field was rather immature. The first attempt to put the field into order was the published pioneering work of Eykhoff [14]. Afterward, the field became completely structured when the books of Ljung [15] and Soderstrom and Stoica [16] laid out a complete theoretical framework and practical methodology to the identification process.

The core of the system identification process is to construct a mathematical model from observed input-output data. It is widely applied in different engineering disciplines to help understand the studied process, predict the system responses, and create better design with new specifications.

This work is organized as follows. Section 2 presents a description of the studied PV system. Section 3 details the system identification methodology. Section 4 discusses the results associated with implementing the PV system identification from applied input-output data, dividing the data into estimation and validation sets. Finally, Section 5 concludes the work.

2. PV System Description

The PV system illustrated in Figure 2 is considered for this study. The PV panel performance is affected by several environmental conditions; however, irradiance has the strongest impact on the panel output power. The panel is a multipurpose module consisting of 36 polycrystalline silicon cells connected in series. Under STC, the open circuit voltage (V_{oc}) is 21.6 V, the short circuit current (I_{sc}) is 5.16 A, the maximum power voltage (V_{mp}) is 17.3 V, and the maximum power current (I_{mp}) is 4.63 A. Figure 3 presents the I - V and P - V characteristics under different irradiances. These data are obtained experimentally [17], and they are not the data

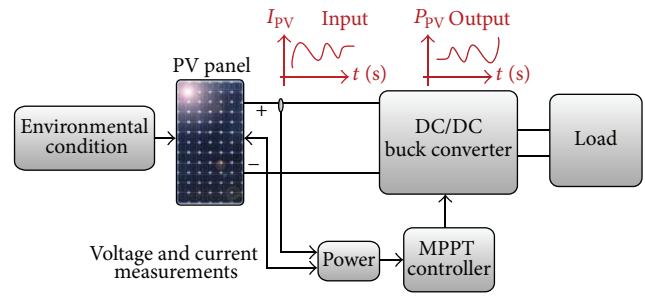
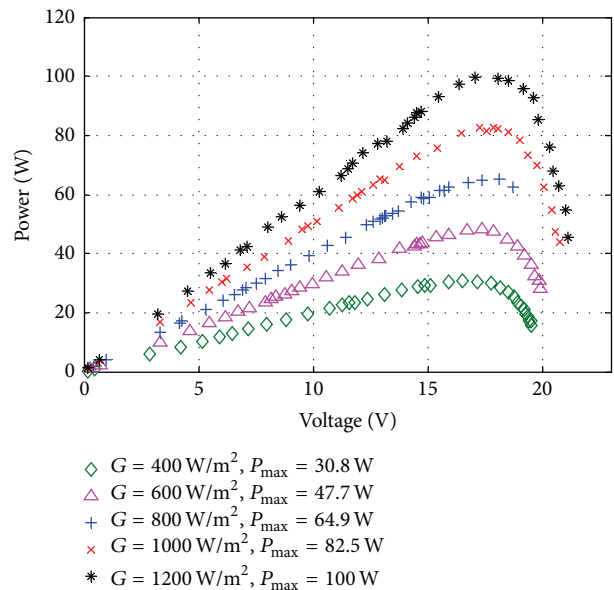
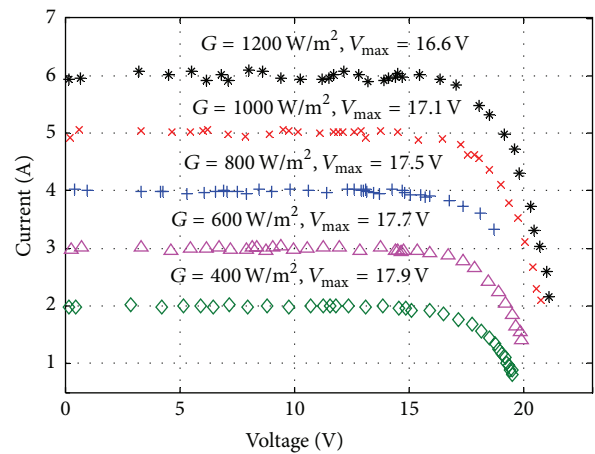


FIGURE 2: PV panel, MPPT, DC/DC buck converter, and a DC load.

FIGURE 3: I - V and P - V characteristic of the PV panel at $T = 25.15^\circ\text{C}$.

that will be used for the system identification procedure; nevertheless, prior information about the system is beneficial. What we are interested in is the current measurement as input and the power measurement as output with respect to time, as indicated in Figure 2.

The I - V and P - V characteristic curves show the standard PV panel/array behavior; as the irradiance increases, the

panel current is directly proportional to the solar intensity per unit area. Cutting the irradiance in half leads to a drop in current by half. Decreasing irradiance also reduces voltage, but it does so following a logarithmic relationship that results in a relatively modest change of voltage.

In general, the operating point of the PV panel is not the maximum power point (MPP) along the I - V curve, at which the panel operates with maximum efficiency and produces maximum power. Thus, a switch-mode power converter (DC/DC buck converter, in our case) with a MPPT is utilized to maintain the PV panel operating point at the MPP. The MPPT controller retains this operating point by controlling the PV panel's voltage or current independently of those of the load.

Depending on the application, the DC/DC converter stage could be a buck converter, boost converter, or buck-boost converter. Several MPPT control algorithms have been proposed in different publications. Perturbation and observation (P&O) or the hill climbing algorithm is the most commonly employed method in commercial PV MPPTs [18–22]. Among other control mechanisms for MPPT are fuzzy logic [23–27], neural network [28–32], and incremental conductance (IncCond) control [33–37]. The IncCond algorithm is adapted in this study because it is more convenient and lends itself well to DSP and microcontroller control.

3. Identification Methodology

In this section, the principle of system identification is described. Dynamic models depend heavily on the amount of a priori knowledge about the dynamic process that is to be incorporated. Generally, modeling any dynamical system can be categorized into two approaches: first-principle modeling and data-driven modeling.

First-principle modeling uses an understanding of the system's physics to derive a mathematical representation, whereas data-driven modeling involves using empirical data to construct a model for the system. The two approaches classify the modeling process in terms of known parameters and structure into black box, grey box, and white box modeling as suggested by Figure 4.

According to [38], white box modeling is when a model is perfectly known; it is possible to construct the model entirely from prior knowledge and physical insight. Grey box modeling is when some physical insight is available, but several parameters remain to be determined from observed data. In black box modeling, no physical insight is available or used, but the chosen model structure belongs to candidate models that are known to have good flexibility and have been successful in the past.

The black box modeling is used for this work. It is usually a trial-and-error process where one estimates the parameters of various structures and compares the results. The PV system constructed and implemented in Figure 2 is used for data collection purposes. The measured input-output data will then be utilized to select model structure and identify the system.

3.1. The PV System Identification Process. Figure 5 illustrates the measured data collected to be used for the system

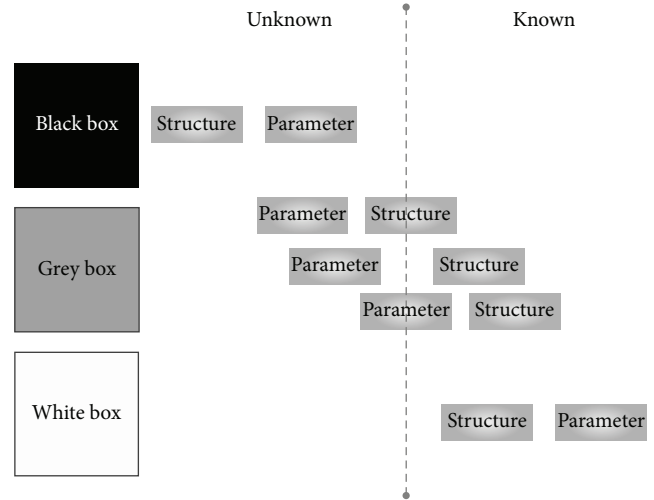


FIGURE 4: Classification of dynamical systems by model structure and parameter.

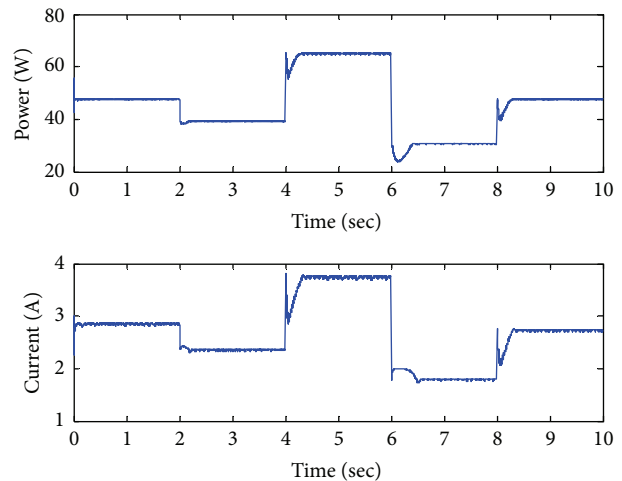


FIGURE 5: Measured input-output data for the PV system.

identification. The measured input-output data were taken from the PV system setup shown in Figure 2. When the irradiance is changing with time, the output maximum power will vary according to the maximum power values in Figure 3. The STC (1000 W/m^2) power is 82.5 W for the selected panel. The irradiance fluctuates, thereby causing the input current outputted from the panel to change. This results in continuous change of the output power of the system.

The flowchart in Figure 6 summarizes the identification process using the measured data. The input-output data are a sampled time domain signal. The next step is to select a suitable structure for the model. Selecting the model structure is the most difficult step in the identification process because there are a multitude of possibilities. Next, one can use the Matlab System Identification Toolbox and compare models to choose the model with the best performance. The final step is to evaluate the resulting model with a validation data set. It is worth mentioning that system identification

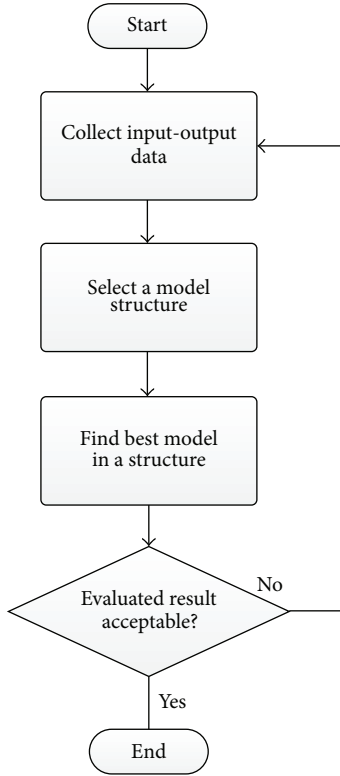


FIGURE 6: Flowchart for system identification procedure.

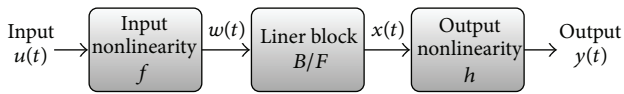


FIGURE 7: Hammerstein-Wiener nonlinear model structure.

is not a straightforward technique; rather, it is an iterative procedure involving several decisions to be made during the process.

3.2. Hammerstein-Wiener Model. A nonlinear block-oriented model is frequently applied for an adequate description of the nonlinear behavior of a system over a range of operating conditions. The identified system is generally subdivided into a linear dynamic block and a nonlinear static block. The Hammerstein-Wiener model is a nonlinear model that is used in many domains for its simplicity. The model is popular because it has convenient block representation, has a transparent relationship to linear systems, and is easier to implement than heavy-duty nonlinear models such as neural networks and Volterra models. It can be used as a black box model structure because it offers flexible parameterization for nonlinear models. The model describes a dynamical system using one or two static nonlinear blocks in series with a linear block. Only the linear block contains dynamic elements. The linear block is a discrete-time transfer function, and the nonlinear blocks are implemented using nonlinearity estimators such as saturation, wavelet, and dead zone. Figure 7 depicts the structure of the nonlinear Hammerstein-Wiener model.

The input signal passes through the first nonlinear block, a linear block, and a second nonlinear block to produce the output signal [39].

The Hammerstein-Wiener structure can be described by the following general equations:

$$\begin{aligned}
 u(t) &= f(u(t)) \\
 x(t) &= \frac{B_{j,i}(q)}{F_{j,i}(q)} w(t) \\
 y(t) &= h(x(t)),
 \end{aligned} \tag{1}$$

where $u(t)$ and $y(t)$ are the inputs and outputs for the system, respectively. f and h are nonlinear functions that correspond to the input and output nonlinearities, respectively. For multiple inputs and multiple outputs, f and h are defined independently for each input and output channel. $w(t)$ and $x(t)$ are internal variables that define the input and output of the linear block, respectively. $w(t)$ has the same dimension as $u(t)$. $x(t)$ has the same dimension as $y(t)$. $B(q)$ and $F(q)$ in the linear dynamic block are linear functions. For ny outputs and nu inputs, the linear block is a transfer function matrix containing entries in the following form:

$$\frac{B_{j,i}(q)}{F_{j,i}(q)}, \tag{2}$$

where $j = 1, 2, \dots, ny$ and $i = 1, 2, \dots, nu$. If only the input nonlinearity is present, the model is called a Hammerstein model. If only the output nonlinearity is present, the model is called a Wiener model.

The available nonlinearity estimators to be used in the identification process, by estimating the parameters of the input and output blocks, are dead zone, piecewise linear, saturation, sigmoid network, and wavelet network [40].

3.2.1. Dead Zone Function. The dead zone function generates zero output within a specified region that is called the dead zone. The lower and upper limits of the dead zone are specified as the start and the end of the dead zone parameters, respectively. The dead zone defines a nonlinear function $y = f(x)$, where f is a function of x . There are three intervals, which can be identified as follows:

$$\begin{aligned}
 f(x) &= x - a & x < a \\
 f(x) &= 0 & a \leq x < b \\
 f(x) &= x - b & x \geq b.
 \end{aligned} \tag{3}$$

$f(x) = 0$ when x has a value between a and b ; this zone is called the “zero interval” zone. See Figure 8.

3.2.2. Piecewise Linear Function. The piecewise linear function is defined as a nonlinear function $y = f(x)$, where f is a piecewise linear (affine) function of x and there are n breakpoints (x_k, y_k) where $k = 1, \dots, n$ and $y_k = f(x_k)$. f is linearly interpolated between the breakpoints. y and x are scalars.

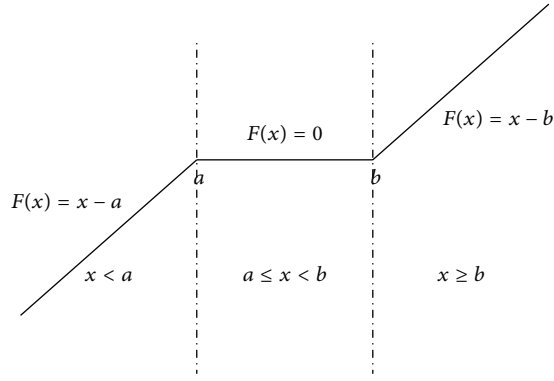


FIGURE 8: Dead zone function.

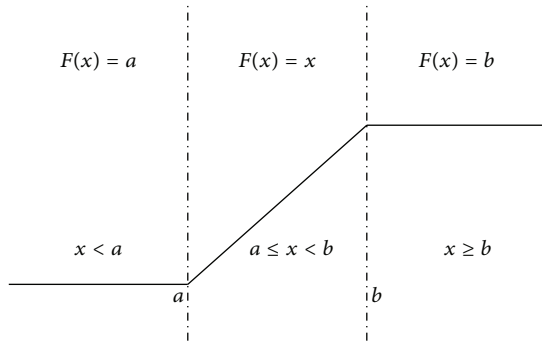


FIGURE 9: Saturation function.

3.2.3. *Saturation Function.* The saturation function can be defined as a nonlinear function $y = f(x)$, where f is a function of x . There are three intervals as shown in Figure 9 and they can be identified as follows:

$$\begin{aligned} f(x) &= a & x < a \\ f(x) &= x & a \leq x < b \\ f(x) &= b & x \geq b. \end{aligned} \quad (4)$$

3.2.4. *Sigmoid Network Function.* The sigmoid network nonlinear estimator uses neural networks comprising an input layer, an output layer, and a hidden layer employing sigmoid activation functions as represented by Figure 10.

It combines the radial basis neural network function using a sigmoid as the activation function. The estimator is based on the following expression:

$$y(t) = (u - r)PL + \sum_i^n a_i f((u - r)Qb_i - c_i) + d, \quad (5)$$

where u is the input and y is the output. r is the regressor. Q is a nonlinear subspace and P is a linear subspace. L is a linear coefficient. d is an output offset. b is a dilation coefficient, c is a translation coefficient, and a is an output coefficient. f is the sigmoid function, given by the following equation:

$$f(z) = \frac{1}{e^{-z} + 1}. \quad (6)$$

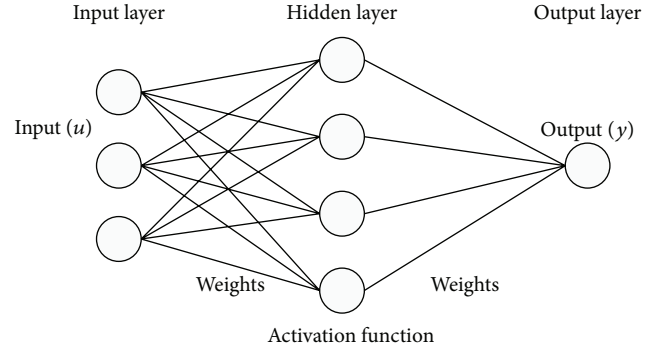


FIGURE 10: Sigmoid network function.

3.2.5. *Wavelet Network Function.* The wavelet estimator is a nonlinear function combining wavelet theory and neural networks. Wavelet networks are feedforward neural networks using a wavelet as an activation function, based on the following expression:

$$\begin{aligned} y(t) &= (u - r)PL + \sum_i^n a_i s_i * f(bs(u - r)Q + cs) \\ &+ \sum_i^n aw_i * g(bw_i(u - r)Q + cw_i) + d, \end{aligned} \quad (7)$$

where u is the input and y is the output, Q is a nonlinear subspace and P is a linear subspace. L is a linear coefficient. d is an output offset. as is a scaling coefficient and aw is a wavelet coefficient. bs is a scaling dilation coefficient and bw is a wavelet dilation coefficient. cs is a scaling translation coefficient and cw is a wavelet translation coefficient. The scaling function $f(\cdot)$ and the wavelet function $g(\cdot)$ are both radial functions and can be written as follows:

$$\begin{aligned} f(u) &= e^{-0.5 * u' * u} \\ g(u) &= (\dim(u) - u' * u) * e^{-0.5 * u' * u}. \end{aligned} \quad (8)$$

In the system identification process, the wavelet coefficient a , the dilation coefficient b , and the translation coefficient c are optimized during model learning steps to obtain the best performance model.

4. Results and Discussion

As mentioned earlier in Section 3, the measured input-output data collected in Figure 5 are the system identification data to be used for the estimation. Table 1 shows the values of irradiance, current, and power with time for the PV system.

Once the identification process results in finding the best model in a structure, another data set (validation data) is used to validate the model. The identification procedure follows the flowchart steps in Figure 6.

4.1. *Model Estimation.* Table 1 represents the variation in power for the data set collected for the estimation. The time

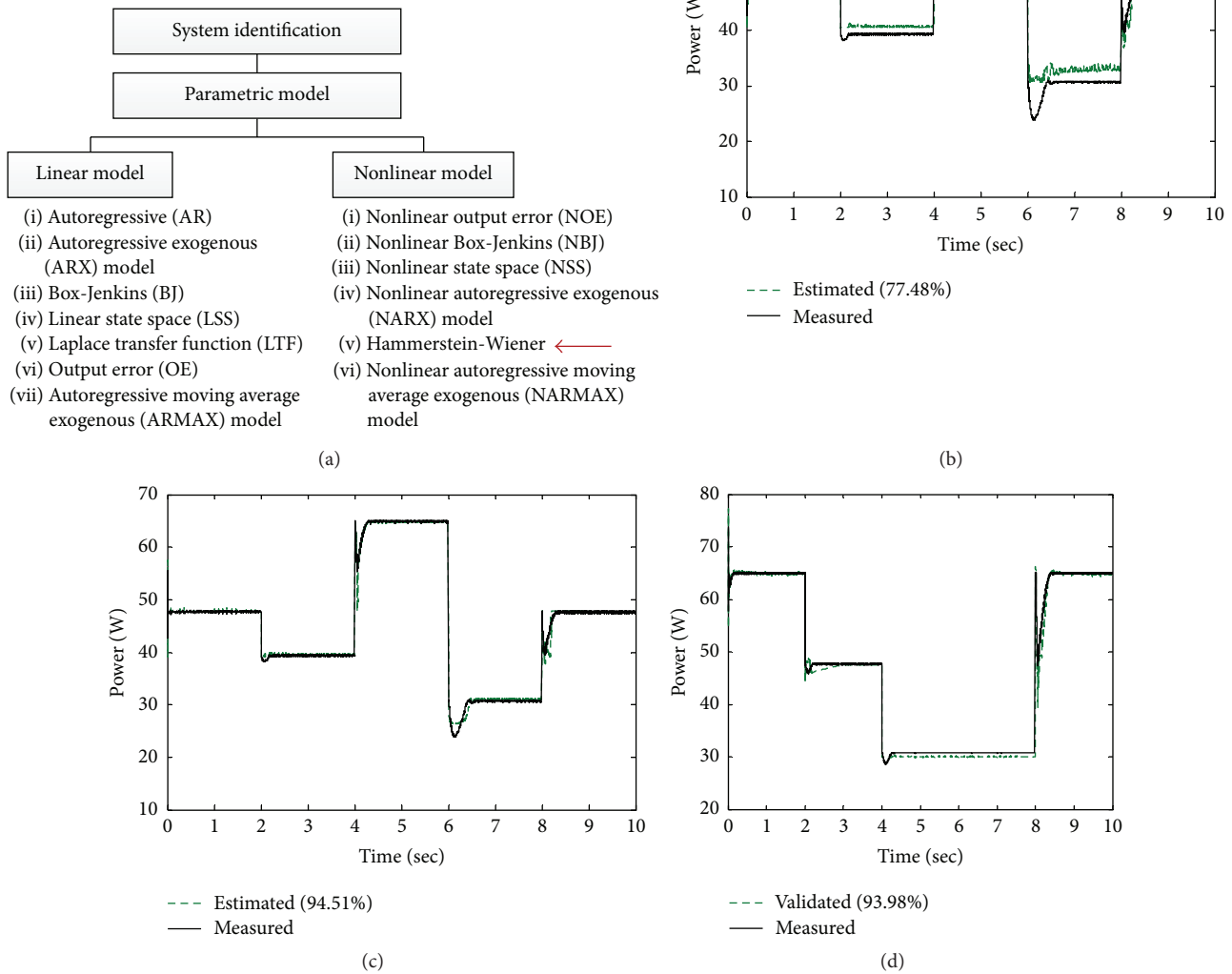


FIGURE 11: (a) System identification classifications. (b) Power output for the identified nonlinear ARX model with the estimation data set. (c) Power output for the identified Hammerstein-Wiener model with the estimation data set. (d) Power output for the identified Hammerstein-Wiener model with the validation data set.

TABLE 1: Variation in power for the data set collected for the estimation.

Irradiance (W/m^2)	Current (A)	Power (W)	Time (s)
400	1.78	30.8	6–8
500	2.31	39.3	2–4
600	2.85	47.7	0–2
600	2.85	47.7	8–10
800	3.75	64.9	4–6

domain data in Figure 5 are imported to the system identification toolbox in Matlab. Such a toolbox integrates techniques for nonlinear and linear models so that the complex problem

of estimating and analyzing nonlinear models appears simple and systematic.

In our case, a model is to be identified for the PV system from the current data as input to the system, and the recorded power is to be identified as the system output. A nonlinear autoregressive exogenous (NARX) model was selected as a reference point. There are several models that can be selected from the toolbox. Figure 11(a) demonstrates the available classifications of system identification; however, discussing the detail of each one is beyond the scope of this paper.

Figure 11(b) shows the result of a nonlinear ARX model type with wavelet network nonlinearity. The figure indicates the model output matches the measured output with 77.48% accuracy. However, this match does not best describe the

TABLE 2: Best fit with different input and output nonlinearity.

Input nonlinearity	Output nonlinearity	Hammerstein-Wiener model		
		Final predicted error (FPE)	Loss function	Best fit (%)
Piecewise linear	Piecewise linear	6.723	6.723	80.25
Piecewise linear	Sigmoid network	5.036	5.036	86.11
Piecewise linear	Saturation	1.751	1.751	92.83
Piecewise linear	Dead zone	1.023	1.023	92.24
Piecewise linear	Wavelet network	2.083	2.082	88.11
Sigmoid network	Piecewise linear	1.265	1.265	77.94
Sigmoid network	Sigmoid network	3.547	3.547	81.05
Sigmoid network	Saturation	2.016	2.016	89.45
Sigmoid network	Dead zone	4.952	4.951	85.37
Sigmoid network	Wavelet network	0.1694	0.1693	63.09
Saturation	Piecewise linear	1.262	1.262	92.22
Saturation	Sigmoid network	1.199	1.199	92.44
Saturation	Saturation	FE	FE	FE
Saturation	Dead zone	FE	FE	FE
Saturation	Wavelet network	0.7606	0.7601	85.83
Dead zone	Piecewise linear	0.3974	0.3974	93.4
Dead zone	Sigmoid network	1.464	1.464	93.98
Dead zone	Saturation	FE	FE	FE
Dead zone	Dead zone	FE	FE	FE
Dead zone	Wavelet network	0.2972	0.2972	90.86
Wavelet network	Piecewise linear	1.717	1.716	91.42
Wavelet network	Sigmoid network	2.038	2.037	89.61
Wavelet network	Saturation	131.5	131.5	-0.7279
Wavelet network	Dead zone	2.054	2.054	90.09
Wavelet network	Wavelet network	0.3643	0.364	93.81

FE: failed estimation.

dynamics of the PV system. The input and output data each contain 100001 samples with sampling interval of 0.0001 seconds.

After the iterative process—by selecting different nonlinear models with their associated input-output nonlinearity, searching methods, and manipulating numerous estimation configurations—Hammerstein-Wiener was found to be the best model that captures the main system dynamics, with a 94.51% fit. See Figure 11(c).

4.2. Model Cross-Validation. Similarly, the model performance is evaluated using cross-validation. In cross-validation, the Hammerstein-Wiener model is confronted with a new data set that is different from the data used to estimate the model. Figure 11(d) provides the new measured data set collected from the PV system, this time with different irradiances, namely, 800 W/m², 600 W/m², 400 W/m², and 800 W/m². This situation emulates an effect of a cloud blocking the irradiance from the PV system. In the same figure, it can be seen that the output of the Hammerstein-Wiener model matches the validation data set well, with 93.98% accuracy. This shows that the estimation process is robust enough to handle different input and that the model estimation is successful. Table 2 lists the results of the best fit with different input and output nonlinearity showing the

93.98% accuracy. The table as well displays an assessment of the estimation in terms of final prediction error (FPE) and loss function.

5. Conclusions

The results of this work showed that the nonlinear Hammerstein-Wiener model was able to provide an accurate description of the PV system dynamics. The model was selected after an iterative process involving trial and error. The model must produce an accurate fit to the data, and the Hammerstein-Wiener model showed an accuracy of 93.98% applying estimation and validation data sets. Developing such a black box model from measured input-output data can contribute to the design and implementation of nonlinear control strategies. In addition, researchers and engineers will be able to predict future performance of PV systems for maintenance and troubleshooting.

Competing Interests

The authors declare that they have no competing interests.

References

- [1] W. T. da Costa, J. F. Fardin, L. D. V. B. M. Neto, and D. S. L. Simonetti, "Identification of photovoltaic model parameters by

- differential evolution,” in *Proceedings of the IEEE International Conference on Industrial Technology (ICIT '10)*, pp. 931–936, IEEE, March 2010.
- [2] D. Sera, R. Teodorescu, and P. Rodriguez, “PV panel model based on datasheet values,” in *Proceedings of the IEEE International Symposium on Industrial Electronics (ISIE '07)*, pp. 2392–2396, Vigo, Spain, June 2007.
 - [3] M. G. Villalva, J. R. Gazoli, and E. R. Filho, “Comprehensive approach to modeling and simulation of photovoltaic arrays,” *IEEE Transactions on Power Electronics*, vol. 24, no. 5, pp. 1198–1208, 2009.
 - [4] G. M. Masters, *Renewable and Efficient Electric Power Systems*, John Wiley & Sons, Hoboken, NJ, USA, 2004.
 - [5] R. Ramaprabha and B. L. Mathur, “MATLAB based modeling to study the influence of shading on series connected SPVA,” in *Proceedings of the 2nd International Conference on Emerging Trends in Engineering and Technology (ICETET '09)*, pp. 30–34, IEEE, Nagpur, India, December 2009.
 - [6] W. Xiao, W. G. Dunford, and A. Capel, “A novel modeling method for photovoltaic cells,” in *Proceedings of the IEEE 35th Annual Power Electronics Specialists Conference (PESC '04)*, vol. 3, pp. 1950–1956, Aachen, Germany, June 2004.
 - [7] E. Saloux, M. Sorinand, and A. Teysseidou, “Explicit model of photovoltaic panels to determine voltages and currents at the maximum power point,” CETC Number 2010-156, CanmetENERGY, Ottawa, Canada, 2010.
 - [8] A. H. Alqahtani, M. S. Abuhamdeh, and Y. M. Alsmadi, “A simplified and comprehensive approach to characterize photovoltaic system performance,” in *Proceedings of the IEEE Energytech Conference*, pp. 1–6, Cleveland, Ohio, USA, May 2012.
 - [9] J. J. Soon and K.-S. Low, “Photovoltaic model identification using particle swarm optimization with inverse barrier constraint,” *IEEE Transactions on Power Electronics*, vol. 27, no. 9, pp. 3975–3983, 2012.
 - [10] Y. A. Mahmoud, W. Xiao, and H. H. Zeineldin, “A parameterization approach for enhancing PV model accuracy,” *IEEE Transactions on Industrial Electronics*, vol. 60, no. 12, pp. 5708–5716, 2013.
 - [11] S. A. Rahman, R. K. Varma, and T. Vanderheide, “Generalised model of a photovoltaic panel,” *IET Renewable Power Generation*, vol. 8, no. 3, pp. 217–229, 2014.
 - [12] L. Cristaldi, M. Faifer, M. Rossi, and S. Toscani, “An improved model-based maximum power point tracker for photovoltaic panels,” *IEEE Transactions on Instrumentation and Measurement*, vol. 63, no. 1, pp. 63–71, 2014.
 - [13] J. Schoukens, “System identification: what does it offer to electrical engineers,” in *Proceedings of the 60th Anniversary of the Foundation of the Faculty of Electrical Engineering and Informatics of the Technical*, University Budapest, December 2009.
 - [14] P. Eykhoff, *System Identification-Parameter and State Estimation*, Wiley, London, UK, 1974.
 - [15] L. Ljung, *System Identification—Theory for the User*, Prentice-Hall, Englewood Cliffs, NJ, USA, 1987.
 - [16] T. Soderstrom and P. Stoica, *System Identification*, Prentice-Hall, Hemel Hempstead, UK, 1989.
 - [17] C. Osorio, *Model-Based Design for Solar Power Systems*, The MathWorks, Natick, Mass, USA, 2009.
 - [18] K. Ishaque and Z. Salam, “A review of maximum power point tracking techniques of PV system for uniform insolation and partial shading condition,” *Renewable and Sustainable Energy Reviews*, vol. 19, pp. 475–488, 2013.
 - [19] A. R. Reisi, M. H. Moradi, and S. Jamasb, “Classification and comparison of maximum power point tracking techniques for photovoltaic system: a review,” *Renewable and Sustainable Energy Reviews*, vol. 19, pp. 433–443, 2013.
 - [20] M. A. G. de Brito, L. Galotto, L. P. Sampaio, G. De Azevedo Melo, and C. A. Canesin, “Evaluation of the main MPPT techniques for photovoltaic applications,” *IEEE Transactions on Industrial Electronics*, vol. 60, no. 3, pp. 1156–1167, 2013.
 - [21] E. B. Youssef, P. Stephane, E. Bruno, and A. Corinne, “New P&O MPPT algorithm for FPGA implementation,” in *Proceedings of the 36th Annual Conference of the IEEE Industrial Electronics Society (IECON '10)*, pp. 2868–2873, IEEE, Glendale, Calif, USA, November 2010.
 - [22] E. Setiawan, I. Hodaka, Y. Yamamoto, and I. Jikuya, “Improvement of maximum power point tracking based on nonlinear control of boost converter,” in *Proceedings of the 1st IEEE Conference on Control, Systems & Industrial Informatics (ICCSII '12)*, pp. 180–184, Bandung, Indonesia, September 2012.
 - [23] C.-S. Chiu and Y.-L. Ouyang, “Robust maximum power tracking control of uncertain photovoltaic systems: a unified T-S fuzzy model-based approach,” *IEEE Transactions on Control Systems Technology*, vol. 19, no. 6, pp. 1516–1526, 2011.
 - [24] N. Patcharaprakiti and S. Premrudeepreechacharn, “Maximum power point tracking using adaptive fuzzy logic control for grid-connected photovoltaic system,” in *Proceedings of the IEEE Power Engineering Society Winter Meeting*, pp. 372–377, IEEE, January 2002.
 - [25] S. A. Khan and M. I. Hossain, “Design and implementation of microcontroller based fuzzy logic control for maximum power point tracking of a photovoltaic system,” in *Proceedings of the International Conference on Electrical and Computer Engineering (ICECE '10)*, pp. 322–325, IEEE, Dhaka, Bangladesh, December 2010.
 - [26] J. Li and H. Wang, “Maximum power point tracking of photovoltaic generation based on the fuzzy control method,” in *Proceedings of the 1st International Conference on Sustainable Power Generation and Supply (SUPERGEN '09)*, pp. 1–6, Nanjing, China, April 2009.
 - [27] S.-J. Kang, J.-S. Ko, J.-S. Choi et al., “A novel MPPT Control of photovoltaic system using FLC algorithm,” in *Proceedings of the 11th International Conference on Control, Automation and Systems (ICCAS '11)*, pp. 434–439, IEEE, Gyeonggi-do, Republic of Korea, October 2011.
 - [28] W.-M. Lin, C.-M. Hong, and C.-H. Chen, “Neural-network-based MPPT control of a stand-alone hybrid power generation system,” *IEEE Transactions on Power Electronics*, vol. 26, no. 12, pp. 3571–3581, 2011.
 - [29] M. Syafaruddin, E. Karatepe, and T. Hiyama, “Artificial neural network-polar coordinated fuzzy controller based maximum power point tracking control under partially shaded conditions,” *IET Renewable Power Generation*, vol. 3, no. 2, pp. 239–253, 2009.
 - [30] T. Esrām, *Modeling and control of an alternating-current photovoltaic module [Ph.D. thesis]*, Department of Electrical Engineering, University of Illinois at Urbana-Champaign, Urbana, Ill, USA, 2010.
 - [31] Y.-H. Liu, C.-L. Liu, J.-W. Huang, and J.-H. Chen, “Neural-network-based maximum power point tracking methods for photovoltaic systems operating under fast changing environments,” *Solar Energy*, vol. 89, pp. 42–53, 2013.
 - [32] A. B. G. Bahgat, N. H. Helwa, G. E. Ahmad, and E. T. El Shenawy, “Maximum power point tracking controller for PV systems using

- neural networks,” *Renewable Energy*, vol. 30, no. 8, pp. 1257–1268, 2005.
- [33] B.-J. Jeon, K.-H. Kim, K. Lee, J.-H. Im, G.-B. Cho, and Y.-O. Choi, “Battery controller design of stand-alone photovoltaic system using IncCond method,” in *Proceedings of the 15th International Conference on Electrical Machines and Systems (ICEMS '12)*, pp. 1–5, October 2012.
- [34] C. Osorio, *Webinar: Model-Based Design for Solar Power Systems*, The MathWorks, Natick, Mass, USA, 2009.
- [35] H. Kumar and R. K. Tripathi, “Simulation of variable incremental conductance method with direct control method using boost converter,” in *Proceedings of the Students Conference on Engineering and Systems (SCES '12)*, March 2012.
- [36] A. Safari and S. Mekhilef, “Simulation and hardware implementation of incremental conductance MPPT with direct control method using cuk converter,” *IEEE Transactions on Industrial Electronics*, vol. 58, no. 4, pp. 1154–1161, 2011.
- [37] A. Safari and S. Mekhilef, “Implementation of incremental conductance method with direct control,” in *Proceedings of the IEEE Region 10 Conference (TENCON '11)*, pp. 944–948, Bali, Indonesia, November 2011.
- [38] J. Sjöberg, Q. Zhang, L. Ljung et al., “Nonlinear black-box modeling in system identification: a unified overview,” *Automatica*, vol. 31, no. 12, pp. 1691–1724, 1995.
- [39] L. Ljung, *System Identification Toolbox 7 User's Guide*, The MathWorks, Natick, Mass, USA, 2008.
- [40] N. Patcharaprakiti, K. Kirtikara, K. Tunlasakun et al., “Modeling of photovoltaic grid connected inverters based on nonlinear system identification for power quality analysis,” in *Electrical Generation and Distribution Systems and Power Quality Disturbances*, InTech, Rijeka, Croatia, 2011.

Research Article

Improving the Performance of a Semitransparent BIPV by Using High-Reflectivity Heat Insulation Film

Huei-Mei Liu,¹ Chin-Huai Young,² Der-Juinn Horng,¹
Yih-Chearnng Shiue,¹ and Shin-Ku Lee³

¹Department of Business Administration, National Central University, Taoyuan 320, Taiwan

²Department of Construction Engineering, National Taiwan University of Science and Technology, Taipei 106, Taiwan

³Research Center for Energy Technology and Strategy, National Cheng Kung University, Tainan 701, Taiwan

Correspondence should be addressed to Shin-Ku Lee; sklee1015@gmail.com

Received 24 February 2016; Revised 8 May 2016; Accepted 22 May 2016

Academic Editor: Prakash Basnyat

Copyright © 2016 Huei-Mei Liu et al. This is an open access article distributed under the Creative Commons Attribution License, which permits unrestricted use, distribution, and reproduction in any medium, provided the original work is properly cited.

Currently, standard semitransparent photovoltaic (PV) modules can largely replace architectural glass installed in the windows, skylights, and facade of a building. Their main features are power generation and transparency, as well as possessing a heat insulating effect. Through heat insulation solar glass (HISG) encapsulation technology, this study improved the structure of a typical semitransparent PV module and explored the use of three types of high-reflectivity heat insulation films to form the HISG building-integrated photovoltaics (BIPV) systems. Subsequently, the authors analyzed the influence of HISG structures on the optical, thermal, and power generation performance of the original semitransparent PV module and the degree to which enhanced performance is possible. The experimental results indicated that the heat insulation performance and power generation of HISGs were both improved. Selecting an appropriate heat insulation film so that a larger amount of reflective solar radiation is absorbed by the back side of the HISG can yield greater enhancement of power generation. The numerical results conducted in this study also indicated that HISG BIPV system not only provides the passive energy needed for power loading in a building, but also decreases the energy consumption of the HVAC system in subtropical and temperate regions.

1. Introduction

Both soaring energy costs and the effects of climate change mean that greater attention is now being paid to reducing energy consumption. According to a report by the International Energy Agency (IEA) [1], to prevent a further rise in the global temperature of 2°C by 2050, it is necessary to set annual reduction goals for greenhouse gas emissions, with reductions in energy use being an important part of this. The energy consumption of the construction sector accounts for around 30% to 40% of a country's total energy consumption and has the greatest potential for energy saving among all sectors. For example, it is estimated that emissions of carbon dioxide will be reduced by approximately 1.5 billion tons per year with the application of the design concepts of net zero energy or zero carbon buildings. As such, in recent years, many countries have been approving the planning, design,

and construction of net zero energy buildings (or zero carbon buildings) and putting such buildings into their national policy objectives, thus further raising interest in this field [2–4].

Among all the available renewable energy sources, solar energy is the most abundant, being an inexhaustible source of clean energy. Moreover, photovoltaic (PV) module technology has been widely used in modern industry to directly convert solar energy into electricity. Traditionally, a PV module is installed in open areas that are exposed to direct sunlight in order to generate electricity. However, in an urban environment, there is limited space on a building's roof, and thus the walls or building curtains can be utilized effectively for this purpose. For instance, a PV module can be combined with construction components, such as glass curtains, walls, windows, or roof structures, to form an integrated design. This design is known as building-integrated photovoltaics

(BIPV), and this technology shows great potential for the development of more effective solar modules. Theoretically, as a BIPV module is combined with building materials, it can effectively reduce overall construction costs and is thus expected to shorten the energy payback time (EPBT).

Researchers in many countries have been assessing the benefits of this technology. For example, in the United Kingdom, Hammond et al. [5] assessed a 2.1 kW_p monocrystalline silicon BIPV module applied to a roof and found that its EPBT was 4.5 years. The results also showed that the implementation of a government program, the “Low Carbon Building Programme” (or LCBP), would facilitate the economic benefits of this BIPV module and further shorten the EPBT. In the United States, Keoleian and Lewis [6] assessed a 2 kW_p thin-film-type (α -Si) BIPV module integrated with a roof. They installed it in different regions from Portland, Oregon, to Phoenix, Arizona, to examine the EPBT, with the results showing that this lay between 3.39 and 5.52 years. Lu and Yang assessed a 22 kW_p monocrystalline silicon BIPV module used on a roof and wall in Hong Kong. When the module was installed in different orientations on the wall, its EPBT ranged from 7.1 years (the best scenario) to 20.0 years (when the module was installed on a vertical wall facing west) [7]. In Malaysia, Seng et al. [8] assessed 1 kW_p BIPV modules using different crystalline Si technologies, namely, monocrystalline, polycrystalline, and thin-film-type α -Si, in which the EPBTs were, respectively, 3.2–4.4, 2.2–3.0, and 1.9–2.6 years. In Europe, Oliver and Jackson [9] integrated a polycrystalline silicon BIPV module into building walls and found that its EPBT was 5.5 years. All these works show that BIPV modules have been widely studied and that many countries are making efforts to reduce the overall cost of installation in order to effectively reduce the EPBT, as well as achieve mass production and universalization.

Compared to the nontransparent BIPV module, the semitransparent BIPV module with improved visible light transmission performance has attracted greater attention in recent years. When a semitransparent PV module is integrated into building curtains, efficient visible light transmission can reduce the energy consumption of indoor lighting. With an appropriate design, solar radiation can even be reflected in an indoor environment, reducing building cooling energy usage directly, and so effectively enhance the thermal and visual comfort of a building. To achieve visible light transmission, this type of PV module mostly uses thin-film solar panel technology.

Copper indium gallium selenide (CIGS), amorphous silicon (a-Si), CdTe, and organic solar cells are widely used on the market. Moreover, CIGS solar cells have been used in building-attached photovoltaics (BAPV) [10]. However, the manufacturing costs of CIGS solar cells are still relatively higher, resulting in a greater EPBT. Therefore, recent studies tend to focus on a-Si thin-film-type solar panels. The module efficiency of a-Si solar cell is currently around 10% [11]. Due to the single-junction structure of such cells, they are unable to absorb the solar energy spectrum effectively and so have a relatively low photoelectric conversion efficiency. Therefore, modern solar cell research has introduced dual-junction solar cells working in tandem (a-Si/ μ c-Si), which can widen the

range of the solar light absorption spectrum by modulating the energy gap through the structure of tandem-junction module, improving the sunlight-to-electrical-energy conversion efficiency. The efficiency has now reached around 12.3% of the energy of standard sunlight (1000 W/m^2) for the tandem-junction modules now available on the market [11]. Although tandem-junction (a-Si/ μ c-Si) technology can increase the power generation efficiency of a module, its efficiency is still lower than that of crystalline silicon-type and CIGS solar cells. Nevertheless, the literature [6–9] shows that the EPBTs of amorphous BIPV modules were shorter than those of crystalline silicon BIPV modules, because the construction costs of the latter are still too high.

Therefore, some a-Si/ μ c-Si manufacturers have moved towards manufacturing BIPV modules in order to develop a semitransparent PV module that can replace architectural glass, so that the building possesses good views and aesthetics. In the United Kingdom, Yun et al. [12] theoretically analyzed vertical solar panel walls and then analyzed the effects that different proportions of transparent windows and solar panels had on the indoor comfort and visible light utilization. They reported that transparent windows covering around 50% to 60% of the entire wall would achieve the best energy-saving effects in a building. The literature thus suggests that using light transmission is essential to zero carbon building design.

In Japan, Wong et al. [13] applied a semitransparent PV module to the skylight of a building. Under optimal conditions, the semitransparent solar skylight allowed 50% radiation transmission and could contribute a maximum of 5.3% of indoor heating and cooling energy consumption, as compared to a roof design using only an opaque BIPV. In China, Li et al. [14] made a theoretical analysis of the application of semitransparent PV modules in offices. Their results also showed that their application not only could reduce energy usage for indoor lighting and air-conditioning equipment, but also had a surplus electricity output, which will be conducive to the development of net zero energy buildings. In Saudi Arabia, Radhi [15] conducted an analysis of semitransparent PV modules applied to the south and west walls of a building. The EPBTs lay between 12 and 13 years, so, in order to effectively develop PV modules, it is necessary to consider and design them as a whole.

In Brazil, Didoné and Wagner [16] simulated the energy-saving performance of semitransparent thin-film PV modules located in two different climates, in Brazil and the German city of Frankfurt. Their results showed that, with proper control, a semitransparent thin-film window can not only save energy for indoor lighting and air conditioning, but also generate surplus electricity. In 2014, Ng and Mithraratne reviewed the development of semitransparent PV modules and studied six types of commercially obtainable thin-film PV modules applied to office buildings in Singapore. Their study used a life cycle assessment (LCA) method to explore the EPBTs, carbon emissions, and cost reductions. The LCA method can be used to facilitate the design of a building [17], and the results showed that the application of a semitransparent PV module is more in line with the concept of zero

carbon building compared to the use of an opaque BIPV module. Many studies have analyzed the energy efficiency of semitransparent PV modules and attempted to reduce the EPBT, with increasing the power generation ability being the main factor in this.

In a previous study [18], our team combined a thin-film-type semitransparent PV module with a high-reflectivity heat insulation film to develop a type of heat insulation solar glass (HISG) that simultaneously possesses power generation, heat insulation, and energy-saving functions. After sunlight passes through the semitransparent PV module, the remaining light source will be reflected by the high-reflectivity heat insulation film to the back side of the semitransparent PV module, so that the module can once again absorb the reflected light and have a higher power output. Moreover, because of the multilayered structure of the HISG, the solar heat passing through the HISG can gradually be isolated in each layer of the material. After the sunlight passes through the first layer (the semitransparent PV module), part of the energy is converted to electrical energy. For the remaining radiant heat, the high-reflectivity heat insulation film will effectively isolate the residual radiant heat and block the ultraviolet light by 100%.

The structure of the dual air gaps can reduce the thermal transmittance (U -value), effectively isolating the conducted heat of the glass, so that the heat cannot be conducted from the glass to the indoor environment, and hence it has very good insulation properties. In terms of saving energy during summer, since the shading coefficient of HISG is very low, the heat of solar radiation cannot easily enter the building, significantly reducing the startup frequency of the air-conditioning compressor and thus achieving reduced energy consumption for cooling. During winter, since the thermal transmittance of the HISG is very low, the glass has good isolation and insulation performance, so warm air can be kept inside the room and cannot easily be dissipated, achieving reduced energy consumption for heating. The functional principles of the HISG are described in Figure 1.

In this research, we adopt three different types of semitransparent PV module technologies and combine three different types of energy-saving films with high reflectance to encapsulate HISG BIPV systems. Subsequently, we explore the optical and thermal properties and overall power generation effects and use simulation software to calculate the power generation and energy-saving effects of each HISG as applied to actual buildings in Taiwan, with a subtropical climate, and in London, England, with a temperate climate.

2. Methodology

2.1. Preparation of Heat Insulation Solar Glass. The proposed HISGs are mainly composed of a thin-film-type semitransparent PV module, high-reflectivity heat insulation film, and rear glass. HISG constructed in this study is a three-layer glazing system. The first layer is a transparent PV module, on the back of which is a 0.4 mm thick layer of high-reflectivity heat insulation film between two layers of spacers. Rear glass

is placed behind the second spacer layer, which forms an air gap on both sides of the high-reflectivity heat insulation film. Three types of semitransparent PV module, a tandem laser module, tandem transparent conducting oxide (TCO) module, and a-Si TCO module, were selected as the front layer of the HISG in this study. The cell structure of these modules is illustrated in Figures 2(a), 2(b), and 2(c). In order to study the effects of heat insulation films with different reflectance values on the gains in power generation, heat insulation, and energy-saving performance of the HISG, this study adopts three different types of Heat Mirror films with different reflectance values.

2.2. Tests of Optical and Thermal Properties. Based on ISO 9050 and ISO 10292 [19, 20], a UV/Vis/NIR spectrophotometer (Hitachi U4100), FTIR spectrometer (Thermo iS50), and thermal conductivity analyzer (TCi) are used to measure the optical properties and thermal performance of the nine types of HISGs. The optical properties include solar direct transmittance (300~2500 nm), solar direct reflectance (300~2500 nm), visible light transmittance (380~780 nm), visible light reflectance (380~780 nm), and ultraviolet light transmittance (300~380 nm). The thermal performance properties include the solar heat gain coefficient (SHGC), shading coefficient (SC), and thermal transmittance (U -value). Since the HISGs used in this study are multilayer ones composed of two or more sheets of flat glass, individual measurements must be made of every component during the optical measurements. The related formulae in ISO 9050 were used to calculate the overall optical and thermal performances. The relevant formulae are as follows.

2.2.1. Visible Light Transmittance, τ_V , and Reflectance, ρ_V , of Triple Glazing. The light transmittance, τ_V , and reflectance, ρ_V , of each component are calculated using the following formulae:

$$\tau_V = \frac{\sum_{380}^{780} D_\lambda \times V(\lambda) \times \tau(\lambda) \times \Delta\lambda}{\sum_{380}^{780} D_\lambda \times V(\lambda) \times \Delta\lambda} \quad (1)$$

$$\rho_V = \frac{\sum_{380}^{780} D_\lambda \times V(\lambda) \times \rho(\lambda) \times \Delta\lambda}{\sum_{380}^{780} D_\lambda \times V(\lambda) \times \Delta\lambda},$$

where D_λ is the relative spectral distribution of illuminant D65 (see ISO/CIE 10526), $\tau(\lambda)$ is the spectral transmittance of glazing, $\rho(\lambda)$ is the spectral reflectance of glazing, $V(\lambda)$ is the spectral luminous efficiency for photopic vision defining the standard observer for photometry, and $\Delta\lambda$ is the wavelength interval.

In the case of multiple glazing, the spectral transmittance $\tau(\lambda)$ and reflectance $\rho(\lambda)$ will be obtained by calculation from the spectral characteristics of the individual components. For the spectral transmittance $\tau(\lambda)$ and reflectance $\rho(\lambda)$ as a function of the spectral characteristics of the individual components of the unit, the following formulae are obtained:

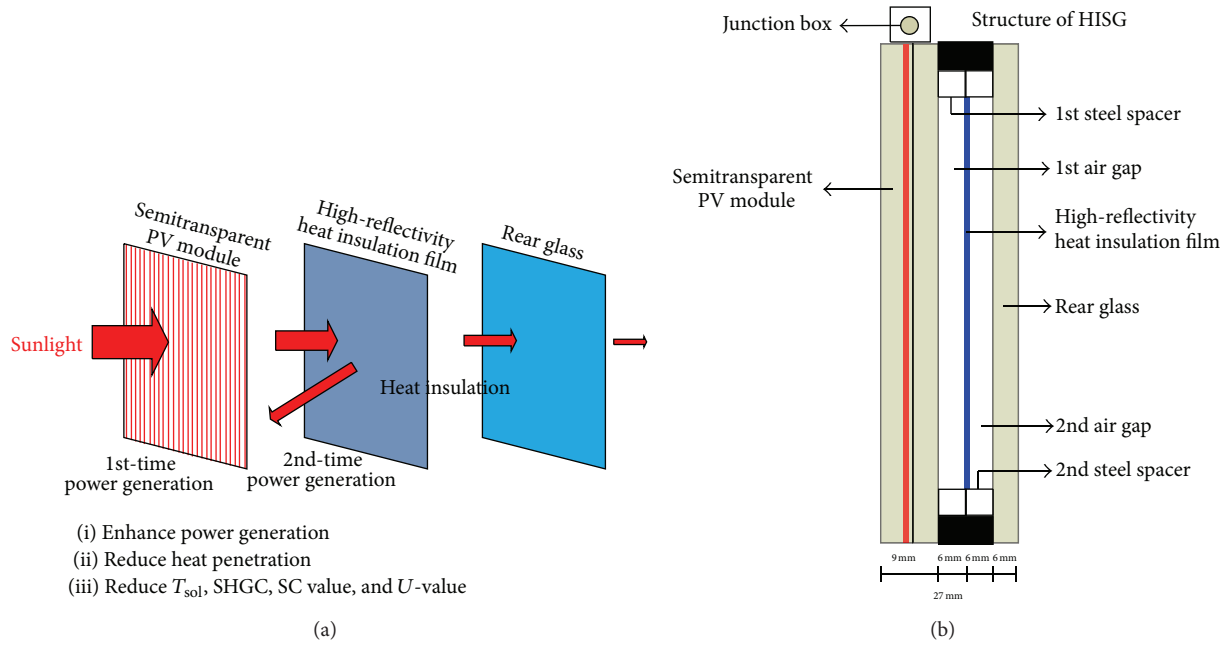


FIGURE 1: Functional principles and cross-sectional structure of heat insulation solar glass.

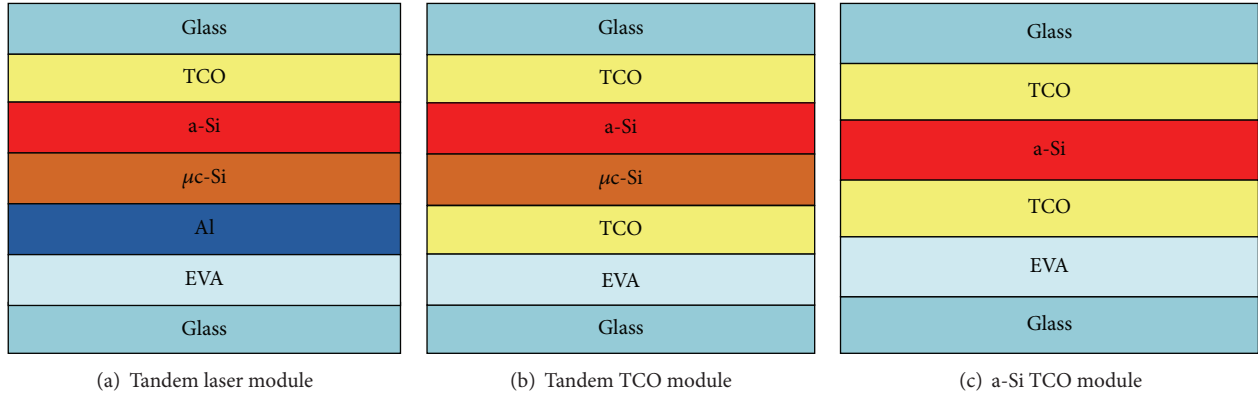


FIGURE 2: Cell structure of the tandem laser, tandem TCO, and a-Si TCO module.

$$\tau(\lambda) = \frac{\tau_1(\lambda) \times \tau_2(\lambda) \times \tau_3(\lambda)}{[1 - \rho_2(\lambda) \times \rho'_1(\lambda)] [1 - \rho_3(\lambda) \times \rho'_2(\lambda)] - \tau_2^2 \rho_3(\lambda) \times \rho'_1(\lambda)} \quad (2)$$

$$\rho(\lambda) = \rho_1(\lambda) + \frac{\tau_1^2(\lambda) \times \rho_2(\lambda) [1 - \rho'_2(\lambda) \times \rho_3(\lambda)] + \tau_1^2(\lambda) \times \tau_2^2(\lambda) \times \rho_3(\lambda)}{[1 - \rho'_1(\lambda) \times \rho_2(\lambda)] [1 - \rho'_2(\lambda) \times \rho_3(\lambda)] - \tau_2^2 \times \rho'_1(\lambda) \times \rho'_3(\lambda)}$$

where $\tau_1(\lambda)$ is the spectral transmittance of the outer (first) pane; $\tau_2(\lambda)$ is the spectral transmittance of the second pane; $\tau_3(\lambda)$ is the spectral transmittance of the third (inner) pane; $\rho_1(\lambda)$ is the spectral reflectance of the outer (first) pane measured in the direction of incident radiation; $\rho'_1(\lambda)$ is the spectral reflectance of the outer (first) pane measured in the

opposite direction of incident radiation; $\rho_2(\lambda)$ is the spectral reflectance of the second pane measured in the direction of incident radiation; $\rho'_2(\lambda)$ is the spectral reflectance of the second pane measured in the opposite direction of incident radiation; $\rho_3(\lambda)$ is the spectral reflectance of the third (inner) pane measured in the direction of incident radiation; $\rho'_3(\lambda)$ is

the spectral reflectance of the third (inner) pane measured in the opposite direction of incident radiation.

2.2.2. Solar Direct Transmittance, τ_e , and Reflectance, ρ_e , of Triple Glazing. The solar direct transmittance and reflectance are obtained as follows:

$$\begin{aligned}\tau_e &= \frac{\sum_{780}^{2500} S_\lambda \times \tau(\lambda) \times \Delta\lambda}{\sum_{780}^{2500} S_\lambda \times \Delta\lambda}, \\ \rho_e &= \frac{\sum_{780}^{2500} S_\lambda \times \rho(\lambda) \times \Delta\lambda}{\sum_{780}^{2500} S_\lambda \times \Delta\lambda},\end{aligned}\quad (3)$$

where S_λ is the relative spectral distribution of the solar radiation.

2.2.3. UV Transmittance. UV transmittance is obtained as follows:

$$\tau_e = \frac{\sum_{300}^{380} S_\lambda \times \tau(\lambda) \times \Delta\lambda}{\sum_{300}^{380} S_\lambda \times \Delta\lambda}. \quad (4)$$

2.2.4. U-Value Calculation. The thermal transmittance of glazing, also known as the U -value, is the rate of heat transfer through one square meter of glazing divided by the difference between the ambient temperatures on each side. The method specified by ISO 10292 is based on a calculation from the following equation:

$$\frac{1}{U} = \frac{1}{h_t} + \frac{1}{h_e} + \frac{1}{h_i}, \quad (5)$$

where h_i is the interior heat transfer coefficient; h_e is the exterior heat transfer coefficient; h_t is the conductance of the multiple glazing unit.

2.2.5. Total Solar Energy Transmittance. The total solar energy transmittance (also known as solar heat gain coefficient) is the sum of the solar direct transmittance τ_e and the secondary heat transfer factor q_i towards the inside:

$$g = \tau_e + q_i. \quad (6)$$

The secondary heat transfer factor results from heat transfer by convection and longwave IR-radiation of that part of the incident solar radiation which has been absorbed by the glazing. The secondary heat transfer factor towards the inside of triple glazing is calculated using the following formula:

$$q_i = \frac{((\alpha_{e1} + \alpha_{e2} + \alpha_{e3})/h_e + (\alpha_{e2} + \alpha_{e3})/\Lambda_{12} + \alpha_{e3}/\Lambda_{23})}{1/h_i + 1/h_e + 1/\Lambda_{12} + 1/\Lambda_{23}}, \quad (7)$$

where α_{e1} is the solar direct absorptance of the outer (first) pane within the triple glazing; α_{e2} is the solar direct absorptance of the second pane within the triple glazing; α_{e3} is the solar direct absorptance of the third pane of the triple glazing; Λ_{12} is the thermal conductance between the outer surface of the outer (first) pane and the center of the second pane; Λ_{23} is the thermal conductance between the center of the second pane and the center of the third pane.

2.2.6. Shading Coefficient (SC). The shading coefficient of glass is a measure of the total amount of heat passing through the glazing compared with that through single clear glass. It is approximately equal to the SHGC divided by 0.87.

2.3. Test of Gains in Power Generation Performance. Tests of the gain in power generation were made based on the standard test conditions (STC) in the test standard given by the International Electrotechnical Commission, IEC 61646 [21], for a thin-film PV module, in order to explore the power generation characteristics of the nine types of HISG described above. The effects of each combination of materials on the gain in power generation capacity of the semitransparent PV module were then analyzed and compared.

2.4. Assessment of Energy-Saving Performance. In this study, Autodesk Ecotect Analysis was adopted to conduct simulations of building power generation and energy by adopting the results of the power generation test, optical test, and thermal test as the material parameters and choosing Tainan in Taiwan and London in the United Kingdom as the simulated locations. The simulation was used to obtain the power generation capacity and energy consumption performance of the HISGs in real-world applications on buildings in subtropical and temperate regions.

2.4.1. Building Model. Ecotect was used in this study to model a single building. The building body consists of a roof and four walls to form an enclosed space, in order to facilitate the simulation of air-conditioning energy consumption. The main body of the building is facing south. The roof has a monopitched roof structure with an incline angle of 23.5° and is composed of 10 pieces \times 10 pieces, giving a total of 100 pieces of PV modules with a size of approximately 14 m \times 11 m. The overall dimensions of the building body are approximately 14 m \times 10 m \times 8.3 m, as illustrated in Figure 3.

2.4.2. Setting Parameters for the Simulation. In terms of the material parameters, the four surrounding walls are defined as being constructed of composite materials (110 mm brick outside plus 75 mm timber frame, with 10 mm plasterboard inside) with a U -value of 1.77 W/mK, whereas values for the material parameters of each PV module come from the results of the power generation and optical and thermal tests in this paper. For the air-conditioning energy consumption, this study uses a mixed-mode air-conditioning system for cooling and heating. The usage time is 24 hours, the comfort temperature range is 20°C–26°C, the startup temperature setting for a cold room is 26°C, and the startup temperature setting for a warm room is 18°C. The simulation of the air-conditioning energy consumption was conducted for a whole year.

3. Results and Discussion

3.1. Optical Properties. The transmittance and reflectance coefficient versus wavelength of each component are shown in Figures 4 and 5, respectively. Table 1 shows the optical

TABLE 1: Optical properties of each component and HISGs.

Module	Solar direct transmittance	Solar direct reflectance	Item		
			Visible light transmittance	Visible light reflectance	UV transmittance
Tandem laser module	7.09	10.07	8.4	5.27	0.01
Tandem TCO module	18.33	6.79	2.20	5.15	0.01
a-Si TCO module	23.49	7.30	4.35	5.12	0.01
Heat insulation film A	68.14	16.88	95.32	4.83	1.75
Heat insulation film B	40.63	30.89	84.12	6.01	1.36
Heat insulation film C	33.15	40.71	61.04	22.33	1.00
Rear glass	81.15	5.04	88.85	5.66	62.39
Tandem laser-A HISG	4.07	10.17	7.23	5.35	0
Tandem laser-B HISG	2.5	10.24	6.39	5.35	0
Tandem laser-C HISG	2.08	10.30	4.78	5.45	0
Tandem TCO-A HISG	10.34	7.44	1.88	5.15	0
Tandem TCO-B HISG	6.26	7.88	1.66	5.15	0
Tandem TCO-C HISG	5.16	8.21	1.23	5.15	0
a-Si TCO-A HISG	13.26	8.37	3.72	5.14	0
a-Si TCO-B HISG	8.03	9.09	3.29	5.14	0
a-Si TCO-C HISG	6.62	9.64	2.43	5.17	0

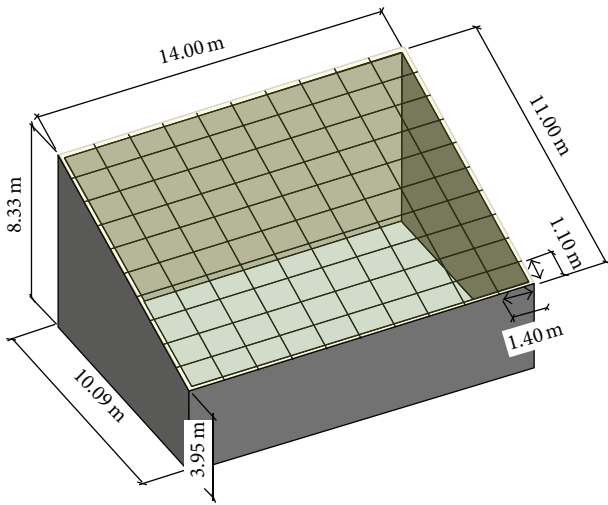


FIGURE 3: The 3D model of the building body.

properties of each component based on ISO 9050. The values of lighting transmittance for the three PV modules were in the 7.09–23.49 range, and those for the three heat insulation films were in the range of 33.15–68.14. The measurement results show that the tandem laser module and heat insulation film C had better heat insulation effects. They could thus be used in hot climates, where there is a need to reduce solar heat transmission, especially in buildings where large transparent surfaces are fitted. Furthermore, the tandem laser module and heat insulation film A had better visibilities, even though with the former the back-contact electrode material is opaque. Part of the power-generating layers and back-contact electrode layer in the tandem laser module were removed

using a transverse laser cutting method to enable the module to be light-transmissible. It is also worth noting that the lower visible light transmittance in other modules is mainly due to absorption of the TCO layers. The UV transmittances of the PV module and heat insulation film are less than 2%, meaning that the performances of the HISGs with regard to isolating UV light were very good.

In the cell structure of the tandem TCO module, the materials of the power-generating layers are the same as those of the tandem laser module, but, in terms of the back-contact electrode, a TCO material with good light transmission and conduction properties was adopted. Though TCO has high optical transparency, it does decrease light transmission from UV to IR. Therefore, the tandem TCO module has a light-transmissible property and its insulation of solar thermal energy is poorer than that of the tandem laser module. In addition, as the color of transmitted light tends to be wine red, part of its visible light transmittance was poorer. The material of the rear electrode in the cell structure of the a-Si TCO module was the same as that of the tandem TCO module. As such, it also has a light-transmissible property and the transmitted light color tends to be orange red. However, in the power-generating layer, the a-Si TCO module had a single-layer structure without a layer of $\mu\text{C-Si}$, so its visible light transmittance was slightly better than that of the tandem TCO module. Furthermore, as it has no $\mu\text{C-Si}$ layer to absorb the solar light, its solar radiation transmittance was slightly poorer than that of the tandem TCO module.

As shown in Figure 6, the measurement results for the solar direct transmittance indicated that the addition of a reflective layer reduces the transmittance of HISGs. For the tandem laser, tandem TCO, and a-Si TCO module, the solar direct transmittance was originally 7.09%, 18.33%,

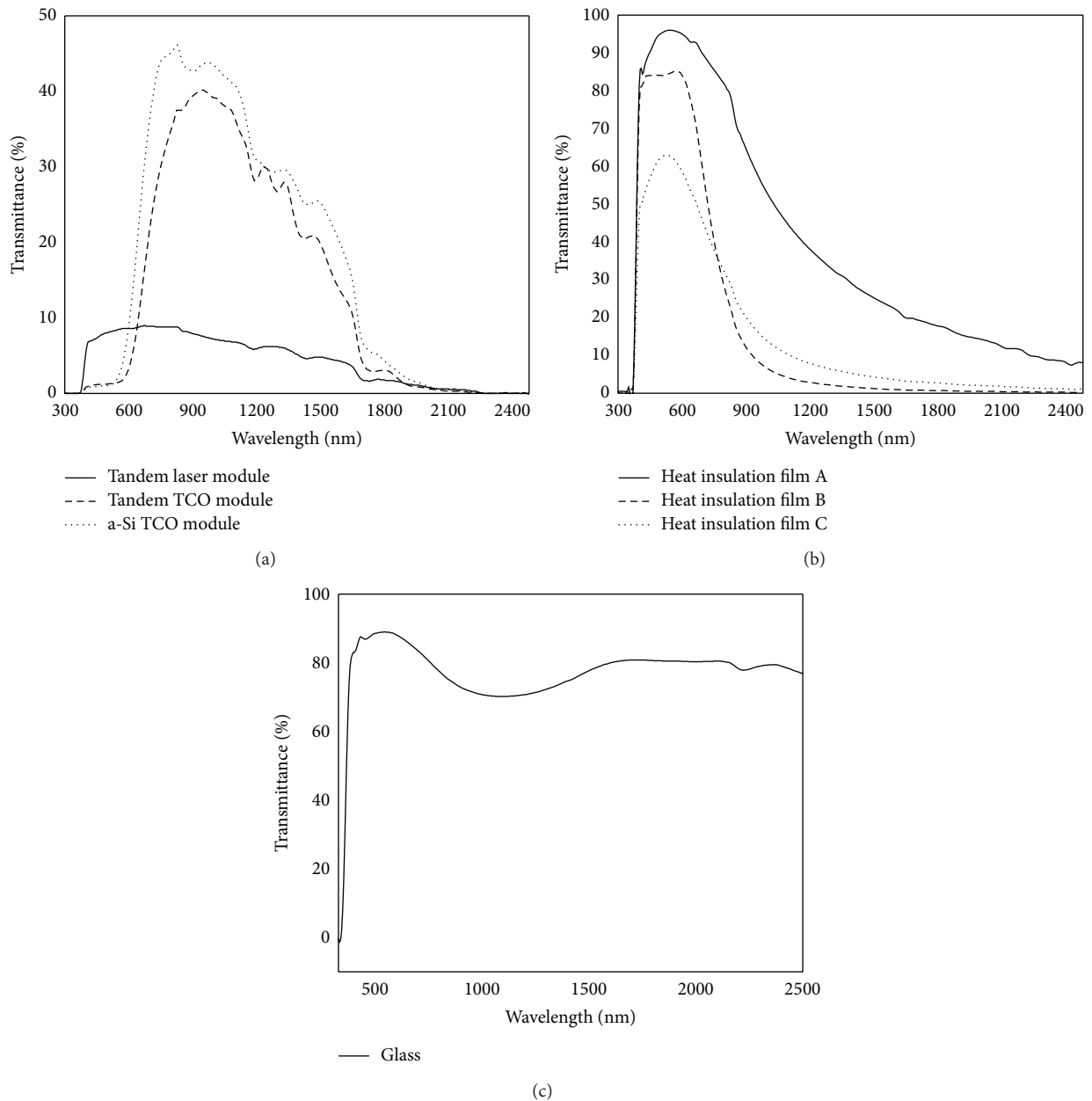


FIGURE 4: Transmittance spectra of each component: (a) semitransparent PV module, (b) heat insulation film, and (c) rear glass.

and 23.49%, but after being encapsulated into the HISG it dropped to 2.08–4.07%, 5.16–10.34%, and 6.62–13.26%, respectively. The visible light transmittance was originally 8.4%, 2.2%, and 4.35%, but after being encapsulated into the HISG it dropped to 4.78–7.23%, 1.23–1.88%, and 2.43–3.72%, respectively.

After the various semitransparent PV modules were integrated into the HISG with the various heat insulation films, all their solar direct reflectance values increased slightly, so the encapsulation was slightly beneficial to the heat insulating effect of the HISGs. Moreover, after being encapsulated into the HISGs, the effects on the visible light reflectance were all less severe, falling to around 5%. Therefore, the HISGs will not necessarily cause environmental light pollution.

With regard to the UV transmittance, since most of the UV light is absorbed by the semitransparent PV module and the heat insulation film, the UV transmittance values of all the HISGs are 0%. This means that the UV isolation performances are very good and able to protect interior furnishings from aging and the skin from damage caused by UV radiation.

3.2. Thermal Properties. The surface emissivity of an object refers to its ability to release heat via thermal radiation after absorbing solar radiation. The surface emissivity of each component is thus an important parameter affecting the heat insulation performance of a HISG. In this paper, the spectral reflectance of each component on the exterior and interior

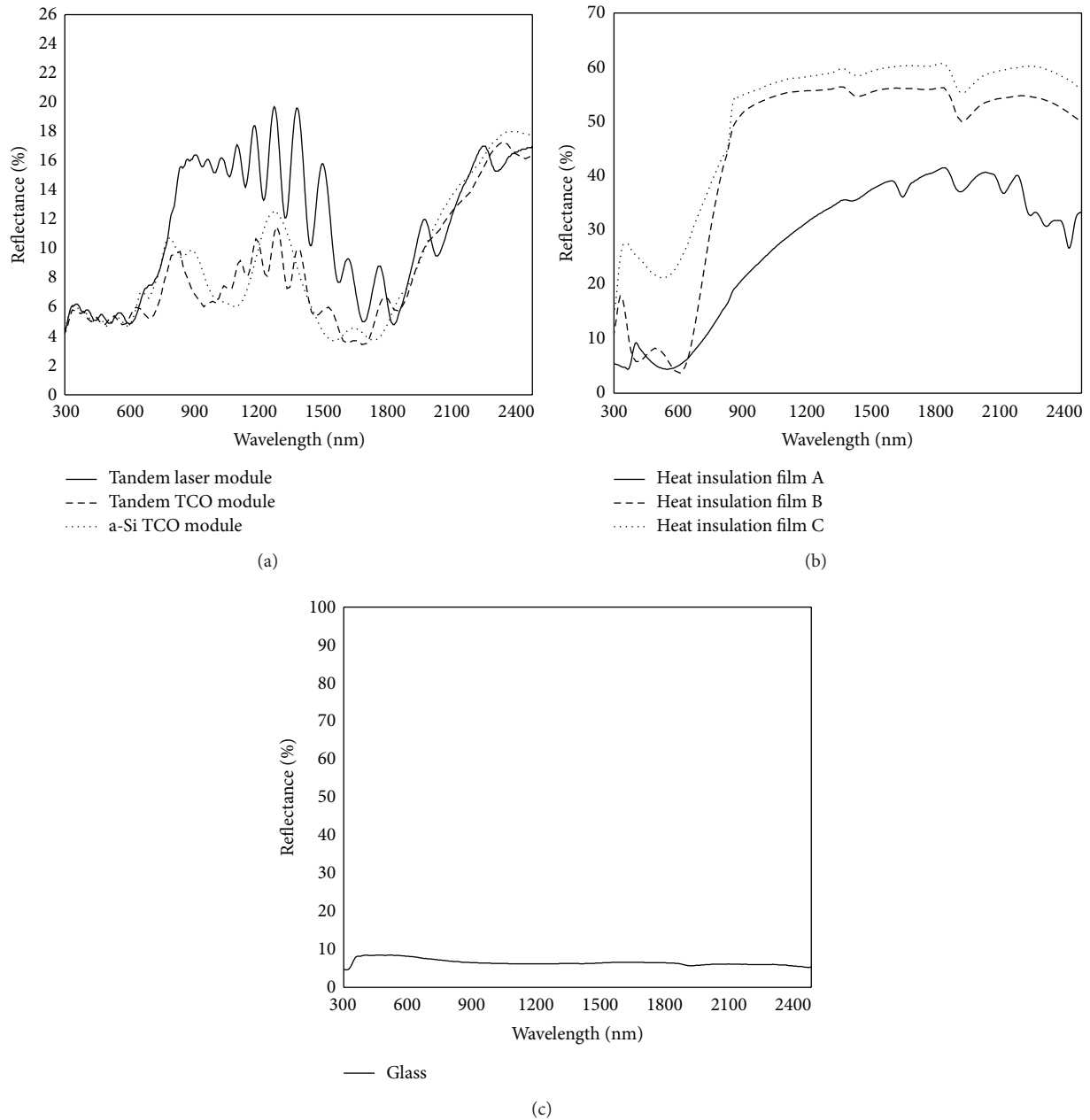


FIGURE 5: Reflectance spectra of each component: (a) semitransparent PV modules, (b) heat insulation films, and (c) rear glass.

sides was measured using FTIR, and then the emissivity value of each component was obtained by ISO 10292, as shown in Table 2. It can be seen that as the surfaces of the semitransparent PV modules and rear glass were not all coated by a film, the emissivity values for the exterior and interior sides were 0.84. While the heat insulation films were mainly composed of PET material, there was no film coating the interior surface of the film, so the emissivity values were all 0.76. Meanwhile, the exterior surfaces of the heat insulation films all had a multilayer metal coating, so the surface emissivity values were lower than the surface emissivity values on the indoor side. The surface emissivity

of heat insulation film C is 0.033, which is thus categorized as a Low-E film.

Table 3 shows the thermal performances of the three types of PV modules and the nine types of HISGs, with the SHGCs, shading coefficients, and overall heat transfer coefficients (U -values). The results indicate that the multilayer structure of the HISG reduced the solar direct transmittance, and since the heat insulation films were coated with transparent metal films this reflected the solar radiation heat, prompting the SHGCs to be reduced to half the levels seen with the semitransparent PV modules. This means that the quantity of solar radiation heat passing through the HISG was half that

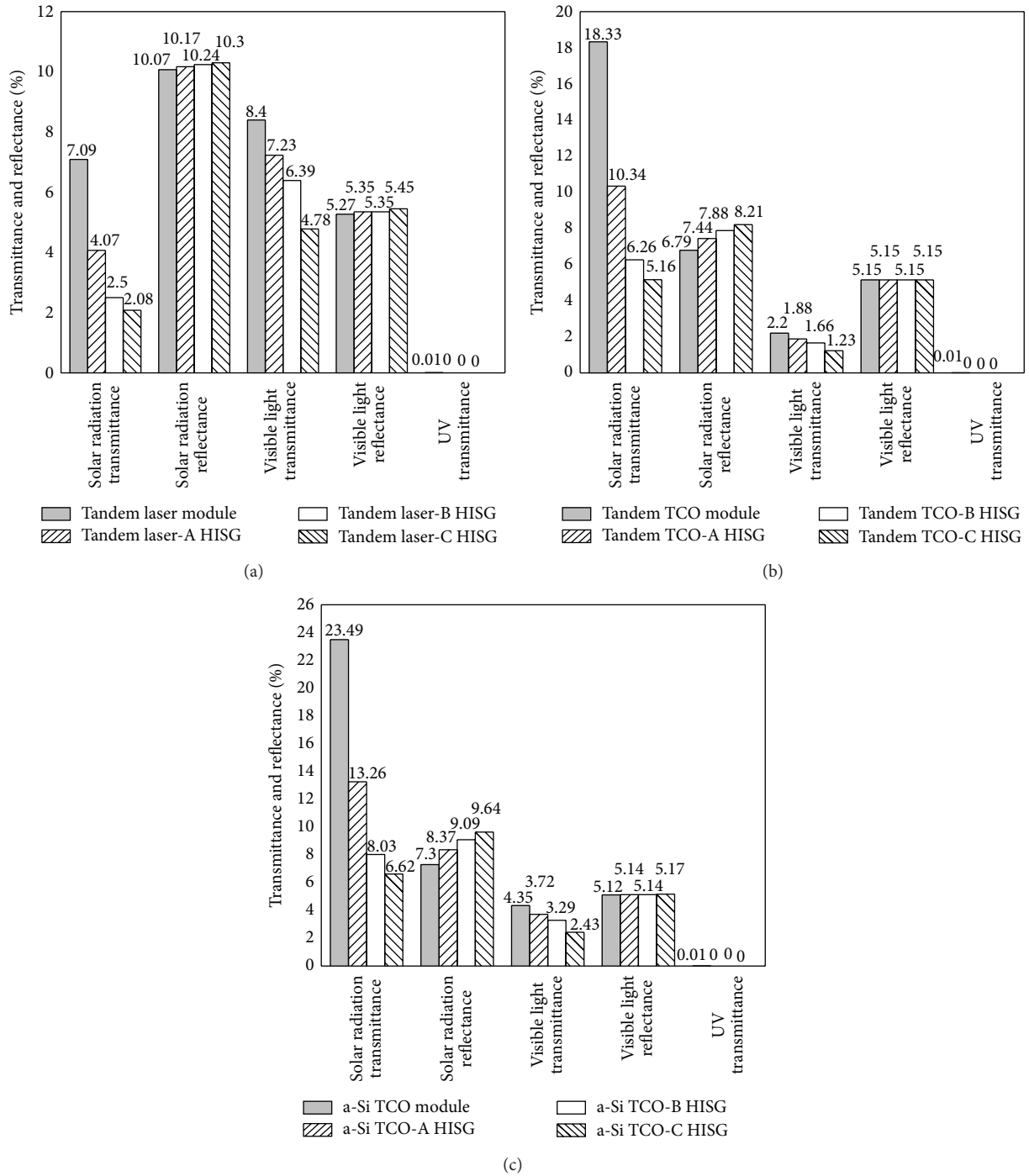


FIGURE 6: Optical properties of the HISGs: (a) tandem laser module, (b) tandem TCO module, and (c) a-Si TCO module.

passing through the semitransparent PV modules. In terms of the U -value, since all the semitransparent PV modules were assembled with $4\text{ mm} \times 4\text{ mm}$ laminated glass, the U -values based on ISO 10292 for all modules were $5.63\text{ W/m}^2\text{-K}$. The addition of heat insulation films and dual air gaps to form a multilayer structure greatly reduced the U -values of the HISGs ($1.755\text{ W/m}^2\text{-K}$ – $1.824\text{ W/m}^2\text{-K}$). Moreover, having heat insulation films with different emissivity values is one

of the main causes of the decline in the U -value. Since heat insulation film C had the lowest surface emissivity, the HISGs assembled using film C also possessed lower U -values ($1.755\text{ W/m}^2\text{-K}$).

3.3. Power Generation Gain Performance. The power generation test results for the front and back sides of each semitransparent PV module are shown in Table 4. The measurement

TABLE 2: Emissivity of each component.

Item	Emissivity of indoor side	Emissivity of outdoor side
Tandem laser module	0.84	0.84
Tandem TCO module	0.84	0.84
a-Si TCO module	0.84	0.84
Heat insulation film A	0.76	0.135
Heat insulation film B	0.76	0.045
Heat insulation film C	0.76	0.033
Rear glass	0.84	0.84

TABLE 3: Thermal properties of the semitransparent PV modules and HISGs.

Module	Item		U-value
	SHGC	Shading coefficient	
Tandem laser module	0.3	0.345	5.63
Tandem laser-A HISG	0.151	0.174	1.824
Tandem laser-B HISG	0.135	0.155	1.757
Tandem laser-C HISG	0.129	0.148	1.755
Tandem TCO module	0.38	0.437	5.63
Tandem TCO-A HISG	0.218	0.25	1.824
Tandem TCO-B HISG	0.184	0.211	1.757
Tandem TCO-C HISG	0.171	0.196	1.755
a-Si TCO module	0.41	0.471	5.63
a-Si TCO-A HISG	0.249	0.286	1.824
a-Si TCO-B HISG	0.207	0.238	1.757
a-Si TCO-C HISG	0.19	0.218	1.755

results show that the power output for the front side of the tandem laser module was 126.029 W, with an efficiency of 8.184%, while that of the back side was only 1.019 W. The reason for this is the cell structure of the tandem laser module, as the bottom back-contact conductive layer is Al, which does not possess power generation characteristics. Therefore, after being illuminated by direct light, there should not be a power generation effect. However, because the tandem laser module was subjected to transverse laser cutting during the manufacturing process, light can pass through from the back side. The light could then undergo refraction or transmission at the rear glass, so some of the light is able to enter the power-generating layer from the laser cut slits, and so the back side

TABLE 4: Results of tests of electrical characteristics in STC for initial states of the original transparent PV module: (a) front side and (b) back side.

(a)			
Test item	Tandem laser module	Tandem TCO module	a-Si TCO module
Module efficiency (%)	8.184	8.11	7.78
Maximum power output (W)	126.029	124.843	119.796
Open circuit voltage (V)	167.382	171.629	111.606
Short circuit current (A)	1.133	1.038	1.595
Maximum voltage (V)	131.026	140.561	86.939
Maximum electric current (A)	0.962	0.888	1.378
Fill factor	0.6644	0.7008	0.6731
(b)			
Test item	Tandem laser module	Tandem TCO module	a-Si TCO module
Module efficiency (%)	0.066	0.723	5.361
Maximum power output (W)	1.019	11.134	82.566
Open circuit voltage (V)	109.965	156.555	108.648
Short circuit current (A)	0.026	0.108	1.213
Maximum voltage (V)	40.348	132.561	83.918
Maximum electric current (A)	0.025	0.084	0.984
Fill factor	0.3506	0.6576	0.6264

of the tandem laser module also possesses a slight power generation effect.

The power output of the front side of the tandem TCO module was 124.843 W, with an efficiency of 8.11%, whereas that of the back side was only 11.134 W. The reason why the efficiency from back-side illumination is low is due to light absorption in the lower bandgap $\mu\text{-Si}$ cell, which allows limited light into the a-Si cell. The current output would be limited by the smaller current value from the a-Si, and so a lower efficiency is generated.

The front-side power output of the a-Si TCO module was 119.796 W, with an efficiency of 7.78%, whereas the back-side power output of the a-Si TCO module reached 82.566 W. The power-generating layer of the a-Si TCO module is the a-Si layer, which is also classified as a cell structure with dual-surface power generation characteristics, so the back-side power output was higher compared to that of the former two modules. However, the reason for the difference in the front-side and back-side power outputs of the a-Si TCO module is that the materials of the front and rear glass were different. The front glass was ultraclear glass with more than 90% visible light transmittance. Meanwhile, in order to increase the loading strength of the BIPV, the rear glass was mostly tempered glass or heat-strengthened glass with

lower transmissivity. In addition, before entering the power-generating layer from the back side, the light still needs to pass through a layer of EVA plastic film, which will also reduce the solar irradiance. The back-side power output of the a-Si TCO module was thus only 69% of the front-side power output.

The results of the electrical tests of each semitransparent PV module and each combination of HISGs are shown in Table 5. The results for power generation gain are shown in Table 6. The experimental results indicated that both the power generation and efficiency of tandem laser HISG exhibited slightly increasing trends; the power generation increased by around 0.01–0.13% and the efficiency increased by around 0.001–0.01%. However, the power generation and efficiency of tandem TCO HISG and a-Si TCO HISG displayed increasing trends. For the tandem TCO HISG, the power generation improved by around 3.27–10.06%, and the efficiency increased by around 0.27–0.82%. For the a-Si TCO HISG, the power generation increased by around 0.94–3.07%, and the efficiency increased by around 0.07–0.24%. The power-generating layer of the tandem TCO module is a-Si/ $\mu\text{c-Si}$, but that of the a-Si TCO module is a single layer of a-Si. The absorption spectrum of the tandem TCO module (300 nm–1100 nm) is wider than that of the a-Si TCO module (300 nm–750 nm). The back side of the tandem TCO HISG can thus absorb higher effective irradiance than the a-Si TCO HISG. This means that the efficiency enhanced rate of the tandem TCO HISG is higher than that of the a-Si TCO HISG. It is also worth noting that selecting an appropriate heat insulation film in order to absorb a larger amount of reflective solar radiation by the back side of the HISG can lead to greater enhancement of power generation.

3.4. Simulation of Energy-Saving Performance. The simulation results for the power generation of each HISG installed in the buildings and the energy consumption of the heating, ventilation, and air-conditioning (HVAC) system are shown in Table 7. As Tainan is located in a subtropical region in Taiwan, where there is sufficient sunlight, the annual power generation of each module was higher than that of the modules in London, and the power outputs ranged between 16,328 kW and 18,727 kW. London is located in a temperate zone with mostly cloudy weather, and thus the annual power generation only ranged between 8493 kW and 9741 kW. These results show that different climate zones and weather patterns are the main factors affecting the power generation of BIPV modules.

The simulation results in Table 7 also show that the power outputs of each HISG were larger than those of the original semitransparent PV modules. That is, the power enhancements of the tandem laser HISG were around 0.01–0.12%, those of the tandem TCO HISG were around 3.27–10.06%, and those of the a-Si TCO HISG were around 0.94–3.07%. The simulated results also reveal that the percentage gains in power generation for each HISG installed on the roofs of buildings as BIPV roofs are consistent with the experimental results under STC from IEC 61646. Therefore, adding heat insulation films onto semitransparent PV modules to form a HISG in order to enhance the power output of the modules is beneficial in reducing the EPBT of the entire BIPV system.

The simulation results for the energy consumption of the HVAC systems of buildings in Tainan, Taiwan, and London, UK, are shown in Tables 8 and 9, respectively. As Tainan is located in a subtropical region, the use of a heater is less common and the HVAC system is mostly used for cooling, so the energy consumption for the latter is much higher than that for heating. On the other hand, London is located in a temperate region, and the HVAC system is mainly used for heating, so the energy consumption for this is much higher than that for cooling.

Furthermore, the main factors affecting the energy consumption of the HVAC system are the shading coefficient and the U -value of the envelope. The shading coefficient and U -value of each HISG are lower than those of the semitransparent PV modules. During summer, solar radiation cannot enter the room easily through the HISG, so cooling energy can be saved. During winter, the U -value of the HISG is very low, owing to the multilayer structure, and although solar radiation cannot enter the room easily, the heat will be retained inside the room and will not dissipate easily, and hence the amount of energy used for heating can also be reduced. Therefore, the simulation results for the HISGs all indicate greater energy-saving performance in the annual energy consumption of the HVAC system. The results show that the HISG can save 29.11–32.19% of cooling energy, 47.34–48.15% of heating energy, and 32.68–35.75% of the total energy consumption of the HVAC system in subtropical regions and 37.27–44.12% of cooling energy, 39.05–39.86% of heating energy, and 39.05–39.86% of total energy consumption of the HVAC system in temperate regions. Among all the HISGs, the HISG encapsulated version using heat insulation film C had the best energy-saving performance.

As seen in the simulation results given above, the HISG can not only enhance the power generation, but also, because of the better heat insulation performance, shorten the EPBT of the entire HISG BIPV application on a building.

4. Conclusion

The concepts of net zero energy, zero energy, and passive energy are becoming more important as part of the energy conservation policies adopted by the construction industry. BIPV technology currently has great potential for effective development of solar module techniques. Theoretically, if a BIPV module is combined with building materials, it can effectively reduce overall construction costs, save energy, modulate the indoor temperature, and shorten the energy payback time (EPBT).

In this work, the authors adopted three different types of semitransparent PV modules and combined three different types of high-reflectivity films to encapsulate HISG BIPV systems. The optical and thermal properties and the overall power generation effects of each HISG were investigated. In addition, Autodesk software was used to calculate the power generation and energy-saving effects of each HISG as applied to actual buildings in Taiwan, with a subtropical climate, and England, with a temperate climate. As a result, due to the three-layer structure of the HISG with a high-reflectivity heat insulation film, the heat insulation performance (SHGC and

TABLE 5: Test results for the various BIPV modules and HISGs under STC.

Test item	Tandem laser module	Tandem laser-A HISG	Tandem laser-B HISG	Tandem laser-C HISG	Tandem TCO module	Tandem TCO-A HISG	Tandem TCO-B HISG	Tandem TCO-C HISG	a-Si TCO module	a-Si TCO-A HISG	a-Si TCO-B HISG	a-Si TCO-C HISG
Efficiency (%)	8.184	8.185	8.189	8.194	8.11	8.37	8.74	8.92	7.78	7.85	7.87	8.02
Maximum power output (W)	126.029	126.042	126.105	126.187	124.843	128.926	134.658	137.399	119.796	120.921	121.125	123.475
Open circuit voltage (V)	167.382	167.253	167.281	167.313	171.629	171.644	171.886	172.036	111.606	111.597	111.613	111.710
Short circuit current (A)	1.133	1.134	1.133	1.134	1.038	1.074	1.125	1.150	1.595	1.612	1.615	1.650
Maximum voltage (V)	131.026	129.433	130.098	129.207	140.561	139.173	138.796	138.027	86.939	87.337	87.341	84.561
Maximum electric current (A)	0.962	0.974	0.969	0.977	0.888	0.926	0.970	0.995	1.378	1.385	1.387	1.460
Fill factor	0.6644	0.6646	0.6654	0.6651	0.7008	0.6996	0.6964	0.6944	0.6731	0.6721	0.6719	0.6698

TABLE 6: Results of power generation gain tests of the semitransparent PV modules and each combination of HISG under STC.

Module	Item			
	Power generation (W)	Power generation enhancement (%)	Module efficiency (%)	Module efficiency enhancement (%)
Tandem laser module	126.029	—	8.184	—
Tandem laser-A HISG	126.042	0.01	8.185	0.001
Tandem laser-B HISG	126.105	0.06	8.189	0.005
Tandem laser-C HISG	126.187	0.13	8.194	0.010
Tandem TCO module	124.843	—	8.11	—
Tandem TCO-A HISG	128.926	3.27	8.37	0.27
Tandem TCO-B HISG	134.658	7.86	8.74	0.64
Tandem TCO-C HISG	137.399	10.06	8.92	0.82
a-Si TCO module	119.796	—	7.78	—
a-Si TCO-A HISG	120.921	0.94	7.85	0.07
a-Si TCO-B HISG	121.125	1.11	7.87	0.09
a-Si TCO-C HISG	123.475	3.07	8.02	0.24

TABLE 7: Power generation results for building body simulations.

Module	Location			
	Tainan, Taiwan (kW)	Power enhancement (%)	London, UK (kW)	Power enhancement (%)
Tandem laser module	17178	—	8935	—
Tandem laser-A HISG	17179	0.01	8936	0.01
Tandem laser-B HISG	17188	0.06	8940	0.06
Tandem laser-C HISG	17199	0.12	8946	0.12
Tandem TCO module	17016	—	8851	—
Tandem TCO-A HISG	17573	3.27	9141	3.27
Tandem TCO-B HISG	18354	7.86	9547	7.86
Tandem TCO-C HISG	18727	10.06	9741	10.06
a-Si TCO module	16328	—	8493	—
a-Si TCO-A HISG	16481	0.94	8573	0.94
a-Si TCO-B HISG	16509	1.11	8587	1.11
a-Si TCO-C HISG	16830	3.07	8754	3.07

TABLE 8: Simulation results for energy consumption of HVAC systems for the building body in the Tainan region of Taiwan.

Module	Cooling energy consumption (kW)	Cooling energy saving (%)	Heating energy consumption (kW)	Heating energy saving (%)	Total HVAC system energy consumption (kW)	Total HVAC energy saving (%)
Tandem laser module	28632	—	6924	—	35556	—
Tandem laser-A HISG	20296	29.11	3639	47.44	23935	32.68
Tandem laser-B HISG	20053	29.96	3590	48.15	23643	33.50
Tandem laser-C HISG	19958	30.29	3591	48.14	23549	33.77
Tandem TCO module	29495	—	6894	—	36390	—
Tandem TCO-A HISG	20793	29.50	3623	47.45	24415	32.91
Tandem TCO-B HISG	20412	30.80	3576	48.13	23988	34.08
Tandem TCO-C HISG	20201	31.51	3583	48.03	23784	34.64
a-Si TCO module	30368	—	6869	—	37236	—
a-Si TCO-A HISG	20952	31.01	3617	47.34	24569	34.02
a-Si TCO-B HISG	20593	32.19	3568	48.06	24161	35.11
a-Si TCO-C HISG	20347	33.00	3577	47.93	23924	35.75

TABLE 9: Simulation results for energy consumption of HVAC systems for the building body in London, UK.

Module	Cooling energy consumption (kW)	Cooling energy saving (%)	Heating energy consumption (kW)	Heating energy saving (%)	Total HVAC system energy consumption (kW)	Total HVAC energy saving (%)
Tandem laser module	306	—	116818	—	117123	—
Tandem laser-A HISG	181	40.85	71203	39.05	71384	39.05
Tandem laser-B HISG	171	44.12	70570	39.59	70741	39.60
Tandem laser-C HISG	173	43.46	70491	39.66	70664	39.67
Tandem TCO module	271	—	117612	—	117883	—
Tandem TCO-A HISG	170	37.27	71497	39.21	71667	39.20
Tandem TCO-B HISG	164	39.48	70753	39.84	70917	39.84
Tandem TCO-C HISG	165	39.11	70734	39.86	70899	39.86
a-Si TCO module	287	—	117214	—	117501	—
a-Si TCO-A HISG	175	39.02	71273	39.19	71448	39.19
a-Si TCO-B HISG	172	40.07	70640	39.73	70812	39.73
a-Si TCO-C HISG	171	40.42	70566	39.80	70737	39.80

U-value) showed an improvement. Although the multilayer structure of HISG would affect the visible light transmittance, in practice, it does not have a significant impact on the view through the glass. Moreover, although the solar direct reflectance values all showed improving trends, the visible light reflectance was only around 5%, which will not necessarily cause environmental light pollution. Compared to the original modules, the power generation and module efficiency of all HISGs were found to have increased. Of all the combinations of HISGs, the gain in power generation of the tandem TCO-C HISG was the highest, as the power generation was improved by 10.06% and the module efficiency was improved by 0.82%. The results of the simulation showed a very similar trend with regard to the level of electrical power generation, based on experimental data that was obtained using the standard test conditions (STC) for measurement contained in IEC 61646. The simulation results also indicated that the HISG has a significant effect on the amount of energy that can be saved when using the HVAC system in both subtropical and temperate regions.

This paper thus provides valuable information for renewable energy planners and architectural designers who are interested in using HISG BIPV systems.

Competing Interests

The authors declare that there are no competing interests regarding the publication of this paper.

Acknowledgments

This study was supported by the Ministry of Science and Technology of Taiwan under Projects MOST 105-3113-F-011-001 and MOST 105-3113-E-006-006-CC2.

References

- [1] M. van der Hoeven, *Energy and Climate Change—World Energy Outlook Special Report*, International Energy Agency, 2015.
- [2] P. Jones, S. S. Hou, and X. Li, “Towards zero carbon design in offices: integrating smart facades, ventilation, and surface heating and cooling,” *Renewable Energy*, vol. 73, pp. 69–76, 2015.
- [3] W. Pan, “System boundaries of zero carbon buildings,” *Renewable and Sustainable Energy Reviews*, vol. 37, pp. 424–434, 2014.
- [4] S. Berry, K. Davidson, and W. Saman, “Defining zero carbon and zero energy homes from a performance-based regulatory perspective,” *Energy Efficiency*, vol. 7, no. 2, pp. 303–322, 2014.
- [5] G. P. Hammond, H. A. Harajli, C. I. Jones, and A. B. Winnett, “Whole systems appraisal of a UK Building Integrated Photovoltaic (BIPV) system: energy, environmental, and economic evaluations,” *Energy Policy*, vol. 40, no. 1, pp. 219–230, 2012.
- [6] G. A. Keoleian and G. M. Lewis, “Modeling the life cycle energy and environmental performance of amorphous silicon BIPV roofing in the US,” *Renewable Energy*, vol. 28, no. 2, pp. 271–293, 2003.
- [7] L. Lu and H. X. Yang, “Environmental payback time analysis of a roof-mounted building-integrated photovoltaic (BIPV) system in Hong Kong,” *Applied Energy*, vol. 87, no. 12, pp. 3625–3631, 2010.
- [8] L. Y. Seng, G. Lalchand, and G. M. Sow Lin, “Economical, environmental and technical analysis of building integrated photovoltaic systems in Malaysia,” *Energy Policy*, vol. 36, no. 6, pp. 2130–2142, 2008.
- [9] M. Oliver and T. Jackson, “Energy and economic evaluation of building-integrated photovoltaics,” *Energy*, vol. 26, no. 4, pp. 431–439, 2001.
- [10] L. Sabnani, A. Skumanich, E. Ryabova, and R. Noufi, *Developing Market Opportunities for Flexible Rooftop Applications of PV Using Flexible CIGS Technology: Market Considerations*, National Renewable Energy Laboratory (NREL), Golden, Colo, USA, 2011.
- [11] M. A. Green, K. Emery, Y. Hishikawa, W. Warta, and E. D. Dunlop, “Solar cell efficiency tables (version 47),” *Progress in Photovoltaics: Research and Applications*, vol. 24, no. 1, pp. 3–11, 2016.
- [12] G. Y. Yun, M. McEvoy, and K. Steemers, “Design and overall energy performance of a ventilated photovoltaic façade,” *Solar Energy*, vol. 81, no. 3, pp. 383–394, 2007.

- [13] P. W. Wong, Y. Shimoda, M. Nonaka, M. Inoue, and M. Mizuno, "Semi-transparent PV: thermal performance, power generation, daylight modelling and energy saving potential in a residential application," *Renewable Energy*, vol. 33, no. 5, pp. 1024–1036, 2008.
- [14] D. H. W. Li, T. N. T. Lam, W. W. H. Chan, and A. H. L. Mak, "Energy and cost analysis of semi-transparent photovoltaic in office buildings," *Applied Energy*, vol. 86, no. 5, pp. 722–729, 2009.
- [15] H. Radhi, "Energy analysis of façade-integrated photovoltaic systems applied to UAE commercial buildings," *Solar Energy*, vol. 84, no. 12, pp. 2009–2021, 2010.
- [16] E. L. Didoné and A. Wagner, "Semi-transparent PV windows: a study for office buildings in Brazil," *Energy and Buildings*, vol. 67, pp. 136–142, 2013.
- [17] P. K. Ng and N. Mithraratne, "Lifetime performance of semi-transparent building-integrated photovoltaic (BIPV) glazing systems in the tropics," *Renewable and Sustainable Energy Reviews*, vol. 31, pp. 736–745, 2014.
- [18] C. H. Young, Y. L. Chen, and P. C. Chen, "Heat insulation solar glass and application on energy efficiency buildings," *Energy and Buildings*, vol. 78, pp. 66–78, 2014.
- [19] International Organization for Standardization, *ISO 9050: Glass in Building—Determination of Light Transmittance, Solar Direct Transmittance, Total Solar Energy Transmittance, Ultraviolet Transmittance and Related Glazing Factors*, International Organization for Standardization, Basel, Switzerland, 2003.
- [20] International Organization for Standardization, "ISO10292: glass in building—calculation of steady-state U values (thermal transmittance) of multiple glazing," Tech. Rep., International Organization for Standardization, Geneva, Switzerland, 1994.
- [21] International Standard, "Thin-film terrestrial photovoltaic (pv) modules—design qualification and type approval," IEC 61646, 2008.

Research Article

Energy Storage Requirements for PV Power Ramp Rate Control in Northern Europe

Julius Schnabel and Seppo Valkealahti

Department of Electrical Engineering, Tampere University of Technology, P.O. Box 692, 33101 Tampere, Finland

Correspondence should be addressed to Seppo Valkealahti; seppo.valkealahti@tut.fi

Received 1 April 2016; Revised 24 May 2016; Accepted 2 June 2016

Academic Editor: Prakash Basnyat

Copyright © 2016 J. Schnabel and S. Valkealahti. This is an open access article distributed under the Creative Commons Attribution License, which permits unrestricted use, distribution, and reproduction in any medium, provided the original work is properly cited.

Photovoltaic (PV) generators suffer from fluctuating output power due to the highly fluctuating primary energy source. With significant PV penetration, these fluctuations can lead to power system instability and power quality problems. The use of energy storage systems as fluctuation compensators has been proposed as means to mitigate these problems. In this paper, the behavior of PV power fluctuations in Northern European climatic conditions and requirements for sizing the energy storage systems to compensate them have been investigated and compared to similar studies done in Southern European climate. These investigations have been performed through simulations that utilize measurements from the Tampere University of Technology solar PV power station research plant in Finland. An enhanced energy storage charging control strategy has been developed and tested. Energy storage capacity, power, and cycling requirements have been derived for different PV generator sizes and power ramp rate requirements. The developed control strategy leads to lesser performance requirements for the energy storage systems compared to the methods presented earlier. Further, some differences on the operation of PV generators in Northern and Southern European climates have been detected.

1. Introduction

Solar radiation fluctuates in annual, daily, and down-to-second timescale. Fast fluctuations are dominantly due to shading caused by moving clouds. Accordingly, the power behavior of photovoltaic generators (PVGs) is known to be rapidly and intensively fluctuating even for large generators [1, 2]. Fast power fluctuations can lead to power quality problems in the power system, and feeding them into a power system in large quantities can also cause serious stability issues. Thus, concerned power system operators are demanding regulation of PV power variability in the form of ramp rate (RR) limitation [3].

Energy storage systems (ESS) have been proposed as the solution for compensating the variability of PV power and other variable energy sources [4–8]. The key issue in utilizing ESS for compensating PV power fluctuations is the sizing of the storage unit to minimize the obvious addition of economic costs. Essential technical sizing variables are the required energy capacity, maximum power output, and the charge-discharge-cycling induced degradation.

Minimization of these variables reduces the added economic burden for the PV power producer. Studies have shown how the right selection of the ESS control strategy can reduce the amount of required energy capacity [9–11] and application induced degradation [12]. Although some of these studies have varied the studied location of the PV system, none have yet examined PV ramp rate limiting in Northern European climate and the effects of such climate on ESS sizing.

In [9], the authors reasoned that both the maximum required ESS power and energy capacity could be analytically derived from a so-called worst fluctuation model (WFM). The model relies on the idea that with proper control the maximum energy surplus or deficiency would be dictated by PVG power fluctuations with the worst possible characteristics. These characteristics were selected to be a fast transition from 100 to 10% of the nominal PVG output power, or vice versa, while the fall or rise of the compensated grid feed-in power would be uninterrupted. The model was validated by comparing the calculated requirements with simulations of virtual storage systems compensating fluctuations of measured PVG power over a full year. The comparison showed

distinct overlap between the calculated requirements and simulation results. However, all the data used in the study originated from a Southern European climate. Intuition says that this climate can differ from other climates, especially those in the Northern latitudes. Moreover, the WFM is a kind of worst-case method for ESS sizing and there is obvious need for more economical control strategies.

In this paper, PV power fluctuations have been studied by utilizing the irradiance measurements of the Tampere University of Technology (TUT) solar PV power station research plant located in Tampere, Finland [13]. Irradiance measurements and existing models for spatial smoothing of PV generator power fluctuations [12, 14] have been utilized to conduct generic investigations without being limited to detailed system specifications. Compensation of the analyzed PV power fluctuations has then been simulated with an arbitrary virtual ESS, for which an enhanced charging control strategy has been developed, tested, and applied to obtain optimal performance requirements for the ESS. The behavior of the ESS has been monitored against two years of measurement data, and conclusions have been drawn about the sizing requirements and degradation of the ESS. The results demonstrate that the introduced ESS control strategy performs better than the earlier applied strategies [9–11], and also some geographical dependency of PV power fluctuations as well as optimal ESS sizing appears.

2. Measurement Data

The data used in this paper was obtained from the TUT solar PV power station research plant located in Tampere, Finland. The plant contains a 13 kWp PV generator consisting of various PV module string formations. All modules are facing closely due south and tilted 45° from the planar roof plane. The PV module strings are attached with a network of 24 pairs of irradiance (Kipp & Zonen SP Lite2) and temperature (PT100) sensors. The irradiance sensors are plane of array sensors mounted next to PV modules with the same 45° tilt angle. The temperature sensors are mounted on the back plates of the same modules. In addition, comprehensive climatic measurements have been conducted. Synchronized measurements have been recorded with a 10 Hz sampling frequency continuously since June 2011 [13].

All measurements used in this paper have been upscaled to a sufficient 1 Hz sampling frequency. Measurement noise has been filtered from all datasets by applying a 5-second moving average. Most of the analyses in this paper rely on measurements from the 2012 leap year. The dataset of 2012 has 17 days with insufficient data, leaving 349 days (95%) for examination. Cross-check of the results has been done with a dataset from 2014, which has 298 viable days (82%). Missing data is due to update and maintenance of the research plant. Both datasets contain extensive amounts of clear sky, overcast, and half cloudy days for diurnal variability and all months are sufficiently represented for seasonal diversity.

An example of a recorded daily irradiance profile is shown in Figure 1, which demonstrates the frequency and severity of irradiance fluctuations. These fluctuations are translated

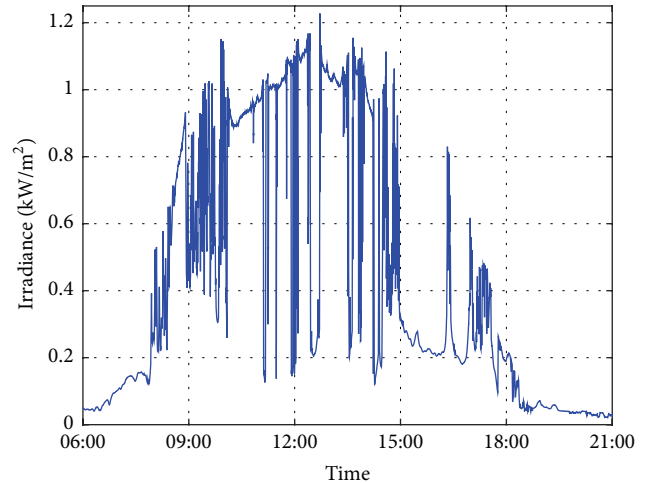


FIGURE 1: Solar irradiance received by PV module of the TUT solar PV power station research plant measured on 26.09.2012.

into the power behavior of any PV generator located in the same area using existing models for spatial smoothing of PV generator power fluctuations [12, 14]. The ramp rates of these irradiance fluctuations give a good qualitative metric for variability. For example, during the day presented in Figure 1 the observed 1-second irradiance ramps exceed the commonly applied ramp rate limit of 10%/min for a total time of 2 hours and 33 minutes and practically all visible fluctuations exceeded the limit. This demonstrates clearly why an increasing number of power system operators are concerned about the growing penetration of grid-connected PV systems and consider imposing ramp rate limits for PV power generation within their grid domains.

3. PV Generator Power Model

In order to achieve general and widely applicable results, the ESS simulations need to be based on data with minimum amount of restrictions and preconditions. In case of real PV power plants, the output power always depends on the power plant layout and the used PV arrays topologies, inverters, maximum power point tracking algorithms, and so forth. Therefore, the used data should rather be an irradiance based approximation of PVG power for obtaining technology independent results. Different methods exist to model PV generator power directly based on irradiance measurements [12].

The model used in this paper relies on the direct proportionality of PVG power to incident irradiance. Spatial smoothing of irradiance over large areas during irradiance transitions [1], which are associated with corresponding PV generators, is taken into account using the low-pass filter method presented in [14]. The method uses a single irradiance point measurement and PVG area as inputs. It is assumed in the method that the PVG covers a symmetric square shaped area. The time series of spatial irradiance $G_s(t)$

can be obtained by applying the first-order low-pass filter transformation as follows:

$$G_s(t) = \frac{G(t)}{\tau s + 1}, \quad (1)$$

where $G(t)$ is the measured irradiance time series of a point sensor, s is the Laplace transform variable, and t is time. For the low-pass filter time constant, the following approximation is applied:

$$\tau = \frac{\sqrt{A}}{2\pi \cdot a}, \quad (2)$$

where constant $a = 2$ Hz/m is obtained from a fit to the cutoff frequencies of power spectra of various PV power plants plotted as a function of plant area A [14]. A is the effective area of the PV power plant realizing the spatial smoothing in the transfer function; that is, the time constant is directly proportional to the effective dimension of the power plant. Hereby, spatial smoothing increases with increasing time constant.

In addition to spatial smoothing of PV power fluctuations, the model takes into account the PV module temperature, which can cause notable offset of power with respect to standard operating conditions. A temperature correction is applied based on measured polycrystalline silicon PV module temperatures of the TUT solar PV power station research plant with a power decrease of $0.5\%/^{\circ}\text{C}$ as follows [13, 15]:

$$P_{\text{mod}}(t) = \frac{G_s(t)}{G_{\text{STC}}} \cdot \left[1 - 0.005 \frac{1}{^{\circ}\text{C}} \cdot (T(t) - T_{\text{STC}}) \right], \quad (3)$$

where G_{STC} and T_{STC} are the irradiance and PV module temperature in standard test conditions (STC), respectively, and T is the measured PV module temperature. Note that (3) gives the modelled power P_{mod} in per-unit convention, which is easily scalable to relevant PV generator sizes.

In this paper, the spatial irradiance model is used to approximate the power behavior of virtual PVGs of different sizes as if they were operating in the TUT solar PV power station research plant area. Further, the results of the ESS simulations are compared to findings of similar studies presented in [9]. For the sake of proper comparison, two PVG sizes of 0.55 and 2.2 MWp were selected for examination with corresponding PV plants characteristics as in the reference power plants located in Southern Europe [9]. An example on the behavior of the spatial irradiance smoothing model can be seen in Figure 2 for the selected two PVG sizes.

4. Energy Storage System Simulations

Simulations of the energy storage system operation were carried out using the presented PV generator power model and measurements from the TUT solar PV power station research plant. The ESS was assumed to be an arbitrary virtual system with no predefined preconditions and limitations on power or energy. As mentioned earlier, two different PV generator sizes of 0.55 and 2.2 MWp nominal output power were studied. Their respected square shaped areas were

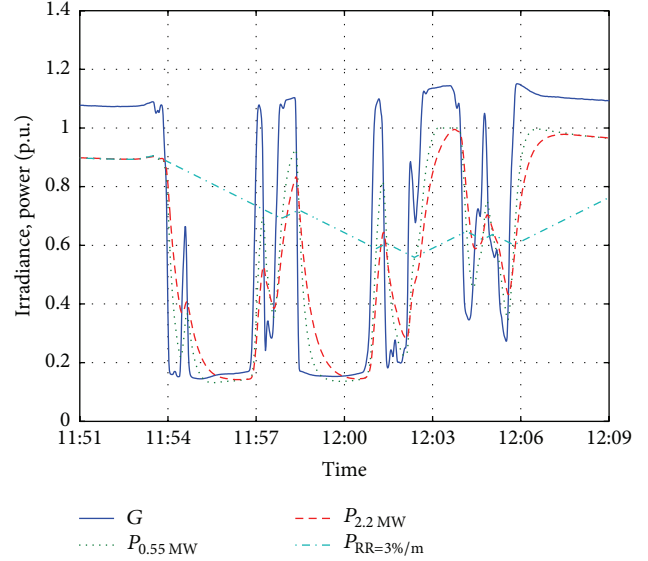


FIGURE 2: Measured point irradiance, simulated power of 0.55 and 2.2 MWp PV generators, and the grid feed-in power of the 0.55 MWp PV generator complying RR limit of 3%/min during 18 minutes on 29.06.2012. Irradiance has been normalized to STC irradiance and power to the corresponding PV generator nominal power.

25 000 m² and 100 000 m², when a ground cover ratio of 0.16 was assumed.

Different ESS control principles exist and their effects on the ESS sizing are notable. The ESS control principle used in this paper is a simple RR limiting control, because it is straightforward to apply and easily comparable and has been applied in practice by electric power companies. It provides a simple way to understand the consequences of different ramp rate limiting requirements and also demonstrates the importance of climatic effects on PV power production.

Compensation of grid feed-in power fluctuations was realized in the simulations in a similar way as in [9]. The modelled PVG power P_{PVG} is fed through the ramp rate limiter to calculate the desired limit compliant grid feed-in power P_{grid} . The limiter simply forces the difference between the present and the next value of P_{grid} to be within a specified RR limit. The amount of ESS power P_{ESS} can then be determined as the difference between the desired grid feed-in power and the PVG power. In this manner, the fluctuations of P_{PVG} are compensated by charging the ESS with the excess power during the upward ramps and discharging the ESS during the downward ramps. Note that in our notation the ESS power is positive when ESS is discharging and feeds power to the grid.

In addition to this basic procedure, the ESS utilizes a state of charge (SOC) control. This control actively balances the ESS energy E_{ESS} towards a reference value $E_{\text{ESS,ref}}$ by charging or discharging the ESS to minimize the required energy storage capacity [9]. A control block diagram of the simulated system utilizing SOC control is displayed in Figure 3.

The SOC control is a feedback-loop, where the PVG power is reserved from the grid feed-in power to balance ESS energy. The amount of reserved power can be controlled

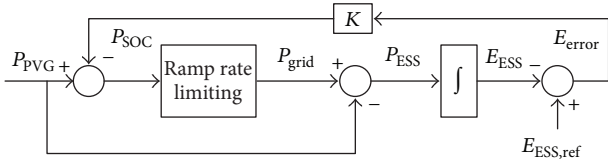


FIGURE 3: Block diagram of the used PV power ramp rate limiting procedure using an energy storage system equipped with state of charge control [9].

by setting an energy reference for the ESS and adjusting the proportional controller gain K . An optimum K value was found to be $1.5 \cdot 10^{-3}$ for all the cases presented in this paper. The reference value for $E_{ESS,ref}$ was set to be 0 Wh for convenience and deviations from this level were monitored to study the PV generator induced requirements for the ESS.

A noteworthy issue associated with SOC control is the possibility of producing an unintentional grid feed-in outage after a large downward fluctuation, while some PVG power due to diffuse radiation is still available. Many of the proposed control procedures in the literature seem to operate in such a way that they actually increase the overall power ramps in special circumstances and even cause grid feed-in power outages. This issue should be taken into account in the control of P_{grid} . The method used in this paper simply holds P_{grid} at a constant level after a large downward ramp has reached the generated power P_{PVG} until the SOC control is ready to increase P_{grid} again [15].

The simulated overall behavior of the RR limitation with ESS using the advanced SOC control strategy can be seen in Figure 4, where the simulated P_{PVG} , P_{grid} , P_{ESS} , and E_{ESS} of the 0.55 MWp PV generator are shown as a function of time for a day with some major fluctuations. The amount of PV generator power fluctuations fed into the grid is reduced due to ESS operation, and the remaining ramps have gentler slopes than in the original P_{PVG} . In order to realize this, the ESS had to be able to provide the grid of at least 0.81 p.u. (0.45 MW) peak power during that day in order to achieve full RR limit compliance.

The required storage of energy by the ESS during the selected day for compensating the fluctuations can be seen also in Figure 4. The negative values refer to discharged energy deficiency and positive values refer to charged energy surplus. The difference between the maximum and minimum energies determines the amount of required energy capacity C_{ESS} of ESS, which was 0.16 h (88 kWh) during that single day. It is also seen in Figure 4 how the ESS eventually reaches the ESS reference value $E_{ESS,ref}$ of 0 Wh after fluctuations.

This is in place to shortly clarify the main differences between our approach for obtaining ESS requirements for Northern European climate and the approach behind the state-of-the-art results for Southern European climate [9], since we compare the results. The starting point difference is that we use solely irradiance measured with 10 Hz sampling frequency and obtain PVG power data by spatial smoothing [10], but 5-second PV power plant data has been utilized in [9]. Then, in [9] a sudden worst-case irradiance fluctuation

from 100% to 10%, or vice versa, is assumed followed with a corresponding exponential decay of PVG power. Instead, one-year irradiance based PVG power data is directly analyzed in our study without any further assumptions about the PVG power decay during the irradiance ramps. The exponentially decaying worst fluctuation model of PVG power applied in [9] seems to work as planned, since real PVG power ramps are much smoother. One more difference of principle between the approaches is that we apply ESS control strategy, which restores ESS back towards the reference charge level after power ramps (see Figures 6, 7, and 9).

5. Energy Storage System Requirements

The example provided in Figure 4 demonstrates how the ESS requirements are formed. In order to produce a more valid examination which takes into account seasonal behavior and diurnal differences, the same study was extended over the course of the full year of 2012. The effective energy capacity and maximum power and cycle counts of the simulated ESS were gathered and analyzed and finally requirements for ESS were deduced. Furthermore, the study was renewed with data from the year 2014 to verify that no significant anomalies were present in 2012.

In order to verify the correctness of our research approach and the feasibility of the developed ESS control strategy, results are compared to results obtained by applying the worst fluctuation model from corresponding PV power plants located in Southern Europe [9]. Since the authors are affiliated mainly with the University of Navarra in Spain, the data gathered from the reference site is titled as the UNav results. The measurement data used in this study obtained in the Northern European climate at the Tampere University of Technology is titled, in turn, as TUT results. Both results are presented as commensurately as possible to reveal the possible differences caused by the applied methods and different climatic conditions.

5.1. Energy Capacity Requirements. The effective energy capacity requirements of ESS C_{ESS} for the two PV generator sizes are presented in Figure 5 as a function of applied RR limit both for the TUT and for the UNav results. The TUT capacities have been calculated using our enhanced ESS charging control strategy and the UNav capacities are based on the WFM charging control. Both TUT and UNav results show that the ESS capacity requirements are directly proportional to the PV generator size, since in both studies the normalized capacities of the two generator sizes are equal as a function applied RR limit. This finding is in line with earlier finding for PV generator sizes from 1kWp up to 100 MWp [15]. The capacity requirement decreases considerably with decreasing power fluctuation control requirement (increasing RR limit) for both results. The ESS capacity requirement increases drastically if the required RR limit is decreased below 5%/min. It is evident that the ESS capacity requirement decreases considerably, if high RR limits are sufficient to ensure power quality and balance in the grid.

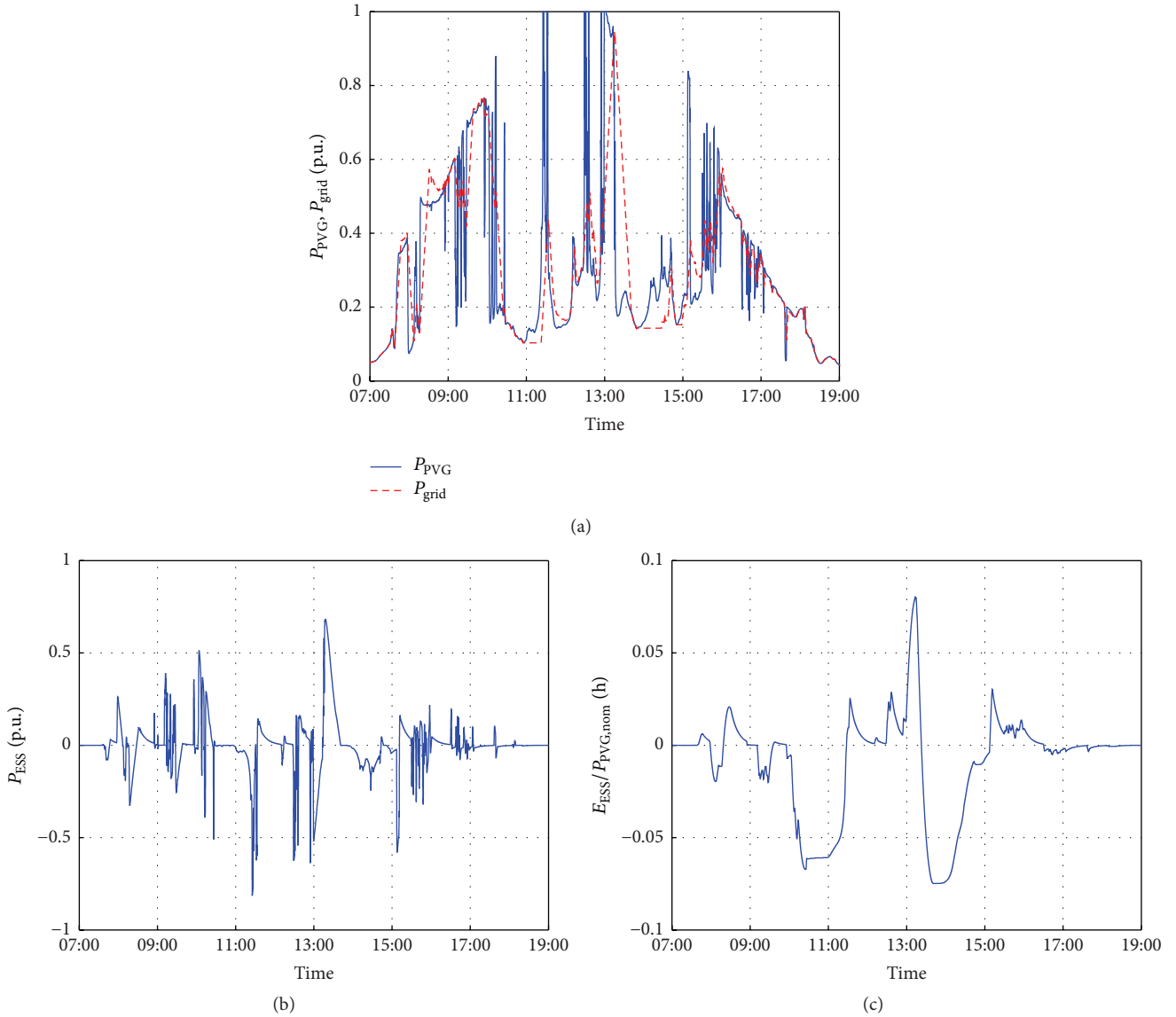


FIGURE 4: (a) Output power and ramp rate limited grid feed-in power of the 0.55 MWp PV generator, (b) power fed to the grid by ESS, and (c) energy stored to ESS while complying to RR limit of 3%/min on 13.08.2012. All variables have been normalized to the generator nominal power.

There are major differences in the ESS capacity requirements between the TUT and UNav results in Figure 5. The difference seems to be highest at low RR limits and decrease with increasing limit. To have a closer look on the ESS capacity requirements between the UNav and TUT systems, their relative difference is shown in Table 1 for several RR limits and the two PV generator sizes. It is clearly revealed how the UNav system requires as much as 50% more ESS capacity than the TUT system when high compensation of power fluctuations is required. For the typical RR limit requirement of 10%/min, the difference is still 24% for the smaller PV generator but decreases down to 5% for RR limit of 30%/min. For the bigger generator, the difference remains high above 30% also for high RR limits. One can conclude that applying the UNav results based on the WFM

TABLE 1: The relative difference of the UNav ESS energy capacity requirements with respect to the TUT requirements for different ramp rate limits and the two sizes of PV generators.

RR limit (%/min)	1	3	5	10	20	30
$C_{0.55\text{MWp}}$ (%)	50	48	32	24	15	5
$C_{2.2\text{MWp}}$ (%)	50	46	34	32	33	34

charging control procedure to PV power systems located in the Northern European climate could lead to drastic oversizing of ESS.

The large differences between the UNav and TUT energy storage capacity requirements are interesting, considering that the WFM charging control approach as such is logical

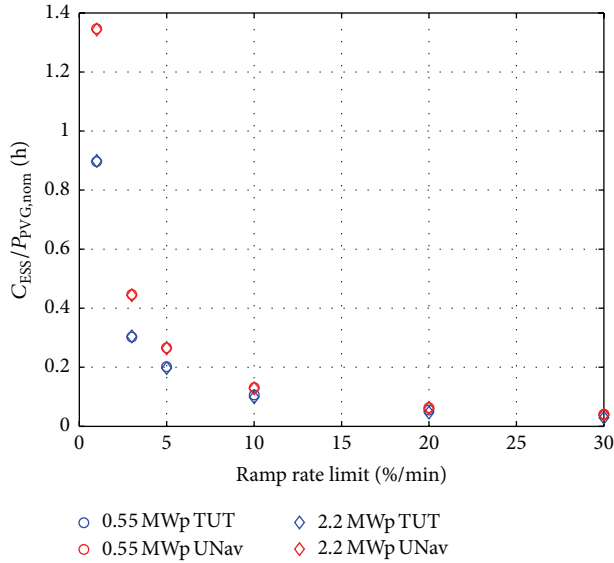


FIGURE 5: Energy capacity requirement for ESS as a function of the ramp rate limit for two sizes of PV generators located at Tampere region in Finland and Navarra region in Spain [9]. Capacities are normalized to the generators nominal power.

and the original aim of the TUT approach was to improve ESS operation mainly on the point of view of the power system operation. In order to find out the origin of these differences, the formation of the maximum absolute ESS capacity requirement of the TUT simulations during the year 2012 is shown in Figure 6 for the 0.55 MWp PV generator complying with RR limit of 3%/min.

From Figure 6, it is clear that the annual minimum of stored energy to ESS in the TUT system is formed entirely during a single large fluctuation, just like by applying the WFM. However, the steadily declining P_{grid} ramp stops declining after reaching a level of 0.3 p.u., which is 0.2 p.u. higher than what the WFM assumes. The WFM model assumes that the power decreases exponentially from 1.0 p.u. to 0.1 p.u. during the irradiance fluctuations. The duration of an uninterrupted P_{grid} ramp is the key factor in determining the minimum value of E_{ESS} in such a fluctuation. The WFM control assumes a ramp time of 33 minutes with RR limit of 3%/min, but in Figure 6 the ramp takes only about 23 minutes with the enhanced TUT control, resulting in lower discharged energy. Also fluctuations of the power fed to the grid decrease considerably when applying the TUT approach.

An example of strict power fluctuation compensation is presented in Figure 7, which displays the formation of the absolute maximum ESS energy deflection from the reference level during the year 2012 for the 0.55 MWp PV generator complying with RR limit of 1%/min. The strict RR limit changes P_{grid} behavior considerably from the 3%/min case. P_{grid} ramp descends for about 85 minutes, which is close to what the WFM also assumes. However, this time P_{PVG} fall is gradual, resulting in gentle slope of discharged energy. With this gentle slope, the discharged total energy of TUT is much smaller than what the WFM gives.

It is important to keep in mind that the moments presented in Figures 6 and 7 show the worst possible fluctuations experienced with the selected RR limits during the year 2012 in the Tampere area. The UNav capacity results, which have been obtained with simulation studies based on real PVG data using the WFM charge control, correlate qualitatively with our results. The WFM control is obviously quite logical providing a useable worst-case estimate for the required ESS capacity. However, the WFM seems to be too strict leading to oversizing of the ESS capacity. For optimum ESS sizing, more thorough analysis based on measurements should be used rather than assumptions based on worst-case models such as the WFM.

5.2. Maximum Power Requirements. Annual maximum ESS power requirements were also analyzed from the ESS simulations and the results can be seen in Figure 8 for the 0.55 and 2.2 MWp PV generators. The maximum power requirement decreases as the RR limit increases, but the decrease is much slower than in the case of the energy storage capacity requirement. The power capacity requirement decreases a bit faster for the 2.2 MWp generator than for the 0.55 MWp generator and the TUT results decrease faster than the UNav results. In practice, the applied RR limit does not seem to be very critical on the point of view of ESS power capacity sizing.

The TUT ESS power requirements differ from the UNav requirements being a bit higher at low RR limits for both generator sizes and clearly lower at high RR limits. In other words, the TUT power requirements have much steeper slopes as a function of the RR limit. Reasons behind these differences were once again found by studying the formation of the TUT requirements in detail. The formation of the power requirements for the 0.55 MWp PVG complying with RR limit of 1%/min is shown in Figure 9 and for the 2.2 MWp PVG complying with RR limit of 20%/min is shown in Figure 10.

In Figure 9, a large downward P_{PVG} fluctuation has required a lot of compensation energy (prior to 11:30), which the SOC control is slowly trying to regain by keeping P_{grid} at a low regulated constant value until 11:37 o'clock. P_{grid} regulation is still ongoing due to the low RR limit of 1%/min when a large upward P_{PVG} fluctuation begins, creating a rapidly increasing demand to charge ESS to compensate the upward ramp. Because the rise is so rapid and the starting point of P_{grid} is very low, the resulting P_{ESS} peak is very high close to 1 p.u. (see Figure 8), which is 0.07 p.u. higher than the UNav result. Also the ESS charging is done for a long time after the ramp with almost the same power as the PV generator produces. It is also demonstrated nicely in Figure 9 how a high requirement to compensate PV power fluctuations (small RR limit) leads to a high requirement for the ESS storage capacity.

The behavior of P_{grid} changes entirely when less demanding compensation of PV generator power fluctuations is required by applying high RR limits. The annual maximum ESS power requirement in Figure 10 reaches only a value of 0.65 p.u., although the generator power goes simultaneously above 1 p.u. The main reason for this is the higher RR limit but also the smoother P_{PVG} behavior has resulted in a higher

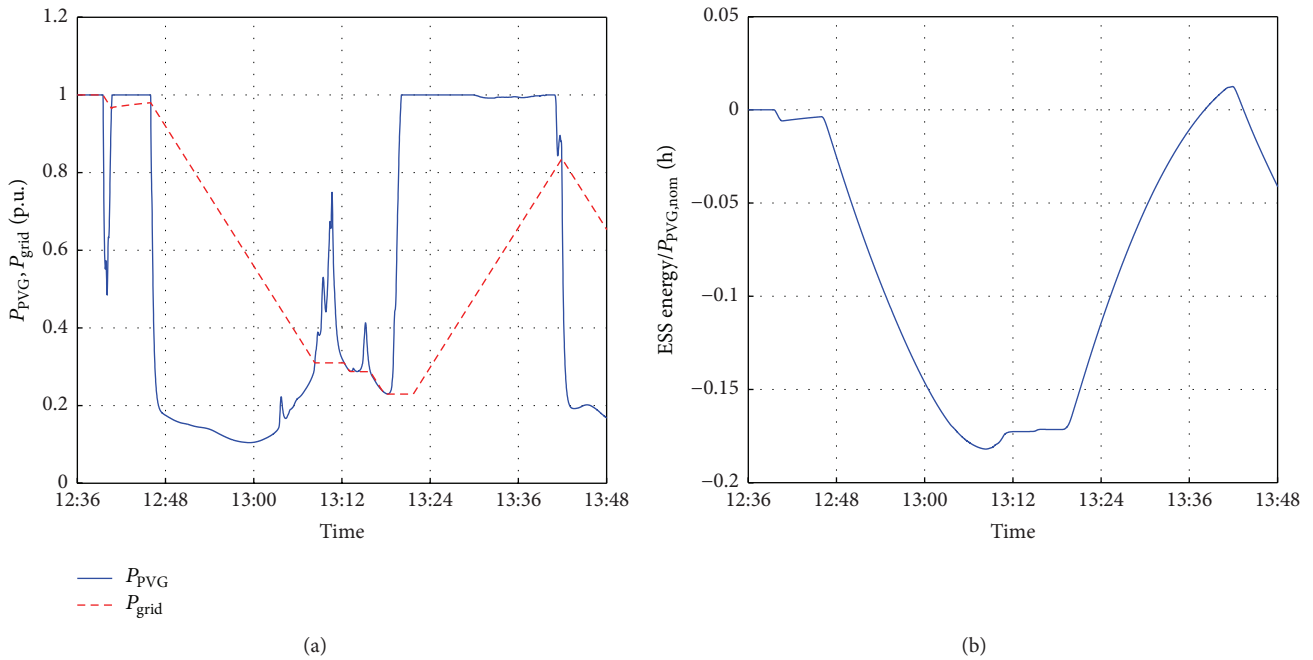


FIGURE 6: (a) 0.55 MWp PV generator and grid feed-in power and (b) the ESS energy during the formation of the minimum ESS energy with respect to the reference level causing the maximum absolute ESS capacity requirement of the TUT simulations on 09.04.2012 while complying with RR limit of 3%/min.

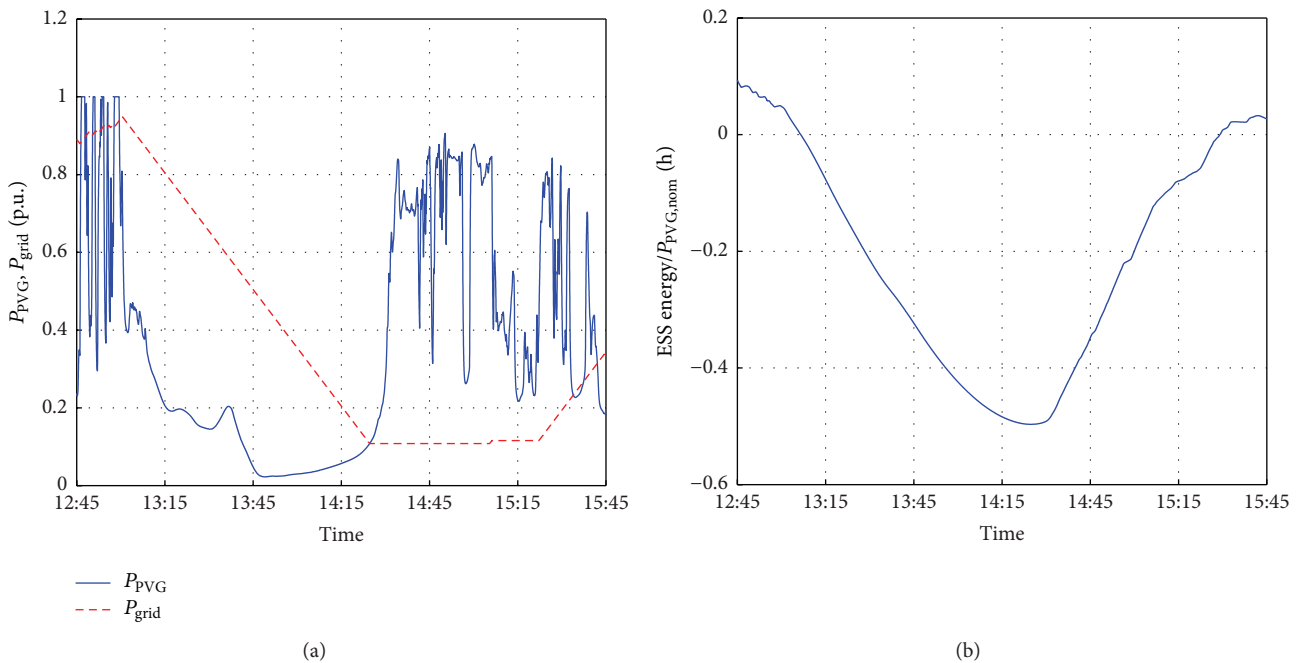


FIGURE 7: (a) 0.55 MWp PV generator and grid feed-in power and (b) the ESS energy during the formation of the minimum ESS energy with respect to the reference level causing the maximum absolute ESS capacity requirement on 27.06.2012 while complying with RR limit of 1%/min.

starting point for P_{grid} before the fluctuation. These translate into a smaller ESS power requirement compared to what UNav results imply.

The WFM charge control assumes that P_{grid} level ranges from 10 to 100% of $P_{PVG,nom}$ during PVG power fluctuation.

The minimum is defined with an assumption that the midday diffuse irradiance will always yield at least 10% of the clear sky PV power generation. Also the irradiance fluctuation is assumed to be a step function leading to an exponential PVG power fluctuation, which is actually never the case with real

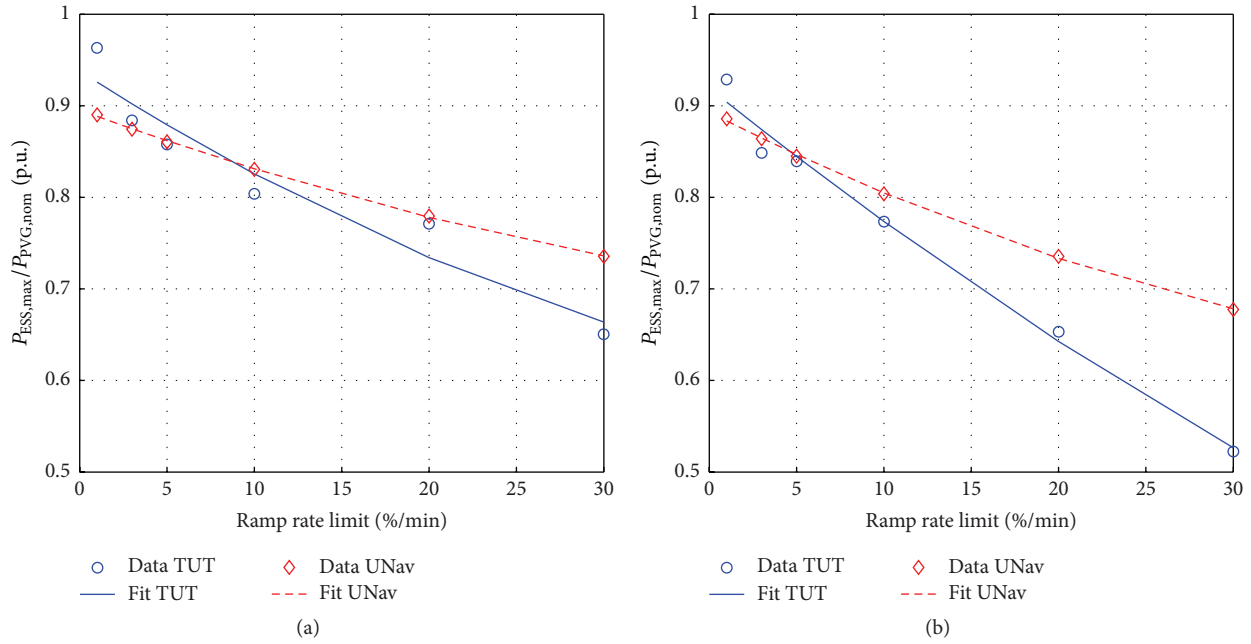


FIGURE 8: Simulated ESS maximum power requirements as functions of the ramp rate limit for (a) the 0.55 MWp and (b) 2.2 MWp PV generators. Values have been normalized to the generators nominal power. Overall trends have been depicted with the second-order polynomial fits. The results obtained by the researchers at the University of Navarra for corresponding PV generators located in western Spain are shown for comparison [9].

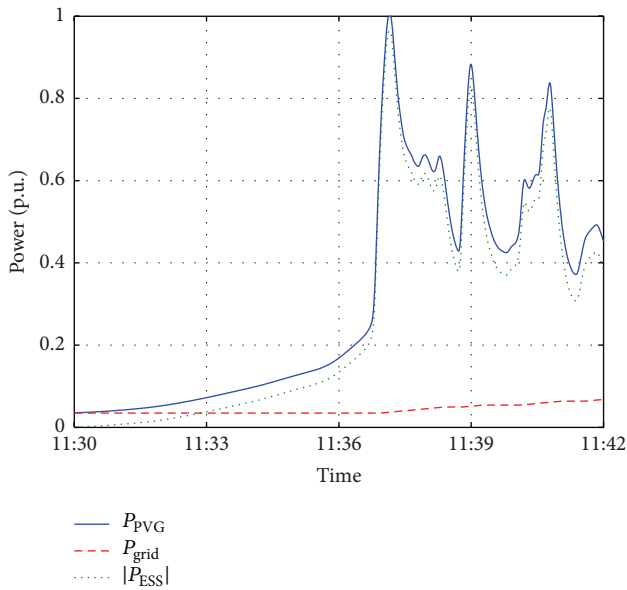


FIGURE 9: Output power of the 0.55 MWp PV generator, grid feed-in power, and the absolute power of ESS during the formation of the maximum ESS power requirement on 08.09.2012 while complying with RR limit of 1%/min.

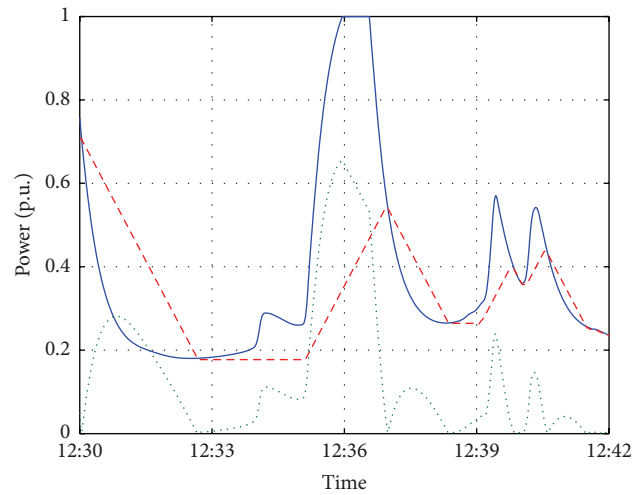


FIGURE 10: Output power of the 2.2 MWp PV generator, grid feed-in power, and the absolute power of ESS during the formation of the maximum ESS power requirement on 07.06.2012 while complying with RR limit of 20%/min.

fluctuations caused by cloud shading. Figures 9 and 10 clearly show that these assumptions do not come true as such in real cases. Those assumptions are reasonable for obtaining a rough worst-case estimate, but they can easily lead to oversizing of ESS.

5.3. Cycling Induced Storage Degradation. In addition to energy capacity and power requirements, a key sizing issue and storage technology selection factor is the determination of the fatigue that the ESS is subjected to in this application. Application induced fatigue can be measured by counting

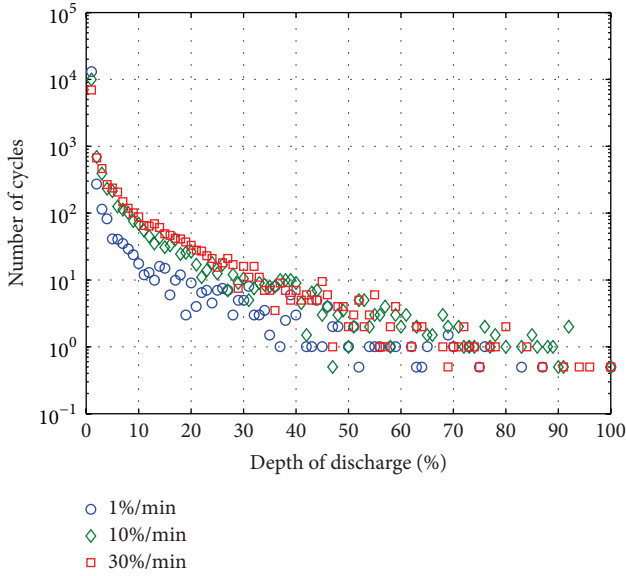


FIGURE 11: Observed number of energy storage charge-discharge cycles as a function of the depth of discharge for compensating the 0.55 MWp PV generator using three different ramp rate limits during the year 2012. The depth of discharge is calculated with respect to the observed effective energy capacity requirements shown in Figure 5.

the number of charge-discharge cycles. With considerable cycling, the ESS can degrade so much that it no longer satisfies its design criteria and has to be replaced. For example, the amount of annual degradation compared to the expected lifetime of the PV system determines whether a specific storage technology is viable in this application or not.

In practice, cycling induced degradation can be determined by counting the number of observed ESS charge-discharge cycles N . ESS can be charged or discharged in random sequences with any amplitude between 1 and 100% of its effective capacity. This amplitude is referred to as the depth of discharge (DOD). ESS can have a different cycle life depending on the DOD. Thus, cycles have to be counted separately for each degree of the DOD. In this paper, the popular rainflow-counting algorithm was used to count the cycles [16]. The cycles were counted for different cases using the two different PVG sizes and various RR limits. The number of cycles as a function of DOD can be seen in Figures 11 and 12 for the two PV generator sizes and different RR limits. It should be noted that DOD is expressed with respect to the effective energy capacity required for each case. Therefore, a higher number of small DOD cases exist when applying high RR limits than when applying low RR limits (Figure 11), which require higher maximum ESS energy capacity. Also some storage technologies might not be able to withstand deep 80–100% discharges, which should be taken into account by adjusting $E_{\text{ESS,ref}}$ and C_{ESS} accordingly.

The number of charge-discharge cycles decreases exponentially with increasing depth of discharge for all the generator sizes and RR limits presented in Figures 11 and 12. This means that the ESS mostly compensates small fluctuations rather than large ones. The number of cycles in Figure 12

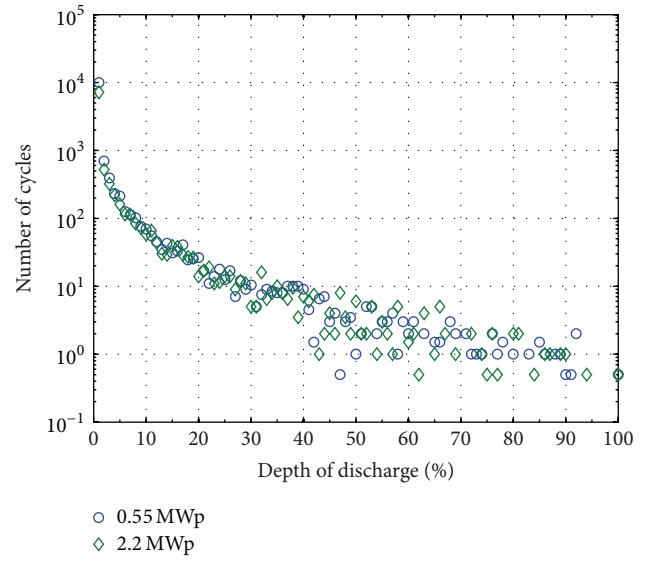


FIGURE 12: Observed number of storage charge-discharge cycles as a function of the depth of discharge for compensating two different generator sizes complying to a ramp rate limit of 10%/min during the year 2012. The depth of discharge is calculated with respect to the observed effective energy capacity requirements shown in Figure 5.

indicates that the PV generator size has no significant effect on overall cycling.

The results from the cycle counting as such do not reveal much, and no trends are visible either. To obtain a more precise indicator for ESS degradation, a comparison to the maximum cycling tolerance of ESS is necessary. This means that a specific ESS needs to be selected. In this paper, as an example, a degradation study is done for ESS containing lithium-titanate batteries from Altairnano [17]. The cycle life curve, that is, the maximum amount of tolerable cycles $N_{\text{ESS,max}}^{\text{DOD}}$ for each DOD value, of this battery is depicted in Figure 13.

The maximum number of cycles as a function of DOD presented in Figure 13 is used as a reference which the observed number of cycles $N_{\text{obs}}^{\text{DOD}}$ for each DOD value has been compared to (Figures 11 and 12). The overall annual degradation is obtained as the sum of individual comparisons over all degrees of DOD as follows:

$$C_{\text{deg}} = \sum_{\text{DOD}=1\%}^{100\%} \frac{N_{\text{obs}}^{\text{DOD}}}{N_{\text{ESS,max}}^{\text{DOD}}} \cdot 100\%. \quad (4)$$

By using (4) and the previously presented annual cycle counts, the cycling induced degradation of an Altairnano ESS was calculated. The results for the two PV generators and different RR limits are presented in Table 2. The main observation is that the amount of degradation is below 0.5% in a year in almost all cases. A conclusion from this is that storage technologies do not cause insuperable fatigue obstacles on ESS application, although the low level of degradation in Table 2 is due to the selection of a highly cycle-durable battery technology.

TABLE 2: Cycling induced degradation of an Altairnano battery energy storage system compensating the power fluctuations of two different PV generators with different ramp rate limits located in Northern European climate during the year 2012.

RR limit (%/min)	1	2	5	10	20	30
$C_{\text{deg},0.55 \text{ MWp}} (\%)$	0.22	0.31	0.36	0.47	0.53	0.47
$C_{\text{deg},2.2 \text{ MWp}} (\%)$	0.20	0.27	0.31	0.42	0.47	0.42

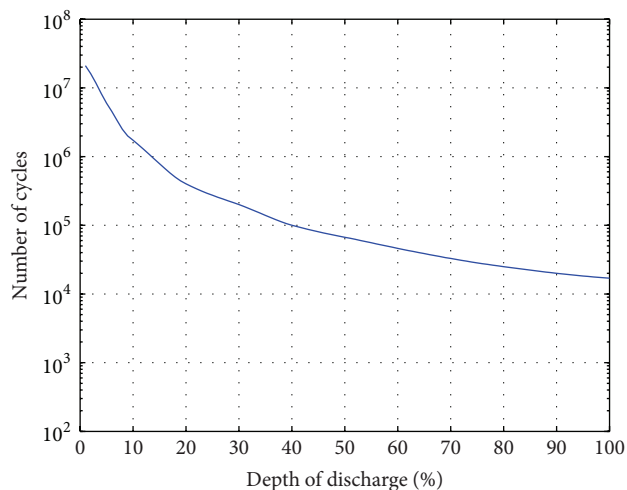


FIGURE 13: Maximum number of cycles as a function of DOD for an Altairnano lithium-titanate battery adapted from [17] (Altairnano[®]).

Degradation increases with increasing RR limit up to the 20%/min and after that seems to reduce. This is in line with the earlier observed smaller number of ESS cycles when applying a small RR limit instead of high RR limits shown in Figure 11. Degradation seems to decrease slightly also with increasing PV generator size, which is in line with the small differences of the number of cycles between the two PVG sizes in Figure 12.

The amount of degradation is of the same order of magnitude with similar degradation studies conducted in Southern Europe with a Li-ion battery technology [11]. Due to differences in determining the ESS requirements, the effective DOD ranges, and the selected ESS technologies, a more thorough comparison is not meaningful. An overall conclusion from this degradation study is that, by selecting the right technology for ESS, PV power fluctuations can be compensated irrespective of the required RR limit without unnecessarily high cycling degradation.

6. Conclusions

Requirements for sizing an energy storage system to compensate PV generator's power fluctuations with various ramp rate limits have been determined in this paper. The study utilized irradiance and PV module back plate temperature measurements performed by the Tampere University of Technology solar PV power research plant located in Tampere,

Finland. A first-order low-pass filter method was applied to estimate spatial smoothing of irradiance over different PV generator areas. PV generator output power was then modelled using the smoothed wide area irradiance and PV module temperature as inputs.

The model was further used to provide scalable and general PV generator behavior as an input for energy storage system simulations. The modelled PV generator power was fed through the ramp rate limiter to calculate the desired limit compliant grid feed-in power. The required energy storage power was then determined as the difference between the grid feed-in and the PV generator power. In addition, an enhanced state of charge control strategy was developed and applied to decrease the magnitude of the grid feed-in power fluctuations. A full year of irradiance and temperature measurements with a sampling frequency of 10 Hz were then used to simulate the operation of the energy storage system for 0.55 and 2.2 MWp PV generators using different ramp rate limits.

Effective energy storage capacity, power, and charge-discharge-cycling were determined from the simulations. The required maximum energy storage capacity was found to be directly proportional to the PV generator nominal power and to decrease exponentially with decreasing requirements to compensate PV generator power fluctuations, that is, with increasing ramp rate limit. The required maximum power of the energy storage system decreases linearly with increasing ramp rate limit. Additionally, it decreases slightly with increasing PV generator size, when normalized to the generator nominal power. Cycling induced degradation of a selected commercial battery technology was shown to be below 0.5% per year for both PV generator sizes and for almost all ramp rate limits. Degradation increases with increasing ramp rate limit up to 20%/min and then decreases. An overall conclusion is that storage technologies do not cause overwhelming obstacles on ESS application for compensation of fast PV power fluctuations.

The sizing requirements presented in this paper were also compared to requirements obtained in similar studies done in a Southern European climate in Spain. The comparison showed significant differences in energy capacity and maximum power requirements between the two studies. Most notably, the capacity requirements for the energy storage system were up to 50% higher in the reference study than in this study when high compensation was required. The large differences are mainly achieved by the enhanced state of charge control strategy applied in our study, but also the climatic differences may have caused some differences. The differences translate directly into smaller ESS sizing requirements and better operation of the storage system. Therefore, in order to determine optimum energy storage systems to limit PV generator power fluctuations, advanced control strategies utilizing local measurements should be used for system sizing.

Competing Interests

The authors declare that they have no competing interests.

References

- [1] J. Marcos, L. Marroyo, E. Lorenzo, and M. García, "Smoothing of PV power fluctuations by geographical dispersion," *Progress in Photovoltaics: Research and Applications*, vol. 20, no. 2, pp. 226–237, 2012.
- [2] R. van Haaren, M. Morjaria, and V. Fthenakis, "Empirical assessment of short-term variability from utility-scale solar PV plants," *Progress in Photovoltaics: Research and Applications*, vol. 22, no. 5, pp. 548–559, 2014.
- [3] V. Gevorgian and S. Booth, "Review of PREPA Technical Requirements for Interconnecting Wind and Solar Generation," 2013, <http://www.nrel.gov/docs/fy14osti/57089.pdf>.
- [4] S. Rahman and K.-S. Tam, "A feasibility study of photovoltaic-fuel cell hybrid energy system," *IEEE Transactions on Energy Conversion*, vol. 3, no. 1, pp. 50–55, 1988.
- [5] B. Yang, Y. Makarov, J. Desteese et al., "On the use of energy storage technologies for regulation services in electric power systems with significant penetration of wind energy," in *Proceedings of the 5th International Conference on the European Electricity Market (EEM '08)*, pp. 1–6, Lisboa, Portugal, May 2008.
- [6] N. Kakimoto, H. Satoh, S. Takayama, and K. Nakamura, "Ramp-rate control of photovoltaic generator with electric double-layer capacitor," *IEEE Transactions on Energy Conversion*, vol. 24, no. 2, pp. 465–473, 2009.
- [7] T. D. Hund, S. Gonzalez, and K. Barrett, "Grid-tied PV system energy smoothing," in *Proceedings of the 35th IEEE Photovoltaic Specialists Conference (PVSC '10)*, pp. 2762–2766, IEEE, Honolulu, Hawaii, USA, June 2010.
- [8] G. Karmiris and T. Tegnér, "Control method evaluation for battery energy storage system utilized in renewable smoothing," in *Proceedings of the 39th Annual Conference of the IEEE Industrial Electronics Society (IECON '13)*, pp. 1566–1570, Vienna, Austria, November 2013.
- [9] J. Marcos, O. Storkel, L. Marroyo, M. Garcia, and E. Lorenzo, "Storage requirements for PV power ramp-rate control," *Solar Energy*, vol. 99, pp. 28–35, 2014.
- [10] I. de la Parra, J. Marcos, M. García, and L. Marroyo, "Control strategies to use the minimum energy storage requirement for PV power ramp-rate control," *Solar Energy*, vol. 111, pp. 332–343, 2015.
- [11] J. Marcos, I. de La Parra, M. García, and L. Marroyo, "Control strategies to smooth short-term power fluctuations in large photovoltaic plants using battery storage systems," *Energies*, vol. 7, no. 10, pp. 6593–6619, 2014.
- [12] C. Rus-Casas, J. D. Aguilar, P. Rodrigo, F. Almonacid, and P. J. Pérez-Higueras, "Classification of methods for annual energy harvesting calculations of photovoltaic generators," *Energy Conversion and Management*, vol. 78, pp. 527–536, 2014.
- [13] D. Torres Lobera, A. Mäki, J. Huusari, K. Lappalainen, T. Suntio, and S. Valkealahti, "Operation of TUT solar PV power station research plant under partial shading caused by snow and buildings," *International Journal of Photoenergy*, vol. 2013, Article ID 837310, 13 pages, 2013.
- [14] J. Marcos, L. Marroyo, E. Lorenzo, D. Alvira, and E. Izco, "From irradiance to output power fluctuations: the PV plant as a low pass filter," *Progress in Photovoltaics: Research and Applications*, vol. 19, no. 5, pp. 505–510, 2011.
- [15] J. Schnabel and S. Valkealahti, "Compensation of PV generator output power fluctuations with energy storage systems," in *Proceedings of the 31st European Photovoltaic Solar Energy Conference and Exhibition*, Hamburg, Germany, September 2015.
- [16] M. Chawla, R. Naik, R. Burra, and H. Wiegman, "Utility energy storage life degradation estimation method," in *Proceedings of the IEEE Conference on Innovative Technologies for an Efficient and Reliable Electricity Supply (CITRES '10)*, pp. 302–308, IEEE, Waltham, Mass, USA, September 2010.
- [17] Altair Nanotechnologies Inc, PowerRack® Product Overview, 2015, <http://www.altairnano.com/products/powerack/>.

Research Article

Characterization of Photovoltaic Panels by means of Thermograph Analysis

Noe Samano, José Alfredo Padilla-Medina, and Nimrod Vázquez

Electronics Engineering Department, Technological Institute of Celaya, 38010 Celaya, GTO, Mexico

Correspondence should be addressed to Nimrod Vázquez; n.vazquez@ieee.org

Received 26 March 2016; Accepted 25 May 2016

Academic Editor: Prakash Basnyat

Copyright © 2016 Noe Samano et al. This is an open access article distributed under the Creative Commons Attribution License, which permits unrestricted use, distribution, and reproduction in any medium, provided the original work is properly cited.

Solar panels have become attractive in order to generate and supply electricity in commercial and residential applications. Their increased module efficiencies have caused not only a massive production but also a sensible drop on sale prices. Methods of characterization, instrumentation for in situ measurements, defect monitoring, process control, and performance are required. A temperature characterization method by means of thermograph analysis is exposed in this paper. The method was applied to multicrystalline modules, and the characterization was made with respect to two different variables, first a thermal transient and second a characterization with respect to the current. The method is useful in order to detect hot spots caused by mismatch conditions in electrical parameters. The description, results, and limitations of the proposed method are discussed.

1. Introduction

The energy availability in photovoltaic (PV) panel strongly depends on temperature and solar irradiation [1]. Actually, the temperature is one of the main factors which affect seriously the efficiency of solar cells. It is well known that the generated voltage with a solar cell varies with temperature [2]. Dependence on the temperature in a typical PV module characteristic is illustrated in Figure 1.

When temperature increases, the generated voltage decreases. Apart from this temperature effect on the cell voltage, there exists another phenomenon which is related to the temperature known as a “hot spot.” A hot spot is a specific well-located region with the higher temperature than the other parts of the cell. While temperature value causes voltage affections, the hot spot phenomenon causes a wide variety of cell problems, as lower efficiency and physical damage.

A thermal transient analysis is reported in the literature [1]: such study was obtained by registering the temperature for a single amorphous silicon module and a couple of monocrystalline modules every minute after a change in environmental conditions. Although the main purpose of this paper was not transient thermal characterization, authors used this for explaining the effect of the module heat in a capacitance during described conditions.

This reported method [1] began by the whole covering of the module in order to reach the equilibrium temperature with the environment. Once steady state temperature is reached, the module was uncovered and a measure of temperature was taken every minute with the aid of thermocouples. Measures were recorded during a period of 24 minutes. Results are shown in Figure 2.

A hot spot may be produced due to the next three reasons: a shadow projected in the module [3–5], a mismatch condition between cells [6–8], or a manufacturing defect [9–11].

Traditionally, the cells in a module are connected in series, and the current at the maximum power point I_{mpp} becomes critical [12]. When a cell in a serial string produces less power than the rest (due to a hot spot), the maximum power of the string cannot match the maximum power of that “poor” cell. This means that the cells cannot give more energy to the output load, although they are able to produce it.

Therefore, the generated current on excess by any “good” cell is forced to circulate through the internal diode by itself. When module works near short-circuit condition, then voltage may exhibit this as a “poor” cell. In these circumstances, the cell dissipates power instead of generating it.

Hot spots detection is important because it is easier for problem identification or finding photovoltaic module defects. Once a hot spot is detected in a module or array, it

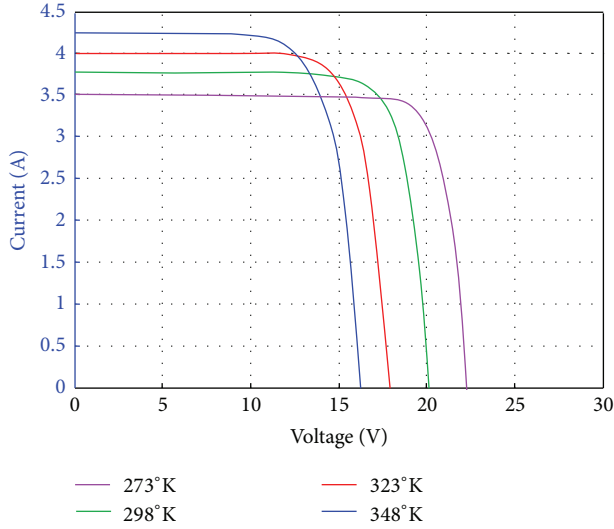


FIGURE 1: Typical PV solar curve and the effect of temperature.

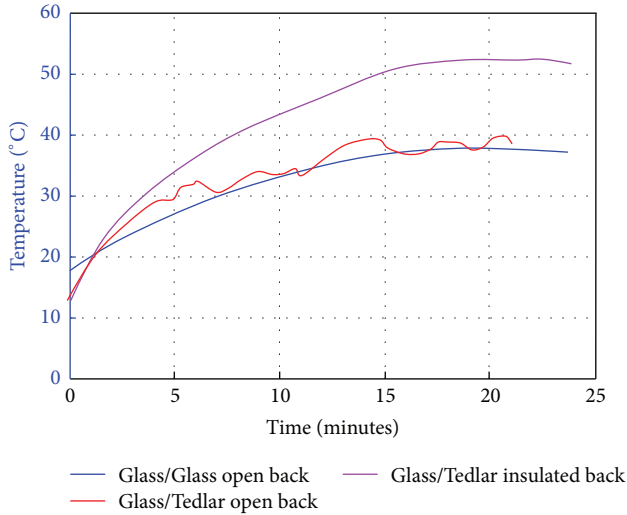


FIGURE 2: Transient of three PV modules as shown in [1].

is evident that an amount of the total power produced by the array is being dissipated in that cell instead of the output load.

Since temperature and hot spots problems are the main factors which affect photovoltaic modules, research on this issue has become important, in order to have a better understanding of these phenomena and, therefore, improve PV system designs.

The PV panel's characterization by means of thermograph analysis for in situ measurements, defect monitoring, process control, and performance is proposed in this paper. Technique on infrared temperature measurement is used for detecting hot spots and establishing the thermal behavior of solar cells.

This paper focused on characterizing thermal behavior. Thermal transients in PV panels were studied at first; and, later, temperature characterization with respect to the module

current was made. These two studies allow us to detect and identify the existence of hot spots in the solar module.

The paper is organized as described next: some facts of PV panels are mentioned in Section 2; the work bench for the characterization is detailed in Section 3; in Section 4, the thermal transient is discussed; the current characterization is presented in Section 5; and some final conclusions are given at the end.

2. Model and Facts in PV Panels

When a PV module is under the sunlight, it produces energy. When the generated energy is not required, it is consumed as heat by the panel itself, since the PV panel is not operating at the maximum power point, its life time is deteriorated no matter if energy is not delivered. It has to be kept in mind that the possible coldest temperature is reached once the PV panel is operating at the maximum power point.

The hot spots existence in a PV panel decreases the life time for cells [13, 14]; also, as a consequence, the amount of generated energy becomes reduced. The effect of a hot spot is similar to the PV panel behavior under partially shaded areas [15, 16], so that multiple maximum power points start to appear, which seriously affect energy production.

A simplified model for the PV panel is found in [16]:

$$i_{PV} = \lambda I_{sc} - \lambda I_s \left(e^{(qv_{PV}/AKT)} - 1 \right), \quad (1)$$

where A is the ideality factor of the diode, K is the Boltzmann constant, q is the electron charge, λ is the percentage of irradiance ($1 = 100\%$), I_{sc} is the short-circuit current of the PV panel, I_s is the saturation current of the diode, T is the temperature of the ambient in $^{\circ}\text{K}$, v_{PV} is the voltage of PV panel, and i_{PV} is the current of PV panel.

It should be noticed that the only variables to be considered are the irradiance, the temperature, the cell voltage, and current, once the PV panel has been built. The other terms are constants. The PV panel power is then

$$p_{PV} = v_{PV} \left[\lambda I_{sc} - \lambda I_s \left(e^{(qv_{PV}/AKT)} - 1 \right) \right]. \quad (2)$$

The maximum power point may be obtained by making the derivative equal to zero, and neglecting the irradiance and temperature variations, the next equation is obtained:

$$\begin{aligned} \frac{d}{dt} p_{PV} &= \left(\lambda I_{sc} + \lambda I_s - \left(\lambda I_s + \frac{qv_{PV}}{AKT} \right) e^{(qv_{PV}/AKT)} \right) \frac{d}{dt} v_{PV}. \end{aligned} \quad (3)$$

From this last expression, it may be deduced that the maximum power point occurs at specific panel voltage (v_{PV}), and the value depends on the construction of the PV cell; then, if a mismatching of cells during construction could happen, the maximum power point would be different and, therefore, a cell temperature variation would also be registered between cells. This is demonstrated by the characterization proposed in this paper.

3. Work Bench and Specifications

The analysis was made for two mc-Si modules with the following characteristics:

- (i) Module type 17(110) P1470X680, of Yingli Solar.
- (ii) Peak power 110 W.
- (iii) Peak voltage 17.5 V.
- (iv) Peak current 6.3 A.
- (v) 36 cells connected in series.
- (vi) Glass top surface.
- (vii) Polymer rear surface.

Both modules were mounted in a structure oriented 20° to the south, in correspondence with the latitude of the installation place.

An infrared camera was used in order to measure the temperature. It was able to detect wavelengths from $7.5 \mu\text{m}$ to $13 \mu\text{m}$ in the region of the far infrared.

Since the front surface of the modules is reflective, the using of the rear surface of the module is a better choice. The temperature on the front side was compared with temperature on the back side of the module by using an infrared thermometer; it was found that practically both data sets have the same value. When thermographs are taken at the back side, it is avoided to have the shadows which normally occur on the front surface of the module due to weather conditions.

A temperature gradient between the back surface and the cell was considered since the temperature measured on the back surface of the modules is not exactly the actual temperature of the cells. Particularly for mc-Si cells in thermal equilibrium, irradiance is near to 1000 W/m^2 , wind speed is less than 3 m/s, and the temperature gradient between both surfaces is about 2 or 3°C , which may just be added as an offset [3].

The thermographs were taken at 1 m distance from the back surface because this is the maximum distance, at which the camera was able to focus clearly. This limitation, added to the lens of 17 mm connected to the camera, made reading the temperature of the whole module in a single image impossible; for solving this issue, 36 cells from the module were measured in order to complete the module thermograph. According to this configuration, only a couple of cells fitted perfectly in the view field from the camera.

The two modules were operated at three different operating points in order to detect the anomalies in the temperature distribution. Then, the thermographs were taken, when the modules generate 6 W, 30 W, and 60 W. The resulting concatenated cells are shown in Figure 3.

It is clearly shown in Figure 3 that some cells in module A are hotter than some other cells while the module generates 6 W and 30 W. On the other side, module B shows a homogenous distribution at the three points of operation, while module A has much contrast. It is also easily seen that module B was colder when it worked near the maximum power point; this occurs because only a portion of the total amount of irradiated energy in the module is converted to

heat; the rest is supplied to the external load. On the opposite, when the module works in an operation point far from the maximum power point, then the irradiated energy in the module mainly becomes on heat.

It may also be easily seen in Figure 3 that module A contains some cells at a temperature which does not match the cells located around it. It is an alert for a hot spot problem in those cells. Due to this, cells 16 and 25 were chosen as the sample for subsequent tests, where cell 16 represents an abnormal situation and cell 25 exhibits a normal condition. Since these cells are neighbors, both were selected to be captured in a single image.

A DC/DC boost converter was used as the load for the PV modules (Figure 4); this was employed in every developed test in this paper. Since the duty cycle for the converter may be changed as wished, this means that the operation point for the module could be changed as fast as needed.

All measures were made with calibrated equipment, model E-25, of FLIR, with a resolution of 160×120 pixels, the spectral range of $7.5 \mu\text{m}$ and $13 \mu\text{m}$, and a precision of $\pm 2\%$. The tests were made by considering more than a single experiment; however, for a matter of simplicity, the reported tests are for just one case.

4. Thermal Transient

As mentioned before, cells 16 and 25 were chosen in module A for temperature analysis and characterization data.

First of all, characterization with respect to time was made, because the obtained information for this case should be of transcendental relevance with respect to the characterization for the operating point of the module. It was found in the literature [1] that the temperature of a c-Si module reaches steady state condition until 24 minutes have passed. For analysis purposes, a mc-Si solar cell was employed in this paper, so that more time was considered for the thermal transient characterization.

The first test was developed with a current value of 0.6 A as operating point for the module, once the thermal equilibrium was reached; the operating point was suddenly changed to a current value of 6 A. The temperature was recorded every minute during a 50-minute period.

A temperature graph for cell 16 is shown in Figure 5(a); it should be observed that although the technique for measuring transient temperature was a little bit different, the behavior during the first 24 minutes is almost the same as that reported in the literature [1]. Although temperature seems to reach its maximum value in approximately 25 minutes, however, the steady state takes more time (see Figure 5(a)). It is worth mentioning that this test was done at midday.

Another test was developed, where the transient was carried out starting from a current value of 6 A and finishing with a current value of 0.6 A. The temperature graph is illustrated in Figure 5(b); particularly for this case, the recorded time was only for a period of 30 minutes; as it may be observed, the curve is very similar to that in Figures 2 and 5(a) but inverse.

Finally, the temperature evolution for cells 16 and 25 was recorded simultaneously, with an operating point for the

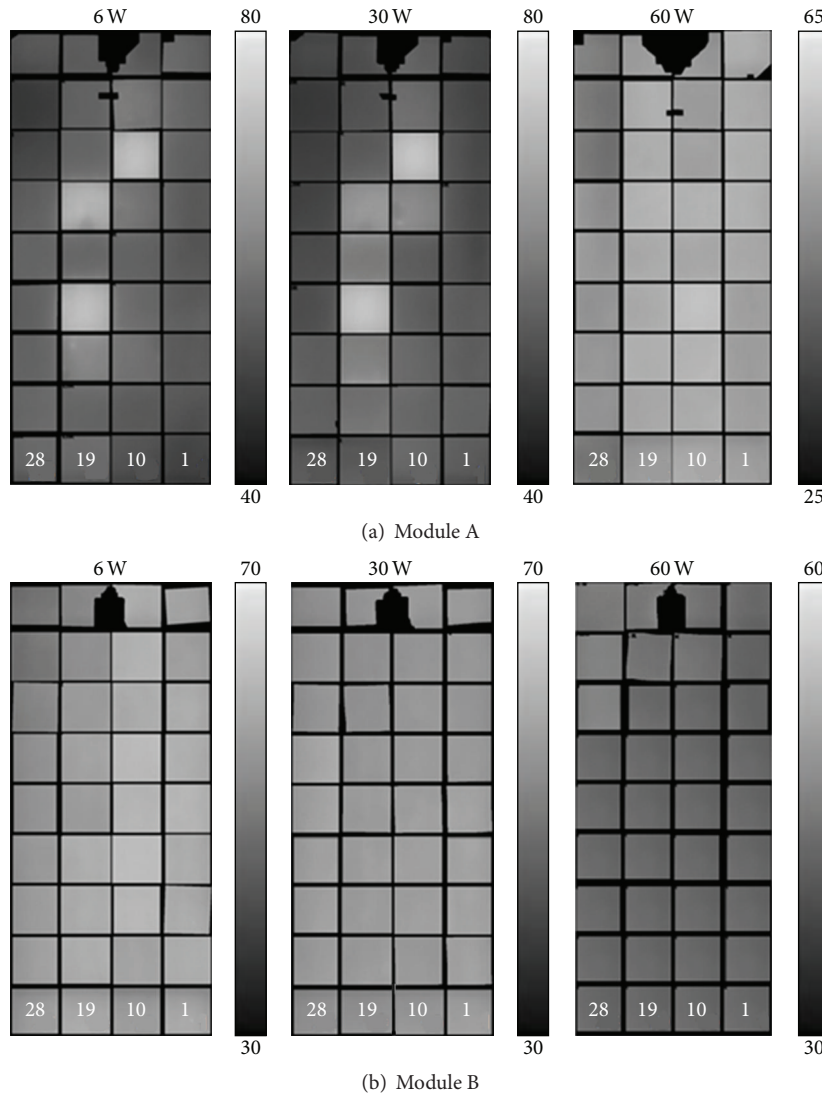


FIGURE 3: Temperature of two mc-Si modules at three operating points.

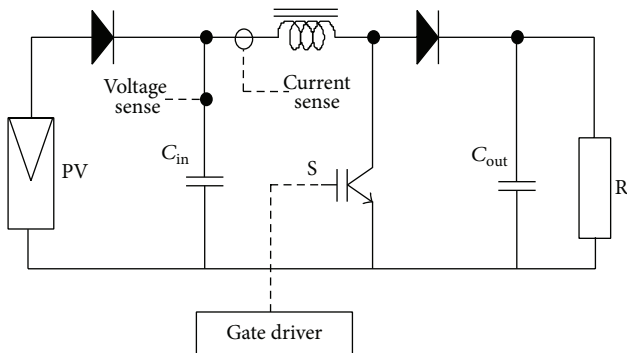


FIGURE 4: PV panel and power stage.

module by passing from a current of 5 A to a current of 6 A. Conditions for this test were established in order to analyze if the behavior, which is shown in Figure 5(a), is reproducible

in spite of having a lower step change. The resulting curve is illustrated in Figure 6(a).

Some interesting facts are implicitly revealed in this figure. In the first place, the shape of the temperature curve is similar to those obtained before, which means that the behavior of transient temperature does not depend on the step change for the operating point or weather conditions. In the second place, it should be noticed that cell 16 becomes hotter while cell 25 gets colder, under the same current step conditions. This is explained because the presence of hot spots produces mismatch conditions for the cells.

The temperature difference between cells 16 and 25 is shown in Figure 6(b). It may easily be observed how in 10 minutes the cells reach their bigger temperature difference, and later it is kept constant.

According to tests described before, the temperature transient takes around 30 minutes, so that any experiment for characterization should at least wait for 30 minutes between every capture.

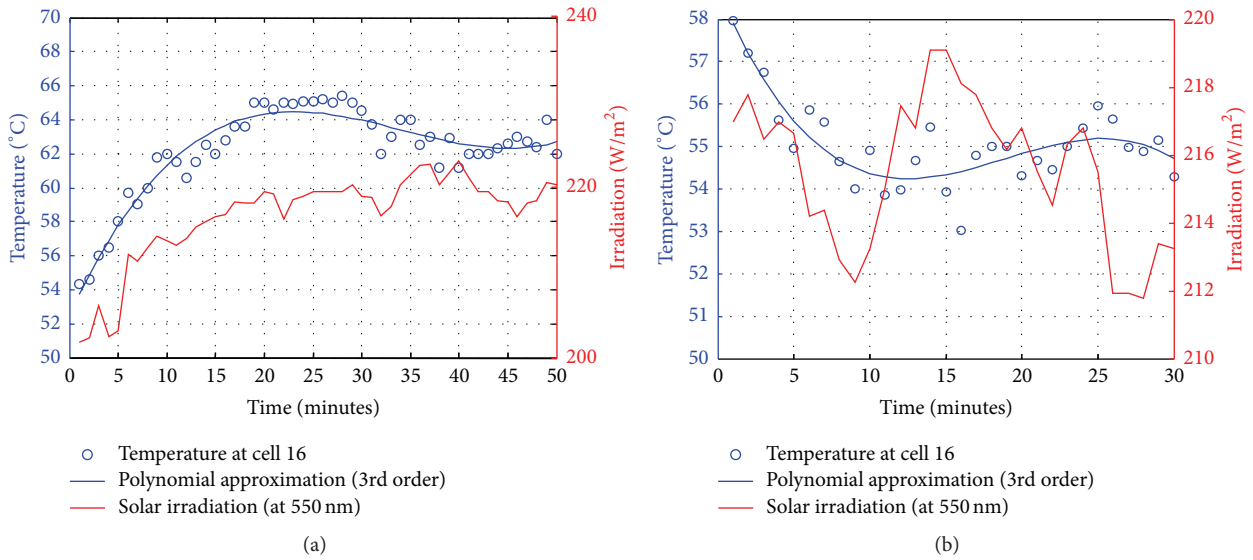


FIGURE 5: Thermal transient of cell 16 of module A. (a) For a current step up. (b) For a current step down.

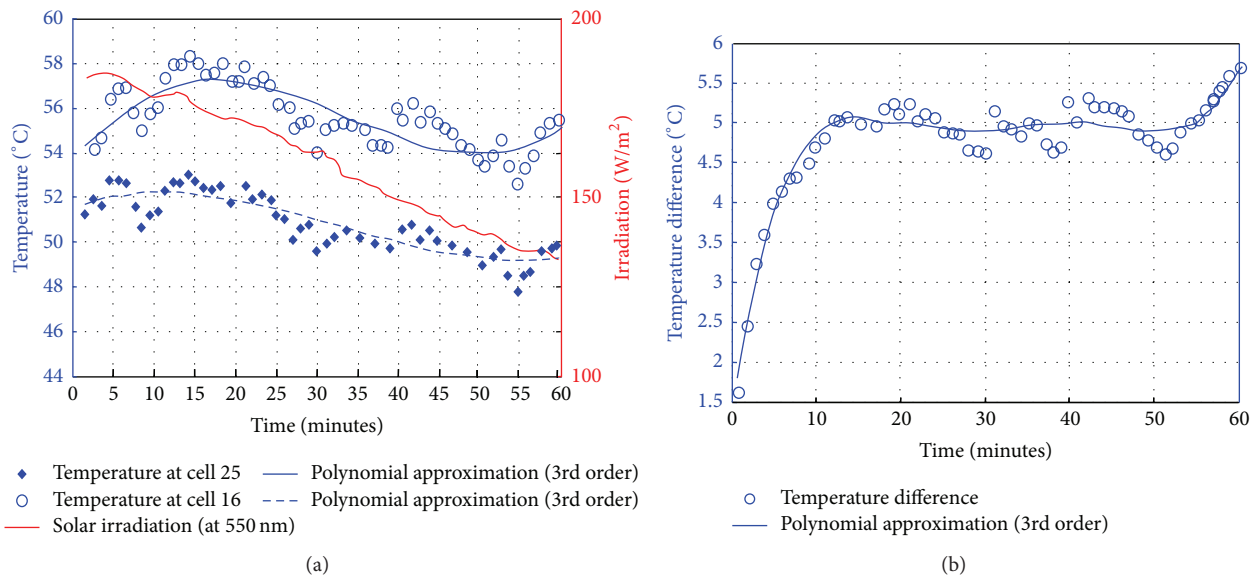


FIGURE 6: Thermal transient of screens 16 and 25 of module A. (a) For a small current step up. (b) Temperature difference.

The statistical analysis has an error of ± 1.3 , for cells 16 and 25. The difference between both cells was statistically significant ($t = -55-13$, $df = 59$, and $p = 1.85e - 52$).

5. Current Characterization

An analysis for the current was developed as a test in order to obtain the best possible characterization. A period of time of 30 minutes was established in order to let the temperature reach the steady state conditions while the applied current to the module was increased at that period of time.

Unfortunately, changes on weather conditions made it very hard to carry out the tests under exactly the same conditions; however, this factor may be diminished. All the tests were developed from 11:00 a.m. to 4 p.m. in order to minimize the effects due to weather conditions; this procedure certainly meant such a great amount of time in order to be able not only to conclude and validate all cells but also to establish all the possible module defects.

The characterization for the current was done for cells 16 and 25, due to a mismatch found from these cells on previous analysis. The temperature was registered while the module

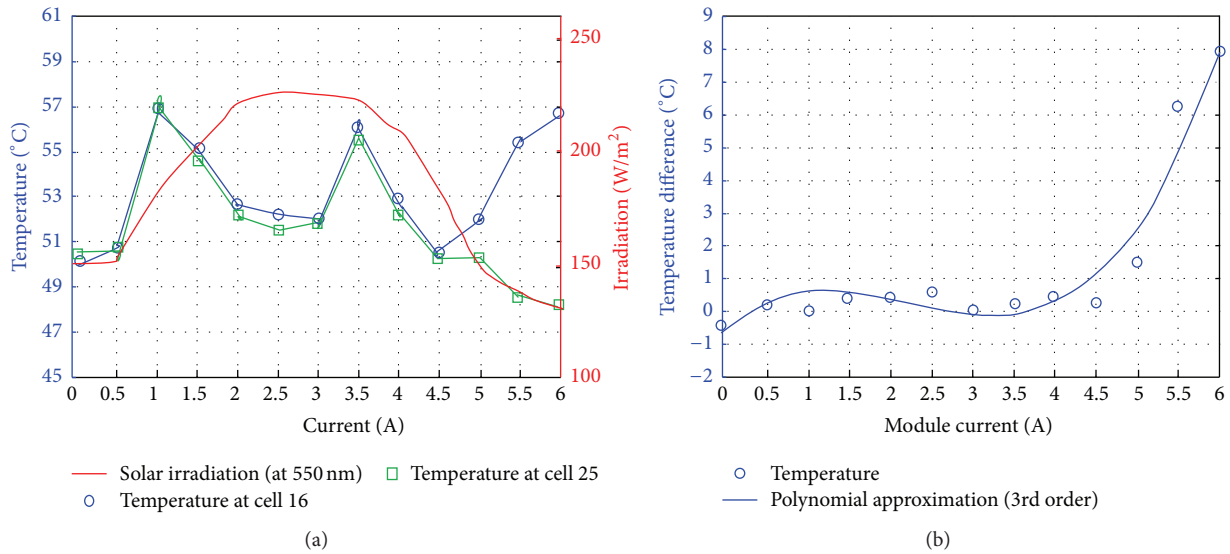


FIGURE 7: Current characterization under 0.5 A increments: (a) temperature graph and (b) temperature difference.

current was increased every 30 minutes; the starting value for current was at 0.5 A, with step increments of 0.5 A, until 6 A value was reached. In other words, the duty cycle for the DC/DC boost converter was changed according to the specified current demand. The test began at 11:00 a.m. and finished at 4:00 p.m. It is evident that the reason for this long term of time is due to the restriction of having to wait 30 minutes for every change of load.

Obtained results from the test are illustrated in Figure 7(a); at first sight, it may seem that no relevant information was found. However, very different conclusions may be drawn from the graph.

It is easily seen in Figure 7(a) that there exists more than a minimum value for temperature, so that it may be assumed that there exist multiple maximum power points. This, then, may imply that there may exist partially shaded areas or mismatch conditions at the PV panel. Since the tests were carried out under no shaded areas, it means that a mismatch occurs.

A better look to the graphs allows us to observe that the temperature for cells 16 and 25 suffers an important difference. Very often, these differences are due to weather conditions; however, their influence should almost be the same on both cells due to the fact of being neighbors, so that a different cause should be considered forward in this particular case.

Data information would be clearer if temperature differences were graphed and compared for both cells (16 and 25). The environmental influence factor is significantly reduced when information is illustrated as it is shown in Figure 7(b). It should also be noticed that, at lower temperature conditions, both cells have almost the same temperature; however, at higher currents, the curves start to deviate from each other since cell 16 becomes hotter and cell 25 becomes colder.

The obtained result, which is illustrated in Figure 6(a), has to be confirmed and validated. For this purpose, the previous

test had to be repeated; however, it was run with a current interval of 1 A at this time. This let us carry out the test in just three hours instead of the six required hours with a step of 0.5 A. Certainly, this represents a lost in curve resolution but shows minor changes due to weather conditions.

A graph for the second test is illustrated in Figure 8(a). It is easily seen that still there are significant variations; however, temperature differences on both cells exhibit similar evolution, as shown in Figure 8(b). Clearly, cell 16 becomes hotter than cell 25, when current increases. As a consequence, cell 16 has a lower capability for generating power compared to other cells. Finally, it is possible to identify mismatch conditions by measuring the temperature at the back of a PV panel; this would also let us identify manufacture defects.

6. Conclusion

The characterization methods and instrumentation for in situ measurements, defect monitoring, and process control and performance are required in order to assure the quality.

A temperature characterization for a mc-Si module with time and current was developed by thermographic analysis. On the one hand, temperature characterization with respect to time made it possible to identify the temperature variations when the operation point changes for the module. On the other hand, temperature characterization with respect to PV panel current made it possible to establish cell mismatching conditions.

This method may effectively be applied for detecting defects in PV panels and hot spots regions produced by mismatch conditions in electric module features.

The main importance of the defects detection is because the PV panel will have low efficiency, but also multiple maximum power points, and then a concern to the converter and algorithm of the power extraction.

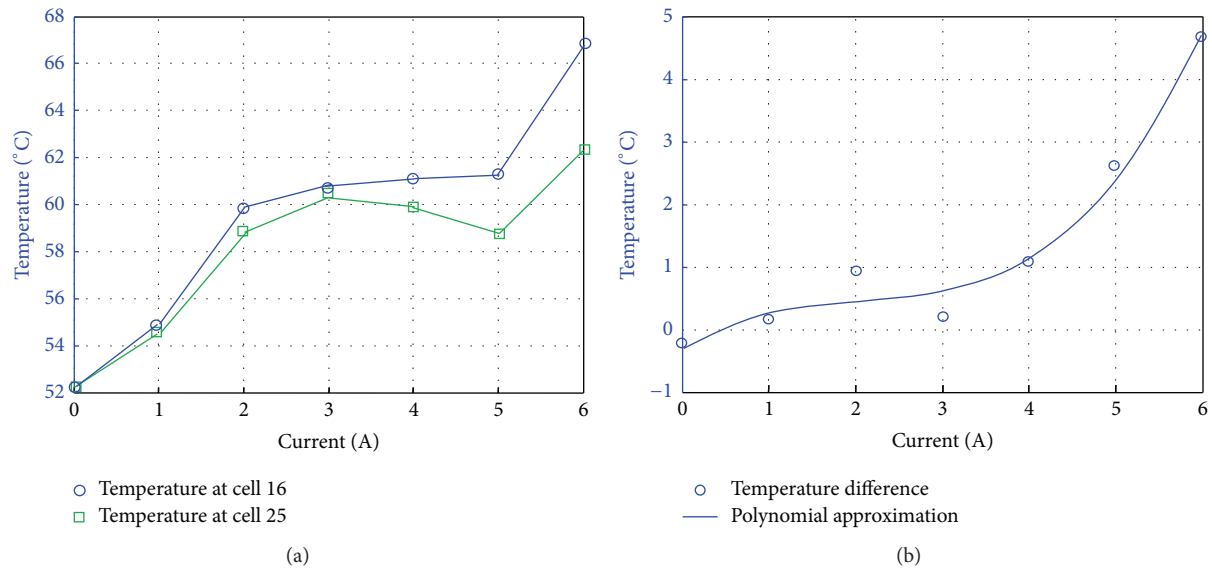


FIGURE 8: Current characterization under 1 A increments: (a) temperature graph and (b) temperature difference.

Competing Interests

The authors declare that they have no competing interests.

References

- [1] D. L. King, J. A. Kratochvil, and W. E. Boyson, "Temperature coefficients for PV modules and arrays: measurement methods, difficulties, and results," in *Proceedings of the IEEE 26th Photovoltaic Specialists Conference*, pp. 1183–1186, Anaheim, Calif, USA, October 1997.
- [2] P. Singh and N. M. Ravindra, "Temperature dependence of solar cell performance—an analysis," *Solar Energy Materials and Solar Cells*, vol. 101, pp. 36–45, 2012.
- [3] C. Deline, "Partially shaded operation of a grid-tied PV system," in *Proceedings of the 34th IEEE Photovoltaic Specialists Conference (PVSC '09)*, Philadelphia, Pa, USA, June 2009.
- [4] V. Quaschnig and R. Hanitsch, "Numerical simulation of current-voltage characteristics of photovoltaic systems with shaded solar cells," *Solar Energy*, vol. 56, no. 6, pp. 513–520, 1996.
- [5] E. Díaz-Dorado, A. Suárez-García, C. Carrillo, and J. Cidrás, "Influence of the PV modules layout in the power losses of a PV array with shadows," in *Proceedings of the 14th International Power Electronics and Motion Control Conference*, Ohrid, Macedonia, 2010.
- [6] J. W. Bishop, "Computer simulation of the effects of electrical mismatches in photovoltaic cell interconnection circuits," *Solar Cells*, vol. 25, no. 1, pp. 73–89, 1988.
- [7] N. D. Kaushika and A. K. Rai, "An investigation of mismatch losses in solar photovoltaic cell networks," *Energy*, vol. 32, no. 5, pp. 755–759, 2007.
- [8] K. Wilson, D. De Ceuster, and R. A. Sinton, "Measuring the effect of cell mismatch on module output," in *Proceedings of the 4th World Conference on Photovoltaic Energy Conference*, pp. 916–919, IEEE, Waikoloa, Hawaii, USA, May 2006.
- [9] A. M. Gabor, M. Ralli, S. Montminy et al., "Soldering induced damage to thin SI solar cells and detection of cracked cells in modules," in *Proceedings of the 21st European Photovoltaic Solar Energy Conference*, Dresden, Germany, 2006.
- [10] J. W. Bishop, "Microplasma breakdown and hot-spots in silicon solar cells," *Solar Cells*, vol. 26, no. 4, pp. 335–349, 1989.
- [11] J. Bauer, J.-M. Wagner, A. Lotnyk et al., "Hot spots in multicrystalline silicon solar cells: avalanche breakdown due to etch pits," *Physica Status Solidi—Rapid Research Letters*, vol. 3, no. 2-3, pp. 40–42, 2009.
- [12] C. Honsberg and S. Bowden, PVEducation.org, <http://www.pveducation.org/pvcdrom/solar-cell-operation/spectral-response>.
- [13] W. Herrmann, W. Wiesner, and W. Vaaben, "Hot spot investigations on PV modules—new concepts for a test standard and consequences for module design with respect to bypass diodes," in *Proceedings of the Conference Record of the Twenty Sixth IEEE Photovoltaic Specialists Conference*, pp. 1129–1132, Anaheim, Calif, USA, 1997.
- [14] E. Molenbroek, D. W. Waddington, and K. A. Emery, "Hot spot susceptibility and testing of PV modules," in *Proceedings of the 22nd IEEE Photovoltaic Specialists Conference*, pp. 547–552, Las Vegas, Nev, USA, October 1991.
- [15] V. Quaschnig and R. Hanitsch, "Numerical simulation of photovoltaic generators with shaded cells," in *Proceedings of the 30th Universities Power Engineering Conference*, pp. 583–586, Greenwich, UK, September 1995.
- [16] G. Liu, P. Wang, W. Wang, and Q. Wang, "MPPT algorithm under partial shading conditions," in *Electrical, Information Engineering and Mechatronics*, vol. 1, pp. 91–98, Springer, London, UK, 2011.

Research Article

Comparison of Different MPPT Algorithms with a Proposed One Using a Power Estimator for Grid Connected PV Systems

Manel Hlaili and Hfaiedh Mechergui

Electrical Engineering, High National School of Engineers of Tunis, University of Tunis, 1008 Tunis, Tunisia

Correspondence should be addressed to Manel Hlaili; hlaili.manel@yahoo.fr

Received 4 April 2016; Accepted 17 May 2016

Academic Editor: Vishal Mehta

Copyright © 2016 M. Hlaili and H. Mechergui. This is an open access article distributed under the Creative Commons Attribution License, which permits unrestricted use, distribution, and reproduction in any medium, provided the original work is properly cited.

Photovoltaic (PV) energy is one of the most important energy sources since it is clean and inexhaustible. It is important to operate PV energy conversion systems in the maximum power point (MPP) to maximize the output energy of PV arrays. An MPPT control is necessary to extract maximum power from the PV arrays. In recent years, a large number of techniques have been proposed for tracking the maximum power point. This paper presents a comparison of different MPPT methods and proposes one which used a power estimator and also analyses their suitability for systems which experience a wide range of operating conditions. The classic analysed methods, the incremental conductance (IncCond), perturbation and observation (P&O), ripple correlation (RC) algorithms, are suitable and practical. Simulation results of a single phase NPC grid connected PV system operating with the aforementioned methods are presented to confirm effectiveness of the scheme and algorithms. Simulation results verify the correct operation of the different MPPT and the proposed algorithm.

1. Introduction

Renewable sources of energy are a hot topic acquiring a growing importance in the world due to its consumption and exhaustion of fossil fuel. The photovoltaic (PV) power system is becoming increasingly important as the most available renewable source of energy since it is clean with little maintenance and without any noise.

Nevertheless, PV systems have problems, such as the conversion with low radiation (in general less than 17%), as well as the nonlinear characteristic that depends on irradiation and temperature in its operation which change the amount of electric power generated [1]. Figures 1 and 2 show the characteristics P - V and I - V for different irradiation and temperature.

Since a PV array is an expensive system to build, it is necessary to exploit all of the available output power. Multilevel converters are particularly interesting for high power applications.

The location of the maximum power point can be determined using different algorithms. Maximum Power Point Tracking (MPPT) techniques are used to maintain the PV

array's operating point at its maximum power point (MPP) and extract the maximum power available in PV arrays.

Different MPPT techniques have been proposed in the literature such as the perturbation and observation (P&O) technique [2], the incremental conductance (IncCond) technique [3], ripple correlation technique [4], short circuit current (SCC) technique [5], and open circuit voltage (OCV) technique [5].

These techniques vary in complexity, cost, speed of convergence, sensors required, hardware implementation, and effectiveness.

Due to the various MPPT methods, different research in PV systems has presented a comparative analysis of MPPT techniques. Indeed, some papers present comparative study among only few methods and others present a comparison of several MPPT methods, based on simulations, under the energy production point of view. The MPPT techniques are evaluated considering different irradiation and temperature variation and calculation of the energy supplied by the complete PV array.

In this paper, the attention will be concentrated on PSIM simulation comparisons between some of these techniques

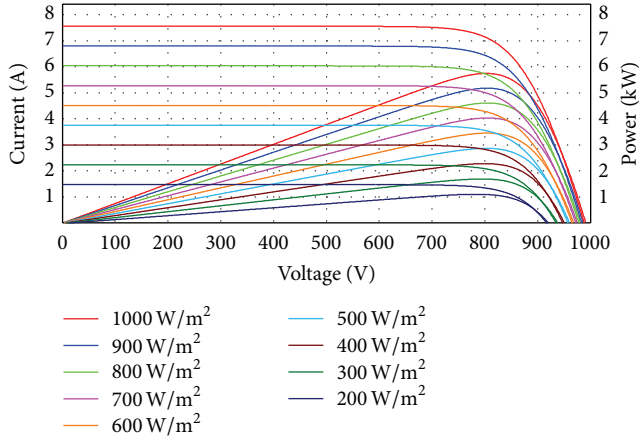


FIGURE 1: I - V and P - V curve with different irradiation.

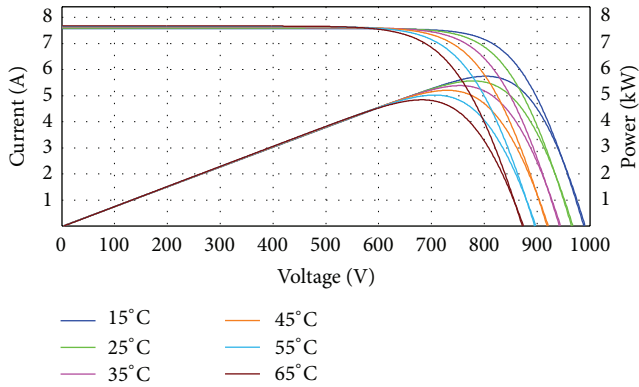


FIGURE 2: I - V and P - V curve with temperature variation.

and a proposed method will be discussed using the short circuit current and the open circuit voltage. Consequently, the purpose of this work is to compare several widely adopted MPPT algorithms between the different MPPT techniques in order to understand which technique has the best performance with the proposed method as well as injecting the high quality sinusoidal current to the grid.

In the simulations, the MPPT techniques have been implemented strictly following the description indicated in the references excluding the proposed algorithm. In particular, we will focus our attention on a grid connected photovoltaic system constructed by connecting a single phase neutral point clamped inverter (SP-NPCI) with an inductor as an output filter, using different embedded MPPT algorithms.

2. Operating Principle

The SP-NPCI output current is controlled in order to follow a sinusoidal reference waveform, synchronized, and in phase with the grid voltage.

Figure 3 shows the scheme of the proposed system with its control.

Using a phase-locked loop (PLL) algorithm, we can extract a unitary signal in phase with the grid voltage. The

amplitude of the reference current I_{ref} is generated by the sum of the DC-link voltage regulator and the output of the MPPT. The MPPT algorithm varies I_{MPPT} according to the environmental conditions in order to keep the operating point of the PV system close to the maximum power point.

The switches T_1 and T_3 , as well as T_2 and T_4 , are switched complementarily. The control of this inverter can be done using a PWM technique. To implement the PWM, two superposed triangular carriers are used. Each carrier is connected to one of the two groups of switches controlled complementarily. The positive part of the carrier fixes the switching state of T_1 and T_3 whereas the negative part controls T_2 and T_4 .

3. MPPT Algorithms

The maximum power supplied by the photovoltaic panels is not always stable and fixed in the same operating point; it varies with the weather conditions, such as solar irradiation, shadow, and temperature. To extract the maximum power, it is necessary to implement an MPPT algorithm that dynamically adjusts the extraction of the power. Convergence speed is one of the most important features among all different MPPT algorithms. Any improvement in the rise time of MPPT improves the reliability of the system and increases the power extraction and efficiency of the whole system.

3.1. Perturbation and Observation (P&O). Perturb and observe algorithm is simple and does not require previous knowledge of the PV generator characteristics or the measurement of solar intensity and cell temperature and is easy to implement with analogue and digital circuits. It perturbs the operating point of the system causing the PV array terminal voltage to fluctuate around the MPP voltage even if the solar irradiance and the cell temperature are constants [6].

Moreover, it is the most widely used and workhorse MPPT algorithm because of its balance between performance and simplicity. However, it suffers from the lack of speed and adaptability which is necessary for tracking the fast transients under varying environmental conditions [7]. It is simple and straightforward technique but degraded performance is achieved due to the trade-off between accuracy and speed upon selecting the step size [8]. Figure 4 shows the P&O algorithm diagram.

3.2. Incremental Conductance (IncCond). The incremental conductance method is based on the principle that the slope of the PV array power curve is zero at the MPP, so that $\Delta P/\Delta V = 0$, with $P = VI$.

Considering that

$$\begin{aligned} \frac{\Delta I}{\Delta V} &= -\frac{I}{V} & \text{if } P = \text{MPP}, \\ \frac{\Delta I}{\Delta V} &> -\frac{I}{V} & \text{if } P < \text{MPP}, \\ \frac{\Delta I}{\Delta V} &< -\frac{I}{V} & \text{if } P > \text{MPP}, \end{aligned} \quad (1)$$

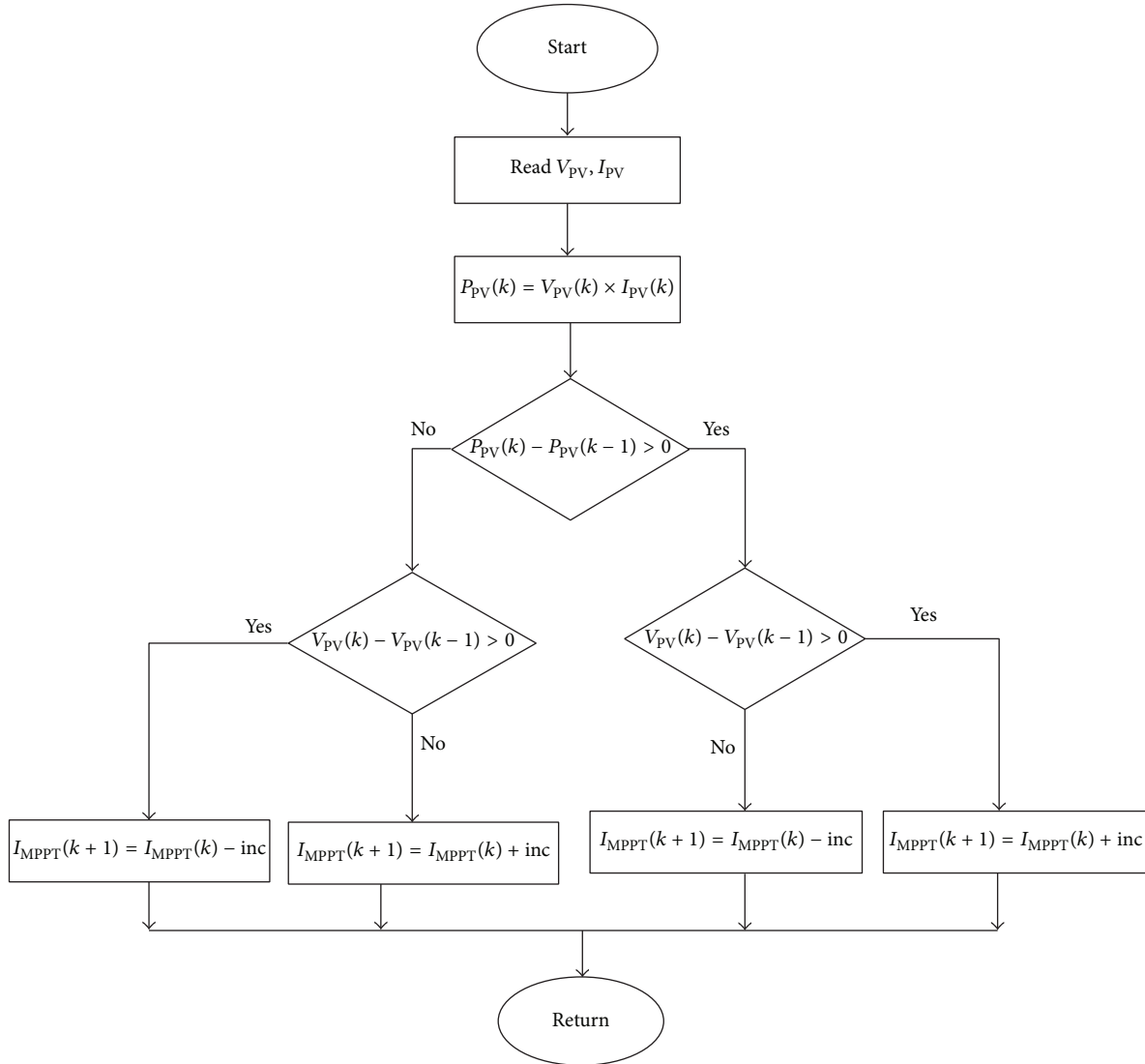


FIGURE 4: Flowchart of perturbation and observation.

The ripple correlation control uses the average function to find out the average term of the instantaneous PV power \bar{P}_{PV} and voltage \bar{V}_{PV} . \tilde{P}_{PV} and \tilde{V}_{PV} can be calculated from

$$\begin{aligned}\tilde{P}_{PV} &= P_{PV} - \bar{P}_{PV}, \\ \tilde{V}_{PV} &= V_{PV} - \bar{V}_{PV}.\end{aligned}\quad (3)$$

The average value of $\tilde{V}_{PV} \times \tilde{P}_{PV}$ function is the output of ∂P :

$$\partial P = \overline{\tilde{P}_{PV} \cdot \tilde{V}_{PV}}. \quad (4)$$

The sign of ∂P is an indication of the region where the PV system is working:

- (i) $\partial P > 0$: the operating point is on the left side of the MPP on the $(P-V)$ characteristic; then, the sign function is +1.

- (ii) $\partial P < 0$: the operating point is on the right side of the MPP on the $(P-V)$ characteristic; then, the sign function is -1.

The knowledge of the instantaneous operating point region makes it possible to change the output reference current in order to approach the maximum power operating point. This method presents very fast dynamics converging asymptotically to the MPP, and it achieves convergent speeds at a rate similar to the switching converter frequency. Figure 6 shows the ripple correlation MPPT algorithm.

3.4. Proposed MPPT. The proposed MPPT is a combination of the open circuit voltage and the short circuit current methods with a variable step size (VSSOCV) in the gain parameters which is multiplied by the open circuit voltage to have the maximum power which can be extracted from the PV panels. In addition to that, we proposed a power

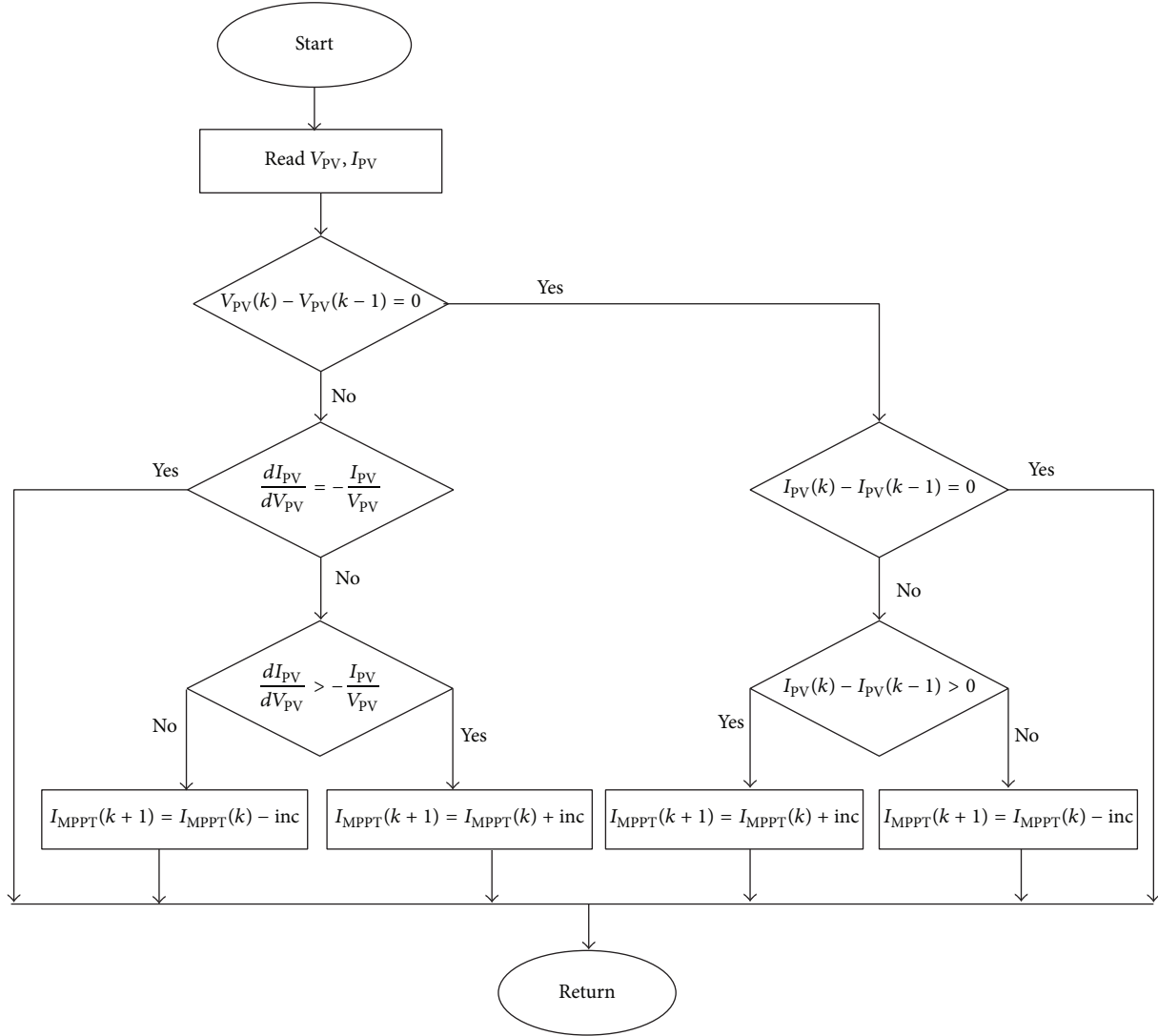


FIGURE 5: Flowchart of the incremental conductance algorithm.

estimator, to measure the power from the DC side of the PV system.

In case the grid current is in phase with the grid voltage, the instantaneous PV power, upon neglecting power losses in NPC inverter, is given by

$$P_{PV} = P_L + P_C + P_{\text{grid}}(t). \quad (5)$$

We can estimate the instantaneous power extracted from the panel using the current and the voltage injected into the grid.

Figure 7 shows that the OCV is proportional to the variation of temperature which is given by

$$V_{OC} = -k_1 * T + k. \quad (6)$$

The maximum voltage extracted from the PV system is equal to

$$V_{MPP} = k_2 * V_{OC}. \quad (7)$$

The factor k_2 is always less than unity. It looks very simple but determining the best value of it is very difficult. It varies from 0.73 to 0.8 [5].

The SCC of the PV panel depends on the irradiation. This relationship can be described by

$$I_{SC} = k_3 * E. \quad (8)$$

The constant k_3 can be determined from the PV characteristic.

Figure 8 shows that the SCC is proportional to the variation of the irradiation.

However, the optimum operating current for maximum output power is proportional to the short circuit current under various irradiation [5]:

$$I_{MPP} = k_4 * I_{SC}, \quad (9)$$

where k_4 is a proportional constant which varies from 0.8 to 0.9. This control algorithm requires the measurement of the SCC.

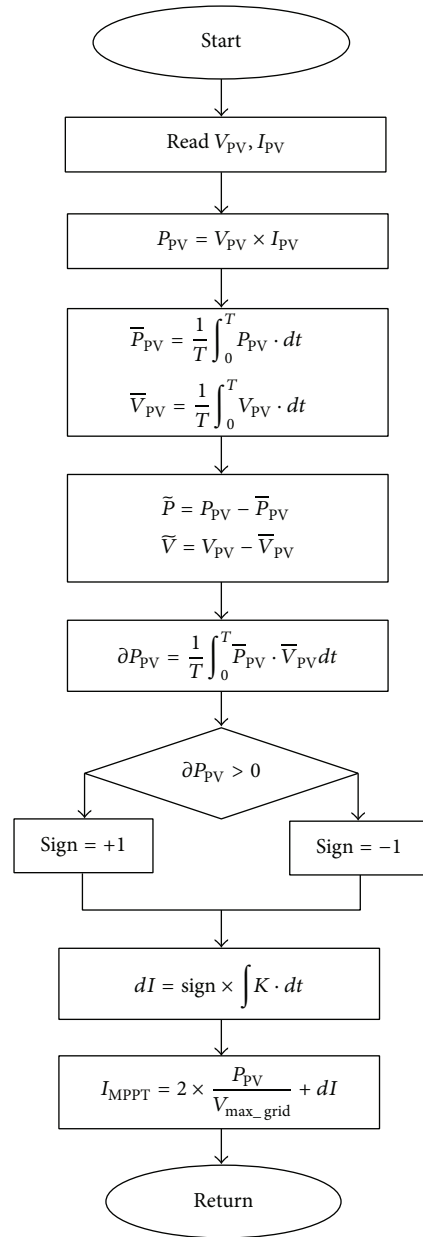


FIGURE 6: Flowchart of ripple correlation MPPT algorithm.

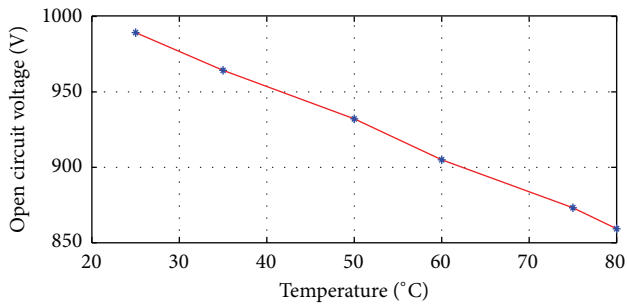


FIGURE 7: Variation of the open circuit voltage according to the temperature.

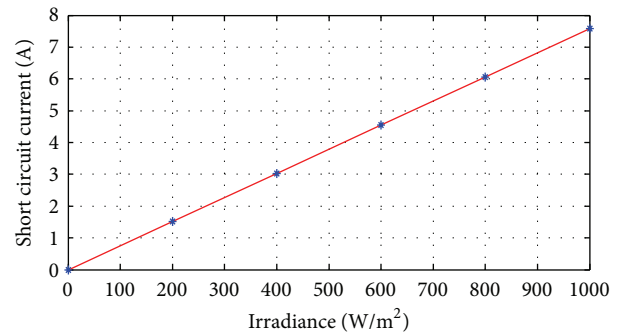


FIGURE 8: Variation of short circuit current according to the irradiation.

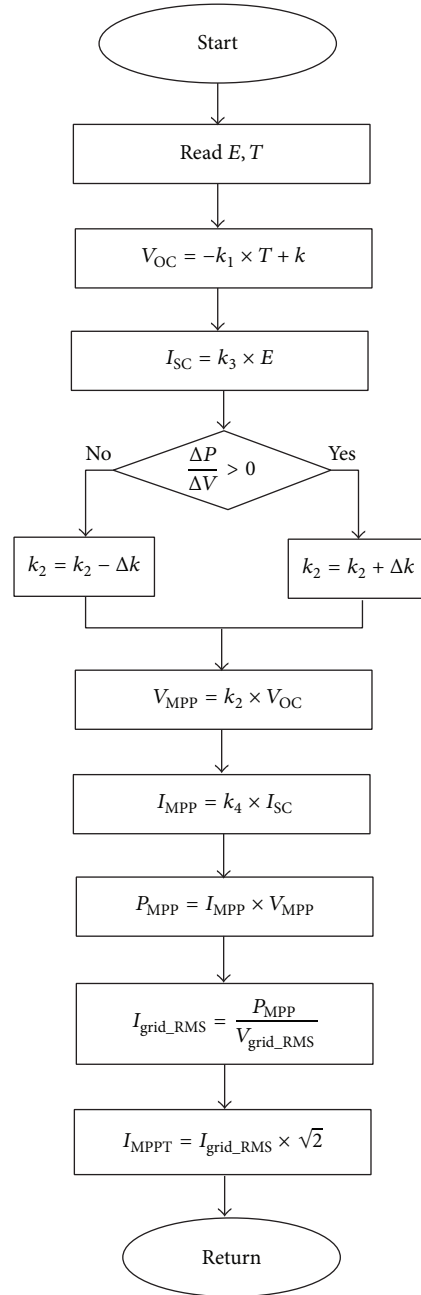


FIGURE 9: Flowchart of the proposed MPPT algorithm.

The proposed method needs using two sensors for the temperature and irradiation measurements.

This method needs also knowing the characteristics of the PV panels to determine the constant of the proposed algorithm in Figure 9.

For this purpose, a low-cost temperature sensor is adopted and is maintaining the right track of MPP but, in practical implementations, can be a problematic issue due to irregular distribution of PV array temperature, which can be avoided in small PV converters.

4. Simulation Results

In order to obtain a good characterization of the proposed topology, simulations were performed using PSIM software. The system was simulated under different operating conditions, in steady state and during transient state caused by solar radiation variations.

The P&O and IncCond techniques are the most widely used because of IncCond and P&O simplicity to implement. But, as it can be seen in Table 1, their THD is high in

TABLE I: Efficiency of the different MPPT.

MPPT	Efficiency ($\eta\%$)	THD (%)			
		1000 W/m ²	800 W/m ²	600 W/m ²	400 W/m ²
VSSOCV	99.95	1.6	1.5	2.0	3.0
IncCond	99.94	4.6	5.7	7.7	24.0
P&O	99.93	1.7	1.9	7.1	9.0
RC	99.86	2.1	3.8	2.0	8.0

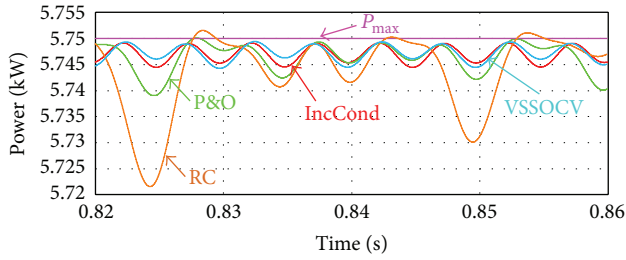
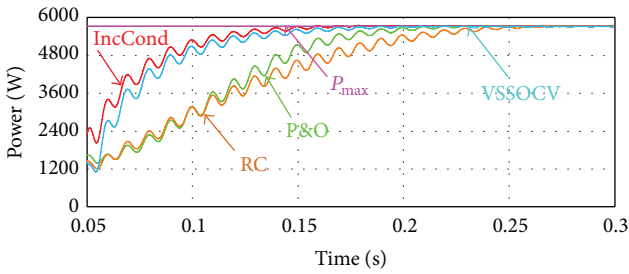
FIGURE 10: Power extracted from PV panels in steady state at 1000 W/m².

FIGURE 11: Power extracted from PV panels during the start-up with different MPPT techniques.

low radiation comparing with the proposed algorithm. Also, Figure 14 shows that it does not have a stable DC-link compared to the proposed MPPT and the ripple correlation method.

The proposed method is efficient and extracts the maximum power but it needs two sensors to measure the irradiation and temperature variation. This method needs only the knowledge of the I - V characteristics. It has also the faster response.

IncCond has the highest rise time as it can be seen in Figure 11. We can see also, in steady state, that RC and P&O have the higher oscillation around the maximum point (Figure 10).

Table 1 shows also the efficiency of each method which is calculated using the maximum theoretical power and the instantaneous extracted power defined as

$$\eta = \frac{P_{\text{actuel}}(t)}{P_{\text{max}}(t)}. \quad (10)$$

All the MPPT methods have an acceptable THD of the injected current which is less than 5% given in the interconnection standards (CEI61727) at 1000 W/m². Table 1 shows all

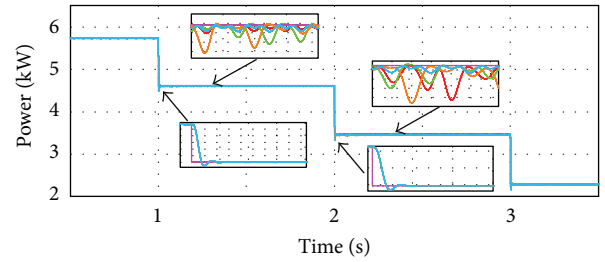
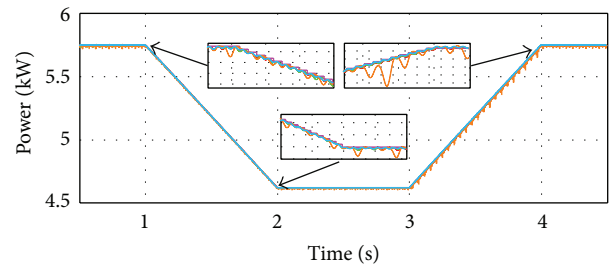
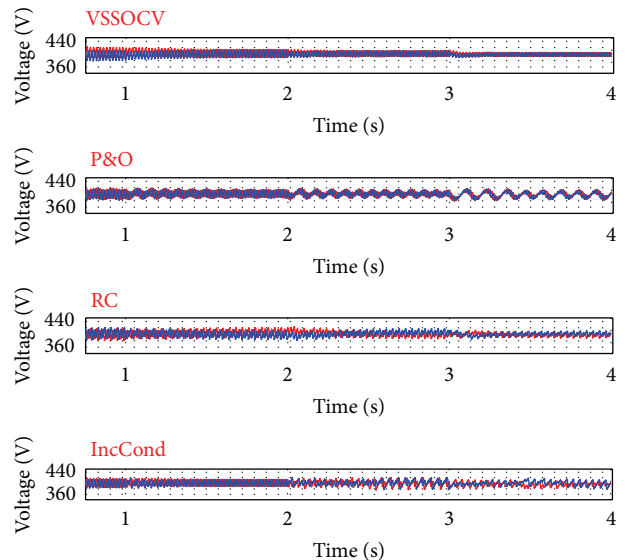
FIGURE 12: Maximum power extracted and theoretical power during a fluctuation in solar radiation from 1000 W/m² to 200 W/m² passing through 600 W/m² and 400 W/m².FIGURE 13: Maximum power extracted and theoretical power during a fluctuation in solar radiation from 1000 W/m² to 800 W/m².

FIGURE 14: DC-link voltage with different MPPT.

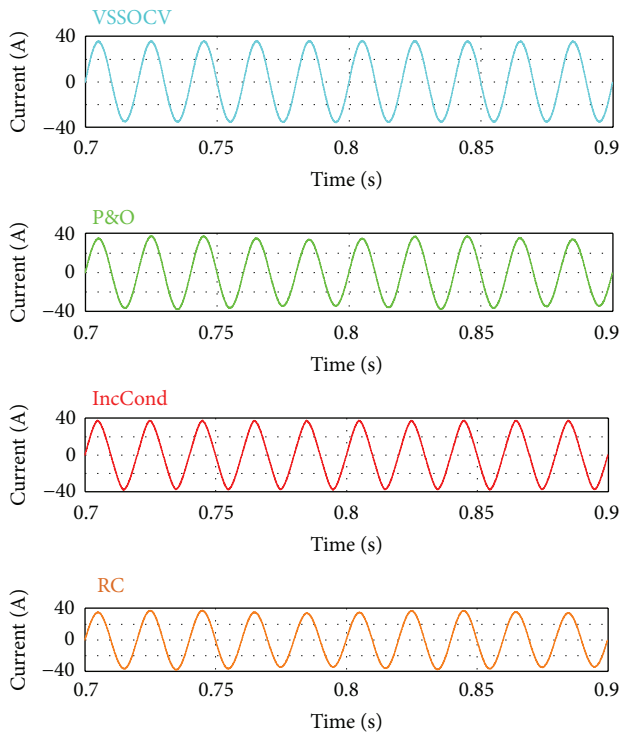


FIGURE 15: Injected current into the grid with different MPPT algorithms.

the THD of the different algorithms at different irradiation. It is clear that the proposed method VSSOCV has the best value of THD regardless of the irradiation.

The techniques are not equivalent concerning the costs and the software complexity but all of them require a microcontroller or DSP with higher performances due to the necessity of high computation capability.

The RC technique has an efficiency lower than the P&O and IncCond techniques, but its THD of the injected current to the grid is better than the P&O and IncCond.

Figures 12 and 13 show that all the techniques can extract the maximum power under different irradiation. Also, we can notice in Figure 15 that the currents injected into the grid are almost similar with the different MPPT.

The results show that the best MPPT technique is the proposed one (VSSOCV).

5. Conclusions

The purpose of MPPT is to extract the high level power from PV systems. This paper presents a comparison of MPPT methods with a proposed one which is the most effective on the basis of MPPT efficiency and considers their suitability for systems which experience a wide range of operating conditions. From this, it is clear that each MPPT method has its own advantages and disadvantages. In addition, the MPPT should be capable of minimizing the ripple around the MPP. Different MPPT methods are compared based on simulations in the PSIM environment in terms of the dynamic response of the PV system and efficiency and implementation

considerations. Therefore, the two techniques incremental conductance (IncCond) and P&O algorithms are simple to implement but they have some inconvenience in the DC-link and the output inverter current. Otherwise, the RC perturbs itself without an external perturbation. These three methods have been evaluated by simulating a grid connected PV system, utilizing a single phase NPC inverter to connect the PV panel to the grid. In particular, the performance of each method has been considered over a wide range of different irradiation conditions. It is shown that the proposed system is able to always extract the maximum power available from the solar PV panels with the proposed MPPT.

Competing Interests

The authors declare that they have no competing interests.

References

- [1] A. Dolara, R. Faranda, and S. Leva, "Energy comparison of seven MPPT techniques for PV systems," *Journal of Electromagnetic Analysis and Applications*, vol. 1, no. 3, pp. 152–162, 2009.
- [2] M. A. Elgendy, B. Zahawi, and D. J. Atkinson, "Assessment of perturb and observe MPPT algorithm implementation techniques for PV pumping applications," *IEEE Transactions on Sustainable Energy*, vol. 3, no. 1, pp. 21–33, 2012.
- [3] H. Kumar and R. K. Tripathi, "Simulation of variable incremental conductance method with direct control method using boost converter," in *Proceedings of the Students Conference on Engineering and Systems (SCES '12)*, pp. 1–5, Allahabad, India, March 2012.
- [4] D. Casadei, G. Grandi, and C. Rossi, "Single-phase single-stage photovoltaic generation system based on a ripple correlation control maximum power point tracking," *IEEE Transactions on Energy Conversion*, vol. 21, no. 2, pp. 562–568, 2006.
- [5] A. Reza Reisi, M. Hassan Moradi, and S. Jamasb, "Classification and comparison of maximum power point tracking techniques for photovoltaic system: a review," *Renewable and Sustainable Energy Reviews*, vol. 19, pp. 433–443, 2013.
- [6] M. A. Elgendy, B. Zahawi, and D. J. Atkinson, "Assessment of perturb and observe MPPT algorithm implementation techniques for PV pumping applications," *IEEE Transactions on Sustainable Energy*, vol. 3, no. 1, pp. 21–33, 2012.
- [7] H. Malek and Y. Chen, "BICO MPPT: a faster maximum power point tracker and its application for photovoltaic panels," *International Journal of Photoenergy*, vol. 2014, Article ID 586503, 9 pages, 2014.
- [8] L. M. Elobaid, A. K. Abdelsalam, and E. E. Zakzouk, "Artificial neural network based maximum power point tracking technique for PV systems," in *Proceedings of the 38th Annual Conference on IEEE Industrial Electronics Society (IECON '12)*, pp. 937–942, Montreal, Canada, October 2012.
- [9] R. G. Tapre and R. G. Deshbhratar, "Comparative study and simulation of different maximum power point tracking (MPPT) techniques in a solar power generation," *International Journal on Recent and Innovation Trends in Computing and Communication*, vol. 3, pp. 143–148, 2015.
- [10] K. Visweswara, "An investigation of incremental conductance based maximum power point tracking for photovoltaic system," *Energy Procedia*, vol. 54, pp. 11–20, 2014.

- [11] S. Z. Mirbagheri, S. Mekhilef, and S. M. Mirhassani, "MPPT with Inc. Cond method using conventional interleaved boost converter," *Energy Procedia*, vol. 42, pp. 24–32, 2013.
- [12] T. Eswam and P. L. Chapman, "Comparison of photovoltaic array maximum power point tracking techniques," *IEEE Transactions on Energy Conversion*, vol. 22, no. 2, pp. 439–449, 2007.

Research Article

Enhanced Light Scattering by Preferred Orientation Control of Ga Doped ZnO Films Prepared through MOCVD

Long Giang Bach,¹ Nam Giang Nguyen,² and Van Thi Thanh Ho³

¹NTT Institute of Hi-Technology, Nguyen Tat Thanh University, Ho Chi Minh City 70000, Vietnam

²Thin Film Solar Cells Laboratory, Department of Chemical Engineering, National Taiwan University of Science and Technology (NTUST), Taipei City 106, Taiwan

³Ho Chi Minh City University of Natural Resources and Environment (HCMUNRE), Ho Chi Minh City 70000, Vietnam

Correspondence should be addressed to Van Thi Thanh Ho; httvn@hcmunre.edu.vn

Received 6 April 2016; Accepted 15 May 2016

Academic Editor: Prakash Basnyat

Copyright © 2016 Long Giang Bach et al. This is an open access article distributed under the Creative Commons Attribution License, which permits unrestricted use, distribution, and reproduction in any medium, provided the original work is properly cited.

We have explored the effective approach to fabricate GZO/ZnO films that can make the pyramidal surface structures of GZO films for effective light scattering by employing a low temperature ZnO buffer layer prior to high temperature GZO film growth. The GZO thin films exhibit the typical preferred growth orientations along the (002) crystallographic direction at deposition temperature of 400°C and SEM showed that column-like granule structure with planar surface was formed. In contrast, GZO films with a pyramidal texture surface were successfully developed by the control of (110) preferred orientation. We found that the light diffuse transmittance of the film with a GZO (800 nm)/ZnO (766 nm) exhibited 13% increase at 420 nm wavelength due to the formed large grain size of the pyramidal texture surface. Thus, the obtained GZO films deposited over ZnO buffer layer have high potential for use as front TCO layers in Si-based thin film solar cells. These results could develop the potential way to fabricate TCO based ZnO thin film using MOCVD or sputtering techniques by depositing a low temperature ZnO layer to serve as a template for high temperature GZO film growth. The GZO films exhibited satisfactory optoelectric properties.

1. Introduction

As a front contact for silicon based thin film solar cells, the Transparent Conductive Oxide (TCO) layers on glass should not only possess satisfactory optoelectric properties, but also exhibit light trapping capability to increase the light absorption within the active layers [1–3]. Textured surface on TCO layers is usually designed to scatter the incident light to elongate the pathway of light and subsequently increase the short circuit current density (J_{sc}) by 20~40% in the solar cells [4–6]. Recently, several techniques were developed for obtaining surface textures. One of the common methods was the wet-etching of sputtered Al-doped ZnO (AZO) films by using acid treatment to create crater-like structure by which the light scattering is increased. Nevertheless, this process costs highly due to the thick AZO film sputtering (~1 μm). Furthermore, complicated treatments are required to obtain

textured topography, like soaking in an acid solution, lithography, and so forth, which increase the fabrication cost and accompany the risk of introducing unexpected impurities [7, 8] into the TCO layers. Moreover, atmosphere pressure chemical vapor deposition (APCVD) of F-doped SnO₂ and low-pressure chemical vapor deposition (LPCVD) of B-doped ZnO, which exhibited pyramidal crystalline habits on the film surface and thus are capable of scattering the incident light, were also proposed [9–13].

In this work, we explored the methodology to increase the light diffuse transmittance through controlling the preferred orientation of polycrystalline Ga doped ZnO (GZO) films grown by the low-pressure chemical vapor deposition (LPCVD) technique using diethyl zinc (DEZn) and trimethyl gallium (TMGa) as the Zn and Ga precursors, respectively. Different from the low process temperature (~150°C) of B-doped ZnO, the GZO films exhibited satisfactory optoelectric

properties at reaction temperatures as high as 400°C. X-ray diffraction measurement indicated that major growth direction was (002) plane and secondary electron microscopy showed that column-like granule structure with planar surface was formed. By depositing a low temperature ZnO layer to serve as a template for high temperature GZO film growth, the main preferred orientation of the GZO films was manipulated to (110) plane and the film surface to the pyramid-like structure. Through this two-step growth, the light diffuse transmittance of the film with a GZO (~800 nm)/ZnO (766 nm) combination exhibited 13% increase at 420 nm wavelength due to the preservation of the pyramidal surface morphology.

2. Results and Discussion

2.1. Effect of Growth Temperature on the Crystalline Orientation of GZO Films. First of all, the GZO films were grown at various deposition temperatures to explore the effects of growth temperature and growth rate on the orientation of the GZO films. The detailed experiment was carried out as our previous work [14]. The XRD measurement was used to determine the crystalline orientation of the GZO films deposited. Figure 1 reveals the XRD patterns of the GZO films grown at various substrate temperatures. Started from (110) plane orientation at low temperatures like 300°C, the main crystalline orientation changed to (002) plane when the substrate was raised to 400°C. When further raised to 450°C, all the crystalline planes including (100), (101), (002), and (110) appeared. With increasing temperature from 300 to 350°C, the growth mode of GZO film was already in the diffusion controlled regime (Figure 2). So the surface with the highest absorption rate will dominate the film growth orientation [15, 16]. As a result, the (002)-oriented films could be obtained due to the enhancement of surface diffusion [17]. At further high temperature like 450°C, all crystal planes appeared because the surface collision rate is rate controlling; thereby all planes could appear. The intensity ratio of (002) plane for GZO film with substrate temperature 400°C increases by large amount compared to GZO film with substrate temperature 350°C due to the higher substrate temperature and the higher crystalline so that the intensity of (002) plane for GZO film with substrate temperature 400°C is higher than the GZO film with substrate temperature 350°C. Besides, the (002) plane is preferred to grow at substrate temperature 400°C than the other planes.

Figure 2 shows the Arrhenius plot of the film growth rate of GZO at various substrate temperatures. It has been demonstrated that the growth of GZO film is characterized by three regimes. For low temperature (below 250°C) the film growth rate increases exponentially with substrate temperature according to an Arrhenius behavior in which the deposition rate is controlled by an activated process such as adsorption, surface diffusion, chemical reaction, and desorption. The growth rate is thus controlled by mass transfer and reaction kinetics. The net activation energy for the ZnO thin films deposition in this region is calculated to be $\sim 3.95 \text{ kcal mol}^{-1}$. Moreover, the growth rate is also proportional to the surface density of the unit structure (N_s), meaning that the

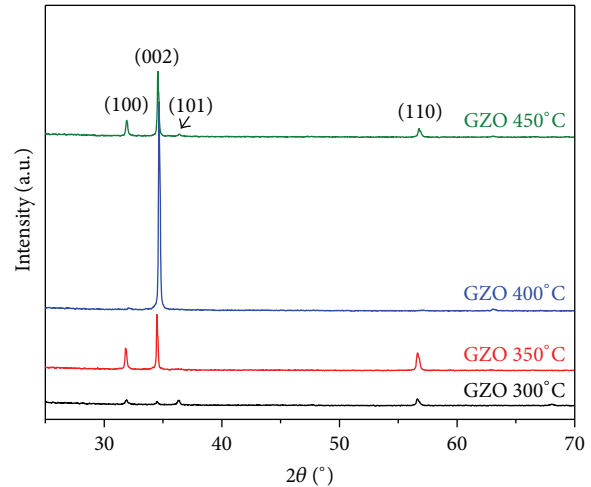


FIGURE 1: X-ray diffraction patterns of GZO film as a function of deposition temperature.

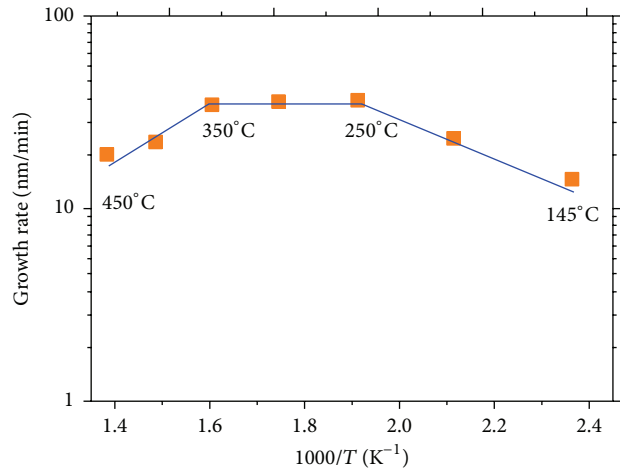
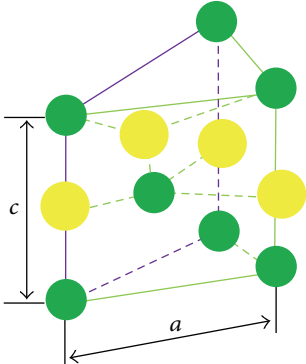
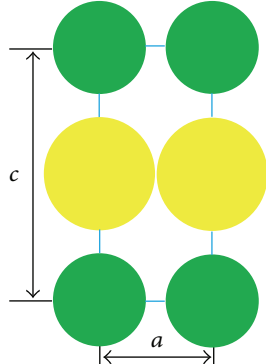
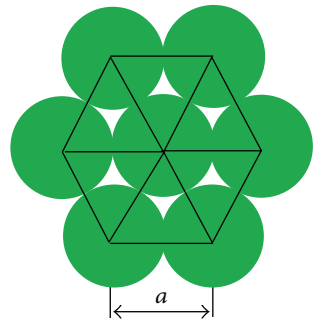


FIGURE 2: Arrhenius plot of the film growth rate of GZO film against the reciprocal of the absolute temperature.

most densely packed plane grows the fastest [14–16]. In the intermediate zone (250–350°C), the growth rate reaches its maximum and remains constant, indicating that the growth rate is diffusion limited, which leads to the fact that the crystallographic plane with the highest absorption rate grows the fastest. At higher temperatures (above 350°C), the logarithmic plot shows a negative slope. At these temperatures, the precursor solvent vaporizes away from the substrate and the precursor chemical reaction is carried out in the vapor phase. The growth mechanism is thus controlled by the surface collision. We found that the (002) preferred orientation of GZO film could be controlled by adjusting the deposition temperature and growth rate. However, the (110) preferred orientation that presents for the pyramidal-like structure could not be controlled within these conditions. According to these issues, we develop a methodology to control the (110) preferred orientation of GZO films by employing a low temperature of ZnO layer before high temperature GZO growth.

TABLE 1: The atomic density of some common planes for ZnO.

Crystal plane	(110)	(100)	(002)
Surface atomic density (N_s) (atom/cm ²)	0.22×10^{16}	0.12×10^{16}	0.11×10^{16}
Crystal plane structure			

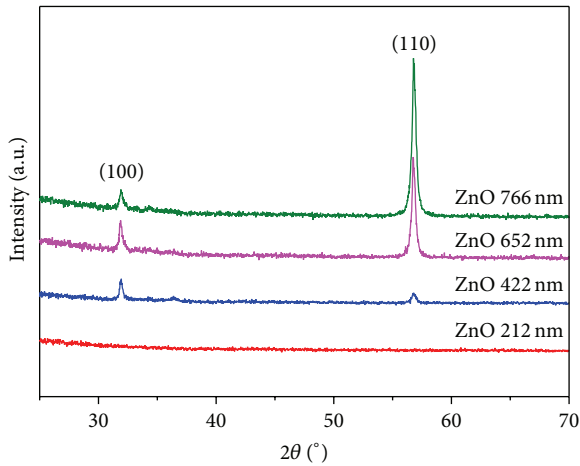


FIGURE 3: Structural properties of ZnO films at various thicknesses. The deposition temperature was 146°C.

2.2. Effect of ZnO Buffer Layer Thicknesses on the Orientation of GZO Films. Figure 3 illustrates the evolution XRD patterns for the first step growth of ZnO layers at various film thicknesses. At a low growth temperatures of 146°C, the films thicker than 212 nm exhibited two diffraction peaks at a value of 2θ of 31.8 and 56.8°, corresponding to the (100) and (110) plane of hexagonal ZnO. When the film thickness is less than 212 nm, no diffraction peaks were observed due to the amorphous nature. Generally for low growth temperature of ZnO by LPCVD at about 150°C, the preferred orientation of ZnO films is (110) plane, which is evident when the film thickness is larger than ~200 nm. This result is understandable because the film growth at this temperature is controlled by surface reaction, by which the crystalline plane with the highest surface atomic density (N_s) is formed favorably. As a result, the (110) plane would be preferred for hexagonal ZnO because it has the highest surface atomic density compared with (100) and (002) plane as shown in Table 1.

Figure 4 demonstrates the effect of the ZnO buffer layer thickness on the natively textured surface of ZnO films prepared at 146°C. As can be seen in Figure 4, all the ZnO thin film surfaces were pyramid-like grain and the grain size was increased together with the increase of ZnO film thickness. These results clearly indicated that the surface grain size of ZnO films could be modified by adjusting the ZnO thickness. Consequently, the GZO films were grown at 400°C onto the various ZnO buffer layer thicknesses.

The crystal structure and orientation of the as-deposited GZO thin film grown on various thickness of ZnO buffer layer were investigated using XRD and the results are depicted in Figure 5. It is worthy to note that a strong (002) peak was observed for GZO film growth onto a thin ZnO buffer layer (~30 nm), indicating the GZO film is highly oriented with its crystallographic c-axis perpendicular to the substrate. This is because the thin ZnO buffer layer plays a role as a seed layer for the GZO film growth and thus there is no significant change in the orientation of GZO film. However, with the increasing in ZnO buffer layer thickness, the preferred orientation changes from the plane with minimum surface energy (002) to the plane with relatively high surface energy (110). This can be explained due to the forming of (110) structure of ZnO buffer layer served as an energy barrier and thus the (110) preferred orientation of GZO film grown on (110) plane is easier than other crystal planes. Evidently, GZO thin films used ZnO as buffer layer whose thickness is thicker than 212 nm are favorable to promote the GZO film growth along (110) preferred orientation. These results conclude that ZnO buffer layer plays an important role in the change of growth direction of GZO film. Further, we studied the effect of deposition temperature of GZO on orientation of GZO film growth by using a thick 422 nm ZnO buffer layer as a template. Figure 6(a) depicts the structure and orientation of GZO/ZnO (422 nm) films grown at different deposition temperature.

Obviously, the orientation of GZO film growth was preferred to (100) and (110) plane in which (110) is the

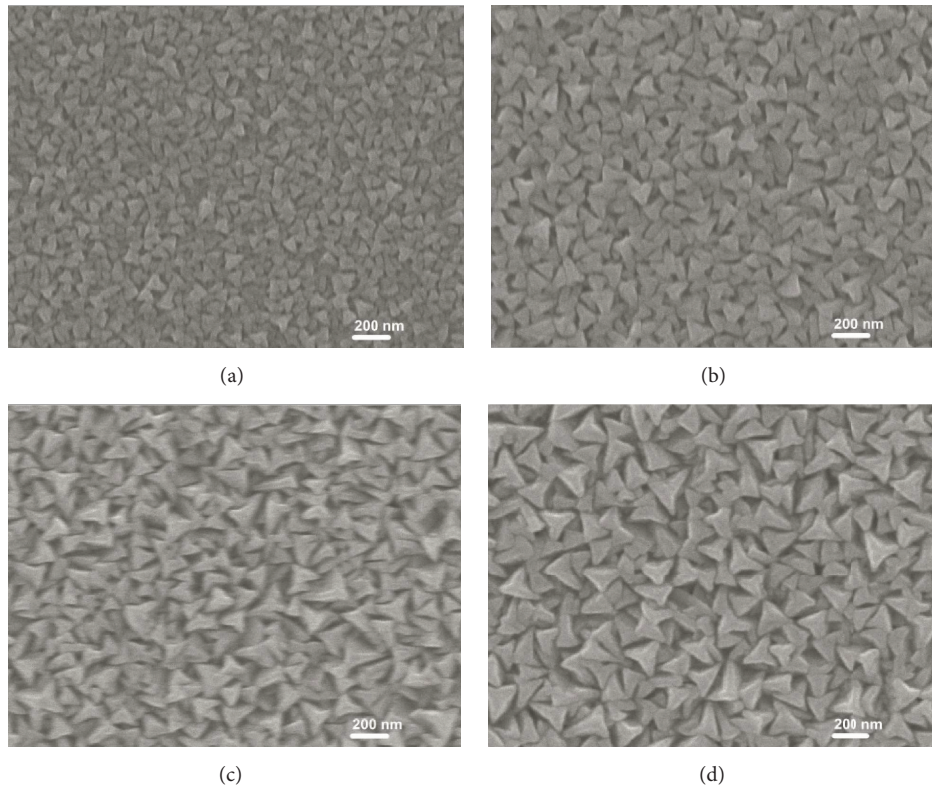


FIGURE 4: Surface morphology of ZnO films at various thicknesses: (a) 212 nm, (b) 422 nm, (c) 652 nm, and (d) 766 nm. The deposition temperature was 146°C.

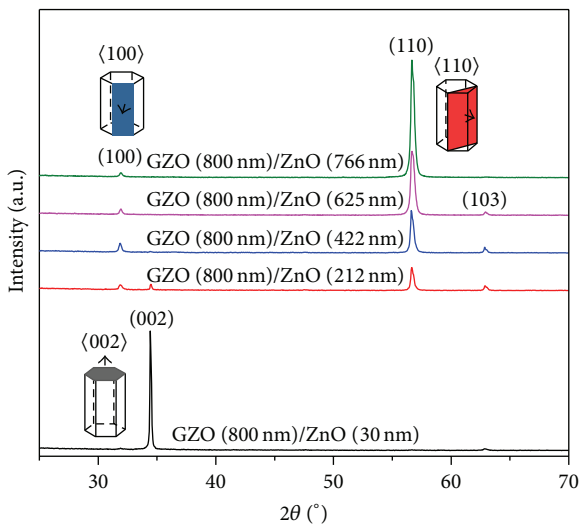


FIGURE 5: X-ray diffraction patterns of the GZO film growth on different thickness of ZnO buffer layer. The deposition temperature of GZO film was 400°C.

main crystal plane, as shown in Figure 6. This result implies that the orientation of GZO film growth might not have been influenced by deposition temperature. The intensity of (100) peak was increased slightly with increasing deposition temperature. From the change of (100) intensity ratio, we

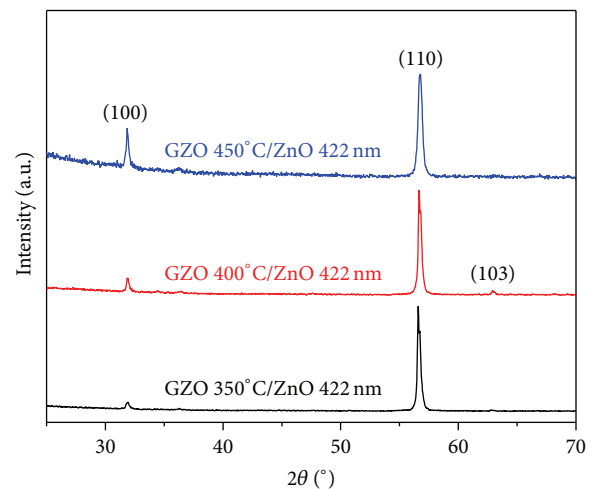


FIGURE 6: X-ray diffraction patterns of the GZO film grown on a thick 422 nm ZnO buffer layer at different deposition temperature.

can estimate the activation energy barrier for (100) plane through the Arrhenius plot of (100) intensity ratio at different deposition temperature.

Figure 7 shows the Arrhenius plot of (100) intensity ratio between 350 and 450°C. From the plot, the activation energy barrier $E_a = -8.314 \times \text{slope}$ (J/mol). The activation energy barrier for (100) crystal plane was estimated

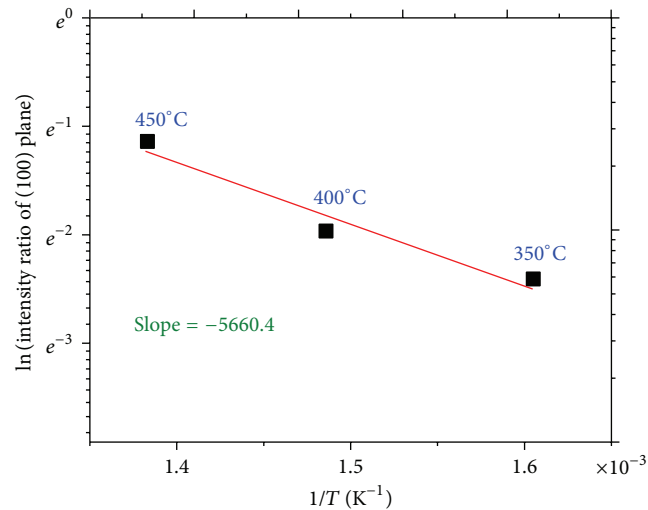


FIGURE 7: The Arrhenius plot of intensity ratio of (100) crystal plane of the GZO film grown on a thick 422 nm ZnO buffer layer against the reciprocal of the absolute temperature.

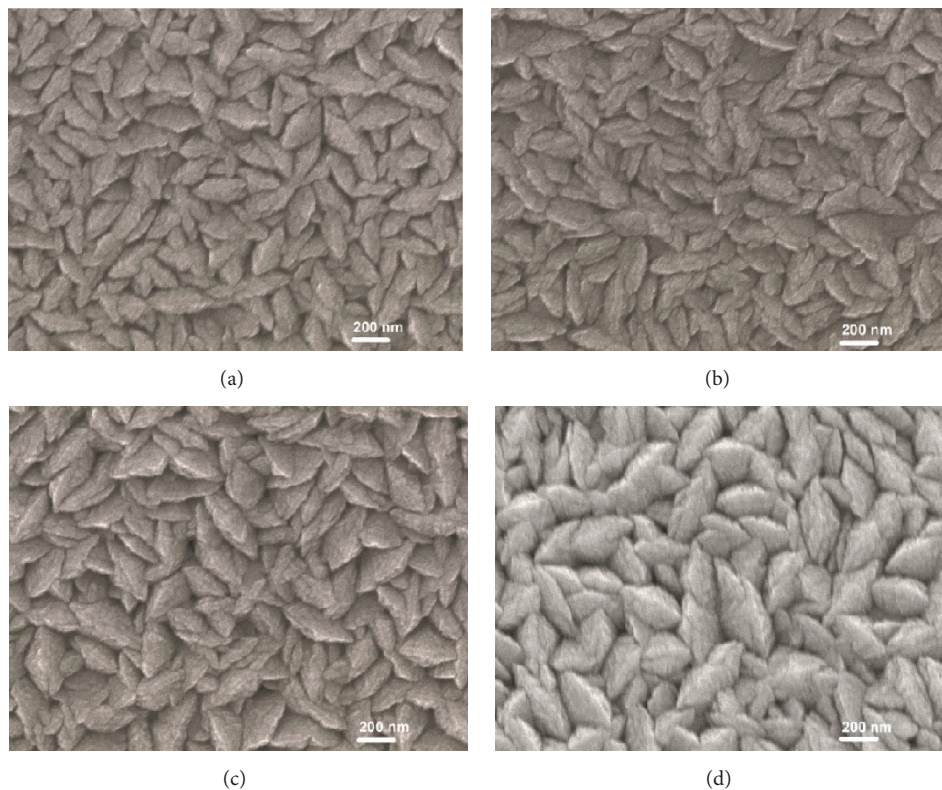


FIGURE 8: Surface morphology of GZO film with thickness ~ 800 nm on different ZnO buffer layer thicknesses: (a) 212 nm, (b) 422 nm, (c) 652 nm, and (d) 766 nm. The deposition temperature of GZO film was 400°C .

$\sim 11.24 \text{ kcal mol}^{-1}$, which is higher than that observed for film growth ($3.9 \text{ kcal mol}^{-1}$). This result indicates that the (100) crystal plane could be controlled at high temperature deposition.

Figures 8(a)–8(d) reveal typical SEM images of natively textured surface GZO thin films deposited on various thickness of ZnO buffer layer. The GZO films grown on different ZnO buffer layer exhibit a well-textured morphology

TABLE 2: Summary of the electrical properties of GZO films prepared at 400°C on various ZnO buffer layer thickness.

Samples	Resistivity (Ω cm)	Mobility ($\text{cm}^2 \text{V}^{-1} \text{s}^{-1}$)	Bulk concentration (cm^{-3})
GZO (800 nm)/ZnO (30 nm)	5.3×10^{-4}	16.25	7.3×10^{20}
GZO (800 nm)/ZnO (212 nm)	5.5×10^{-4}	16.10	7.1×10^{20}
GZO (800 nm)/ZnO (422 nm)	5.7×10^{-4}	16.30	6.8×10^{20}
GZO (800 nm)/ZnO (652 nm)	5.8×10^{-4}	16.35	6.7×10^{20}
GZO (800 nm)/ZnO (766 nm)	5.9×10^{-4}	16.45	6.5×10^{20}

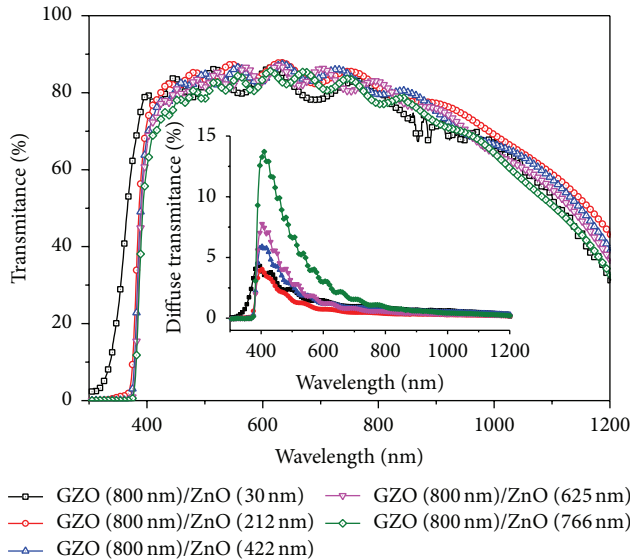


FIGURE 9: Optical properties of GZO film with thickness ~800 nm on different ZnO buffer layer thicknesses. The deposition temperature of GZO film was 400°C.

with pyramidal texture surface, confirming that the highly textured morphology of the GZO films is preserved well after two-step growth. The surface morphology of the GZO (800 nm)/ZnO (766 nm) film shows the largest pyramidal grain size, indicating that the grain size of GZO layer strongly depends on the grain size of ZnO buffer layer.

The optical properties illustrate the transmittance and light trapping efficiency of the bilayer GZO (800 nm)/ZnO films. As shown in Figure 9, the average optical transmittances were over 80% at the wavelength from 400 to 800 nm. However, the transmittance of the films decreased slightly in the long-wavelength range above 1000 nm because of the absorption of free carriers in the ZnO films caused by gallium doping. As shown and indicated by Figures 8-9, the light scattering properties had a good relationship with the surface morphologies. The thicker the ZnO buffer layer, the higher the diffuse transmittance that was obtained due to the increasing of surface texture grain size. This suggests that the facile way to improve the light scattering capability of GZO layers is to increase the ZnO buffer layer thickness. However, one has to consider also the transparency of the GZO layer, which may be drastically reduced for too thick layers [18]. As

a result, the light diffuse transmittance of the film with a GZO (800 nm)/ZnO (766 nm) exhibited 13% increase at 420 nm wavelength due to the larger grain size of the pyramidal texture surface.

In order to be used as front contact in thin film solar cells, electrical property of these GZO/ZnO films must be considered, as shown in Table 2. It can be revealed that the increasing of ZnO buffer layer thickness leads to slight increase in resistivity and slight reduction of carrier concentration of GZO film. Nevertheless, all the GZO films with various ZnO buffer layer thicknesses exhibit a relatively low resistivity of $10^{-4} \Omega$ cm. In addition, the mobilities of GZO films are increased slightly when increasing ZnO buffer layer thicknesses due to the pyramid-like grains size being increased which was verified by SEM (Figure 8).

3. Conclusions

GZO films with a pyramidal texture surface were successfully developed by the control of (110) preferred orientation. The films exhibited satisfactory optoelectronic properties. By employing the low temperature ZnO buffer layer, we improved the light diffuse transmittance of the film up to 13% at 420 nm wavelength. Thus, the obtained GZO films deposited ZnO buffer layer has high potential for use as front TCO layers in Si-based thin film solar cells. These results could develop the potential way to fabricate high haze TCO thin film using MOCVD or sputtering techniques by depositing a low temperature ZnO layer to serve as a template.

Competing Interests

The authors declare that they have no competing interests.

Authors' Contributions

Nam Giang Nguyen and Van Thi Thanh Ho conceived and designed the experiments and then they analyzed the experimental results and wrote the paper; Long Giang Bach performed the experiments.

Acknowledgments

The authors would like to thank Professor Lu-Sheng Hong, National Taiwan University of Science and Technology, for the support for this work.

References

- [1] A. Shah, P. Torres, R. Tscharnner, N. Wyrsh, and H. Keppner, "Photovoltaic technology: the case for thin-film solar cells," *Science*, vol. 285, no. 5428, pp. 692–698, 1999.
- [2] H. Sai, H. Jia, and M. Kondo, "Impact of front and rear texture of thin-film microcrystalline silicon solar cells on their light trapping properties," *Journal of Applied Physics*, vol. 108, no. 4, Article ID 044505, 2010.
- [3] M. Berginski, J. Hüpkes, M. Schulte et al., "The effect of front ZnO:Al surface texture and optical transparency on efficient light trapping in silicon thin-film solar cells," *Journal of Applied Physics*, vol. 101, no. 7, Article ID 074903, 2007.
- [4] O. Isabella, J. Krč, and M. Zeman, "Modulated surface textures for enhanced light trapping in thin-film silicon solar cells," *Applied Physics Letters*, vol. 97, no. 10, Article ID 101106, 2010.
- [5] V. E. Ferry, M. A. Verschuuren, M. C. V. Lare, R. E. I. Schropp, H. A. Atwater, and A. Polman, "Optimized spatial correlations for broadband light trapping nanopatterns in high efficiency ultrathin film a-Si:H solar cells," *Nano Letters*, vol. 11, no. 10, pp. 4239–4245, 2011.
- [6] G. Yue, L. Sivec, J. M. Owens, B. Yan, J. Yang, and S. Guha, "Optimization of back reflector for high efficiency hydrogenated nanocrystalline silicon solar cells," *Applied Physics Letters*, vol. 95, no. 26, Article ID 263501, 2009.
- [7] S. Calnan, J. Hüpkes, B. Rech, H. Siekmann, and A. N. Tiwari, "High deposition rate aluminium-doped zinc oxide films with highly efficient light trapping for silicon thin film solar cells," *Thin Solid Films*, vol. 516, no. 6, pp. 1242–1248, 2008.
- [8] H. Zhu, J. Hüpkes, E. Bunte, J. Owen, and S. M. Huang, "Novel etching method on high rate ZnO:Al thin films reactively sputtered from dual tube metallic targets for silicon-based solar cells," *Solar Energy Materials and Solar Cells*, vol. 95, no. 3, pp. 964–968, 2011.
- [9] H. L. Ma, D. H. Zhang, S. Z. Win, S. Y. Li, and Y. P. Chen, "Electrical and optical properties of F-doped textured SnO₂ films deposited by APCVD," *Solar Energy Materials and Solar Cells*, vol. 40, no. 4, pp. 371–380, 1996.
- [10] N. Amin, T. Isaka, A. Yamada, and M. Konagai, "Highly efficient 1 μm thick CdTe solar cells with textured TCOs," *Solar Energy Materials and Solar Cells*, vol. 67, no. 1–4, pp. 195–201, 2001.
- [11] S. Fay, S. Dubail, U. Kroll, J. Meier, Y. Ziegler, and A. Shah, "Light-trapping enhancement for thin-film silicon solar cells by roughness improvement of the ZnO front TCO," in *Proceedings of the 16th European Photovoltaic Solar Energy Conference and Exhibition (EU PVSEC '00)*, p. 361, Glasgow, Scotland, 2000.
- [12] T. Oyama, M. Kambe, N. Taneda, and K. Masumo, "Requirements for TCO substrate in si-based thin film solar cells -toward tandem," in *Proceedings of the Light Management in Photovoltaic Devices-Theory and Practice*, vol. 1101 of *MRS Proceedings*, Materials Research Society, 2008.
- [13] M. Kambe, K. Masumo, N. Taneda, T. Oyama, and K. Sato, "Improvement of light-trapping effect on microcrystalline silicon thin film solar cells fabricated on high haze transparent conducting oxides films," in *Proceedings of the Technical Digest/17th International Photovoltaic Science and Engineering Conference (PVSEC '07)*, p. 1161, Fukuoka, Japan, December 2007.
- [14] N. Giang Nguyen, V. T. Thanh Ho, and L.-S. Hong, "Low-resistivity, high-transmittance Ga:ZnO films prepared through metalorganic chemical vapor deposition using an inexpensive solution of diethylzinc in n-hexane as the Zn precursor," *Applied Physics Letters*, vol. 102, no. 18, Article ID 181912, 2013.
- [15] K. Nishioka, N. Mizutani, and H. Komiyama, "A model for predicting preferential orientation of chemical-vapor-deposited films," *Journal of the Electrochemical Society*, vol. 147, no. 4, pp. 1440–1442, 2000.
- [16] Y. Kajikawa, S. Noda, and H. Komiyama, "Preferred orientation of chemical vapor deposited polycrystalline silicon carbide films," *Chemical Vapor Deposition*, vol. 8, no. 3, pp. 99–104, 2002.
- [17] N. Fujimura, T. Nishihara, S. Goto, J. Xu, and T. Ito, "Control of preferred orientation for ZnO_x films: control of self-texture," *Journal of Crystal Growth*, vol. 130, no. 1-2, pp. 269–279, 1993.
- [18] S. Fay, J. Steinhauser, S. Nicolay, and C. Ballif, "Polycrystalline ZnO: B grown by LPCVD as TCO for thin film silicon solar cells," *Thin Solid Films*, vol. 518, no. 11, pp. 2961–2966, 2010.

Research Article

An Efficient Metal-Free Hydrophilic Carbon as a Counter Electrode for Dye-Sensitized Solar Cells

Mojgan Kouhnavard,¹ Norasikin Ahmad Ludin,² Babak Vazifekkhah Ghaffari,¹ Kamaruzzaman Sopian,² Norshazlinah Abdul Karim,² and Mikio Miyake¹

¹Malaysia-Japan International Institute of Technology, Universiti Teknologi Malaysia (UTM), 54100 Kuala Lumpur, Malaysia

²Solar Energy Research Institute (SERI), Universiti Kebangsaan Malaysia (UKM), 43600 Bangi, Selangor, Malaysia

Correspondence should be addressed to Norasikin Ahmad Ludin; sheekeen@ukm.edu.my

Received 20 November 2015; Accepted 22 February 2016

Academic Editor: Prakash Basnyat

Copyright © 2016 Mojgan Kouhnavard et al. This is an open access article distributed under the Creative Commons Attribution License, which permits unrestricted use, distribution, and reproduction in any medium, provided the original work is properly cited.

This study presents a new cost-effective metal-free counter electrode (CE) for dye-sensitized solar cells (DSSCs). CE was prepared by doctor blading a hydrophilic carbon (HC) particle on a fluorine-doped tin oxide substrate. Thereafter, HC CE was characterized using X-ray diffraction, profilometry, four-point probe testing, and cyclic voltammetry. A 2 μm thick HC CE revealed a comparable catalytic activity to that of the Pt electrode under the same experimental conditions. DSSC based on HC CE was analyzed and showed J_{sc} of 6.87 mA/cm² close to that of DSSC with Pt CE (7.0 mA/cm²). More importantly, DSSC based on HC CE yielded a power conversion efficiency (η) of 2.93% under AM 1.5 irradiation (100 mW/cm²), which was comparable to that of DSSC based on standard Pt CE. These findings suggest that HC CE could be a promising CE for low-cost DSSCs.

1. Introduction

Silicon solar cell currently has the largest market share of 85% with conversion efficiency of approximately 25% [1]. However, this solar cell could not compete with conventional energy sources because of the high production cost that is mostly caused by the high purification process of the material. This issue motivated the scientist to find new methods to exploit the cheaper and highly efficient solar energy. Dye-sensitized solar cells (DSSCs), as third-generation solar cells, are the major variant in this approach [2, 3]. Since DSSC was invented by pioneers O'Regan and Grätzel in 1991 [4], this solar cell type has been introduced as one of the low-cost and highly efficient solar cells because of the availability of materials, low cost, and simple fabrication processes [5–9]. Over the last 10 years, the highest efficiency of DSSCs ever reported is approximately 12% [10, 11].

In principle, DSSCs comprise three main components, namely, photoanode, counter electrode (CE), and electrolyte (commonly iodide), as shown in Figure 1. The photoanode is an oxide semiconductor, such as TiO₂, deposited on a transparent conductive oxide (TCO) substrate. Thereafter, the

TiO₂ surface is sensitized with dye (ruthenium complex), thereby contributing to the photon absorption and consequent electron injection. The electrolyte contains iodide-triiodide (I^-/I_3^-) redox couples transferring the electrons from the photoanode to the CE. The Pt deposited on the TCO substrate is commonly used as a standard CE because of its high conductivity and catalytic activity toward the redox couples in the electrolyte.

This type of DSSC with current material has a total production cost between \$36 and \$158/m² [12]. The major contribution (50%–60%) to the manufacturing cost of DSSCs arises from substrates, dyes, electrolytes, and Pt CEs. Therefore, the cost reduction improvement of DSSC is of immense interest [12]. Accordingly, researchers have been conducting studies to develop new sensitizers, photoanodes, redox couples, and CEs to fabricate cheap and efficient devices. Among these components, metal-free CEs are the best option to complement natural resources because Pt is expensive and rare. Pt corrosion in triiodide-containing solutions that generates platinum iodides, such as PtI₄, is also reported [13].

In this subject matter, carbon based CEs, such as graphite [14, 15], carbon black [16], graphene [17], activated carbon

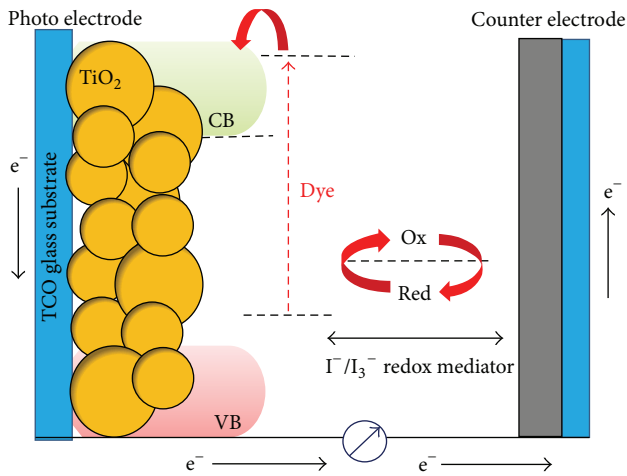


FIGURE 1: Schematic diagram of DSSC.

[18], and carbon nanotubes [19], are of significant research interest as potential low-cost replacements for Pt due to their high conductivity, large surface area, and catalytic activity toward the redox couples in the electrolyte [20].

Among them, graphite-based CEs often exhibit a low catalytic activity toward the redox couple. However, Veerappan et al. reported that submicrosized graphite electrode exhibits an improved performance by adjusting the particle size and film thickness [21]. Small graphite particles (flakes) are shown to have significant defects, that is, a considerable number of catalytic sites compared to micrographite ($>20 \mu\text{m}$).

The current research investigated a new low-cost hydrophilic carbon (HC) particle as CE to lead the commercialization of DSSC by making DSSCs more environment-friendly and less expensive device. The HC particle was produced using a simple electrolysis of a synthetic graphite plate [22]. Previous studies have reported that the HC particle has a good crystalline structure with an average particle size between 300 nm and 400 nm [22, 23].

2. Experimental Method

2.1. CE Preparation. The HC powder from Shion Co., Ltd. (Nagoya, Japan) was used to prepare HC CE. The HC paste was prepared by grinding 260 mg of HC powder with 0.4 mL of TiO_2 colloid, 0.8 mL of water, and 0.4 mL of 10% Triton X-100 (Fisher Chemical) aqueous solution. The TiO_2 colloid was prepared according to the procedures reported previously [24].

Prior to the deposition of CE on a fluorine-doped tin oxide (FTO) glass, FTOs with sheet resistance of approximately $8 \Omega/\text{sq}$ (Pilkington) were cut into $1.5 \text{ cm} \times 2 \text{ cm}$. For the electrolyte inlet/outlet, two small holes were drilled in the middle of the substrate. The substrate was cleaned in an ultrasonic bath with acetone and isopropanol for 20 min in each step followed by drying under nitrogen flow.

Using the doctor blade technique, the paste was spread on the FTO substrate using a double scotch tape and a glass rod followed by sintering in a cylinder furnace at 450°C at air

ambient for 30 min. For comparison, a thin layer of Pt paste (Dyesol Co.) was deposited on the entire surface of the FTO glass substrate using the same technique to deposit HC CE. This process was followed by sintering at 450°C for 30 min.

2.2. DSSC Preparation. Prior to the photoanode deposition, the FTO substrate with sheet resistance of $15 \Omega/\text{sq}$ was cut, cleaned, and dried similar to the description for HC CE in Section 2.1. Thereafter, the 90-T transparent titania paste (Dyesol Co.) was deposited on the conductive side of the FTO glass using the doctor blade technique [25, 26]. After deposition, the layer was annealed using a cylinder furnace set at 500°C in air for 30 min. The second layer of TiO_2 -WER-40 (Dyesol Co.) was further deposited on top of the first layer as a scattering layer. The second layer was annealed using similar technique and temperature. TiCl_4 treatment was performed by dipping the freshly sintered TiO_2 films into an aqueous solution of 40 mM of TiCl_4 tetrahydrofuran (Sigma Aldrich) at 70°C for 30 min. The TiO_2 film was rinsed in deionized water and ethanol and dried under nitrogen flow. After the TiCl_4 treatment, the TiO_2 film was sintered at 500°C for 30 min. The sintered electrode was maintained at 100°C for approximately 30 min before immersing into the dye solution. The TiO_2 film was then soaked for approximately 24 h at room temperature in a dye solution containing 0.3 mM of N719 (Solaronix) in acetonitrile and tert-butyl alcohol (1:1 volume ratio). After sensitization, the sensitized TiO_2 was rinsed with isopropanol and dried under nitrogen flow. To fabricate a DSSC, the photoanode and CE (Pt) with an active area of 1 cm^2 were encapsulated using a piece of hot melt film (Surlyn 1702; Solaronix) with a thickness of $25 \mu\text{m}$ and melted using hot press at 120°C for 20 s. A similar fabrication procedure was applied to assemble a photoanode with HC CE; the only difference was the sealant thickness, which was $90 \mu\text{m}$. After sealing, two drops of iodine-based electrolyte were injected between the two electrodes through the predrilled holes on the FTO glass. Thereafter, the holes were sealed using the same sealant with a small glass slide to cover the hole and pressed for 10 s at 120°C . In this research, a liquid electrolyte based on iodine was prepared by dissolving 0.06 M of iodine (Sigma Aldrich) in 0.5 M of 4-tert-butyl pyridine (Sigma Aldrich) and 0.5 M of 1-butyl-3 methyl imidazolium iodide in acetonitrile solvent and 1-butyl-3 methyl imidazolium iodide ($>98\%$; io.li.tec.).

3. Measurements

The HC CE crystal structure before and after the annealing treatment was identified through X-ray diffraction (XRD; Bruker) with $\text{Cu-K}\alpha$ radiation ($\lambda = 1.5418 \text{ \AA}$). The thickness and surface morphologies, both in top and in cross-sectional views of a sintered HC CE, were identified using a field emission scanning electron microscope (FESEM; JEOL, JSM7000F). The HC CE atomic ratio was recorded using the energy dispersive X-ray spectroscopy (EDX) analysis. Surface profilometry (Bruker) was performed to determine the thickness and roughness of CEs. The sheet resistance of HC CE was measured using a four-point probe (Keithley, 2400 auto calculating) resistivity test system. Cyclic voltammetry

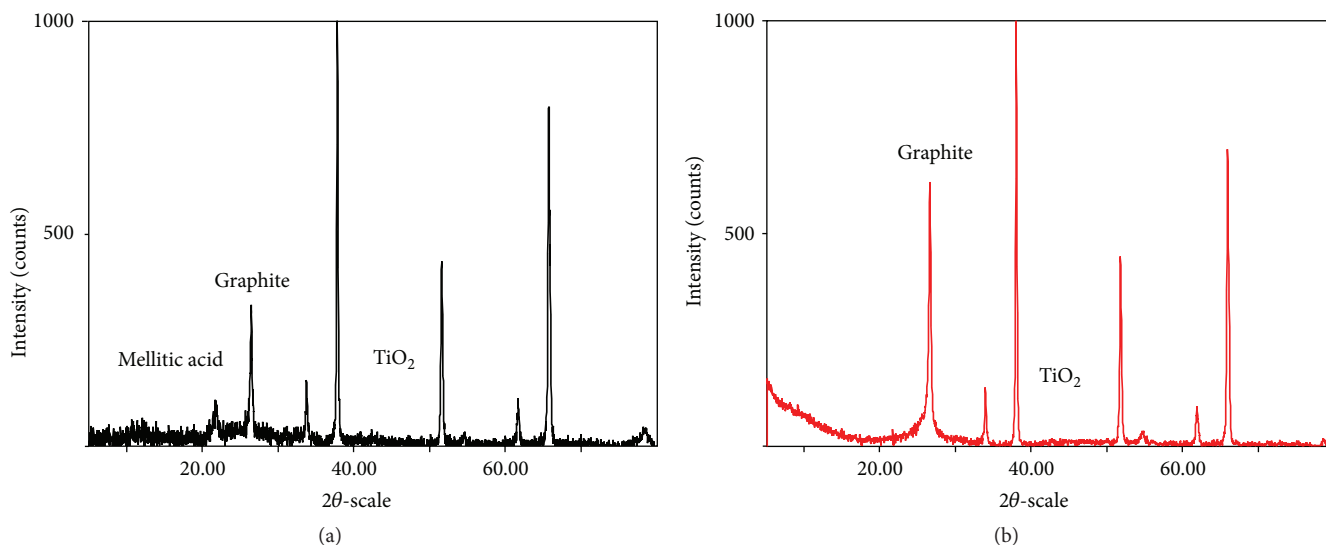


FIGURE 2: The X-ray diffraction pattern of (a) preheated and (b) sintered HC film.

(CV) analysis was conducted using Solartron with three electrode configurations, including Ag/AgCl (3 M KCl) used as a reference electrode, Pt wire as CE, and Pt and HC films as working electrodes, in an acetonitrile solution containing 10 mM of LiI, 1 mM of I_2 , and 0.1 M of $LiClO_4$ as supporting electrolytes at a scan rate of 50 mV/s. The active exposed surface area for CEs was 1 cm^2 . To measure the DSSC performance, current-voltage (I - V) characteristic analysis of a light exposed cell was performed using a Keithley model 2400 source-measuring unit. A solar simulator with 150 xenon lamps served as the light source with light intensity of 100 mW/cm^2 .

4. Results and Discussion

In CE, triiodide ions (I_3^-), which are produced by the reduction of oxidized sensitizer, are rereduced to I^- ions. For this reaction to occur, a CE must have a high electrocatalytic activity [27]. A high crystalline structure is considerably preferable for achieving a high electrocatalytic activity, thereby reducing internal defects, decreasing electron-loss pathway, and subsequently increasing energy conversion efficiency [28]. XRD measurement was conducted in this study to identify the HC CE crystal structure before and after annealing treatment, as shown in Figure 2. The HC film has a good crystalline structure that contains graphite and mellitic acid (benzene hexacarboxylic acid: $C_{12}H_6O_{12}$) with hexagonal and orthorhombic phase shapes, respectively. Further, the amorphous structures of TiO_2 could be observed with monoclinic phase shape. The peak of (002) at $2\theta = 26.4^\circ$ contributed to the graphite, whereas other peaks well fitted with those of cassiterite (referring to FTO). No changes were observed in the position of the graphite peaks after annealing. However, the crystallinity of graphite intensified from 215 counts to 663 counts after annealing.

Figure 3 displays the top and cross-sectional views of the FESEM images of the HC film on a FTO substrate along

with its atomic ratio. The inset (Figure 3(a)) shows the high-magnification image of the film. The HC film uniformly covered the substrate surface, thereby resulting in a crack-free HC film. A highly porous structure of the film with spherical HC particle was also observed. The cross-sectional view (Figure 3(b)) indicates thicknesses of 2.15 and $1\text{ }\mu\text{m}$ for the HC film and FTO covered glass substrate, respectively.

The atomic ratio of the HC film was estimated through EDX analysis (Figure 3(c)). The result showed that HC CE mostly contained carbon ($\approx 80\%$) with 4% titanium and 16% oxygen. Annealing treatment of the HC film was also performed under nitrogen flow to reduce the oxygen ratio in the film. However, this approach caused the carbon layer to fall off from the FTO substrate. It can be suggested that the oxygen functional groups in the HC film improved the adhesion between the FTO substrate and the HC layer, as well as among the HC particles.

Carbonaceous materials with rough surface provide considerable reduction sites or the surface area for CE to react with electrolytes, thereby resulting in the electrode's high catalytic activity [29]. Film thickness is also an important factor in determining the CE properties because it affects both the conductivity and catalytic activity of the electrode [30, 31]. Profilometry measurement was conducted to identify the surface roughness and thickness of HC CE. The results showed average roughness and thickness of 0.9 and $2.09\text{ }\mu\text{m}$, respectively, for HC CE, whereas they were 180 and 240 nm, respectively, for the Pt electrode prepared under the same condition. The layer thickness identified by the profilometry measurement was nearly in agreement with the FESEM results showing a thickness of $2.15\text{ }\mu\text{m}$ for the HC film.

Electrical conductivity and catalytic activity are two major factors that significantly affect the CE performance in DSSCs. Therefore, large conductivity and catalytic activity could result in higher energy conversion efficiency. The sheet resistance of HC CE was recorded using the four-point probe technique. The sheet resistivity of HC CE was determined to

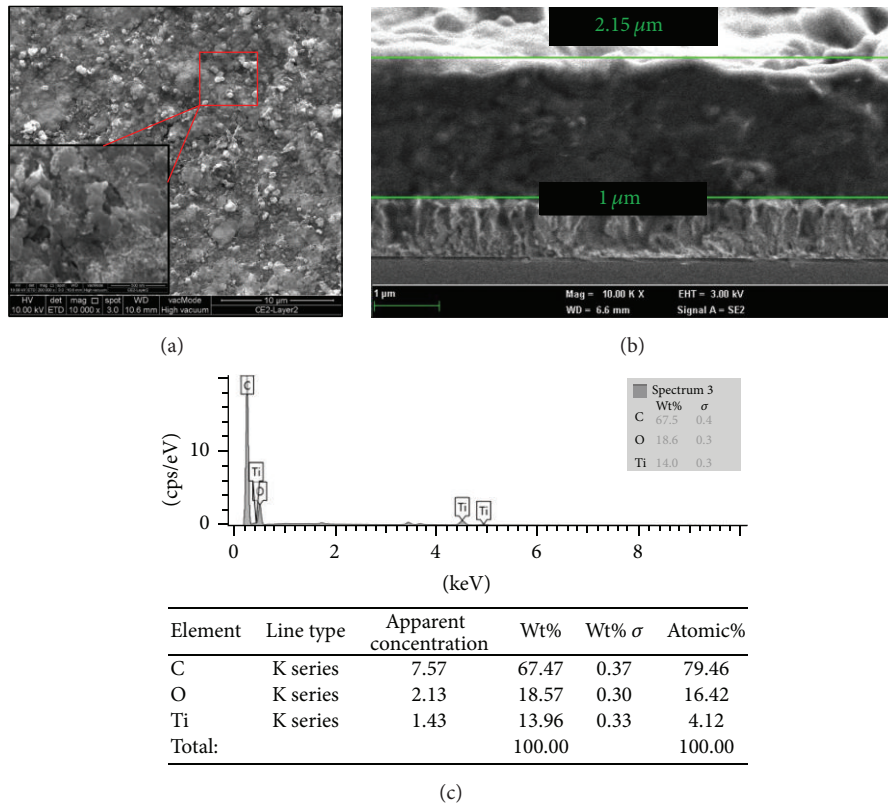


FIGURE 3: (a) Top view and (b) cross-sectional view of FESEM image for the HC film on FTO covered glass substrate (c) weight and atomic ratio of HC film estimated by EDX analysis.

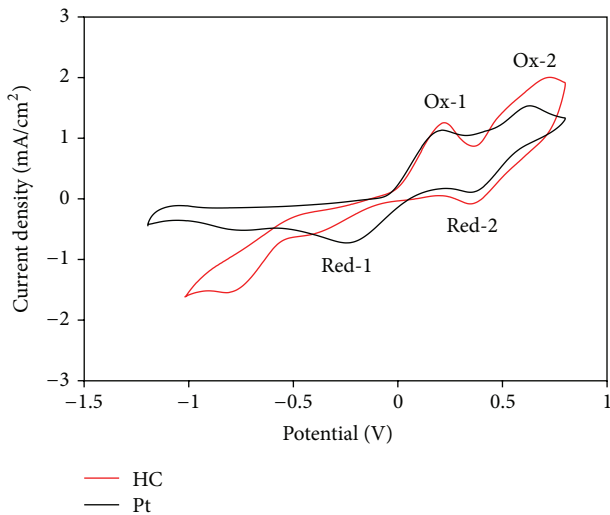


FIGURE 4: Cyclic voltammograms of Pt and HC film obtained at a scan rate of 50 mV/s electrode.

be slightly higher than that of the Pt electrode, with values of 7.8 and 3.17 Ω/sq, respectively.

CV was also performed to characterize the catalytic activity of HC CE toward the redox couples. Figure 4 shows the cyclic voltammogram of Pt and HC CEs, in which the potential interval ranged from -1V to 1V versus Ag/AgCl

at a scan rate of 50 mV/s. In the CV curves, two pairs of oxidation and reduction peaks (Ox-1/Red-1 and Ox-2/Red-2, respectively, as labeled in Figure 4) were resolved well in the range from -1V to 1V. The left and right pairs are assigned to (1) and (2), respectively. Consider the following:



The peaks obtained at the positive side are known as anodic peaks, which refer to the oxidation of iodide and triiodide. The peaks obtained at the negative section are the cathodic peaks, which correspond to the reduction of triiodide [32]. Consequently, the overall feature of CV for the HC electrode was similar to that for the Pt electrode, whereas HC CE represented a slightly faster oxidation rate (Ox-1 and Ox-2). In detail, HC CE exhibited Ox-1 and Ox-2 of 0.70 mA/cm² and 0.45 mA/cm², respectively, whereas they were 0.68 mA/cm² and 0.40 mA/cm², respectively, for the Pt electrode. HC CE revealed a lower reduction current density (Red-1) than that of the Pt electrode (0.75 mA/cm²), thereby contributing to a lower catalytic activity of HC CE because of the few catalytic sites for triiodide reduction. Nevertheless, a comparable catalytic activity to the Pt electrode was observed for HC CE, which could be attributed to the electrode's porous structure and large surface area, mainly favored by the addition of TiO₂ colloid to the HC particle, as reported earlier [24].

TABLE 1: Photovoltaic parameters of the cells shown in Figure 6. The errors are the SD values calculated from three measurements of three different devices for each film.

CE	R_s (Ω)	J_{sc} (mA/cm^2)	V_{oc} (V)	FF%	$\eta\%$
Pt	41.02 ± 1.20	7.0 ± 0.1	0.75 ± 0.00	68.71 ± 0.12	3.57 ± 0.06
HC	43.94 ± 0.78	6.87 ± 0.11	0.74 ± 0.00	57.26 ± 0.62	2.93 ± 0.06

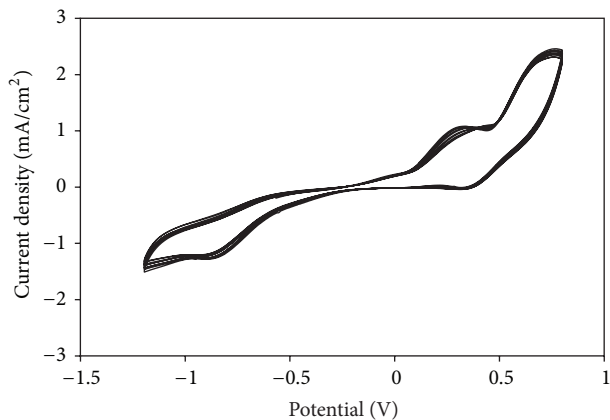


FIGURE 5: 50 successive cycles of HC CE obtained at a scan rate of 50 mV/s.

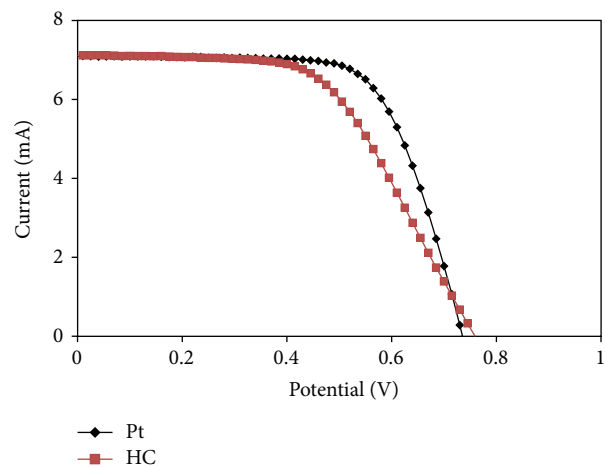


FIGURE 6: Comparison of I - V characteristics of DSSCs fabricated with Pt and HC CE under 1 sun illumination ($\text{AM}1.5$, $100 \text{ mW}/\text{cm}^2$).

A total of 50 consecutive CV scans were performed to investigate the stability of HC CE. Figure 5 shows the result. The shapes of the curves presented no evident change in the consecutive scans, thereby exhibiting stable anodic and cathodic peak currents. Thus, HC CE had reasonable chemical stability and was firmly deposited on the FTO substrate.

Three complete DSSC devices based on each HC and Pt CE were tested to study the performance of DSSC using the I - V measurement. Thereafter, the average value and standard deviation among different devices were calculated. Figure 6 shows the I - V curves of DSSC using HC and Pt CEs. The measurement was conducted under an AM 1.5 solar simulator at $100 \text{ mW}/\text{cm}^2$ intensity.

Table 1 presents a summary of the detailed photovoltaic parameters of HC and Pt CEs, including short current density (J_{sc}), open-circuit voltage (V_{oc}), fill factor (FF), cell efficiency (η), and series resistance (R_s). Note that DSSC using HC CE had J_{sc} of $6.87 \text{ mA}/\text{cm}^2$, which approximated that of DSSC with a Pt CE of $7.0 \text{ mA}/\text{cm}^2$. Comparable J_{sc} was favored by the high surface roughness of HC CE, thereby resulting in a comparable efficiency of 2.93% to the Pt-based DSSC with efficiency of 3.57%.

The lower cell efficiency using HC CE was mainly caused by its lower FF than that of the Pt-based cells. The lower FF was probably caused by the higher series resistance of HC CE (41.02Ω) than that of the Pt-based cell, which may be attributed to the significantly larger thickness of HC CE. Although a high thickness substantially increased the surface area for triiodide reduction, such characteristic also increased the average electron transport length before reaching the site for triiodide reduction, as well as the internal series resistance [33].

Nevertheless, HC CE has its own advantages of having a large surface area and high porosity that could compensate the effects of the higher series resistance, thereby resulting in comparable efficiency to that of the Pt-based cell.

Moreover, no apparent difference in V_{oc} of Pt- and HC-based DSSCs was observed. It should be also noted that these results were not high compared with the results reported in previous studies. The objective of the current research was not to obtain an optimized device but to conduct a comparative study on alternative CE to replace Pt.

5. Conclusion

This study investigated a new type of CE for triiodide reduction in DSSCs. CE was prepared using HC particle and successfully deposited on an FTO glass substrate using the doctor blade technique. The results indicated HC CE's high surface roughness and good conductivity and catalytic activity. Furthermore, DSSC with HC CE exhibited a comparable photovoltaic performance with an efficiency of 2.93% to DSSCs with Pt CE (3.57%). The low photovoltaic performance was due to the high series resistance of the HC-based DSSC. Although the high-cost Pt CE still appears the best among the tested CEs and exhibited the best performance, the HC particle has the potential to be employed as a CE for DSSC and can be expected to lead to a low-cost and stable DSSC. Future studies can focus on advanced coating methods, such as screen printing, to attain stable and uniform coating for the considerably low resistivity of HC CE. Other conductive materials, such as polymers, nanocarbon, and CNT, may also be incorporated into the fabrication methods of HC CE to

increase the electrode's conductivity and catalytic activity, thereby making it highly comparable to Pt CE.

Competing Interests

The authors declare that there are no competing interests regarding the publication of this paper.

Acknowledgments

The authors acknowledge the financial assistance provided by Ministry of Higher Education Malaysia (LEP 2.0/14/ukm/NT/03/1) and appreciate the contribution of the Solar Energy Research Institute (SERI) of Universiti Kebangsaan Malaysia.

References

- [1] D. M. Chapin, C. S. Fuller, and G. L. Pearson, "A new silicon p-n junction photocell for converting solar radiation into electrical power," *Journal of Applied Physics*, vol. 25, no. 5, pp. 676–680, 1954.
- [2] Y. Chiba, A. Islam, Y. Watanabe, R. Komiya, N. Koide, and L. Han, "Dye-sensitized solar cells with conversion efficiency of 11.1%," *Japanese Journal of Applied Physics*, vol. 45, no. 24–28, pp. L638–L640, 2006.
- [3] P. Poudel and Q. Qiao, "Carbon nanostructure counter electrodes for low cost and stable dye-sensitized solar cells," *Nano Energy*, vol. 4, pp. 157–175, 2014.
- [4] B. O'Regan and M. Grätzel, "A low-cost, high-efficiency solar cell based on dye-sensitized colloidal TiO₂ films," *Nature*, vol. 353, no. 6346, pp. 737–740, 1991.
- [5] J. Chen, K. Li, Y. Luo et al., "Flexible carbon counter electrode for dye-sensitized solar cells," *Carbon*, vol. 47, no. 11, pp. 2704–2708, 2009.
- [6] L. L. Chen, J. Liu, J. B. Zhang, X. W. Zhou, X. L. Zhang, and Y. Lin, "Low temperature fabrication of flexible carbon counter electrode on ITO-PEN for dye-sensitized solar cells," *Chinese Chemical Letters*, vol. 21, no. 9, pp. 1137–1140, 2010.
- [7] S. Ito, N.-L. C. Ha, G. Rothenberger et al., "High-efficiency (7.2%) flexible dye-sensitized solar cells with Ti-metal substrate for nanocrystalline-TiO₂ photoanode," *Chemical Communications*, no. 38, pp. 4004–4006, 2006.
- [8] L. Kavan, J. H. Yum, and M. Grätzel, "Optically transparent cathode for dye-sensitized solar cells based on graphene nanoplatelets," *ACS Nano*, vol. 5, no. 1, pp. 165–172, 2011.
- [9] M. Sibiński, M. Jakubowska, K. Znajdek, M. Słoma, and B. Guzowski, "Carbon nanotube transparent conductive layers for solar cells applications," *Optica Applicata*, vol. 41, no. 2, pp. 375–381, 2011.
- [10] A. Yella, H.-W. Lee, H. N. Tsao et al., "Porphyrin-sensitized solar cells with cobalt (II/III)-based redox electrolyte exceed 12 percent efficiency," *Science*, vol. 334, no. 6056, pp. 629–634, 2011.
- [11] M. Grätzel, "Dye-sensitized solar cells," *Journal of Photochemistry and Photobiology C: Photochemistry Reviews*, vol. 4, no. 2, pp. 145–153, 2003.
- [12] A. Fakharuddin, R. Jose, T. M. Brown, F. Fabregat-Santiago, and J. Bisquert, "A perspective on the production of dye-sensitized solar modules," *Energy and Environmental Science*, vol. 7, no. 12, pp. 3952–3981, 2014.
- [13] E. Olsen, G. Hagen, and S. Eric Lindquist, "Dissolution of platinum in methoxy propionitrile containing LiI/I₂," *Solar Energy Materials and Solar Cells*, vol. 63, no. 3, pp. 267–273, 2000.
- [14] S. E. Bourdo and T. Viswanathan, "Graphite/Polyaniline (GP) composites: synthesis and characterization," *Carbon*, vol. 43, no. 14, pp. 2983–2988, 2005.
- [15] X. Li, Y. S. Wei, Q. Q. Jin, and T. Z. Ren, "Expanded graphite/carbon nanotube as counter electrode for DSSCs," *Advanced Materials Research*, vol. 311–313, pp. 1246–1249, 2011.
- [16] K. Aitola, J. Halme, N. Halonen et al., "Comparison of dye solar cell counter electrodes based on different carbon nanostructures," *Thin Solid Films*, vol. 519, no. 22, pp. 8125–8134, 2011.
- [17] J. D. Roy-Mayhew, D. J. Bozym, C. Punckt, and I. A. Aksay, "Functionalized graphene as a catalytic counter electrode in dye-sensitized solar cells," *ACS Nano*, vol. 4, no. 10, pp. 6203–6211, 2010.
- [18] M. Wu, X. Lin, T. Wang, J. Qiu, and T. Ma, "Low-cost dye-sensitized solar cell based on nine kinds of carbon counter electrodes," *Energy and Environmental Science*, vol. 4, no. 6, pp. 2308–2315, 2011.
- [19] J. G. Nam, Y. J. Park, B. S. Kim, and J. S. Lee, "Enhancement of the efficiency of dye-sensitized solar cell by utilizing carbon nanotube counter electrode," *Scripta Materialia*, vol. 62, no. 3, pp. 148–150, 2010.
- [20] M. Kouhnavard, N. A. Ludin, B. V. Ghaffari, K. Sopian, and S. Ikeda, "Carbonaceous materials and their advances as a counter electrode in dye-sensitized solar cells: challenges and prospects," *ChemSusChem*, vol. 8, pp. 1510–1533, 2015.
- [21] G. Veerappan, K. Bojan, and S.-W. Rhee, "Sub-micrometer-sized graphite as a conducting and catalytic counter electrode for dye-sensitized solar cells," *ACS Applied Materials and Interfaces*, vol. 3, no. 3, pp. 857–862, 2011.
- [22] S. Ikeda, S. Kawasaki, Y. Hayashi et al., "Preparation of hydrophilic nano-carbon particles by electrolysis and their environmental applications," *ECS Meeting Abstracts*, abstract MA2012-02 3523, 2012.
- [23] S. Ikeda, S. Kawasaki, A. Nobumoto et al., "Preparation and applications of hydrophilic nano-carbon particles," *Advanced Materials Research*, vol. 832, pp. 767–772, 2014.
- [24] M. Kouhnavard, N. A. Ludin, B. V. Ghaffari, S. Ikeda, K. Sopian, and M. Miyake, "Hydrophilic carbon/TiO₂ colloid composite: a potential counter electrode for dye-sensitized solar cells," *Journal of Applied Electrochemistry*, vol. 46, no. 2, pp. 259–266, 2016.
- [25] Ceramic Industry, *Advanced Forming: Advances in Tape Casting Technology*, 2001.
- [26] F. Padinger, C. J. Brabec, T. Fromherz, J. C. Hummelen, and N. S. Sariciftci, "Fabrication of large area photovoltaic devices containing various blends of polymer and fullerene derivatives by using the doctor blade technique," *Opto-Electronics Review*, vol. 8, no. 4, pp. 280–283, 2000.
- [27] N. Papageorgiou, W. F. Maier, and M. Grätzel, "An iodine/triiodide reduction electrocatalyst for aqueous and organic media," *Journal of the Electrochemical Society*, vol. 144, no. 3, pp. 876–884, 1997.
- [28] S. Mukherjee, B. Ramalingam, L. Griggs et al., "Ultrafine sputter-deposited Pt nanoparticles for triiodide reduction in dye-sensitized solar cells: Impact of nanoparticle size, crystallinity and surface coverage on catalytic activity," *Nanotechnology*, vol. 23, no. 48, Article ID 485405, 2012.

- [29] T. N. Murakami and M. Grätzel, "Counter electrodes for DSC: application of functional materials as catalysts," *Inorganica Chimica Acta*, vol. 361, no. 3, pp. 572–580, 2008.
- [30] S. H. Huh, S.-H. Choi, and H.-M. Ju, "Thickness-dependent solar power conversion efficiencies of catalytic graphene oxide films in dye-sensitized solar cells," *Current Applied Physics*, vol. 11, no. 3, pp. S352–S355, 2011.
- [31] X. Fang, T. Ma, G. Guan, M. Akiyama, T. Kida, and E. Abe, "Effect of the thickness of the Pt film coated on a counter electrode on the performance of a dye-sensitized solar cell," *Journal of Electroanalytical Chemistry*, vol. 570, no. 2, pp. 257–263, 2004.
- [32] K. Imoto, K. Takahashi, T. Yamaguchi, T. Komura, J.-I. Nakamura, and K. Murata, "High-performance carbon counter electrode for dye-sensitized solar cells," *Solar Energy Materials and Solar Cells*, vol. 79, no. 4, pp. 459–469, 2003.
- [33] P. Joshi, L. Zhang, Q. Chen, D. Galipeau, H. Fong, and Q. Qiao, "Electrospun carbon nanofibers as low-cost counter electrode for dye-sensitized solar cells," *ACS Applied Materials and Interfaces*, vol. 2, no. 12, pp. 3572–3577, 2010.

Research Article

A Power Case Study for Monocrystalline and Polycrystalline Solar Panels in Bursa City, Turkey

Ayşegül Taşcıoğlu, Onur Taşkın, and Ali Vardar

Department of Biosystems Engineering, Faculty of Agriculture, Uludag University, 16059 Bursa, Turkey

Correspondence should be addressed to Ali Vardar; dravardar@uludag.edu.tr

Received 23 January 2016; Revised 8 February 2016; Accepted 18 February 2016

Academic Editor: Vishal Mehta

Copyright © 2016 Ayşegül Taşcıoğlu et al. This is an open access article distributed under the Creative Commons Attribution License, which permits unrestricted use, distribution, and reproduction in any medium, provided the original work is properly cited.

It was intended to reveal the time dependent power generation under different loads for two different solar panels under the conditions of Bursa province in between August 19 and 25, 2014. The testing sets include solar panels, inverter, multimeter, accumulator, regulator, pyranometer, pyrhelimeter, temperature sensor, and datalogger. The efficiency of monocrystalline and polycrystalline solar panels was calculated depending on the climatic data's measurements. As the result of the study, the average performances of monocrystalline and polycrystalline panels are 42.06 and 39.80 Wh, respectively. It was seen that 87.14 W instantaneous power could be obtained from monocrystalline solar panel and that 80.17 W instantaneous power could be obtained from polycrystalline solar panel under maximum total radiation (1001.13 W/m^2). Within this frame, it was determined that monocrystalline solar panel is able to operate more efficiently under the conditions of Bursa compared to polycrystalline solar panel. When the multivariate correlations coefficients were examined statistically, a significant relationship in positive direction was detected between total and direct radiation and ambient temperature on energy generation from monocrystalline and polycrystalline panel.

1. Introduction

Today, one of the most significant requirements of developed and developing countries is energy. Even if there are various methods of energy production and consumption, all the countries require cheap, large, and clean energy sources [1]. As the fossil fuels will be consumed after a specific period and as their production is very expensive, it becomes obligatory to determine alternative energy sources and to benefit from these sources with high efficiency. Moreover, the use of energy sources which cannot be renewed at a large extent had significantly increased the environmental problems. Thus, tendency towards renewable energy sources with low environmental effects is advantageous in all aspects [2]. Renewable energy sources are defined as energy flows which are replaced at the same speed as they are used. All renewable energy sources on Earth arise from the effect of solar radiation which can be directly or indirectly converted to energy by using different technologies.

Even if it is the most expensive renewable energy technology, "photovoltaic" technology is the easiest energy

technology in respect of design and installation. But its main superiority arises from the fact that it is an environment friendly technology with low maintenance cost [3]. Besides these, photovoltaic systems are also modular. In other words, they can be assembled anywhere required. In case of increase of requirement, new photovoltaic models can be easily added to the system in a short while. This is not in subject for other energy production systems. In particular the photovoltaic systems that are installed close to end users decrease the requirement for transmission and distribution devices and increase the reliability of local electric service.

Crystalline silicon offers an improved efficiency when compared to amorphous silicon while still using only a small amount of material [4]. Silicon has several advantages such as abundance on Earth, low contamination rate, high durability, and the wide experience of the microelectronics industry. The most widely used silicon cells in manufacturing are monocrystalline and polycrystalline, although many other technologies have been developed [5]. In the first commercial solar panels, monocrystalline structured silicon had been

used which was being enlarged by the crystal pulling method. In this technique, which is still the commonly used method in photovoltaic industry, first pure silicon is obtained through various chemical and thermal reactions of silicon oxide in arc furnaces. And then, a monocrystalline structured silicon piece is dipped in the silicon melt. When the core is removed from the melt, the cooling silicon melt becomes piled all around the core. This silicon is divided into slices after getting chunk. This happens in two phases. First the pile is cut in the form of rectangle blocks. And then these blocks are separated to slices and processed in the form of panel. The high amount of material loss during production is the disadvantage of these cells. They are produced with a thickness of about 0.5 mm. Their color is dark blue, and their approximate weight is less than 10 gr. Polycrystalline silicon production technologies are easier. The commonly used method in production is the casting method. In polycrystalline silicon, the starting material is prepared as in the monocrystalline silicon. The required purity degree is also similar. The melted silicon with a semiconductor quality is casted into the moulds and left for cooling. And then the obtained blocks are cut in square form. The cost of solar panels obtained from materials produced by this technology is low compared to their efficiency [6].

Solar panels are nonlinear energy sources, and the operation points of the system also change along with the change in weather conditions [7]. Thus, the current/voltage values, power outputs, and efficiency of photovoltaic devices depend on climatic parameters [8, 9]. Within the scope of this study, it was intended to determine time dependent power performances and power values that can be generated under different loads of monocrystalline and polycrystalline solar panels having a rated power of 100 W by determining total and direct radiation and ambient temperature values for Bursa, Turkey.

2. Materials and Methods

In this study, the power performance of monocrystalline and polycrystalline panels experiments was performed under outdoor meteorological conditions of field laboratory of Department of Biosystems Engineering, Faculty of Agriculture, Bursa, Turkey (40°15'N, 28°53'E). A schematic view and photographs of this apparatus are shown in Figures 1 and 2, respectively. The experiments were conducted from August 19 to August 25, 2014, from 07:00 to 20:00 h. The apparatus was placed far from the shade of trees or buildings during the whole duration of the experiment.

In the testing system, there are monocrystalline (80 × 98 cm) and polycrystalline (67 × 100 cm) solar panels with a power of 100 W. Switch number 1 activates the monocrystalline solar panel (YLE100, Turkwatt, Turkey), and switch number 2 activates the polycrystalline solar panel (TW45P, Turkwatt, Turkey). Due to the design of the system, it is not possible to activate both panels at the same time. There are 10 load levels on the system showing resistance feature. Each generates a resistance of 10 W. The generated load (resistance) amount is able to be adjusted by an 11-graded switch. Thus, the system is able to be fed with a load in between 10 W and 100 W. The 11th grade of the switches was designed

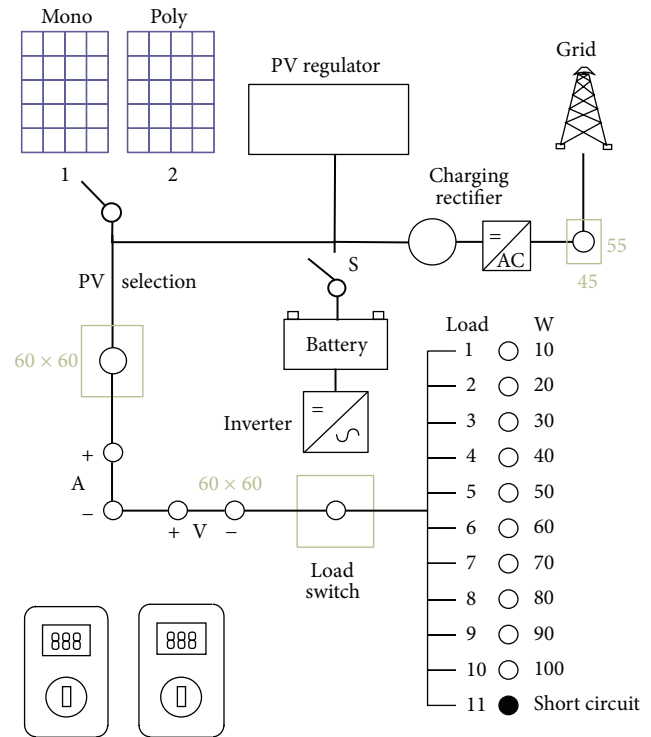


FIGURE 1: Schematic view.



FIGURE 2: Photograph of apparatus.

as short circuit. Within the scope of the study, electrical measurement system consisting of voltmeter (UT60E, UNI-T, China) and amperemeter (UT60E, UNI-T, China) was used in the determination of the current, voltage, and power values generated by the solar panels.

The measured climatic data used in this study were recorded by the datalogger (Cr1000, Campbell Scientific, USA). The dataset consists of 1 min averaged measurements of total radiation (CM11 pyranometer, Kipp&Zonen, Netherlands), direct radiation (CHP1 pyr heliometer, Kipp&Zonen, Netherlands), and ambient temperature (41342, Young, USA). All instruments as shown in Figure 3 were used with their original calibration factors.

The latitude of the solar panels and their inclination angle with the surface affects the generated energy amounts. In order to obtain electric energy from the solar panel systems in the most efficient manner, the panels should be positioned to be perpendicular to sunlight and to face south [10, 11].



FIGURE 3: Climatic station.

In respect of angular relations in between solar radiation and Earth, the most significant angle is the declination angle. It is also defined as the angle in between the solar radiation and equatorial plane at 12:00 o'clock. It arises due to the angle of $23^{\circ}45'$ in between the axis of the world and its orbital plane. If the world sun direction is at north of the equatorial plane, the declination angle is deemed as positive. The approximate value of declination angle (δ) can be calculated by the Cooper equation [12]. In the equation, n is the number of days of the year:

$$\delta = 23,34 \cdot \sin \left(360 \cdot \frac{n + 284}{365} \right). \quad (1)$$

Using tracking systems is the best way to collect maximum daily energy. This mechanical device follows the direction of the sun all day. The trackers are expensive, need energy for operation, and are not always applicable. Therefore, it is often practicable to orient the solar panel at an optimum tilt angle, β [13], where Φ is the latitude:

$$\beta = \Phi - \delta. \quad (2)$$

And efficiency is the expression of how much the solar panel is able to convert the solar radiation to useful energy. In the study, considering the solar radiation data measured by pyranometer, the radiation values reaching the solar panel are determined. These values are addressed as radiation reaching the unit surface area at unit time, and they are presented as power. Considering the power values generated by solar panels and measured by the data measurement systems, the efficiency of solar panels may be determined by the equation. In here η symbolizes the efficiency (%), P symbolizes the average power output (W), H symbolizes the total solar radiation (W/m^2), and PV symbolizes the surface area (m^2) [14]:

$$\eta = \frac{P}{PV \cdot H} \times 100. \quad (3)$$

And, statistically, a multivariate correlations analysis was performed to evaluate any significant differences on the

energy production between total radiation, direct radiation, and ambient temperature. All calculations were carried out using the software JMP (version 7.0, NC, USA).

3. Results and Discussion

Within the scope of this study, time dependent power performances and power values of monocrystalline and polycrystalline solar panels under different loads were intended by determining total and direct radiation and temperature values for Bursa, Turkey. The optimal tilt angle of solar panels used within this scope was adjusted to be 27° , and they were positioned to face south. Similar analyses were made to choose optimal tilt angle for the solar panel in order to collect the maximum solar radiation in Madinah, Saudi Arabia. It was found that the loss in the amount of collected energy when using the yearly average fixed angle is around 8% compared with the monthly optimum tilt angle [13].

Figures 4(a)–4(h) show the daily and average climatic results obtained from the study of the hourly values in the area of Bursa, Turkey. Based on the average results in Figure 4(h) one can conclude that the average ratio of total radiation during the experimental week is around $495.34 W/m^2$; that the average ratio of direct radiation during the experimental week is around $541.61 W/m^2$; that the ambient temperature during the experimental week is around $27.75^{\circ}C$. At 13:00, it reached the highest average total radiance by $886.09 W/m^2$ and highest average direct normal irradiance by $764.34 W/m^2$.

In the tests performed in between 07:00 and 20:00, the highest total radiation had been realized by $1001.13 W/m^2$ on 19.08.2014 at 13:00, and direct radiation had been $825.6 W/m^2$ at that time, and instantaneous power generation of $87.14 W$ had been realized by the monocrystalline panel and of $80.17 W$ had been realized by the polycrystalline panel. Within this frame, it was determined that monocrystalline solar panel generates $6.93 W$ more instantaneous power than the polycrystalline solar panel (Figure 5(a)).

And the highest power values that the monocrystalline and polycrystalline solar panels are able to generate under different loads are as follows. During the testing period of monocrystalline solar panel, $13.56 W$ power was obtained under 10 W load, $26.97 W$ power was obtained under 20 W load, $39.56 W$ power was obtained under 30 W load, $53.39 W$ power was obtained under 40 W load, $62.17 W$ power was obtained under 50 W load, $74.6 W$ power was obtained under 60 W load, $85.7 W$ power was obtained under 70 W load, $87.14 W$ power was obtained under 80 W load, $79.14 W$ power was obtained under 90 W load, $76.7 W$ power was obtained under 100 W load, and $7.09 W$ power was obtained as highest under short circuit. During the testing period of polycrystalline solar panel, $13.39 W$ power was obtained under 10 W load, $27.93 W$ power was obtained under 20 W load, $38.55 W$ power was obtained under 30 W load, $47.93 W$ power was obtained under 40 W load, $60.31 W$ power was obtained under 50 W load, $75.38 W$ power was obtained under 60 W load, $79.55 W$ power was obtained under 70 W load, $80.17 W$ power was obtained under 80 W load, $72.02 W$ power was obtained under 90 W load, $57.4 W$ power was

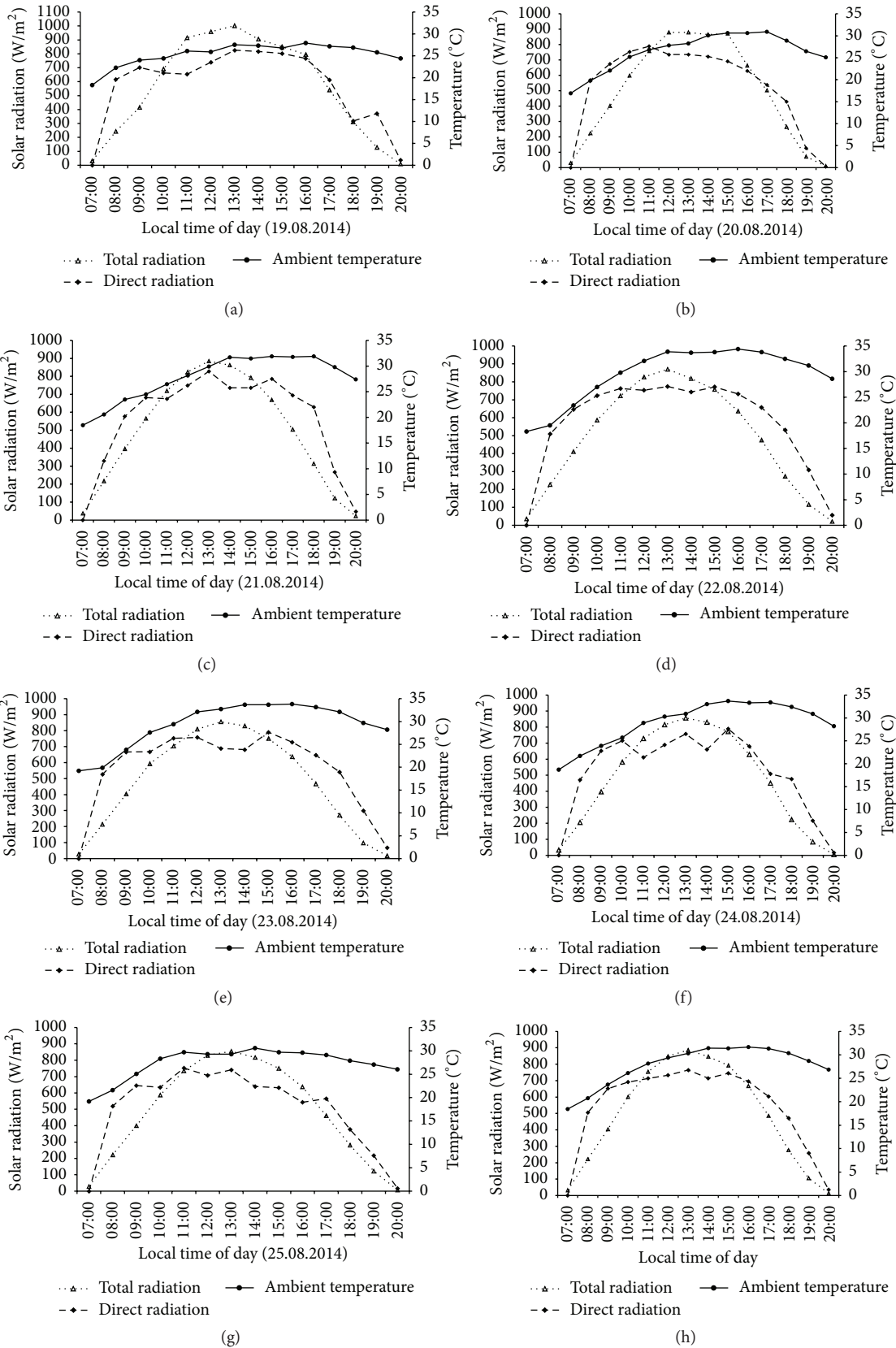


FIGURE 4: Daily and average results of climatic conditions.

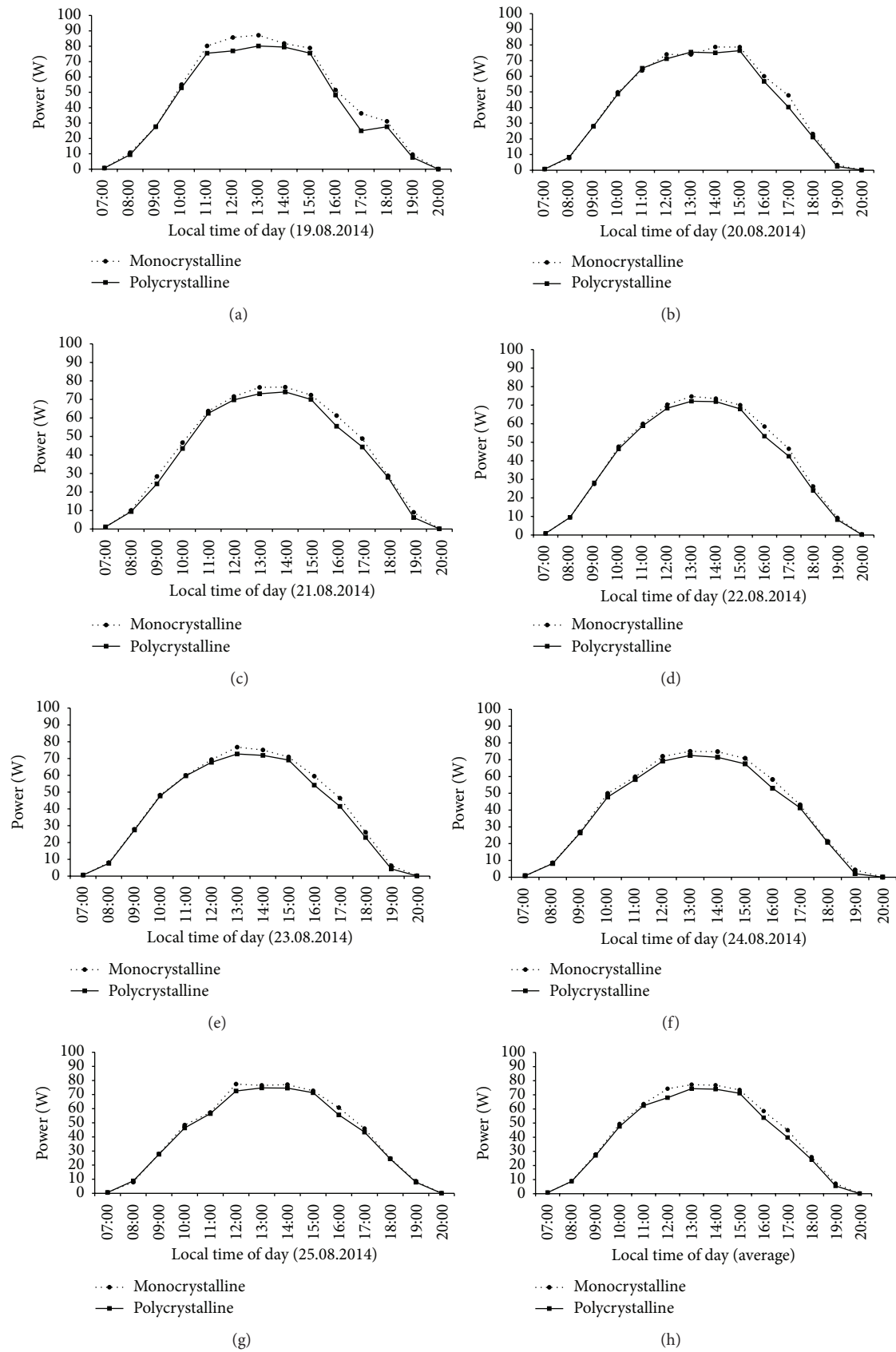


FIGURE 5: Hourly power output performance.

TABLE 1: Multivariate correlations coefficients.

	Direct radiation	Ambient temperature	Monocrystalline solar panel	Polycrystalline solar panel
Total radiation	0,8810**	0,5255**	0,9876**	0,9832**
Direct radiation		0,4986**	0,8442**	0,8439**
Ambient temperature			0,5940**	0,5881**
Monocrystalline solar panel				0,9938**

** shows the high level of importance statistically.

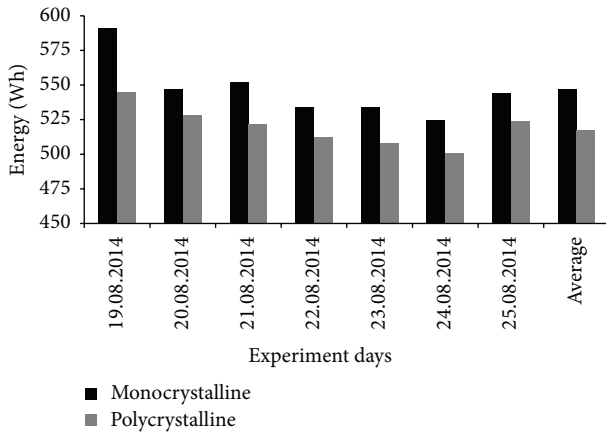


FIGURE 6: Energy output performance.

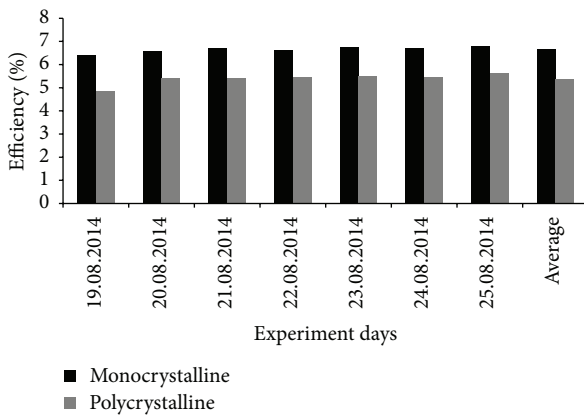


FIGURE 7: Panels efficiencies ratio.

obtained under 100 W load, and 6.3 W power was obtained under short circuit.

Figure 6 presents the daily energy production performance of panels. Depending on the radiation intensity to the panel surface differences are observed between energy productions. Average energy performances of monocrystalline and polycrystalline are 546.82 Wh and 517.52 Wh, respectively. Maximum and minimum energy production from panels were actualized on 19.08.2014 and 24.08.2014, respectively. The results obtained from the measurement show that monocrystalline solar panel performed better compared to polycrystalline at every experiment day.

Figure 7 shows the bar graph for daily module efficiency for each type of solar panel in this experiment.

The average conversion efficiencies of monocrystalline and polycrystalline arrays are 6.65% and 5.38%, respectively. It can be seen that highest monocrystalline module efficiency in day 7 (6.82%) and lowest in day 1 (6.39%) show a significantly higher efficiency compared to polycrystalline, which is 1.21% and 1.52%, respectively. A similar panel efficiency was found to be 11.02% and 4.32% for the Solarex photovoltaic monocrystalline and polycrystalline panels, respectively [15]. Power performances of solar panels in Singapore are presented by Jiang and Wong, who found a maximum efficiency of 8.12% for the monocrystalline panel and 7.45% for polycrystalline panel [16]. Also, average efficiencies of the monocrystalline and polycrystalline photovoltaic panels in Brasil were found to be 9.40% and 6.57%, respectively [5]. However, some works show the polycrystalline panels with a better performance, such as Ghazali and Abdul Rahman who show that polycrystalline panel is higher power output compared to monocrystalline panel in 4-day period with efficiency of 7.97% (day 1), 3.49% (day 2), 2.41% (day 3), and 7.52% (day 4) [14]. Considering the previous studies, more researches must be done in order to determine which specific conditions cause each kind of panel to perform better. From this experiment, it can be concluded that monocrystalline solar panels are the most suitable type of photovoltaic module to be used under Bursa, Turkey, climate condition.

The correlation coefficients relevant to the examined features are given in Table 1. According to the obtained findings, very high significant relation in positive direction was found in between total radiation and energy generation from monocrystalline and polycrystalline panel. High significant relation in positive direction was found in between direct radiation and energy generation from monocrystalline and polycrystalline panel. Also, there was a statistically nonsignificant relation in positive direction between ambient temperature and energy generation from monocrystalline and polycrystalline panel.

4. Conclusion

Developing a clean and renewable energy helps energy independence in Turkey. Solar energy with the types of polycrystalline and monocrystalline panels is most commonly used with different characteristic and efficiency. In this study, it has been shown that the efficiency of photovoltaic panels is influenced by climate conditions, type of used solar cells, and so forth. The daily average photovoltaic panel efficiency was 6.65% and 5.38% for the monocrystalline and polycrystalline, respectively. More researches must be done in order to determine which specific conditions cause each kind

of panel to perform better. This paper would be useful for the photovoltaic panel manufactures, researchers, and generating members to decide for Bursa, Turkey.

Competing Interests

The authors declare that there are no competing interests regarding the publication of this paper.

Acknowledgments

This study was done with the financial support of the Project no. Z-2013/31 approved by the Scientific Research Project Unit of Uludag University.

References

- [1] V. Ari, *Energy sources, energy planning and energy strategies of Turkey [M.S. thesis]*, Department of Mining Engineering, Institute of Natural and Applied Sciences, University of Cukurova, Adana, Turkey, 2007.
- [2] Usage Areas of Energy, 2014, <http://enerjisistemleri.blogspot.com.tr/2010/12/resim-galerisi.html>.
- [3] H. H. Öztürk and D. Kaya, *Electricity Generation from Solar Energy: Photovoltaic Technology*, Umuttepe Publications, Kocaeli, Turkey, 2013.
- [4] B. Parida, S. Iniyani, and R. Goic, "A review of solar photovoltaic technologies," *Renewable and Sustainable Energy Reviews*, vol. 15, no. 3, pp. 1625–1636, 2011.
- [5] C. E. C. Nogueira, J. Bedin, R. K. Niedzialkoski, S. N. M. de Souza, and J. C. M. das Neves, "Performance of monocrystalline and polycrystalline solar panels in a water pumping system in Brazil," *Renewable and Sustainable Energy Reviews*, vol. 51, pp. 1610–1616, 2015.
- [6] A. I. Ismael, *Electrical energy analyses in monocrystal of solar cell systems [M.S. thesis]*, Gazi University Institute of Science and Technology, Ankara, Turkey, 2012.
- [7] Q. Kou, *A method for estimation the long-term performance of photovoltaic pumping system [M.S. thesis]*, The University of Wisconsin-Madison, Solar Energy Laboratory, Madison, Wis, USA, 1996.
- [8] J. Carstensen, G. Popkirov, J. Bahr, and H. Föll, "CELLO: an advanced LBIC measurement technique for solar cell local characterization," *Solar Energy Materials and Solar Cells*, vol. 76, no. 4, pp. 599–611, 2003.
- [9] D. H. W. Li, G. H. W. Cheung, and J. C. Lam, "Analysis of the operational performance and efficiency characteristic for photovoltaic system in Hong Kong," *Energy Conversion and Management*, vol. 46, no. 7-8, pp. 1107–1118, 2005.
- [10] S. Turhan and I. Çetiner, "Performance evaluation of photovoltaic systems," in *Proceedings of the National Roof & Wall Symposium*, vol. 6, Bursa, Turkey, 2012.
- [11] A. Özgöçmen, *Electricity generation using solar cells [M.S. thesis]*, Gazi University, Institute of Science and Technology, Ankara, Turkey, 2007.
- [12] D. S. Strebkov, A. E. Irodionov, V. P. Tarasov, and E. G. Bazarova, "Optimum orientation of a nontracking solar concentrator," *Thermal Engineering*, vol. 55, no. 12, pp. 997–1000, 2008.
- [13] M. Benganem, "Optimization of tilt angle for solar panel: case study for Madinah, Saudi Arabia," *Applied Energy*, vol. 88, no. 4, pp. 1427–1433, 2011.
- [14] M. A. Ghazali and A. M. Abdul Rahman, "The performance of three different solar panels for solar electricity applying solar tracking device under the Malaysian climate condition," *Energy and Environment Research*, vol. 2, no. 1, pp. 235–243, 2012.
- [15] U. Stutenbaeumer and B. Mesfin, "Equivalent model of monocrystalline, polycrystalline and amorphous silicon solar cells," *Renewable Energy*, vol. 18, no. 4, pp. 501–512, 1999.
- [16] F. Jiang and A. Wong, "Study on the performance of different types of PV modules in Singapore," in *Proceedings of the 7th International Power Engineering Conference (IPEC '05)*, pp. 1–109, Singapore, December 2005.

Research Article

New 1,3,4-Oxadiazole Based Photosensitizers for Dye Sensitized Solar Cells

Umer Mehmood,^{1,2,3} Ibnelwaleed A. Hussein,^{3,4} and Muhammad Daud³

¹Center of Research Excellence in Renewable Energy, Research Institute, King Fahd University of Petroleum & Minerals (KFUPM), P.O. Box 5050, Dhahran 31261, Saudi Arabia

²Polymer and Process Engineering Department, University of Engineering & Technology Lahore, Lahore 54000, Pakistan

³Department of Chemical Engineering, King Fahd University of Petroleum & Minerals (KFUPM), P.O. Box 5050, Dhahran 31261, Saudi Arabia

⁴Gas Processing Center, College of Engineering, Qatar University, P.O. Box 2713, Doha, Qatar

Correspondence should be addressed to Ibnelwaleed A. Hussein; ihussein@qu.edu.qa

Received 16 September 2015; Accepted 25 October 2015

Academic Editor: Vishal Mehta

Copyright © 2015 Umer Mehmood et al. This is an open access article distributed under the Creative Commons Attribution License, which permits unrestricted use, distribution, and reproduction in any medium, provided the original work is properly cited.

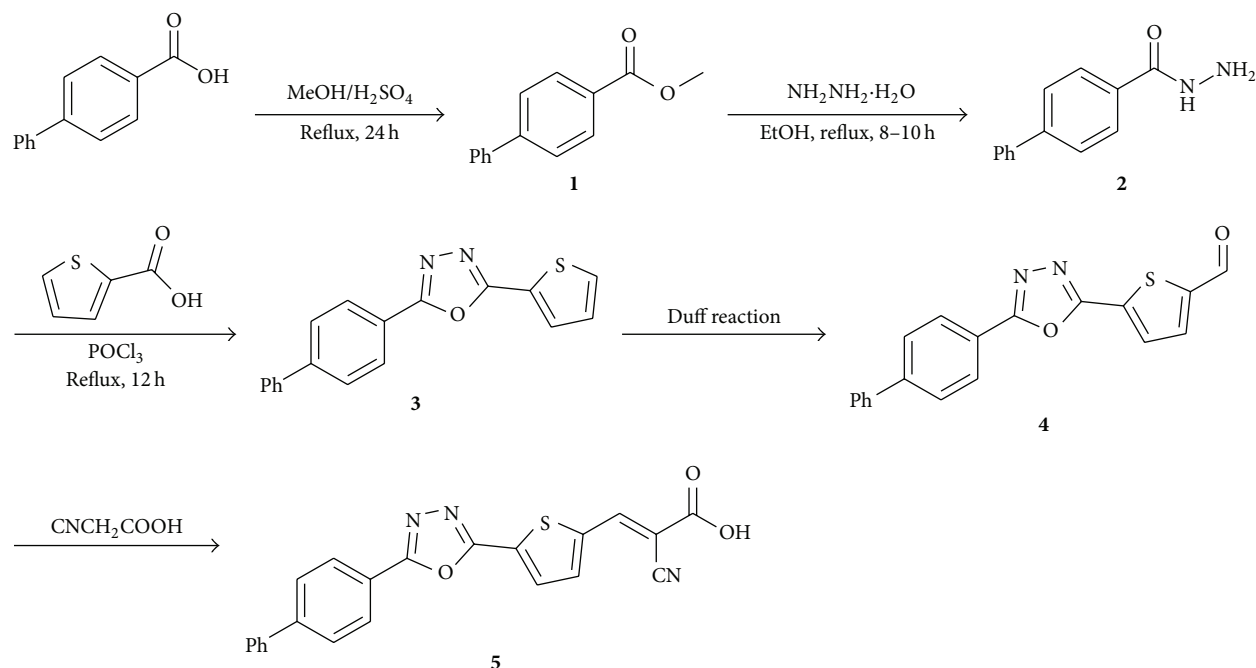
1,3,4-Oxadiazole based photosensitizers with biphenyl, naphthalene, anthracene, and triphenylamine as the electron-donating moiety were synthesized for solar cell applications. In these photosensitizers, cyano groups were introduced as the electron acceptor and the anchor group because of their high electron-withdrawing ability and strong bonding to the semiconductor. Oxadiazole isomers were used as the π -conjugation system, which bridges the donor-acceptor systems. The electrochemical and optical properties of the sensitizers were investigated both in their native form and upon incorporation into dye sensitized solar cells. The results of UV-visible absorption spectroscopy, electrochemical impedance spectroscopic measurements, and photocurrent voltage characteristics indicate that 1,3,4-oxadiazole pi-spacer with the anthracene moiety has the highest efficiency of 2.58%. Density functional theory was employed to optimize the structures of the sensitizers and the TiO₂ cluster.

1. Introduction

The wide spread application of the photovoltaic (PV) cells is limited mainly due to their high cost to energy output ratio. PV cells are generally classified as inorganic based cells and organic based ones. Inorganic PV cells (Si or quantum dots based solar cells) cost has dropped a lot in the last decades but is still noncompetitive compared to conventional electricity production sources. The motive to achieve high cost/efficiency ratios derived the emergence of the thin film dye sensitized solar cell. It was developed by O'Regan and Grätzel in 1991. The efficiency of this PV cell, which became known as dye sensitized solar cell (DSSC), was reported as 7.1 to 7.9% [1]. DSSCs have got attention due to an ideal tradeoff between efficiency and cost performance [2–5].

The dye, which is the major component of the DSSC, absorbs sunlight and produces excitons [6, 7]. It is chemically

bonded to the porous surface of a semiconductor. Currently, DSSCs based on ruthenium(II) polypyridyl complexes have the best conversion efficiencies (PCE) of 11% under standard (Global Air Mass 1.5) illumination [8–10]. But it is still low for commercial applications. The low absorption of light in the red/near infrared region (NIR) is the major drawback in the ruthenium based sensitizers that limits the further improvement in efficiency. To overcome these problems, metal-free organic sensitizers have been developed [11]. The basic structural unit of organic dye is donor- π spacer-acceptor. Substituents acting as the donor and the acceptor are separated by a π -conjugated spacer. The studies suggest that the donor groups to form efficient sensitizers should be selected from the electron rich aryl amines family including phenylamine, aminocoumarin, indoline, (difluorenyl)triphenylamine, and biphenyl. The π -conjugated connector must be selected from compounds containing thiophene and oxadiazole units



SCHEME 1: Synthesis of novel dyes.

due to their outstanding charge transfer characteristics. Acrylic acid group is considered the best acceptor moiety [12]. Tian et al. synthesized methylthiophene based photosensitizers for high-performance DSSCs. They introduced vinyl unit as pi-bridge and found that the DSSC assembled with 2-cyano-3-(5-(4-(diphenylamino)phenyl)-4-methylthiophenyl-2-yl) acrylic acid showed an efficiency of 8.27% under simulated AM 1.5 G solar irradiation (100 mW cm^{-2}) [13]. Mao et al. synthesized a series of new metal-free organic dyes with either a boron dipyrromethene (BODIPY) phenylene or thiophene as a pi-conjugated bridge. The structure-property relationship of these dyes shows that the introduction of a methoxy group as the donor and a BODIPY thiophene unit as the pi-conjugated bridge are favorable to improve the efficiency of DSSCs [14]. Diketopyrrolopyrrole (DPP) sensitizers were synthesized by Qu et al. The sensitizer containing diketopyrrolopyrrole moiety as the pi-bridge exhibited good stability and better photovoltaic performance of up to 4.41% power conversion efficiency [15].

DFT/TD-DFT is an effective tool to investigate the ground and excited state properties of photosensitizer complexes as compared to other high level quantum approaches because the computed orbitals are suitable for the typical MO-theoretical analyses and interpretations [16]. Many theoreticians have successfully applied this approach in the designing of photosensitizers [17–24].

2. Computer Simulation

Amsterdam Density Functional (ADF) program (2013.01) was used to perform the DFT calculations. Generalized gradient approximation (GGA) at OLYP level with triple- ζ polarization basis function was used to optimize structures of

TiO_2 and dyes. Relativistic effects were considered in all the calculations by applying zero order regular approximation in its scalar approximation [21, 22, 25].

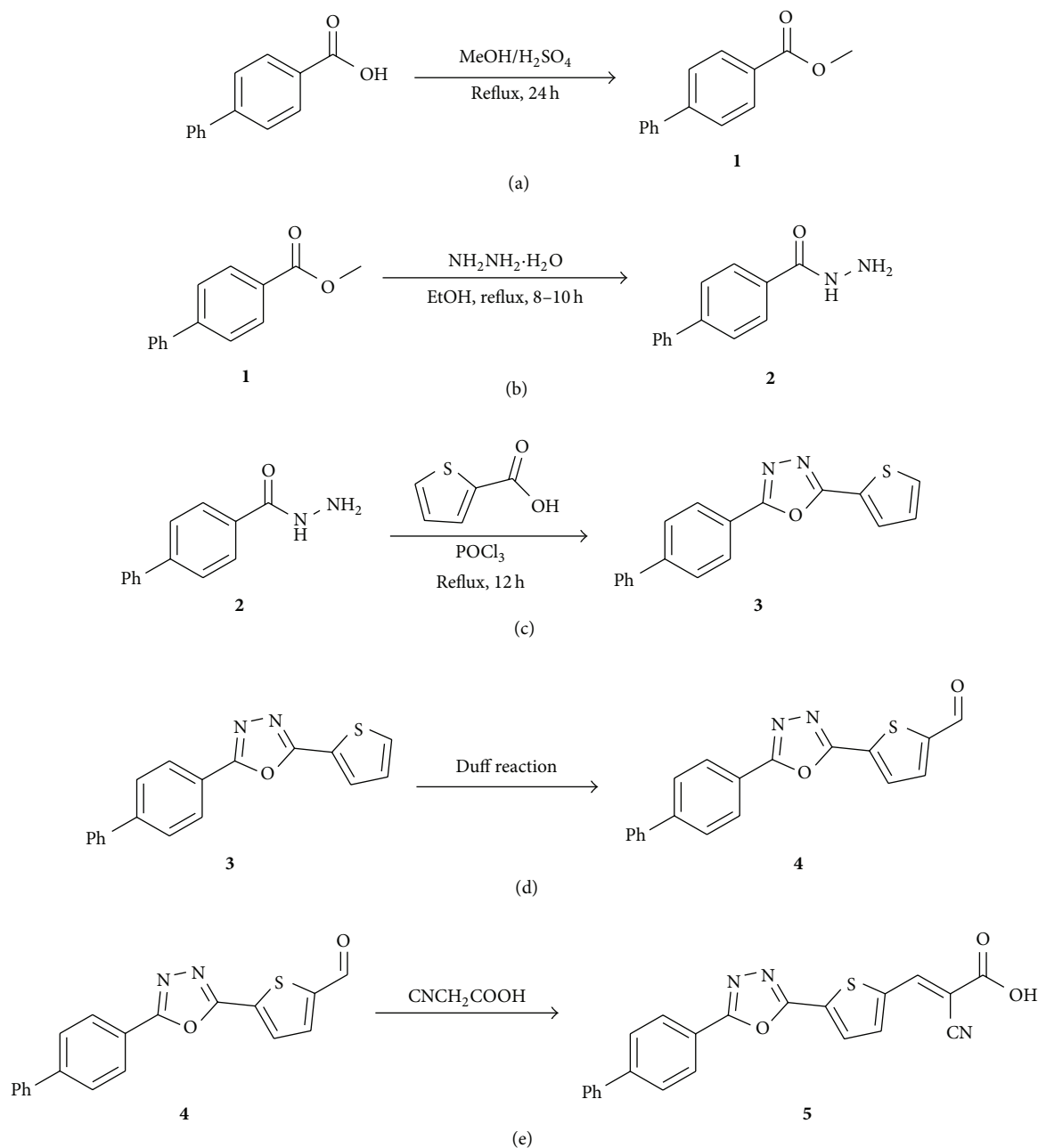
3. Synthesis of Dyes

Novel dyes were synthesized according to Scheme 1.

Step 1 (see Scheme 2(a): synthesis of ester (1)). A solution of biphenyl-4-carboxylic acid (5 g) in methanol (25 mL) in the presence of a catalytic amount of sulfuric acid (0.5 mL) was heated under reflux for 24 h. The mixture was cooled to room temperature and then concentrated in vacuo. The resulting residue was diluted with water (50 mL) and extracted with ethyl acetate ($2 \times 50 \text{ mL}$). The combined organic layers were washed with saturated sodium bicarbonate solution followed by water. The organic layer was dried over sodium sulfate and concentrated under reduced pressure to give the pure ester **1** in quantitative yield.

Step 2 (see Scheme 2(b): synthesis of hydrazide (2)). To a stirred solution of methyl biphenyl-4-carboxylate (**1**, 5 g) in ethanol (50 mL), hydrazine monohydrate (100% solution) (24 g) was added. The resulting mixture was stirred at 80°C for 8 h and then concentrated under reduced pressure. The residue was diluted with ice cooled water (50 mL) and the solid was filtered and washed with water ($2 \times 50 \text{ mL}$). The title compound was obtained as a pale amorphous solid in 88% yield.

Step 3 (see Scheme 2(c): synthesis of 1,3,4-oxadiazole (3)). To a mixture of hydrazide (**2**, 3.5 g) and thiophene-2-carboxylic



SCHEME 2

acid (2.1 g), POCl₃ (20 mL) was added slowly at room temperature and the resulting mixture was stirred for 2 h at 110°C. After the solution was cooled, excess POCl₃ was removed under reduced pressure. The residue was diluted with water and then neutralized with aqueous sodium bicarbonate. The white precipitate was collected by filtration and washed with water. The resulting solid (4.8 g) was further purified by column chromatography to give the pure oxadiazole (4 g).

Step 4 (see Scheme 2(d): formylation of thiophene ring by duff reaction (4)). A mixture of oxadiazole (3, 4 g), hexamethylenetetramine (8 g) in 40 mL of trifluoroacetic acid was heated under reflux (90–110°C). The progress of the reaction

was monitored by TLC. Up on completion, the mixture was quenched with saturated sodium bicarbonate solution. The precipitated solids were filtered and then washed with water. The resulting solid was purified by column chromatography to give the desired aldehyde 4 (2.5 g).

Step 5 (see Scheme 2(e): synthesis of cyanoacrylic acid 5 through Knoevenagel condensation (5)). To a solution of carboxaldehyde 4 (2 g) and ammonium acetate (0.1 equiv.) in acetic acid (20 mL), cyanoacetic acid was added (1.1 equiv.). The resulting mixture was heated under reflux for 4 h and the progress of the reaction was monitored by TLC. After completion, the mixture was cooled and diluted with ice water. The precipitate

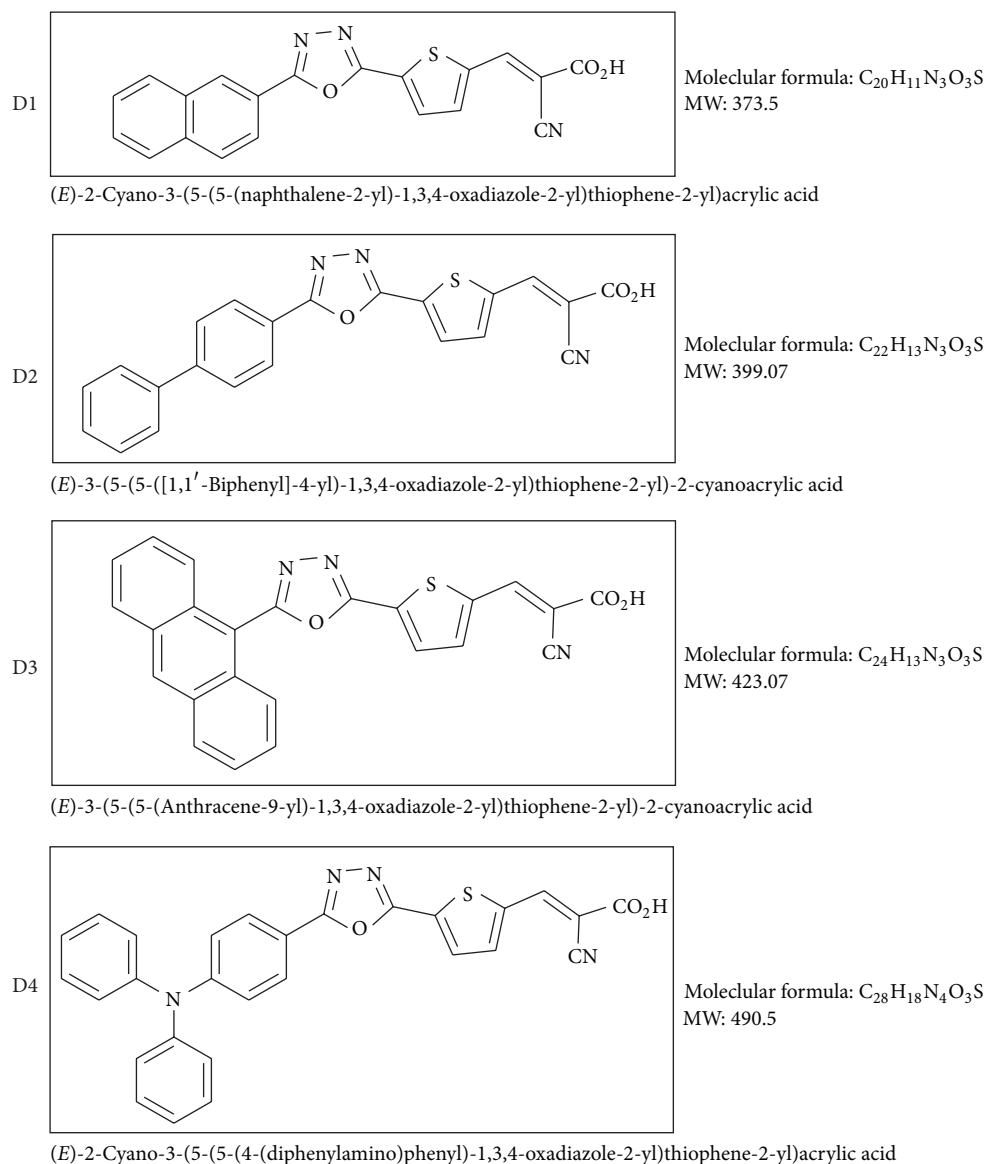


FIGURE 1: Structures of the novel 1,3,4-oxadiazole based photosensitizers.

was filtered and washed with water. The resulting solid was recrystallized from toluene: methanol mixture (9 : 1) to afford the required dye **5** in pure form.

All other dyes (D1, D3, and D4) were prepared in the same manner. The structure and names of the dyes are shown in Figure 1.

4. Fabrication and Characterization of DSSCs

A 2 mM solution of each dye was prepared in chloroform. TiO₂ paste was deposited on conductive glass substrate and then sintered at 450 °C for 30 minutes. The electrodes were immersed in the dye solution for 24 hours. After sensitization, the samples were washed with ethanol to eliminate unanchored dye. A platinum coated counter electrode was prepared by depositing platinum paste (Plastical T, Solaronix)

on FTO glass substrate and then heated at 450 °C for 10 minutes. Then, DSSCs were fabricated employing the sensitized anode, counter electrode, 60 μm sealing spacer (Meltonix 1170, Solaronix), and I⁻/I₃⁻ redox couple electrolyte prepared in methoxypropionitrile with a 50 mM redox concentration (Iodolyte Z-50, Solaronix). The visible spectra of dyes in methanol and anchored to TiO₂ films at glass substrates were recorded with JASCO-670 UV/VIS spectrophotometer. Keithley 2400 Source Meter was used to measure the *I-V* characteristics of the DSSCs using IV-5 solar simulator (Sr #83, PV Measurement, Inc.) at AM1.5G (100 mWcm⁻²). The silicon solar cell was used as a reference for calibration. The EIS was measured in dark conditions of illumination via Bio-Logic SAS (VMP3, s/n: 0373), with an AC signal of 10 mV in amplitude, in the frequency range between 10 Hz and 500 KHz.

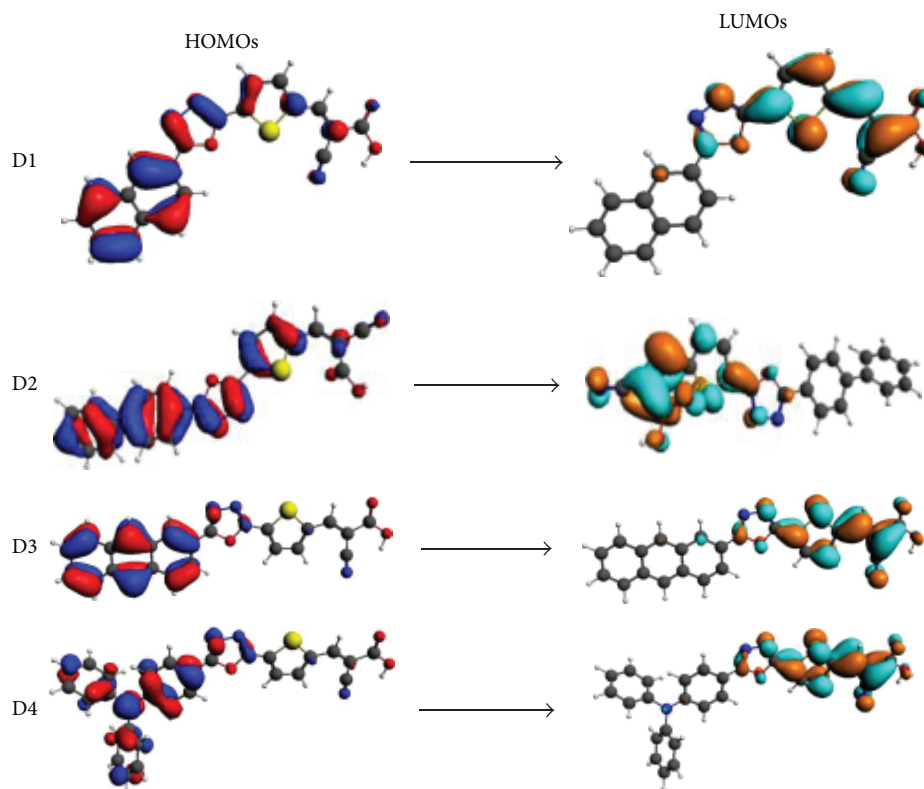


FIGURE 2: Simulated HOMOs and LUMOs of the dyes.

TABLE 1: FMO and band gaps of dyes D1 to D4.

Dyes	LUMOs (eV)	HOMOs (eV)	Band gap (eV)
D1	-3.956	-5.657	1.701
D2	-3.867	-5.682	1.815
D3	-3.694	-4.869	1.175
D4	-3.840	-5.180	1.340

5. Results and Discussion

5.1. Energy Levels of Photosensitizers. The frontier molecular orbital (FMO) of dyes provides the necessary driving force for the charge transfer. We used a DFT technique to find the band gaps of TiO_2 cluster and novel photosensitizers. The electron distribution of the HOMOs and LUMOs of D1, D2, D3, and D4 is shown in Figure 2. Clearly, the HOMOs of these compounds are the highest electron density located at donor moieties. The LUMOs are located in the anchoring group through the pi-bridge. Thus, the HOMO-LUMO excitation induced by light irradiation could move the electron distribution from the donor moieties to the anchoring unit through the pi-bridge segment. $(\text{TiO}_2)_8$ cluster was also simulated to find its conduction band (-4.0 eV) and band gap (3.18 eV).

Table 1 shows that the HOMOs of sensitizers are in the sequence of D3 (-4.689) > D4 (-5.180) > D1 (-5.657) > D2 (-5.682). The LUMOs energy levels are in the sequence of D3 (-3.694) > D4 (-3.840) > D2 (-3.867) > D1 (-3.956). The electron-donating moieties significantly affect the HOMO

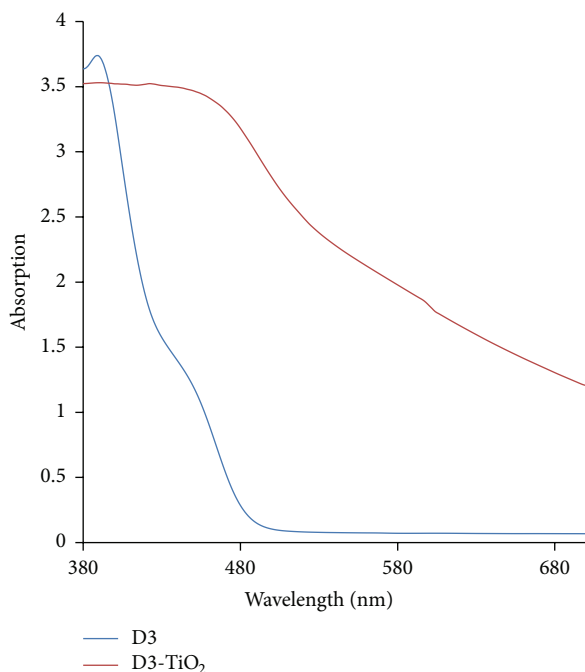
and LUMO energy levels of the dyes. Similarly, the $H-L_{\text{gap}}$ of the dyes are in the order of D3 (1.175) < D4 (1.340) < D1 (1.701) < D2 (1.815). These results suggest that dyes 1–4 can inject electrons to the conduction band of titanium oxide.

5.2. Absorption Spectra of Dyes. The absorption spectra of D3 in chloroform and adsorbed on TiO_2 are shown in Figure 3. Two distinct absorption bands of D3 in chloroform can be observed: one relatively weak band is in the region (380–400 nm) corresponding to the $\pi-\pi^*$ electron transitions of the conjugated molecules and the other is around 430–460 nm that can be assigned to an intramolecular charge transfer (ICT) between electron-donor and electron acceptor anchoring moieties. However, the absorption shifts to lower energy values when anchored to TiO_2 . This is due to the fact that on the electrode the carboxylate groups bind to the TiO_2 surface in which Ti^{4+} acts as proton. The interaction between the carboxylate group and the surface Ti^{4+} ions may lead to increased delocalization of the π^* orbital. The energy of the π^* level is decreased by this delocalization, which explains the red shift for the absorption spectra.

5.3. Photovoltaic Performance. DSSCs were fabricated using D1, D2, D3, and D4 dyes having an effective area of 0.35 cm^2 . The photovoltaic parameters of DSSCs are recorded in Table 2 and the corresponding photocurrent voltage ($J-V$) characteristics are showed in Figure 4. Solar cell based on D3 sensitizer shows the best performance among the four dyes. It can be

TABLE 2: PV properties of DSSCs.

Dyes	j_{sc} (mA/cm ²)	V_{oc} (mV)	FF (%)	η (%)
D1	0.479	448	50	0.11
D2	0.952	455	51	0.23
D3	8.178	632	50	2.58
D4	2.196	587	40	0.52

FIGURE 3: Absorption spectra of D3 in chloroform and anchored to TiO₂.

clearly seen that the electron donor moiety of dyes plays a key role in the photovoltaic performance. Thus, introducing the anthracene unit as an electron donor moiety improves the photocurrent of DSSC. Moreover, the higher HOMO and LUMO energy levels of D3 do not only generate charge separation but also accelerate the dye regeneration to avoid charge recombination.

5.4. EIS Analysis. EIS analysis is performed to investigate the interface resistances in DSSCs. Figure 5 shows the Nyquist plot of DSSCs which were assembled with novel photosensitizers. Generally, a normal impedance spectrum of DSSCs is represented by three arcs (semicircles). The first semicircle represents the resistance of electron transfer at counter electrode/electrolyte (R_1), second signifies the resistance of charge transfer at the photoanode/electrolyte interface (R_2), and third indicates the diffusion of I^-/I_3^- in electrolyte (Zw) [26, 27]. Only second arc comes out in the Nyquist plot in Figure 5. It is probable that the other two arcs corresponding to R_1 and Zw are overshadowed by large semicircle representing R_2 [28, 29]. The R_2 signifies the charge recombination rate; for example, a larger R_2 specifies a slower charge recombination. The R_2 value for DSSC assembled with

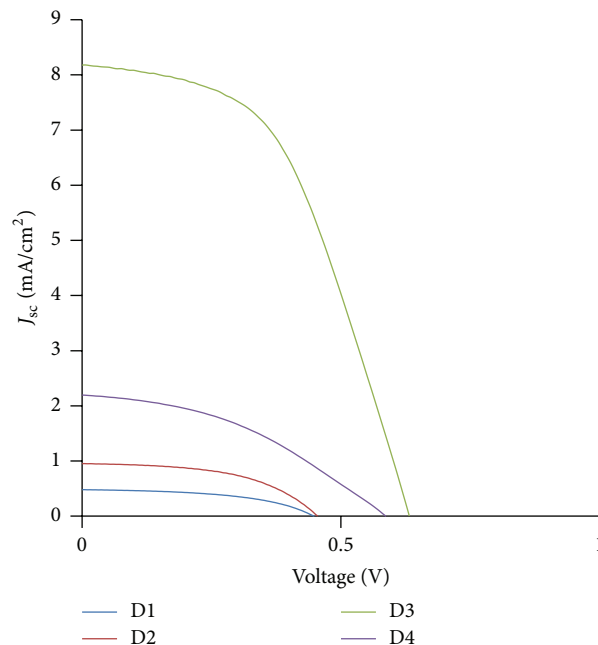


FIGURE 4: Current-voltage curves of DSSCs.

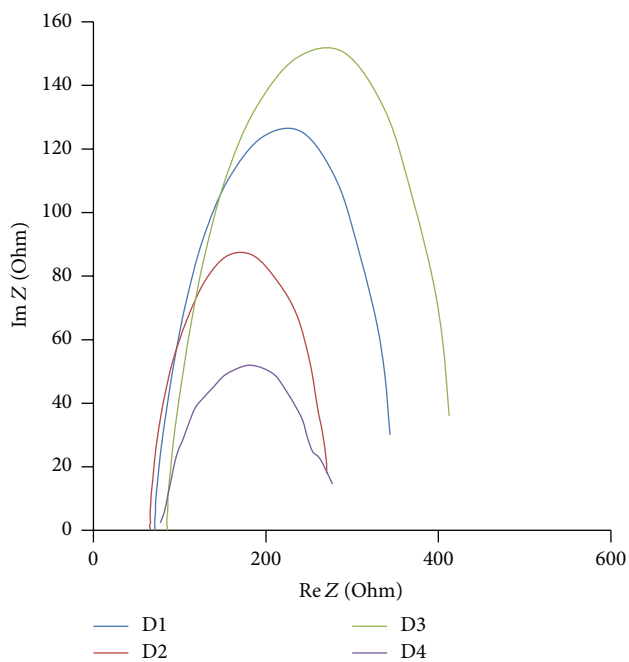


FIGURE 5: Nyquist plots of the DSSCs.

D3 is greater than that of D1, D2, and D4. The higher R_2 of D3 relative to D1, D2, and D4 could be attributed to the steric hindrance of the bulky anthracene unit.

6. Conclusion

A series of novel dyes D1, D2, D3, and D4 have been prepared for DSSCs. The results indicate that the donor moiety in organic dyes strongly influences the performance of DSSCs.

The incorporation of anthracene unit as a donor moiety improves the efficiency of DSSC as compared to other donor units, that is, biphenyl, naphthalene, and triphenylamine. Among the four photosensitizers synthesized, maximum efficiency of 2.58% was obtained with DSSCs based on D3 ($J_{sc} = 8.178 \text{ mA/cm}^2$, $V_{oc} = 632 \text{ mV}$, $FF = 0.5$). These results advocates that the photosensitizers based on anthracene unit are auspicious candidates for DSSCs.

Conflict of Interests

The authors declare that there is no conflict of interests regarding the publication of this paper.

Acknowledgments

The authors would like to acknowledge the funding provided by King Abdulaziz City for Science and Technology (KACST) through Project no. 11-ENE1635-04 as part of the National Science, Technology and Innovation Plan. The authors would like to acknowledge the Center of Research Excellence for Renewable Energy at KFUPM.

References

- [1] B. O'Regan and M. Grätzel, "A low-cost, high-efficiency solar cell based on dye-sensitized colloidal TiO_2 films," *Nature*, vol. 353, pp. 737–740, 1991.
- [2] N. Robertson, "Optimizing dyes for dye-sensitized solar cells," *Angewandte Chemie—International Edition*, vol. 45, no. 15, pp. 2338–2345, 2006.
- [3] A. Hagfeldt, G. Boschloo, L. Sun, L. Kloo, and H. Pettersson, "Dye-sensitized solar cells," *Chemical Reviews*, vol. 110, no. 11, pp. 6595–6663, 2010.
- [4] C. Klein, M. K. Nazeeruddin, P. Liska et al., "Engineering of a novel ruthenium sensitizer and its application in dye-sensitized solar cells for conversion of sunlight into electricity," *Inorganic Chemistry*, vol. 44, no. 2, pp. 178–180, 2005.
- [5] U. Mehmood, S. Ahmed, I. A. Hussein, and K. Harrabi, "Co-sensitization of TiO_2 -MWCNTs hybrid anode for efficient dye-sensitized solar cells," *Electrochimica Acta*, vol. 173, pp. 607–612, 2015.
- [6] U. Mehmood, S. Ahmed, I. A. Hussein, and K. Harrabi, "Improving the efficiency of dye sensitized solar cells by TiO_2 -graphene nanocomposite photoanode," *Photonics and Nanostructures—Fundamentals and Applications*, vol. 16, pp. 34–42, 2015.
- [7] U. Mehmood, K. Harrabi, I. A. Hussein, and S. Ahmed, "Enhanced photovoltaic performance of dye-sensitized solar cells using TiO_2 -graphene microplatelets hybrid photoanode," *IEEE Journal of Photovoltaics*, 2015.
- [8] M. K. Nazeeruddin, F. De Angelis, S. Fantacci et al., "Combined experimental and DFT-TDDFT computational study of photoelectrochemical cell ruthenium sensitizers," *Journal of the American Chemical Society*, vol. 127, no. 48, pp. 16835–16847, 2005.
- [9] F. Gao, Y. Wang, D. Shi et al., "Enhance the optical absorptivity of nanocrystalline TiO_2 film with high molar extinction coefficient ruthenium sensitizers for high performance dye-sensitized solar cells," *Journal of the American Chemical Society*, vol. 130, no. 32, pp. 10720–10728, 2008.
- [10] C.-Y. Chen, M. Wang, J.-Y. Li et al., "Highly efficient light-harvesting ruthenium sensitizer for thin-film dye-sensitized solar cells," *ACS Nano*, vol. 3, no. 10, pp. 3103–3109, 2009.
- [11] U. Mehmood, S.-U. Rahman, K. Harrabi, I. A. Hussein, and B. V. S. Reddy, "Recent advances in dye sensitized solar cells," *Advances in Materials Science and Engineering*, vol. 2014, Article ID 974782, 12 pages, 2014.
- [12] C. Wang, G.-Y. Jung, Y. Hua et al., "An efficient pyridine- and oxadiazole-containing hole-blocking material for organic light-emitting diodes: synthesis, crystal structure, and device performance," *Chemistry of Materials*, vol. 13, no. 4, pp. 1167–1173, 2001.
- [13] Z. Tian, M. Huang, B. Zhao et al., "Low-cost dyes based on methylthiophene for high-performance dye-sensitized solar cells," *Dyes and Pigments*, vol. 87, no. 3, pp. 181–187, 2010.
- [14] M. Mao, J.-B. Wang, Z.-F. Xiao, S.-Y. Dai, and Q.-H. Song, "New 2,6-modified BODIPY sensitizers for dye-sensitized solar cells," *Dyes and Pigments*, vol. 94, no. 2, pp. 224–232, 2012.
- [15] S. Qu, B. Wang, F. Guo et al., "New diketo-pyrrolo-pyrrole (DPP) sensitizer containing a furan moiety for efficient and stable dye-sensitized solar cells," *Dyes and Pigments*, vol. 92, no. 3, pp. 1384–1393, 2012.
- [16] G. te Velde, F. M. Bickelhaupt, E. J. Baerends et al., "Chemistry with ADF," *Journal of Computational Chemistry*, vol. 22, no. 9, pp. 931–967, 2001.
- [17] J. Wang, H. Li, N.-N. Ma, L.-K. Yan, and Z.-M. Su, "Theoretical studies on organoimido-substituted hexamolybdates dyes for dye-sensitized solar cells (DSSC)," *Dyes and Pigments*, vol. 99, no. 2, pp. 440–446, 2013.
- [18] W. Fan, D. Tan, and W.-Q. Deng, "Acene-modified triphenylamine dyes for dye-sensitized solar cells: a computational study," *ChemPhysChem*, vol. 13, no. 8, pp. 2051–2060, 2012.
- [19] W. Sang-aroon, S. Saekow, and V. Amornkitbamrung, "Density functional theory study on the electronic structure of Monascus dyes as photosensitizer for dye-sensitized solar cells," *Journal of Photochemistry and Photobiology A: Chemistry*, vol. 236, pp. 35–40, 2012.
- [20] X. Zarate, E. Schott, T. Gomez, and R. Arratia-Pérez, "Theoretical study of sensitizer candidates for dye-sensitized solar cells: peripheral substituted dizinc pyrazinoporphyrazine-phthalocyanine complexes," *The Journal of Physical Chemistry A*, vol. 117, no. 2, pp. 430–438, 2013.
- [21] U. Mehmood, I. A. Hussein, M. Daud, S. Ahmed, and K. Harrabi, "Theoretical study of benzene/thiophene based photosensitizers for dye sensitized solar cells (DSSCs)," *Dyes and Pigments*, vol. 118, pp. 152–158, 2015.
- [22] U. Mehmood, I. A. Hussein, K. Harrabi, and B. V. Reddy, "Density functional theory study on dye-sensitized solar cells using oxadiazole-based dyes," *Journal of Photonics for Energy*, vol. 5, no. 1, Article ID 053097, 2015.
- [23] D. Rocca, R. Gebauer, F. De Angelis, M. K. Nazeeruddin, and S. Baroni, "Time-dependent density functional theory study of squaraine dye-sensitized solar cells," *Chemical Physics Letters*, vol. 475, no. 1–3, pp. 49–53, 2009.
- [24] U. Mehmood, I. A. Hussein, K. Harrabi, M. Mekki, S. Ahmed, and N. Tabet, "Hybrid TiO_2 -multiwall carbon nanotube (MWCNTs) photoanodes for efficient dye sensitized solar cells (DSSCs)," *Solar Energy Materials and Solar Cells*, vol. 140, pp. 174–179, 2015.

- [25] U. Mehmood, I. A. Hussein, K. Harrabi, and S. Ahmed, "Density functional theory study on the electronic structures of oxadiazole based dyes as photosensitizer for dye sensitized solar cells," *Advances in Materials Science and Engineering*, vol. 2015, Article ID 286730, 8 pages, 2015.
- [26] K. Lee, C. Hu, H. Chen, and K. Ho, "Incorporating carbon nanotube in a low-temperature fabrication process for dye-sensitized TiO₂ solar cells," *Solar Energy Materials and Solar Cells*, vol. 92, no. 12, pp. 1628–1633, 2008.
- [27] Y.-L. Xie, Z.-X. Li, Z.-G. Xu, and H.-L. Zhang, "Preparation of coaxial TiO₂/ZnO nanotube arrays for high-efficiency photo-energy conversion applications," *Electrochemistry Communications*, vol. 13, no. 8, pp. 788–791, 2011.
- [28] S. Li, Y. Lin, W. Tan et al., "Preparation and performance of dye-sensitized solar cells based on ZnO-modified TiO₂ electrodes," *International Journal of Minerals, Metallurgy, and Materials*, vol. 17, no. 1, pp. 92–97, 2010.
- [29] A. S. Nair, R. Jose, Y. Shengyuan, and S. Ramakrishna, "A simple recipe for an efficient TiO₂ nanofiber-based dye-sensitized solar cell," *Journal of Colloid and Interface Science*, vol. 353, no. 1, pp. 39–45, 2011.